



UNIVERSITAT
ROVIRA i VIRGILI

Solar-driven hybrid refrigeration systems based on thermochemical processes

JAUME FITÓ DE LA CRUZ

**DOCTORAL THESIS
2017**

Jaume Fitó de la Cruz

**SOLAR-DRIVEN HYBRID REFRIGERATION SYSTEMS BASED
ON THERMOCHEMICAL PROCESSES**

DOCTORAL THESIS

Supervised by
Prof. Alberto Coronas
Prof. Sylvain Mauran

Department of Mechanical Engineering



**UNIVERSITAT
ROVIRA i VIRGILI**

Tarragona, October 2017

“This page intentionally left blank”



UNIVERSITAT
ROVIRA I VIRGILI

DEPARTAMENT D'ENGINYERIA MECÀNICA

Escola Tècnica Superior d'Enginyeria Química (ETSEQ).
Avgda Paisos Catalans, 26 ; 43007 Tarragona (Spain)

Declaration

We STATE that the present study, entitled “Solar-driven hybrid refrigeration systems based on thermochemical processes”, presented by Jaume Fitó de la Cruz for the award of the degree of Doctor, has been carried out under our supervision at the CREVER research group in the Department of Mechanical Engineering of this university, and that it fulfills all the requirements to be eligible for the International Doctorate Award.

Tarragona, October 6th, 2017

*Prof. Dr. Alberto Coronas
Universitat Rovira i Virgili (Spain)*

*Prof. Dr. Sylvain Mauran
Univ. de Perpignan Via Domitia (France)*

“This page intentionally left blank”

A mis padres.

“This page intentionally left blank”

Acknowledgements

My deepest gratitude is for my advisor, Prof. Dr. Alberto Coronas, who believed in my potential and invested the effort and resources without which this doctoral thesis would not have been possible to begin with. I appreciate every single advice he gives me. His tenacity inspires and boosts the motivation of everyone around him. I thank him for his guidance and his patience with me, and I sincerely hope my general performance met (at least) his high expectations. Any further acknowledgement in this list exists thanks to his decision of accepting me in his research group (the CREVER) in the first place.

I wholeheartedly thank Prof. Dr. Sylvain Mauran, from the PROMES laboratory in France, for his wise guidance as co-advisor of my doctoral thesis. I also thank Dr. Nathalie Mazet, Dr. Maxime Perier-Muzet and Dr. Driss Stitou for their collaboration in our studies and their advices during the course of my thesis. This acknowledgement is extensible to all those students and staff members who helped me during my stays at PROMES.

My thanks to Dr. Manel Vallès, Dr. Daniel Salavera, Dr. Joan Carles Bruno, Dr. Mahmoud Bourouis and Dr. Juan Prieto for their kind help and their patient answers to my never-ending questions about the design of my experimental setup. Thanks to Dr. Dereje Sendeku Ayou for his help during my first steps as a PhD student.

My thanks to Prof. M. P. Maiya for accepting my stay at the Indian Institute of Technology Madras (IITM) in the frame of the NARILAR project. I extend my thankfulness and appreciation to every other student or staff member that made my stay quite pleasant: Guru Balan, Gokul Raj, Isabella, Anurak, Yadu, Harish, Vijesh, and many others. I do not have enough words to describe the great hospitality of each and every person I met there.

I thank my former and current colleagues of the CREVER research group, as well as staff members: Adriana, Hifni, Maycon, Miguel Ángel (shout-out to the pressure transmitters of his idle experimental setup, which protected me from a sudden and inconvenient 3-week delay), Andry, Isabel, Antonio, Felipe, Arturo, Maria José, Samuel, Rubén, Sergi and many others. I also thank Esteban for his help in building the experimental setup.

I bid farewell to my late lab colleague, James Muye Mwangome, who passed away on 11 August, 2017. Thanks, James, for almost 3 years of enriching work-related discussions and interesting conversations about science, economy, religion or just life in general. Thank you for your huge help while I was building my experimental setup. You were a really nice person to share office with, and I send my condolences to your family and friends. The Lord claimed your soul shortly before you could defend your thesis, but to my eyes, you are a doctor. See you on the other side, Dr. James Muye Mwangome.

This thesis is dedicated to my parents, Jaime and Julia. I would have never made it this far without them. I thank my sister, Mercedes, all my relatives (grandparents, uncles, aunts, cousins...) and all my friends, for their warm support and understanding, and for giving my personal life a meaning and a purpose.

Last, but certainly not least, I thank God. I am convinced of Its existence and desire for our happiness and self-fulfillment. Its help comes in so subtle ways, that we tend to think that either luck or our overestimated intelligence solved the problem. Behind every stroke of luck, opportune idea, successful decision or kind person willing to help us, the Love of God is there.

Abstract

The field of refrigeration is affected either directly or indirectly by all forecasted concerns on global warming, population increase, price rise and uncertain availability of fossil fuels. Renewable energy sources are a promising response, and among these, solar energy has yield satisfying results in refrigeration. A shortcoming of this source is its intermittence, which is classically solved with auxiliary primary energy coming from fossil fuels. Another solution is to increase the solar coverage through sensible or latent thermal storage, with some drawbacks related to thermal losses.

Thermochemical processes are based on an interaction (either sorption or reaction) between a gas and a sorbent or a reactive salt, which is usually in solid state. These systems can be applied to refrigeration and can store energy. Given the nature of the process, the heat supplied to the system is not affected by thermal losses and can be stored for relatively long amounts of time. In addition, the higher energy density of these systems (up to 10-fold and 4-fold that of sensible and latent storage, respectively) reduces the volume of equipment per unit mass of refrigerant. The fact that these systems store liquefied refrigerant, which can be stored indefinitely at ambient temperature and immediately released for cold production, is also worth mentioning.

A major drawback of thermochemical systems is the intermittence of the process itself, because the sorbent pair or reactive salt are in solid state. Unless this intermittence is solved, it is a limitation for applications where there is a continuous demand of cold.

To overcome this limitation, this thesis proposes hybrid refrigeration systems that revolve around thermochemical processes. The novelty lies in the hybridization with well-known, state-of-the-art refrigeration systems. The resulting hybrid systems are expected to operate with solar energy, store energy, and have a small degree of autonomy (a few hours within a daily operating cycle). In addition, some of the components are shared by the two processes, making the overall system compact.

Two solar-based energy sources were targeted: on one hand, low-grade solar thermal energy (< 120 °C), which can be utilized for single-effect absorption refrigeration cycles; on the other hand, solar-PV energy, which can be applied for compression refrigeration cycles. As a result, this thesis proposes two solar-driven hybrid refrigeration systems with thermochemical processes as the central piece. In both systems, the refrigerant fluid, the condenser and the evaporator are shared by the subsystems, for the sake of compactness.

The first one is an absorption/thermochemical (ABS/TCH) hybrid system driven by low-grade solar thermal energy ($< 120\text{ }^{\circ}\text{C}$). The configuration, components, pressure and temperature levels and operating modes are discussed. A preliminary performance estimation with some ammonia-based and water-based working pairs finds the NH_3/NaSCN and $\text{NH}_3/\text{BaCl}_2$ pairs suitable for the ABS and TCH subsystems, respectively. A preliminary evaluation of the hybrid system in a simulated application shows that, with increasing mass of stored refrigerant and area of solar collector field, solar coverage increases from that of solar absorption without storage to a limit value (< 1), while the global COP decreases from that of the ABS subsystem (around 0.7) to that of the TCH subsystem (around 0.3).

The second hybrid system consists of compression/thermochemical (COMP/TCH) refrigeration and is driven by solar-PV electricity or grid-distributed electricity. It also requires a heat source, but thanks to the compressor, it can utilize low-grade sources (as low as $30\text{ }^{\circ}\text{C}$), which is interesting for waste heat utilization. After system definition, operating modes description and working pair selection, the study focuses on simulating the compression-assisted decomposition phase in the TCH subsystem. A 2-front quasi-steady reaction model is presented which allows to account for heat and mass transfer limitations. This model is used to preliminarily study the influence of some operating conditions and design parameters on the system's advancement degree - reaction time ($X-t$) curve.

The 2-front reaction model is later validated through an experimental study of the non-assisted and compression-assisted decomposition phases of the TCH subsystem. An experimental setup was built similar to the COMP/TCH hybrid system, with all measurements focused on the reactor/compressor interaction. The experiments showed activation temperature reduction of the TCH process and yielded enough experimental data for model validation. The values of permeability and thermal conductivity of the reactive salt were adjusted for a non-assisted decomposition phase, and after adjustment, model predictions were confronted to the remaining decomposition phase experiments, as well as synthesis phase and, finally, compression-assisted decomposition phase. It is concluded that the adjusted model predicts the $X-t$ curve with acceptable accuracy for almost all experiments, with some discrepancies in the compression-assisted decomposition phase.

The systems proposed in this doctoral thesis are interesting in their concept, and the first results seem promising for further research.

Keywords: *Solar refrigeration, hybrid systems, thermochemical heat transformer, performance simulation, experimental study.*

Contributions by the author

Articles in Peer-Reviewed Scientific Journals

- **Fitó J.**, Mauran S., Stitou D., Mazet N., Coronas A. Definition, simulation and parametric study of a solar-driven hybrid absorption-thermochemical refrigeration system. *Applied Energy*. (*Manuscript in preparation*)
- **Fitó J.**, Mauran S., Stitou D., Mazet N., Coronas A. Definition, performance simulation and experimental validation of a solar-driven hybrid compression-thermochemical refrigeration system. *Energy Conversion and Management*. (*Manuscript in preparation*)
- **Fitó J.**, Mauran S., Stitou D., Mazet N., Coronas A. Definition of performance indicators for solar-driven hybrid refrigeration systems based on thermochemical processes. *Solar Energy*. (*Manuscript in preparation*)

Papers in Congresses, Conferences, Seminars, Workshops and Symposia

- **Fitó, J.**, Mauran, S., Stitou, D., Mazet, N., Coronas, A. (2015). New solar hybrid absorption/thermochemical refrigeration cycle. Proceedings of the 28th International Conference on Efficiency, Cost, Optimization, Simulation and Environmental Impact of Energy Systems (ECOS2015), Pau, France. ISBN: 978-2-9555539-0-9. (*Oral presentation*)
- **Fitó, J.**, Mauran, S., Stitou, D., Mazet, N., Coronas, A. (2015). Simulation of a solar hybrid absorption/thermochemical refrigeration system for a residential application. Proceedings of the 9th National Congress on Thermodynamics Engineering (CNIT2015), Cartagena, Spain. (*Oral presentation*)
- **Fitó J.**, Mauran S., Stitou D., Mazet N., Coronas A. (2015). Solar absorption/thermochemical hybrid refrigeration systems. I Jornadas Hispano-Brasileñas de Sostenibilidad Energética en Edificios y Procesos, Tarragona, Spain. (*Oral presentation*)
- **Fitó J.**, Mauran S., Coronas A. (2016). Development of solar-driven hybrid refrigeration cycles with thermochemical storage. 6th International Seminar on Thermodynamic Engineering of Fluids (ISTEF2016), Tarragona, Spain. (*Oral presentation*)

- **Fitó, J., Mauran, S., Stitou, D., Mazet, N., Coronas, A. (2016).** Solar-driven hybrid absorption-thermochemical refrigeration systems: performance estimation. Proceedings of the 12th IIR Gustav Lorentzen Natural Working Fluids Conference (GL2016), Edinburgh, United Kingdom. (*Oral presentation*)
- **Fitó, J., Mauran, S., Stitou, D., Mazet, N., Coronas, A. (2016).** Performance study of a solar-driven hybrid compression-thermochemical refrigeration cycle with energy storage. IVth International Symposium on Innovative Materials for Processes in Energy Systems (IMPRES2016), Taormina, Italy. (*Poster presentation*)
- **Fitó, J., Mauran, S., Stitou, D., Mazet, N., Coronas, A. (2017).** Modeling and numerical simulation of a compression-assisted thermochemical refrigeration system activated with low-grade heat. 10th National Congress on Thermodynamics Engineering (CNIT2017), 28-30 June, Lleida, Spain. (*Oral presentation*)
- **Fitó J., Mauran S., Stitou D., Mazet N., Coronas A. (2017).** Experimental study of a thermochemical refrigeration system assisted with vapor compression. 7th International Seminar on Thermodynamic Engineering of Fluids (ISTEF2017), Tarragona, Spain. (*Oral presentation*)

Contents

Declaration	iii
Dedication	v
Acknowledgements	vii
Abstract	ix
Contributions by the author	xi
Contents	xv
List of figures	xviii
List of tables	xxii
Nomenclature	xxiii
1 Introduction and thesis objectives	1-1
1.1 Thermochemical processes	1-4
1.2 Solar refrigeration with energy storage	1-8
1.3 Hybridization of thermochemical processes with continuous refrigeration systems	1-13
1.4 General and specific thesis objectives	1-14
1.5 Thesis structure	1-16
1.6 References	1-17
2 Solar hybrid absorption / thermochemical refrigeration system	2-1
2.1 Introduction and objectives	2-1
2.2 System description	2-1
2.2.1 Components	2-1
2.2.2 Operating modes	2-4
2.2.2.1 "ABS" mode	2-5
2.2.2.2 "TCH-charge" mode	2-8
2.2.2.3 "ABS + TCH-charge" mode	2-9
2.2.2.4 "TCH-discharge" mode	2-10
2.2.2.5 "ABS + TCH-discharge" mode	2-12
2.2.2.6 "OFF" mode	2-13
2.3 System preliminary design	2-13
2.3.1 Working pair selection	2-13
2.3.1.1 Discussion and pre-selection	2-14
2.3.1.2 Analysis and selection	2-17
2.3.1.3 System operating conditions	2-20
2.3.2 Performance simulation	2-21
2.3.2.1 Hypotheses and assumptions	2-21
2.3.2.2 Simulation model	2-21
2.3.2.3 Preliminary sensitivity study	2-25
2.3.2.4 Preliminary yearly simulation	2-26
2.4 Results and discussion	2-31
2.4.1 Absorption subsystem	2-31

2.4.2	Thermochemical subsystem	2-31
2.4.3	Hybrid system preliminary yearly simulation	2-41
2.5	Conclusions and perspectives	2-45
2.6	References	2-45
3	Solar hybrid compression / thermochemical refrigeration system	3-1
3.1	Introduction and objectives	3-1
3.2	System description	3-4
3.2.1	Components	3-4
3.2.2	Operating modes	3-7
3.2.2.1	“COMP” mode	3-8
3.2.2.2	“TCH-charge” mode	3-9
3.2.2.3	“COMP + TCH-charge” mode	3-10
3.2.2.4	“TCH-discharge” mode	3-11
3.2.2.5	“COMP + TCH-discharge” mode	3-12
3.2.2.6	“OFF” mode	3-13
3.3	System preliminary design	3-13
3.3.1	Working pair selection	3-13
3.3.2	Application and operating conditions	3-14
3.3.3	Considerations about the compressor	3-14
3.3.4	Equilibrium drop	3-15
3.4	Quasi-steady simulation model	3-16
3.4.1	Hypotheses and assumptions	3-16
3.4.2	Variables and parameters	3-20
3.4.3	Model equations	3-20
3.5	Simulation results and discussion	3-22
3.5.1	Reactor pressure and reaction advancement degree	3-22
3.5.2	Influence of thermal conductivity	3-23
3.5.3	Influence of permeability	3-23
3.6	Conclusions and perspectives	3-25
3.7	References	3-26
4	Experimental study of the compression-assisted decomposition phase in the hybrid compression / thermochemical refrigeration system	4-1
4.1	Introduction and objectives	4-1
4.2	Methodology	4-2
4.2.1	System design	4-2
4.2.1.1	Application	4-3
4.2.1.2	Working pair	4-4
4.2.1.3	Dimensioning	4-4
4.2.2	Experimental design	4-7
4.2.3	Data treatment	4-8
4.3	Setup description	4-9
4.3.1	Components	4-9
4.3.1.1	Thermochemical reactor	4-11

4.3.1.2	Solid composite	4-14
4.3.1.3	Vapor compressor	4-14
4.3.1.4	Ammonia reservoir tank and level indicator	4-15
4.3.1.5	Condenser and evaporator	4-15
4.3.1.6	Thermal baths	4-16
4.3.1.7	Data acquisition unit	4-16
4.3.1.8	Other components	4-17
4.3.2	Main operating modes and procedures	4-19
4.3.2.1	Compression-assisted decomposition phase	4-19
4.3.2.2	Synthesis phase	4-20
4.3.2.3	Non-assisted decomposition phase	4-21
4.3.2.4	Compression refrigeration subcycle (unused)	4-21
4.3.3	Auxiliary procedures	4-23
4.3.3.1	Sensor calibration	4-23
4.3.3.2	Leak tests	4-23
4.3.3.3	Composite preparation and charge into the reactor	4-23
4.3.3.4	Salt dehydration	4-24
4.3.3.5	Charge of ammonia	4-25
4.4	Results and discussion	4-26
4.4.1	Analysis of results	4-26
4.4.2	Model validation	4-31
4.4.2.1	Criteria	4-31
4.4.2.2	Parameter adjustment	4-32
4.4.2.3	Model-Experiments confrontation	4-35
4.5	Conclusions and perspectives	4-42
4.6	References	4-43
5	General conclusion and future outlook	5-1
5.1	General conclusion	5-1
5.2	Future outlook	5-2
Appendices		
A	EES code and additional results of the preliminary parametric study of the hybrid absorption / thermochemical refrigeration system	A-1
B	Matlab code for simulation of the synthesis and decomposition phases of the hybrid compression / thermochemical refrigeration system	A-14
C	Technical specifications of the main components of the setup for experimental study of the non-assisted and compression-assisted decomposition phase	A-26
D	Detailed procedures for manipulation of the setup inspired on the hybrid compression / thermochemical refrigeration system	A-36
E	Extended results from the experimental study of the synthesis, decomposition and compression-assisted decomposition phases of the hybrid compression/thermochemical refrigeration system	A-50

List of Figures

Figure 1.1	Prototype of a cascaded thermochemical process driven by solar thermal energy for deep-freezing [27].	1-8
Figure 1.2	Illustrative graph of the mismatch between on-site power generation and load curves, with power shortage area (I), power surplus area (II) and generation/consumption matching area (III) [30].	1-9
Figure 1.3	Experimental setup (before insulation) built by N'Tsoukpoe K.E. [33] for the study of a LiBr-H ₂ O absorption process for long-term solar thermal storage.	1-10
Figure 1.4	Flow diagram of a solar powered absorption refrigeration system with the H ₂ O/LiBr working pair and advanced energy storage technology [16].	1-11
Figure 1.5a	Diagram of experimental setup with SrBr ₂ /H ₂ O working pair for thermal storage of solar energy [37].	1-12
Figure 1.5b	Picture of the reactor prototype [37].	1-12
Figure 2.1a	Flow diagram of the hybrid absorption / thermochemical system (basic configuration).	2-2
Figure 2.1b	Temperature and pressure levels of the system on the Clausius-Clapeyron diagram.	2-2
Figure 2.2	"ABS" operating mode represented on a Solar Hybrid Absorption Thermochemical Refrigeration System (SHATRS).	2-6
Figure 2.3a	"ABS" operating mode represented on the flow diagram of the Hybrid Absorption / Thermochemical Refrigeration System (HATRS).	2-7
Figure 2.3b	"ABS" operating mode represented on the Clausius-Clapeyron diagram.	2-7
Figure 2.4a	"TCH-charge" mode shown in the basic configuration.	2-8
Figure 2.4b	"TCH-charge" mode shown on the Clausius-Clapeyron diagram.	2-8
Figure 2.5	"TCH-charge" mode shown on the SHATRS.	2-9
Figure 2.6a	"ABS + TCH-charge" mode shown in the basic configuration.	2-9
Figure 2.6b	"ABS-TCH-charge" mode shown on the Clausius-Clapeyron diagram.	2-9
Figure 2.7a	"TCH-discharge" mode shown in the basic configuration.	2-10
Figure 2.7b	"TCH-discharge" mode shown on the Clausius-Clapeyron diagram.	2-10
Figure 2.8	"TCH-discharge" mode on the SHATRS.	2-12
Figure 2.9a	"ABS + TCH-discharge" mode shown in the basic configuration.	2-13
Figure 2.9b	"ABS + TCH-discharge" mode shown in the Clausius-Clapeyron diagram.	2-13
Figure 2.10	Clausius-Clapeyron diagram with some suitable reactive pairs for the TCH subsystem (with max/min stoichiometric coefficients) and an example of working pair for the ABS subsystem.	2-18

Figure 2.11a	Absorption subsystem's Coefficient Of Performance (COP) for selected generator and evaporator temperatures.	2-31
Figure 2.11b	Solution circulation ratio (f) as a function of generator temperature for selected evaporator temperatures.	2-31
Figure 2.12a	Effect of evaporator temperature (T_{evap}) on the thermochemical subsystem's COP for selected pairs at a cooling water inlet temperature of $T_{\text{cw,in}} = 20$ °C.	2-32
Figure 2.12b	Effect of cooling water's inlet temperature on the thermochemical subsystem's COP for the two most promising pairs at selected evaporator temperatures.	2-32
Figure 2.13	Evolution of the relationship between storage density and cooling power in an ammonia / strontium chloride thermochemical subsystem as a function of several operating conditions.	2-33
Figure 2.14	Evolution of the relationship between storage density and cooling power of the thermochemical subsystem as a function of composite implementation parameters, in the ammonia / strontium chloride system.	2-35
Figure 2.15	Evolution of the relationship between COP and cooling power of the thermochemical subsystem as a function of operating conditions, in the ammonia / strontium chloride system.	2-38
Figure 2.16	Evolution of the relationship between COP_{TCH} and cooling power of the thermochemical subsystem as a function of composite implementation parameters, in the ammonia / strontium chloride system.	2-39
Figure 2.17	Evolution of the relationship between storage density and cooling power of the thermochemical subsystem as a function of operating conditions, in the ammonia / calcium chloride system.	2-40
Figure 2.18	Evolution of the COP_{TCH} - cooling power relationship of the thermochemical subsystem as a function of operating conditions, in the ammonia / calcium chloride system.	2-41
Figure 2.19	Driving heat provided by solar system (dotted line, left axis), demand of cooling (straight line, left axis), cooling provided by the absorption subsystem (squared line, left axis) and by the thermochemical subsystem (crossed line, left axis) and stored cooling capacity associated to liquid refrigerant at the reservoir (circle line, right axis); profiles for one week in the example case.	2-42
Figure 2.20	Second day of simulation of the SHATRS (zoomed from Fig. 2.19).	2-43
Figure 2.21a	Effect of number of solar thermal collectors on hybrid system's COP for different working pairs and mass of refrigerant (in kg) in the TCH subsystem.	2-44
Figure 2.21b	Effect of the same parameters on the Coefficient of Satisfaction of the Demand (CSD).	2-44
Figure 3.1a	Basic configuration of the hybrid compression / thermochemical refrigeration system (HCTRS).	3-4
Figure 3.1b	HCTRS on the Clausius-Clapeyron diagram.	3-4

Figure 3.2	Diagram of the solar PV-driven hybrid compression thermochemical refrigeration system (SHCTRS).	3-7
Figure 3.3a	“COMP” mode on the flow diagram of the HCTRS.	3-9
Figure 3.3b	“COMP” mode on the Clausius-Clapeyron diagram.	3-9
Figure 3.4a	“TCH-charge” mode on the flow diagram of the HCTRS.	3-10
Figure 3.4b	“TCH-charge” mode on the Clausius-Clapeyron diagram.	3-10
Figure 3.5a	“COMP + TCH-charge” mode on the flow diagram of the HCTRS.	3-10
Figure 3.5b	“COMP + TCH-charge” mode on the Clausius-Clapeyron diagram.	3-10
Figure 3.6a	“TCH-discharge” mode on the flow diagram of the HCTRS.	3-11
Figure 3.6b	“TCH-discharge” mode on the Clausius-Clapeyron diagram.	3-11
Figure 3.7a	“COMP + TCH-discharge” mode on the flow diagram of the HCTRS.	3-12
Figure 3.7b	“COMP + TCH-discharge” mode on the Clausius-Clapeyron diagram.	3-12
Figure 3.8a	Graphical demonstration of the equilibrium drop reduction due to the vapor compression.	3-15
Figure 3.8b	Numerical example of the equilibrium drop.	3-15
Figure 3.9a	View of the thermochemical reactor during the decomposition phase.	3-17
Figure 3.9b	Front view of the solid reactive composite during the reaction progress.	3-17
Figure 3.10a	Evolution of reactor pressure and reaction’s advancement degree during decomposition phase in power-oriented configuration.	3-23
Figure 3.10b	Evolution of reactor pressure and reaction advancement degree during decomposition phase in storage-oriented configuration.	3-23
Figure 3.11	Evolution of the reaction’s advancement degree during decomposition phase without compressor for different values of thermal conductivity of the charged and discharged salt (λ_0 and λ_1 , respectively).	3-24
Figure 3.12	Evolution of the reaction’s advancement degree during decomposition phase without compressor for different values of permeability (k) of the charged and discharged salt.	3-24
Figure 4.1	Flow diagram of the experimental setup of the hybrid thermochemical / compression refrigeration system.	4-3
Figure 4.2	Picture of the experimental setup before insulation.	4-10
Figure 4.3	Picture of the experimental setup after insulation.	4-11
Figure 4.4a	Diagram of the thermochemical reactor (dimensions in mm).	4-11
Figure 4.4b	Picture of the thermochemical reactor before thermal jacket and insulation.	4-11
Figure 4.5a	Diagram of the reactor’s bottom (dimensions in mm).	4-12
Figure 4.5b	Reactor’s bottom (inner part with welded nut).	4-12
Figure 4.5c	Reactor’s bottom (outer part).	4-12
Figure 4.6a	SS316 confine disc screwed into the SS316 threaded rod.	4-13
Figure 4.6b	SS316 confine disc and full-length SS316 threaded rod.	4-13
Figure 4.7a	Reactor’s thermal jacket under construction.	4-13
Figure 4.7b	Reactor’s thermal jacket after construction.	4-13

Figure 4.8	Teflon disks for thermal confinement of the solid composite.	4-14
Figure 4.9	Compressor's characteristic curve [2].	4-14
Figure 4.9	Compressor's technical specifications [2].	4-14
Figure 4.10	Flow diagram of the decomposition phase assisted with vapor compression.	4-19
Figure 4.11	Flow diagram of the setup during the synthesis phase.	4-20
Figure 4.12	Flow diagram of the setup during the thermal-only decomposition phase.	4-21
Figure 4.13	Flow diagram of the setup during operation of the compression refrigeration subcycle.	4-22
Figure 4.14	Flow diagram of the setup during the salt dehydration procedure.	4-25
Figure 4.15	Flow diagram of the setup during the ammonia charge procedure.	4-26
Figure 4.16	Pressure and temperature profiles of the first experience with compression-assisted decomposition.	4-27
Figure 4.17	$X-t$ curve obtained from the first experience with compression-assisted decomposition.	4-28
Figure 4.18	Pressure and temperature profiles of the second experience with compression-assisted decomposition.	4-28
Figure 4.19	Pressure and temperature profiles during the first 5 minutes of the second experience with compression-assisted decomposition.	4-29
Figure 4.20	Comparison of $X-t$ curves during compression-assisted decomposition and non-assisted decomposition. Evolution of reactor pressure during compression-assisted decomposition.	4-30
Figure 4.21	Evolution of the estimated mass of ammonia in the solid composite along all the experiments carried out with the setup.	4-30
Figure 4.22	Comparison of predicted $X-t$ curves for parameters at nominal case and several values of $\lambda_0 = \lambda_1$ with data from experiment D2 (non-assisted decomposition phase).	4-33
Figure 4.23	Adjustment of parameters $\lambda_0 = \lambda_1$ by the least squares method for experiment D2.	4-34
Figure 4.24	Verification of parameter adjustment for decomposition D2.	4-35
Figure 4.25	Confrontation of experimental and predicted $X-t$ curves for experiment D4 (non-assisted decomposition phase).	4-36
Figure 4.26	Confrontation of experimental and predicted $X-t$ curves for experiment D6 (non-assisted decomposition phase).	4-37
Figure 4.27	Confrontation of experimental and predicted $X-t$ curves for experiment S5 (synthesis phase).	4-38
Figure 4.28	Confrontation of experimental and predicted $X-t$ curves for experiment S2 (synthesis phase).	4-39
Figure 4.29	Confrontation of experimental and predicted $X-t$ curves for experiment S4 (synthesis phase).	4-40
Figure 4.30	Confrontation of experimental and predicted $X-t$ curves for experiment D7 (compression-assisted decomposition phase).	4-41
Figure 4.31	Confrontation of experimental and predicted $X-t$ curves for experiment D8 (compression-assisted decomposition phase).	4-42

List of Tables

Table 1.1	Brief summary of experimental studies with thermochemical processes driven by low-grade heat.	1 - 7
Table 2.1	Identification of all possible operation scenarios in the solar hybrid ABS/TCH refrigeration system and their corresponding operation modes.	2 - 5
Table 2.2	Operating conditions for the HATRS in the present study.	2 - 21
Table 2.3	Nominal case and max/min values for the parametric study.	2 - 26
Table 2.4	Weather- and application-related parameters for system simulation.	2 - 27
Table 2.5	Working pairs considered in the simulations.	2 - 30
Table 3.1	Description of operating modes in the SHCTRS.	3 - 8
Table 3.2	Nominal case and minimum / maximum values of the design parameters and variables.	3 - 20
Table 4.1	Minimum and maximum values of several design variables for experimental setup dimensioning.	4 - 6
Table 4.2	Max/min values of main reaction-related design parameters.	4 - 6
Table 4.3	List of experiments carried out and their operating conditions.	4 - 8
Table 4.4	Parameters adjusted for model validation.	4 - 31
Table 4.5	Nominal, minimum and maximum values of parameters used for estimation of the overall heat transfer coefficient composite-coating (h_w).	4 - 32
Table A.1	Initial configuration of the valves for charging ammonia into the experimental setup.	A - 47
Table A.2	List and operating conditions of all reactions carried out with the experimental hybrid compression/thermochemical refrigeration system.	A - 50

Nomenclature

Abbreviations

A	Absorber
ABS	Absorption
C	Compressor
CDD	Cooling Degree Days
COMP	Compression
COP	Coefficient Of Performance
CSD	Coefficient of Satisfaction of the Demand
D#	Decomposition phase experiment (# goes from 1 to 8)
DC	Direct Current
DHW	Domestic Hot Water
E	Evaporator
ENG	Expanded Natural Graphite
EV	Expansion Valve
G	Gas
G	Generator
HATRS	Hybrid absorption / thermochemical refrigeration system
HCTRS	Hybrid compression / thermochemical refrigeration system
L	Liquid
MX	Metal halide
P	Pump
PV	Photovoltaic
R	Reactor
S	Solid
S#	Synthesis phase experiment (# goes from 1 to 8)
SHATRS	Solar hybrid absorption thermochemical refrigeration system
SHCTRS	Solar hybrid compression thermochemical refrigeration system
SHX	Solution Heat Exchanger
SP	Solution Pump
TCH	Thermochemical
TRL	Technology Readiness Level
V	Valve
VLE	Vapor-Liquid Equilibrium
TV	Three-way valve

Symbols

A	Area, m^2
a	Quadratic contribution in compressor's characteristic curve
b	Klinkenberg coefficient, Pa

b	Linear contribution in compressor's characteristic curve
C	Specific heat, $J/(mol \cdot K)$
c	Independent term in compressor's characteristic curve
De	Energy storage density, kWh/m^3
e	Wall thickness, m
f	Circulation ratio, $kg \cdot s^{-1}/(kg \cdot s^{-1})$
f	Volumetric fraction
h	Specific enthalpy, kJ/kg
h	Convective heat transfer rate, $W/(m^2 \cdot K)$
k	Permeability, m^2
M	Molar mass, $kg/kmol$
m	Mass, kg
\dot{m}	Mass flow rate, kg/s
n	Reaction rate, $mole/(mole \cdot total \cdot s)$
P	Pressure, bar
Q	Heat, kJ
\dot{Q}	Heat flow rate, kW
\dot{q}	Specific heat flow rate (referred to surface), kW/m^2
R	Universal gas constant, $J/(mol \cdot K)$
r	Radius, m
S	Surface, m^2
s	Specific entropy, $kJ/(kg \cdot K)$
t	Time, s
T	Temperature, $^{\circ}C$
U	Global heat transfer coefficient, $W/(m^2 \cdot K)$
\tilde{V}	Apparent volume, m^3
\dot{V}	Volumetric flow rate, m^3/s
W	Work, kJ
\dot{W}	Power, kW
w	Mass fraction, $kg/kg-total$
X	Reaction advancement degree
x	Molar fraction, $mole/moles-total$
Greek symbols	
α	Correction factor
Δ	Increment
ρ	Density, kg/m^3
ν	Reaction's stoichiometric coefficient, $mole-gas/mole-salt$
μ	Moles of refrigerant in the fully discharged salt
μ	Viscosity, $Pa \cdot s$
ε	Effectiveness
ε	Porosity
ν	Specific volume, m^3/kg

λ	Thermal conductivity, $W/(m \cdot K)$
$\tilde{\rho}$	Apparent density, kg/m^3
η	Efficiency
Subscripts	
0	Reference point
A	Absorber
a	Compressor suction
ABS	Absorption subsystem
Amb	Ambient
b	Demand
b	Effective axial thermal conductivity
b0	Isotropic expanded natural graphite
C	Condenser
c	Reactive composite
c	Reactor's thermal coating
cold	Cold fluid in the heat exchanger
coll	Collector
comp	Compressor
Cond	Condenser (Figure 3.4)
Cu	Reactor coating's copper wall
Cu-Inox	Copper wall and SS316 wall contact area
cw	Cooling water
day	Daytime
dec	Decomposition phase
dif	Diffusor
E	Evaporator
e	Heat exchanger
e	Energy storage density
EVAP	Evaporator
eq	Equilibrium
ex	Heat exchanger
exp	Experimental
f1	Reaction front 1
f2	Reaction front 2
FC	Heat exchange fluid
G	Generator
g	Refrigerant gas
gen	Generator
gsat	Saturated gas
h	Heat source
high	High level
hot	Hot fluid in the heat exchanger

in	Inlet
Inox	Reactor's stainless steel wall
low	Low level
lsat	Saturated liquid
m	Medium level
max	Maximum
min	Minimum
need	Demand
night	Nighttime
out	Outlet
p	Constant pressure
p	Reactor's wall
pump	Pump
PV	Photovoltaic
r	Reaction
rad	Solar irradiation
ref	Refrigerant (eq. 3.11)
R1	Endothermic reaction
R2	Exothermic reaction
S	Surface
s	Reactive salt
s0	Fully discharged reactive salt
s1	Fully charged reactive salt
sa	Anhydrous reactive salt
sim	Simulated
ss	Strong solution
solar	Solar energy
st	Stainless steel
sw	Reactive composite – Reactor wall contact area
syn	Synthesis phase
TCH	Thermochemical subsystem
th	Thermal-only decomposition phase
v	Vaporization
w	Heat transfer from coating fluid to reactive composite
ws	Weak solution
<i>Superscripts</i>	
ABS	Absorption subsystem
AUX	Auxiliary system
HYB	Hybrid system
net	Net, useful
TCH	Thermochemical subsystem
TOT	Total

CHAPTER 1

Introduction and Thesis Objectives

Climate change and global warming are facts. World population is experiencing a notable increase, being above 7 billion inhabitants as of 2017, and is expected to continue to grow.

It can be affirmed that the increase in population leads naturally to an increase in demand of cold, since many of the human needs and activities are bound to cold production.

The vehicle that drives us daily to our workplace has a refrigeration system for the engine, and is generally equipped with an air conditioning system for summertime. Some of the food we buy is delivered inside refrigerators at shopping centers, and those shopping centers use air conditioning in summer. Later, we store that food inside our fridge. Some of the medicaments and vaccines that we need at some points in our lives are kept at low temperatures. Surgery areas in hospitals maintain a rather low room temperature, just to prevent disease propagation among patients. Some of the gadgets (e.g. phones, computers, tablets...) that we use either for work or in personal life are equipped with a small-scale refrigeration system.

As new inhabitants access these cold-demanding services, while the rest of the population keeps it, the global demand of cold increases. And from the point of view of cold production systems and their impact on the environment, an increased demand has three main implications:

- First, increased consumption of primary energy [1]. Some of these cold production systems and machines are driven by either thermal or electrical energy that has been generated from a non-renewable source, generally fossil fuels. These sources generate some of the greenhouse gas (GHG) emissions (CO_2 , NO_x ...) that are to be avoided in the upcoming years.
- Second, potentially increased use of GHG. Conventional cycles and machines for cold production used to operate with GHG as well; this includes HFCs and CFCs [2]. Although these working fluids are being progressively retired from the market [3], the exponentially increased

manufacture of refrigerators *before* the regulations means that there may be still many refrigerators operating with these fluids. This becomes a problem especially after retirement of those machines.

- Third, increased heat wastage. Refrigeration systems and heat pumps are known to reject heat to a sink, which is usually the environment. The impact of this waste heat on environment may be irreversible if not dealt with. The recent legislation is starting to induce a better utilization of waste heat through the application of emission-based taxes.

The rapid growth of emerging countries is exacerbating these three problems. Therefore, solutions that lead to fewer GHG emissions are necessary, in order to satisfy the current and expected energy needs [4].

From the point of view of GHG emissions related with fossil fuel-based primary energy sources, to substitute these sources with renewable energy is arguably the best solution. This is also known as *to decarbonize* energy systems. The category of 'renewable' includes the abundant and cost-free energies of solar, geothermal, biomass, and wind energy.

Research on this topic has grown remarkably in the recent decades and continues to grow, since renewable sources are still under-utilized. The current state of the art contains reference studies on the implementation of renewable energy sources in refrigeration systems with different working principles. Solar thermal and solar photovoltaic energy are two interesting ones [5].

Despite being the most appealing solution to tackle our strong dependence on fossil fuels, it is not a simple one, since it usually implies a whole re-design of the already existing systems, and its implementation can only be done progressively. Nevertheless, this solution should be a must-apply for new thermal systems, and this may be the case of new projects in developing countries [2].

Another frequently addressed solution is to increase the energetic efficiency in cold production systems. This is a direct solution to the increased consumption of primary energy, and an indirect solution to GHG emissions bound to non-renewable energy sources. In addition, it is oftentimes more accessible and less costly than re-designing the system or the machine for operation driven with renewable energy sources. For these reasons, this may be a more attractive solutions for developed countries with refrigeration systems and machines that are already built and installed.

Another solution is to substitute those existing working fluids that contribute to GHG emissions for other working fluids with similar properties but not environmentally dangerous. This could be regarded as an intermediate solution between re-designing the systems for renewable sources and *retrofitting* to increase energetic efficiency. This solution affects especially HFCs and fosters the use of natural refrigerants.

To reduce heat wastage, improved energy efficiency and waste heat recovery, as well as process *retrofitting* for the utilization of low-grade heat sources, are solutions expected to play a major role.

The international community has adopted several initiatives to solve all the problems described above. From them, the major three initiatives worth mentioning are the Montreal Protocol, the Kyoto Protocol and the Paris Agreement.

The Montreal Protocol (abridged name for 'The Montreal Protocol on Substances that Deplete the Ozone Layer') [6] was adopted in Montreal (Canada) on 16 September 1987, and went into effect on 1st January 1989. It aimed to cut back the consumption and production of several types of Chlorofluorocarbons (CFCs) and halons, reducing them to 80% of 1986 levels by 1994, and 50% of 1986 levels by 1999. Since then, the Protocol has had 8 amendments to further improve its objectives, and its effects on reducing the concentration of chlorine in the stratosphere are already visible.

The Kyoto Protocol was adopted in Kyoto (Japan) on 11 December 1997 and enforced on 16 February 2005. Up to date, the Protocol has undergone 2 commitment periods. On the first one (2008 - 2012), its participant Parties (a total of 37 industrialized countries and the European Community) committed to reduce GHG emissions by an average of 5% with respect to 1990 levels. On the second commitment period (2013 to 2020), the Parties committed to reduce GHG emission by at least 18% below 1990 levels [7]. The Protocol enforced stricter emission-reducing targets to developed countries, and the composition of Parties in the first and second commitment periods is different.

The Paris Agreement (also known as the Paris Climate Accord) was adopted at the COP21 of the UNFCCC in Paris (France) on 12 December 2015, and will be in effect from 2020. The Agreement aims to hold the increase in the global average temperature to well below 2°C above pre-industrial levels and limit the temperature increase to 1.5°C above pre-industrial levels, in order to reduce the risks and impacts of climate change [8]. To reach these objectives, contributions will be obtained from several sectors, including energy, transport, agriculture and buildings, from the participant Parties.

1.1 THERMOCHEMICAL PROCESSES

The phenomenon taking place in thermochemical processes was traditionally known as “thermochemical transformation”, used by some authors like [9]. “Transformation” refers to the fact that these systems transform thermal energy into chemical energy and *vice versa*.

As a matter of fact, these processes can be used for either cold or heat production, depending on the setup. However, the operation of a refrigeration machine with these processes is discontinuous if the sorbent is a solid.

On the other hand, thermochemical processes excel in energy storage. The thermal energy supplied to these systems is stored in the form of either chemical bonds or chemical potential, and can be later recovered through the inverse process [10]. Due to the high energy density of the working pairs and the negligible heat losses, these systems are good candidates for energy storage even in long periods, i.e. seasonal storage [11]. For these reasons, these systems are better known by their storage function, which is promising for solar applications [12]. In summary, the term “thermochemical storage” is used quite more often than “thermochemical refrigeration” in literature.

Thermochemical storage includes processes with and without sorption. The category of thermochemical storage with sorption includes chemical adsorption and chemical absorption. The fundamental difference between physical sorption and chemical sorption lies in the kind of force involved: while physical sorption is due to Van der Waals forces, chemical sorption is due to valence forces [13].

Difference from physical sorption to chemical sorption also lies in the thermodynamic variance of the process: while for physical ab- and adsorption the valence equals two, for chemical sorption it equals one. From this point of view, solid-gas chemical sorption processes are usually called “monovariant” [14].

Energy storage with reversible solid-gas reactions offers high energy density since they are based on reaction heat, which is higher than sensible and latent heat, and this reduces equipment’s volume and cost. The main limitation of the storage systems based on reversible solid-gas reaction is the presence of a solid, which introduces a limitation in heat and mass transfer that affects negatively the system’s kinetics. Some solutions exist in the literature for this problem, for instance the use of fluidized reactive beds [11].

The terminology used to designate thermochemical storage with solid-gas reversible reactions differs from a source to another: “solid-gas chemical reaction”, “thermochemical reaction” or “solid-gas thermochemical sorption”.

A crucial parameter for comparison between thermal energy storage systems is the energy storage density (ESD) [15, 16]. According to Hadorn [17], the volume required to store the same amount of energy can be theoretically up to 10 times smaller with reaction systems than with sorption systems.

Usually, it is difficult to compare directly the values of ESD reported in the literature for different types of energy storage technologies. This is due to the units in which this indicator is expressed: while some studies refer this value to the mass of refrigerant fluid (or overall mass of the working pair), others refer it to the storage volume. When the studies refer to volume of storage, sometimes they refer to volume of the species, while sometimes they refer to the overall volume of the vessel in which the storage is done. Even if the ESD can be expressed in energy per unit mass of species, these species are not the same from one storage type to the other, and that means that the final repercussion (economical, for instance) is still unclear. The conversion from mass of the species to volume of storage is not an obvious step, and depends on several parameters: type of refrigerant and sorbent pair –if applicable-; configuration of the reactor, reservoir, vessel or component that contains the species, when relevant... Therefore, before comparing quantitatively different types of energy storage, a reliable methodology to express the indicators in the same units should be applied.

Mugnier and Goetz [18] compared the energy storage capacity of selected sorption refrigeration working pairs, including absorption, adsorption, solid/gas reaction and phase change materials (PCM). The highest reported ESDs were: 277 Wh/kg for absorption working pairs; 353 Wh/kg for solid/gas reaction working pairs; 82 Wh/kg for adsorption working pairs; and 85 Wh/kg for phase change materials. All these values refer to the mass of the involved species (i.e. refrigerant and its sorbent pair, except in the case of PCM, where only one specie is involved).

The higher ESD of the absorption thermal energy storage as well as thermochemical storage makes them more interesting than conventional thermal energy storage systems for solar refrigeration.

Table 1.1 contains information about several experimental studies with thermochemical storage available in the literature.

Table 1.1. Brief summary of experimental studies with thermochemical processes driven by low-grade heat.

Working pair	Application(s)	Heat source temperature	Delivery temp.	ESD	Units	Source(s)	Year
NH ₃ /BaCl ₂	Refrigeration	70 °C to 95 °C	-8 °C to 0 °C	-	-	[19]	2007
NH ₃ /BaCl ₂	Deep-freezing	70 °C	-23 °C	-	-	[20]	2007
NH ₃ /BaCl ₂	Air conditioning	80 °C	15 °C	-	-	[21]	2009
NH ₃ /LiCl	Icemaker	80 °C	-5 °C	-	-	[22]	2009
NH ₃ /CaCl ₂	Icemaker	82.4 °C	-15.2 °C	-	-	[23]	2006
NH ₃ /CaCl ₂	Icemaker	97 °C	-18.3 °C	-	-	[24]	2007
NH ₃ /CaCl ₂	Icemaker	100 °C	-15 °C	-	-	[25]	2006
NH ₃ /NaBr	Air conditioning	65 °C	15 °C	-	-	[26]	2008
SrBr ₂ /H ₂ O	Cooling	80 °C	18 °C	40	kWh/m ³ (reactor)	[14]	2008
	Heating		35 °C	60	kWh/m ³ (reactor)		
	Cooling		7 °C	42	kWh/m ³		
LiBr/H ₂ O	DHW production	80 °C	65 °C	88	kWh/m ³	[15]	2014
	Heating		43 °C	110	kWh/m ³		

Mauran et al. [14] reported experimental results of a thermochemical system providing cooling in summer and heating in mid-seasons for a residential case. The setup operated with the $\text{H}_2\text{O}/\text{SrBr}_2$ working pair, being the salt contained in a 1 m^3 thermochemical reactor with expanded natural graphite in the form of consolidated material, to increase heat and mass transfer. With source heat provided at a maximum temperature of $T_{\text{hs,max}} = 80 \text{ }^\circ\text{C}$ by flat plate solar collectors, the system provided heating at an inlet temperature of $T_{\text{heat}} = 35 \text{ }^\circ\text{C}$ in mid-seasons (external ambient temperature of $T_{\text{ext,mid}} = 7 \text{ }^\circ\text{C}$), and cooling at an inlet temperature of $18 \text{ }^\circ\text{C}$ in summer (external ambient temperature of $T_{\text{ext,sum}} = 35 \text{ }^\circ\text{C}$). From the experimental results, the study forecasted ESD values up to 218 kWh/m^3 by applying different configurations at the reactor and the reactive solid composite. This study notes once again the double cooling/heating function provided by thermochemical systems, making them versatile.

Zhang et al [15] reported experimental ESDs of 42 kWh/m^3 for cooling, 88 kWh/m^3 for domestic hot water production, and 110 kWh/m^3 for heating.

Alongside with limitations related to the high temperature heat sources, thermochemical processes also can encounter barriers in cold production at very low temperatures ($-30 \text{ }^\circ\text{C}$ and below). For a given working pair in a single-stage thermochemical process, the lower the cold production temperature, the lower the temperature inside the reactor during the synthesis phase. This means that, if the reactor temperature becomes too low, it would be not possible to dissipate the reaction heat with cooling water.

For the $\text{NH}_3/\text{BaCl}_2$ working pair, Le Pierrès et al [27] addressed this limitation by designing a thermochemical process with an internal, thermal cascade. Thanks to this cascade their process, designed for deep-freezing with a low-grade heat source, allows the production of cold at $-23 \text{ }^\circ\text{C}$ and below using a heat source of about $70 \text{ }^\circ\text{C}$. This means that the process can be driven by solar heat using flat plate collectors [28]. Their prototype of this system proved the feasibility of this process and yielded an experimental global COP of 0.06. This value is within the typical range of experimental thermochemical refrigeration systems driven by solar heat, and in addition, it must be taken into account that the process produces cold at a lower temperature than the other solar refrigeration systems. The mean annual exergetic yield was 0.06 approx. [20].



Figure 1.1. Prototype of a cascaded thermochemical process driven by solar thermal energy for deep-freezing [27].

1.2 SOLAR REFRIGERATION WITH ENERGY STORAGE

Solar refrigeration is a logical answer to the increasing needs of refrigeration without increasing the number of GHG emissions. Solar energy is an abundant, free, and under-utilized energy source. In addition, there is usually a direct relation between solar irradiation and demand of cold [29]: many of the countries with the highest sun irradiation have also high ambient temperatures, which lead to higher needs of air conditioning and refrigeration.

Systems that can deliver refrigeration from solar energy are usually classified into two main categories: solar electric and solar thermal. Solar electric refrigeration consists basically of photovoltaic (PV) panels connected to a refrigeration device driven by electricity (powered through either DC current or AC current with an alternator). Inside this category the main options are solar electric vapor compression refrigeration, electrically driven thermo-acoustic refrigeration, and magnetic cooling.

One important technological barrier for further improvement of solar refrigeration is the lack of coordination (Fig. 1.2) between the solar resource and the demand of cold. Eventually, this problem affects any system driven by renewable energy: while the resource is intermittent, the demand is usually continuous. This lack of coordination usually receives the name of ‘mismatch’ [30], and has been more and more frequently addressed in the recent years. The direct answer to mismatch is the implementation of some form of energy storage.

Several options exist for the implementation of energy storage in refrigeration systems. In the case of refrigeration systems driven by electricity produced from solar energy, the simplest solution is the use of batteries. Bilgili

[31] carried out the simulation of a compression refrigeration system driven by solar-PV energy and equipped with a battery.

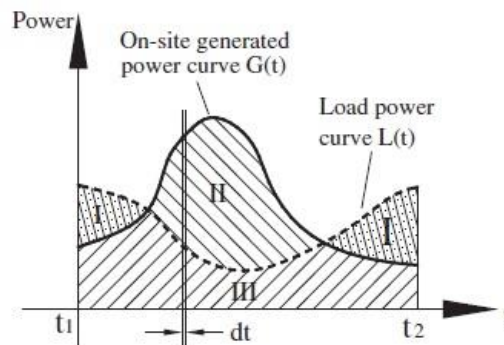


Figure 1.2. Illustrative graph of the mismatch between on-site power generation and load curves, with power shortage area (I), power surplus area (II) and generation/consumption matching area (III) [30].

For solar-driven absorption refrigeration, energy storage with crystallization of the solution has been studied in the recent decades. For the continuous operation of absorption refrigeration machines, crystallization has been always regarded as an undesirable phenomenon, since the crystallized solution cannot be pumped. However, during a period of energy storage in which refrigeration is not needed, it is possible to store crystallized solution. Consequently, the system will also require another tank or reservoir to store liquefied refrigerant. The energy is then stored as refrigeration potential, in the form of two separate compounds stored in different places. When the cold is needed, the stored refrigerant is vaporized and reabsorbed by the solution, reducing the mass fraction of salt and dissolving it, allowing the solution to be pumped once again for continuous operation.

With this idea, N'Tsoukpoe et al. [32] introduced an absorption-based lithium bromide/water system for long-term storage of solar heat. In their study, a dynamic simulation model was presented and described in detail. It was used to investigate the influence of some relevant parameters (heat exchanger size, solution flow rate, absorption percentage) and operating conditions (heat supply temperature, crystallization ratio, heat demand) on the system performance. This evaluation of system performance took into account the thermal efficiency and the storage density as key indicators. Interestingly, the study reports crystallization of the solution appears to increase the storage density by as much as three times. The study provided several results for the dynamic evolution of the system.

The results of their simulations were later used to design a prototype (Fig. 1.3) for experimental validation of the model [33]. The experimentation proved

the thermal storage of the system, and its suitability for space heating purposes using a heating floor (with an absorber outlet solution at a temperature of up to 40 °C). The temperature of the absorber heat transfer fluid was between 22 °C and 26 °C. According to the report, heat and mass transfer are two important issues to bear in mind for an appropriate design of the absorber in such systems.

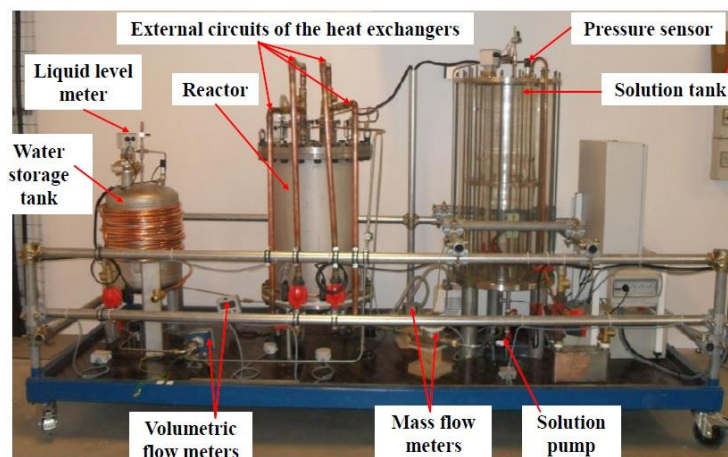


Figure 1.3. Experimental setup (before insulation) built by N'Tsoukpoe K.E. [33] for the study of a LiBr-H₂O absorption process for long-term solar thermal storage.

Xu et al. [16] presented a solar powered absorption refrigeration cycle prepared to store refrigeration potential in a solution tank. The study also presents the model equations for dynamic simulation of the system, as well as an example case study. The study obtained that, for the system working with water/lithium bromide under typical operating conditions, the energy storage density of the system (ESD) is 368.5 MJ/m³ (i.e. 102.4 kWh/m³) referred to the volume of stored water. When the condenser is air-cooled, the COP is 0.7525 and the required solar collector field area is 66 m², while when it is water-cooled, those values are 0.7555 and 62 m² respectively. The ESD remains unaffected by the solution heat exchanger efficiency.

Traditionally, the storage of thermal energy in residential solar thermal systems is performed with water storage tanks, since their aim is usually the production of domestic hot water (DHW). This form of thermal storage is known as sensible heat storage. While this technology is in a high state of development, the maximum energy density attainable with it is rather low, if we compare it to other forms of thermal storage. According to the literature [34,35], to store the same given amount of heat, the volume required by thermochemical storage is up to 34 times smaller than with hot water, up to 20 times smaller than with phase change materials (PCM) and up to 10 times smaller than with sorption storage. However, these figures are referred to non-

porous reactive salt, which would encounter serious agglomeration problems. In reality, with adequate porosity, these numbers would not be as high as depicted here, but they would still be promising.

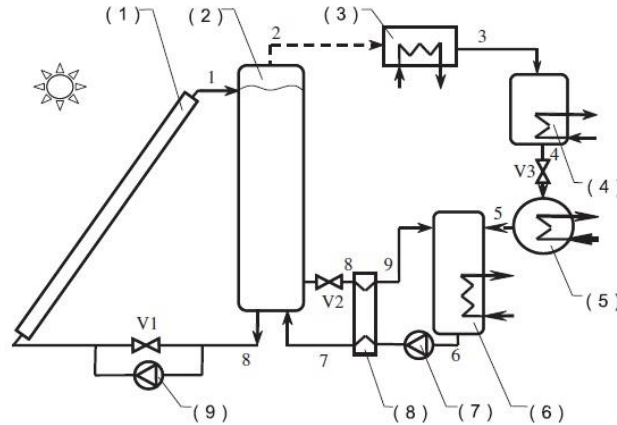


Figure 1.4. Flow diagram of a solar powered absorption refrigeration system with the H₂O/LiBr working pair and advanced energy storage technology [16].

The adaptation of solid/gas thermochemical reactions to solar thermal systems for either heating or cooling has been investigated in some studies. As an example, Lahmidi et al. [36] developed a simple model for the dynamic simulation of the decomposition and synthesis phases of a thermochemical system operating with the H₂O/SrBr₂ working pair, with a focus on the progress of the reaction within the reactive solid inside the reactor. The model assumes a single and straight reactive front that advances across the reactive layer. This reactive front represents the absorption/desorption of water within the salt. In this system, the activation temperature needed in the reactor for the decomposition phase is 353 K, which enables the use of flat plate solar collectors. The maximum attainable heating storage capacity with this system was estimated as 250 kWh/m³ (referred to volume of fixed reactive bed with adequate porosity for process operation), far greater than the storage capacity of 52 kWh/m³ reachable with a hot water storage tank working in the temperature range of 353 K to 308 K.

Later on, the use of the system characterized by [36] was studied experimentally by Mauran et al. [14]. This study describes a prototype reactor using monovariant solid/gas thermochemical reaction between H₂O and SrBr₂, to provide up to 60 kWh of heating or 40 kWh of cooling, with a reactor volume of 1 m³. Mean heating/cooling powers were determined to be about 2.5-4 kW. To improve these powers, the authors point out the improvement of heat transfer rate between the reactive layer and the exchanger wall as the main challenge.

To improve the energy storage densities of the systems with H_2O and SrBr_2 , Michel et al. [11] characterized and modelled a high density reactive bed.

A large scale prototype was designed and built with $\text{SrBr}_2/\text{H}_2\text{O}$ as a reactive pair, and operating with moist air [37]. The prototype contained 400 kg of hydrated salt and had 105 kWh of storage capacity as well as a reactor energy density of 203 kWh/m^3 . The results of this study are promising in terms of feasibility and performance of such storage process. For a high-density reactive bed of 388 kWh/m^3 , the obtained hydration specific powers ranged from 0.75 W/kg to 2 W/kg . As for key parameters in the control of such systems, the equilibrium pressure drop and the mass flow rate of moist air were identified as the two most relevant ones.

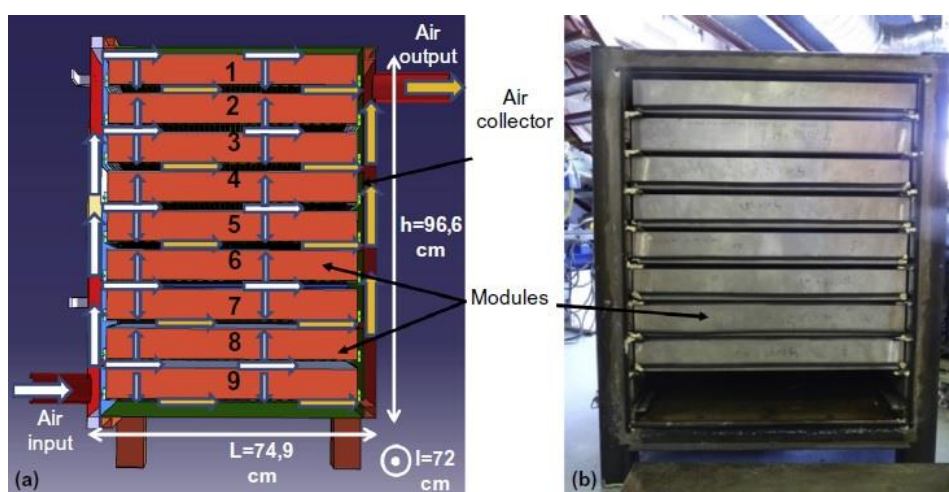


Figure 1.5. (a) Diagram of experimental setup with $\text{SrBr}_2/\text{H}_2\text{O}$ working pair for thermal storage of solar energy [37]; (b) Picture of the reactor prototype [37].

The use of thermochemical refrigeration for solar air-conditioning has also been investigated experimentally. Stitou et al. [38] provided experimental values of the performance of a solar air-conditioning pilot plant in France. This pilot plant operates with the working pair $\text{NH}_3/\text{BaCl}_2$ and has a daily cooling capacity of 20 kWh. The activation temperature is between $60 \text{ }^\circ\text{C}$ and $70 \text{ }^\circ\text{C}$, which is attained with a 20 m^2 field of flat plate solar collectors. The study covers a 2-year period of experimental data, and states that the mentioned pilot plant enables a daily cooling productivity at $4 \text{ }^\circ\text{C}$ of 0.8 kWh to 1.2 kWh of cold per m^2 of flat plate solar collector. The plant yields a global solar COP of $0.15\text{-}0.23$.

1.3 HYBRIDIZATION OF THERMOCHEMICAL PROCESSES WITH CONTINUOUS REFRIGERATION SYSTEMS

The novelty and interest of this doctoral thesis is the hybridization of thermochemical processes with continuous refrigeration systems to obtain autonomous refrigeration systems that operate with intermittent energy sources, with a focus on solar energy.

Combining the technologies of absorption refrigeration and reversible solid-gas reactions can provide hybrid systems with the continuous operation and high thermal performance of absorption systems, plus the high-efficiency energy storage of the thermochemical systems. Such hybrid systems would be able to compensate the mismatch and operate continuously with an intermittent driving source such as solar heat. In addition, with proper design and dimensioning, they can be suitable for autonomous off-grid operation. In addition, both absorption and thermochemical systems work with natural working fluids, which have no negative impact on the ozone layer nor a greenhouse effect.

Systems with thermochemical processes have a technology readiness level (TRL) of about 3.5. This means that it is still in development phase, before being transferred to industrial processes. Principally any real system with thermochemical process that exists nowadays is either a prototype or a demonstration system. Worth mentioning is the Coldway society in France, which commercializes thermochemical transformers for cold chain sustain in the transport of food or medical products [39]. Therefore, the existing literature on the hybridization of thermochemical systems with other refrigeration systems is rather scarce. Nevertheless, some interesting studies exist in this topic. The following paragraphs will attempt to summarize the relevant ideas and results of these studies.

Stitou et al. [40] described interesting concepts for the thermal coupling of solid/gas thermochemical processes with liquid/gas absorption. The study aims at the use of solid/gas chemical reactions at the high temperature regions for further development of liquid/gas absorption cycles. While the well-known liquid/gas absorption working pairs (water/lithium bromide and ammonia/water) pose some problems related with corrosiveness and thermal decomposition at high temperatures, solid/gas thermochemical working pairs do not suffer from these restrictions. Therefore, the already developed technologies of single-effect and double-effect liquid/gas absorption can be thermally coupled with solid/gas reaction in the high temperature region to obtain further refrigeration effects. The study proposes and evaluates several

possible coupling configurations with different working pairs. Also, it develops a method for evaluation of the COP of the global machine.

Rezaie [41] concludes that if the main objective is to reduce CO₂ emissions, then hybrid systems are a reasonable option, since they can, by the combination of two or more different technologies, cover the weaknesses of each one by using the strengths of the other one. However, these kinds of systems are obviously more expensive than simple systems, as it is shown in different case studies.

Some studies exist about electricity and cold cogeneration through thermochemical sorption systems with an added expander.

Jiang [42] studied an experimental resorption system for cogeneration of power and refrigeration. The setup consisted of a high temperature salt (HTS) bed, a low temperature salt (LTS) bed, a turbine, two oil tanks, a cooling tank and a chilled water tank.

1.4 GENERAL AND SPECIFIC THESIS OBJECTIVES

The main purpose of this thesis is to develop hybrid continuous refrigeration systems based on thermochemical processes. By “hybrid”, we mean that these systems are the result of merging at least two separate systems together, but in the global system, some of the elements are shared. As a consequence, the global system is compact, and all the systems included in it can be renamed as “subsystems”.

To develop the hybrid systems, the thermochemical processes are combined with solar-driven continuous refrigeration systems, which can belong to two main categories: solar thermal, or solar electric.

From the thermal category, solar absorption refrigeration systems were selected, leading to solar hybrid absorption / thermochemical refrigeration systems (SHATRS). As for the electrically driven category, compression refrigeration systems were selected, leading to hybrid compression / thermochemical refrigeration systems (SHCTRS).

These hybrid systems can operate continuously with an intermittent energy source, thanks to the energy storage capacity of the thermochemical refrigeration systems. The heat source temperature of these systems is 100 °C or lower. This is especially true for the SHCTRS, where the vapor compressor assists in reducing the activation temperature of the process.

To achieve the thesis' overall objective stated above, the following specific objectives were set:

Thermodynamic analysis and discussion on the fundamentals of the hybridization of thermochemical refrigeration with other refrigeration cycles, specially absorption refrigeration and compression refrigeration. Review of suitable working pairs and their temperature levels for each hybrid system.

Definition of performance criteria and screening of suitable working pairs for refrigeration systems with energy storage, especially for the hybrid systems developed in this doctoral thesis. This definition includes: Coefficient Of Performance (COP); Specific Cooling Power (SCP); Energy Storage Density (ESD); Coefficient of Satisfaction of the Demand (CSD).

Screening of suitable working pairs, static dimensioning and parametric study of the hybrid absorption / thermochemical refrigeration systems in all their operating modes.

Static dimensioning and parametric study of the hybrid compression / thermochemical refrigeration systems. Determination of the mass of the involved species (refrigerant fluid and reactive salt) to meet a certain demand of cold. Determination of the influence of the main thermodynamic variables (condenser temperature, reactor temperature, evaporator temperature...), as well as relevant design parameters (reactor configuration, mass ratio of heat transfer enhancer...), on the reaction progress.

Dynamic simulation of the synthesis and decomposition stages of the reactive medium within the thermochemical subsystem in hybrid compression / thermochemical refrigeration systems. Determination of the interesting variables such as: reaction time, evolution of reactor temperature and pressure across the reaction, evolution of refrigerant flow rate, among others.

Development of an experimental setup of a thermochemical refrigeration system with compression of the refrigerant fluid during the decomposition stage of the reactive solid (named as compression-assisted thermochemical refrigeration). Comparison of the experimental results with the results predicted with the dynamic simulation of the hybrid compression / thermochemical refrigeration systems.

1.5 THESIS STRUCTURE

This first chapter provided a brief overview on the state of the art of thermochemical processes and their hybridization with refrigeration systems, along with other interesting concepts bound to solar driven systems, such as

source intermittence and source/demand mismatch. The structures of the remaining chapters is described below.

Chapter 2 presents the basic concept of the solar hybrid absorption / thermochemical refrigeration system (SHATRS). After presenting and describing the basic system and its main components, its temperature and pressure levels, as well as its operation modes are described on the Clausius-Clapeyron diagram. The main advantages, drawbacks and restrictions of the system are listed, and a discussion is offered on the suitable refrigerants and working pairs, for both the thermochemical and the absorption subsystems. The performance of this system is simulated and evaluated against a hypothetical refrigeration demand. This chapter also describes the hypotheses, model and results of a sensitivity analysis applied on the main parameters of a real system operating in accordance with the presented configuration.

Chapter 3 is devoted to the presentation of the solar-driven hybrid compression / thermochemical refrigeration system (SHCTRS). In this system, a compressor is connected between the reactor and the condenser inlet. With this compressor, the condenser pressure can be achieved with lower reactor temperatures. This enables the activation of the endothermic reaction with low-grade heat sources, with an special interest in waste heat. First, the basic concept of the system is shown in a flow diagram and its main components are described. The thermodynamic cycle is shown on the Clausius-Clapeyron diagram, and the effect of the compressor (reduction in the activation temperature of the decomposition process) is described. The main advantages, drawbacks and restrictions of these systems are discussed, including several recommendations about the compressor. Then, the model used for dynamic simulation of the decomposition and synthesis stages is explained. This model is used to simulate the evolution of several interesting variables during the decomposition and synthesis stages under the conditions of the experiments that are later described in Chapter 4.

In *Chapter 4*, the simulation model developed in Chapter 3 for the SHCTRS is confronted with experimental results. For the experiences, a setup that is very similar to the SHCTRS was built, although the study is centered on the thermochemical reactor. This chapter describes: the experimental setup, components, and relevant aspects of its design; the procedures for the two main stages (endothermic reaction and exothermic reaction); the conditions under which the experiments were carried out; and the most relevant results.

Finally, *Chapter 5* provides the general conclusions. This chapter contains a list and description of the main contributions of this study to the state of the art, as well as outlooks based on those relevant research points not exhaustively

investigated within the frame of this study. These outlooks may be useful for future research directions.

1.6 REFERENCES

- [1] U.S. Energy Information Administration. (2016). International Energy Outlook 2016. [https://www.eia.gov/outlooks/ieo/pdf/0484\(2016\).pdf](https://www.eia.gov/outlooks/ieo/pdf/0484(2016).pdf) [Last viewed on 04/09/2017].
- [2] Energy Technology Perspectives 2016. https://www.iea.org/publications/freepublications/publication/EnergyTechnologyPerspectives2016_ExecutiveSummary_EnglishVersion.pdf
- [3] The Role of Refrigeration in the Global Economy. http://www.iifir.org/userfiles/file/publications/notes/NoteTech_29_EN.pdf [Last viewed on 01/09/2017]
- [4] Climate Change 2001. (2001). The Scientific Basis. Third Assessment Report. UN Intergovernmental Panel on Climate Change. Cambridge University Press, ISBN 0521 01495 6.
- [5] UNEP, Global Alliance for Building and Construction. (2016). Towards zero-emission efficient and resilient buildings. Global Status Report 2016. <https://wedocs.unep.org/rest/bitstreams/45611/retrieve> [Last viewed on 02/09/2017].
- [6] Montreal Protocol. <https://www.britannica.com/event/Montreal-Protocol> [Last viewed on 02/09/2017].
- [7] Kyoto Protocol. http://unfccc.int/kyoto_protocol/items/2830.php [Last viewed on 02/09/2017]
- [8] Paris Agreement. http://unfccc.int/files/essential_background/convention/application/pdf/english_paris_agreement.pdf [Last viewed on 02/09/2017].
- [9] Castaing-Lasvignottes, J. (1994). Transformateur thermochimique solide-gaz : Analyse système, performances expérimentales et simulées en production de froid et/ou de chaleur. Université de Perpignan, France.
- [10] Kerskes, H., Mette, B., Bertsch, F., Asenbeck, S., Drück, H. (2012). Chemical energy storage using reversible solid/gas-reactions (CWS) – results of the research project. Energy Procedia 30, 294-304.
- [11] Michel B., Mazet N., Mauran S., Stitou D., Xu J. (2012). Thermochemical process for seasonal storage of solar energy: Characterization and modeling of a high density reactive bed. Energy 47 (1), pp. 553-563.
- [12] Mette B., Kerskes H., Drück H. (2012). Concepts of long-term thermochemical energy storage for solar thermal applications – Selected examples. Energy Procedia 30, 321-330.
- [13] N'Tsoukpoe K.E., Liu H., Le Pierrès N., Luo L. (2009). A review on long-term sorption solar energy storage. Renewable and Sustainable Energy Reviews 13, 2385-2396.
- [14] Mauran, S., Lahmidi, H., & Goetz, V. (2008). Solar heating and cooling by a thermochemical process. First experiments of a prototype storing 60kWh by a solid/gas reaction. Solar Energy, 82(7), 623–636.

- [15] Zhang, X., Li, M., Shi, W., Wang, B., Li, X. (2014). Experimental investigation on charging and discharging performance of absorption thermal energy storage system. *Energy Conversion and Management* 85, 425-434.
- [16] Xu, S.M., Huang, X.D., Du, R. (2011). An investigation of the solar powered absorption refrigeration system with advanced energy storage technology. *Solar Energy* 85, 1794-1804.
- [17] Hadorn, J.C. (2008). Advanced storage concepts for active solar energy. IEA SHC Task 32 2003-2007. In: *Proceeding of first international conference on solar heating, cooling and buildings*, Lisbon, Portugal.
- [18] Mugnier, D., Goetz, V. (2001). Energy storage comparison of sorption systems for cooling and refrigeration. *Solar Energy* 71(1), 47-55.
- [19] Rivera C., Pilatowsky I., Méndez E., Rivera W. (2007). Experimental study of a thermo-chemical refrigerator using the barium chloride-ammonia reaction. *International Journal of Hydrogen Energy* 32, 3154-3158.
- [20] Le Pierrès N., Mazet N., Stitou D. (2007). Experimental results of a solar powered cooling system at low temperature. *International Journal of Refrigeration* 30 (6), pp. 1050-1058.
- [21] Chen H., Li T., Wang L., Wang R., Oliveira R. G. (2009). Sorption performance of consolidated composite sorbent used in solar-powered sorption air-conditioning system. *Huagong Xuebao / CIESC Journal* 60(5), 1097-103.
- [22] Kiplagat J. K., Wang R. Z., Oliveira R. G., Li T. X. (2010). Lithium chloride – Expanded graphite composite sorbent for solar powered ice maker. *Solar Energy* 84, 1587-1594.
- [23] Lu Z. S., Wang R. Z., Wang L. W., Chen C. J. (2006). Performance analysis of an adsorption refrigerator using activated carbon in a compound adsorbent. *Carbon* 44, 747-752.
- [24] Oliveira R. G., Wang R. Z. (2007). A consolidated calcium chloride-expanded graphite compound for use in sorption refrigeration systems. *Carbon* 45, 390-396.
- [25] Wang L. W., Wang R. Z., Lu Z. S., Xu Y. X., Wu J. Y. (2006). Split heat pipe type compound adsorption ice making test unit for fishing boats. *International Journal of Refrigeration* 29, 456-468.
- [26] Oliveira R. G., Wang R. Z., Kiplagat J. K., Wang C. Y. (2009). Novel composite sorbent for resorption systems and for chemisorption air conditioners driven by low generation temperature. *Renewable Energy* 34, 2757-2764.
- [27] Le Pierrès N., Stitou D., Mazet N. (2007). New deep-freezing process using renewable low-grade heat: From the conceptual design to experimental results. *Energy* 32 (4), pp. 600-608.
- [28] Le Pierrès N., Mazet N., Stitou D. (2007). Modelling and performances of a deep-freezing process using low-grade solar heat. *Energy* 32, 154-164.
- [29] Kim, D. S., & Infante Ferreira, C. a. (2008). Solar refrigeration options - a state-of-the-art review. *International Journal of Refrigeration*, 31(1), 3-15.
- [30] Cao S., Hasan A., Sirén K. (2014). Matching analysis for on-site hybrid renewable energy systems of office buildings with extended indices. *Applied Energy* 113, 230-247.

- [31] Bilgili, M. (2011). Hourly simulation and performance of solar electric-vapor compression refrigeration system. *Solar Energy* 85, 2720-2731.
- [32] N'Tsoukpoe K.E., Le Pierrès N., Luo L. (2012). Numerical dynamic simulation and analysis of a lithium bromide/water long-term solar heat storage system. *Energy* 37, pp. 346-358.
- [33] N'Tsoukpoe K.E., Le Pierrès N., Luo L. (2012). Experimentation of a LiBr-H₂O absorption process for long term solar thermal storage. *Energy Procedia* 30, pp. 331-341.
- [34] Bales, C., Solar Energy Research Center (SERC). (2006). Chemical and sorption heat storage. In: *Proceedings of DANVAK seminar, DANVAK seminar (solar heating systems – Combisystems – heat storage)*.
- [35] Hadorn, J.C, editor. (2005). *Thermal energy storage for solar and low energy buildings – State of the Art. IEA SHC Task 32 book*. Lleida, Spain: Servei de Publicacions de la Universitat de Lleida. ISBN 84-8409-877-X.
- [36] Lahmidi H., Mauran S., Goetz V. (2006). Definition, test and simulation of a thermochemical storage process adapted to solar thermal systems. *Solar Energy* 80, 883-893.
- [37] Michel B., Mazet N., Neveu P. (2014). Experimental investigation of an innovative thermochemical process operating with a hydrate salt and moist air for thermal storage of solar energy: Global performance. *Applied Energy* 129, 177-186.
- [38] Stitou D., Mazet N., Mauran S. (2012). Experimental investigation of a solid/gas thermochemical storage process for solar air-conditioning. *Energy* 41(1), 261-270.
- [39] <http://www.coldway.com> [Last viewed on 28/09/2017]
- [40] Stitou D., Spinner B., Satzger P., Ziegler F. (2000). Development and comparison of advanced cascading cycles coupling a solid/gas thermochemical process and a liquid/gas absorption process. *Applied Thermal Engineering* 20 (14), pp. 1237-1269.
- [41] Rezaie B., Esmailzadeh E., & Dincer I. (2011). Renewable energy options for buildings: Case studies. *Energy and Buildings* 43(1), 56–65.
- [42] Jiang L., Wang L.W., Liu C.Z., Wang R.Z. (2016). Experimental study on a resorption system for power and refrigeration cogeneration. *Energy* 97, 182-190.

"This page intentionally left blank"

CHAPTER 2

Solar hybrid absorption / thermochemical refrigeration system

2.1 INTRODUCTION AND OBJECTIVES

Following the considerations in Chapter 1, absorption refrigeration driven by solar thermal energy is an interesting hybridization to provide thermochemical processes with continuous operation, and at the same time, integrate energy storage in absorption refrigeration. Consequently, in this Chapter we present a hybrid refrigeration system driven by solar energy and made up of absorption refrigeration and thermochemical process.

The system is proposed, its temperature and pressure levels are discussed, and its components and operating modes are described. After discussion and brief literature review on eligible working pairs, a refrigerant fluid is selected for the hybrid system, an absorbent salt is selected for the absorption subsystem, and a reactive salt is selected for the thermochemical subsystem. The performance of this system is simulated and preliminarily studied with respect to some design variables and parameters.

2.2 SYSTEM DESCRIPTION

2.2.1 Components

Fig. 2.1a shows the hybrid absorption/thermochemical refrigeration system (HATRS) in its most simple configuration. It is similar to a conventional absorption refrigeration cycle, but with an added reactor.

In this configuration, two subsystems can be defined: a conventional absorption refrigeration subsystem, and a thermochemical subsystem.

The conventional absorption refrigeration subsystem is made up of a generator (G), a condenser (C), an evaporator (E), an absorber (A), and a solution heat exchanger (SHX) as main components. It provides cold continuously while the heat source is available.

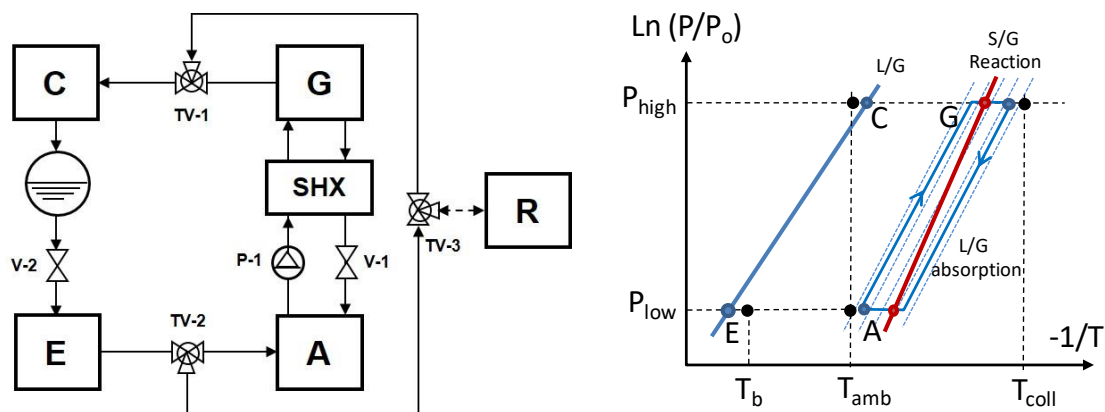


Figure 2.1. (a) Flow diagram of the hybrid absorption / thermochemical refrigeration system (basic configuration); (b) Temperature and pressure levels of the system on the Clausius-Clapeyron diagram.

The thermochemical system is made up of a reactor (R), the abovementioned condenser (C) and the abovementioned evaporator (E). It provides energy storage for a short-medium period and refrigeration for a relatively short amount time.

As shown in Fig. 2.1a, both the absorption and the thermochemical subcycles share the same condenser and evaporator, for the sake of compactness.

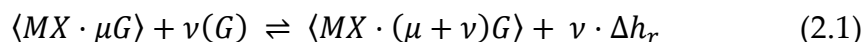
The hybridization of the absorption subcycle with the thermochemical subcycle is carried out through some valves: the valve TV-1, which allows circulation (into the condenser) of the refrigerant fluid coming from either the generator or the reactor; and the valve TV-2, which derives the refrigerant fluid from the evaporator to either the reactor or the absorber. The three-way valve TV-3 is adjusted depending on whether refrigerant fluid has to flow into or out of the reactor. Accordingly, the stream between valve TV-3 and the reactor is displayed as a left-right dashed arrow.

Fig. 2.1b displays the thermodynamic cycle on the Clausius-Clapeyron diagram. The cycle has a high pressure level (P_{high}) and a low pressure level (P_{low}), separated by pump P-1 as well as valves V-1 and V-2 in Fig. 2.1a. From the operational point of view, the three main temperature levels of the cycle are the high, medium, and low temperature level. Within the frame of this study, the high temperature level was designated as the temperature of the solar collector (T_{coll}), which provides driving heat to both the generator and the reactor. The medium temperature level was designated as the ambient temperature (T_{amb}), which receives exhaust heat from the absorber, the reactor and the condenser. The low temperature level was designated as the

temperature at which the refrigeration effect is needed (T_b); heat is transferred from this temperature level to the evaporator's temperature level.

In Fig. 2.1b, the line connecting the operating conditions (T , P) of the condenser and the evaporator corresponds to the vapor-liquid equilibrium line of the pure refrigerant fluid. The two blue lines connecting those of the generator and the absorber correspond to vapor/liquid equilibrium lines of the refrigerant/absorbent mixture, at different absorbent concentrations. From these two lines, the leftmost one corresponds to the mixture with the highest concentration of refrigerant (usually named 'rich solution'), while the rightmost one refers to the mixture with the lowest concentration of refrigerant (usually named 'poor solution'). The red line represents the solid/gas equilibrium of the reversible reaction taking place inside the reactor. Within this line, two operating points are shown: the point at the highest temperature (and pressure) corresponds to the temperature at which refrigerant gas flows from the reactor to the condenser, while the point at the lowest temperature corresponds to the temperature at which the reactor receives the refrigerant gas coming from the evaporator.

Inside the reactor, a reversible solid/gas reaction takes place [1], with its general form shown in eq. (2.1).



$\langle MX \rangle$ is a solid reactive salt (usually a metal halide) which has fixed either μ or $(\mu + \nu)$ moles of refrigerant gas (G) per mole of salt [2]. Therefore, μ is the number of moles of refrigerant gas contained in the solid composite when the gas has been fully retired from it (through an endothermic reaction), ν is the number of moles of refrigerant gas that react with the solid salt, and $(\mu + \nu)$ is the number of moles of refrigerant in the solid composite when both compounds have fully reacted (in an exothermic reaction). Δh_r is the enthalpy of reaction per mole of refrigerant gas. Note that μ may be equal to zero.

The system formed by the two salts $\langle MX \cdot \mu G \rangle$ and $\langle MX \cdot (\mu + \nu)G \rangle$ and the gas (G) is monovariant. This means that, at a given pressure (which is fixed by either the condenser or the evaporator in the operation of the hybrid system), the reaction's equilibrium temperature is fixed independently of the mole proportion of the two salts. This is the first notable difference in comparison with absorption systems, which are bivariant (i.e. both temperature and salt fraction must be given for the equilibrium pressure to be fixed).

Moreover, the transformation process taking place inside the reactor is intrinsically non-stationary, with the composition of the reactive fixed bed

evolving between $\langle \text{MX} \cdot \mu \text{G} \rangle$ and $\langle \text{MX} \cdot (\mu + \nu) \text{G} \rangle$. The sense of this reaction depends on the constraint temperature that is applied to the reactor at a given pressure. For a constraint temperature lower than the equilibrium one, the reaction evolves from left to right in eq. (2.1), thus taking place the exothermic reaction and releasing, for each mole of salt, an amount of heat equal to $\nu \cdot \Delta h_r$ at the constraint temperature. Inversely, for a higher temperature than the equilibrium one, the reaction evolves from right to left and is endothermic.

The relation between the system's temperature and pressure at its equilibrium line is shown in eq. (2.2), where the reference pressure (P^0) is $P^0 = 1$ bar. The values of Δh_r^0 and Δs_r^0 were given by [3] for each reactive pair, and were assumed constant with respect to temperature.

$$\ln\left(\frac{P_{eq}}{P^0}\right) = \frac{-\Delta h_r^0}{R \cdot T_{eq,r}} + \frac{\Delta s_r^0}{R} \quad (2.2)$$

2.2.2. Operating modes

Table 2.1 identifies the operation scenarios. A total of 7 scenarios and 6 operating modes are identified.

The leftmost column (“#”) contains the identifier: each row is one possible scenario and is identified with a number from #1 to #7. Second column from the left (“ Q_{hs} ”) shows whether source heat (Q_{hs}) is available ($Q_{hs} > 0$) or unavailable ($Q_{hs} = 0$). The third column (“ Q_{demand} ”) displays whether or not there is a demand of cold to satisfy at the moment ($Q_{demand} > 0$ or $Q_{demand} = 0$, respectively), and the fourth column (“ABS”) decides accordingly whether or not the absorption subsystem proceeds (ON/OFF).

Fifth column evaluates whether or not the maximum cold production deliverable by the ABS subsystem with the given source heat satisfies the demand of cold. Depending on the case shown by this column, the sixth column (“TCH”) shows whether the thermochemical subsystem is storing refrigerant (CHARGE), de-storing refrigerant (DISCHARGE) or simply not operating (OFF).

After all considerations in the first six columns, the seventh column (“Mode”) identifies the operating mode that proceeds in the scenario described, and the eight column (“Notes”) provides some annotations.

Scenarios #1, #3, #4 and #6 show the behavior of the subsystems when the heat source is available, while scenarios #2, #5 and #7 refer to those cases in which there the heat source is unavailable or insufficient. Each operating mode and scenario is discussed in the sections below.

Table 2.1. Identification of all possible operation scenarios in the solar hybrid ABS/TCH refrigeration system and their corresponding operation modes.

#	Q_{hs}	Q_{demand}	ABS	Demand satisfied by ABS?	TCH	Mode	Notes
1	>0	>0	ON	Y	OFF	ABS	Source satisfies demand, no surplus.
2	=0	>0	ON	N	OFF	ABS	Demand, no source, no stored refrigerant: Auxiliary source.
3	>0	=0	OFF	Surplus	CHARGE	TCH-charge	Source, no demand, store refrigerant.
4	>0	>0	ON	Surplus	CHARGE	ABS + TCH-charge	Source surplus: store refrigerant.
5	=0	>0	OFF	N	DISCHARGE	TCH-discharge	Demand, no source: release refrigerant.
6	>0	>0	ON	N	DISCHARGE	ABS + TCH-discharge	Source is insufficient: release refrigerant.
7	=0	=0	OFF	=0	OFF	OFF	No source, no demand, systems off.

2.2.2.1 "ABS" mode

There are periods in which there is indeed demand of cold, there is source heat available, and this source heat is sufficient to activate the absorption refrigeration subsystem (in Table 2.1: ABS is ON). If the absorption refrigeration subsystem produces enough cold to satisfy the demand, and there is little or no surplus of source heat, the thermochemical subsystem remains inoperative (in Table 2.1: TCH is OFF). This situation is described in scenario #1 from Table 2.1.

This scenario is improbable to occur for long periods of time in a real application. Usually, due to the mismatch described in Chapter 1, the source heat will either be insufficient to satisfy the demand of cold, thus needing the contribution of the TCH subsystem or an auxiliary heat source, or it will be available in surplus, thus leading to the activation of the TCH subsystem to store the extra energy (this scenario is described later on). However, it may be likely to happen during dawn and dusk, where the cold production and cold demand curves cross each other.

Fig. 2.2 shows how this mode could be operated in a solar hybrid absorption / thermochemical refrigeration system (both for scenarios #1 and #2). The overall setup consists of the hybrid absorption/thermochemical refrigeration cycle (previously described in [4]), coupled to a solar loop made up of a solar thermal panel field and a service pump.

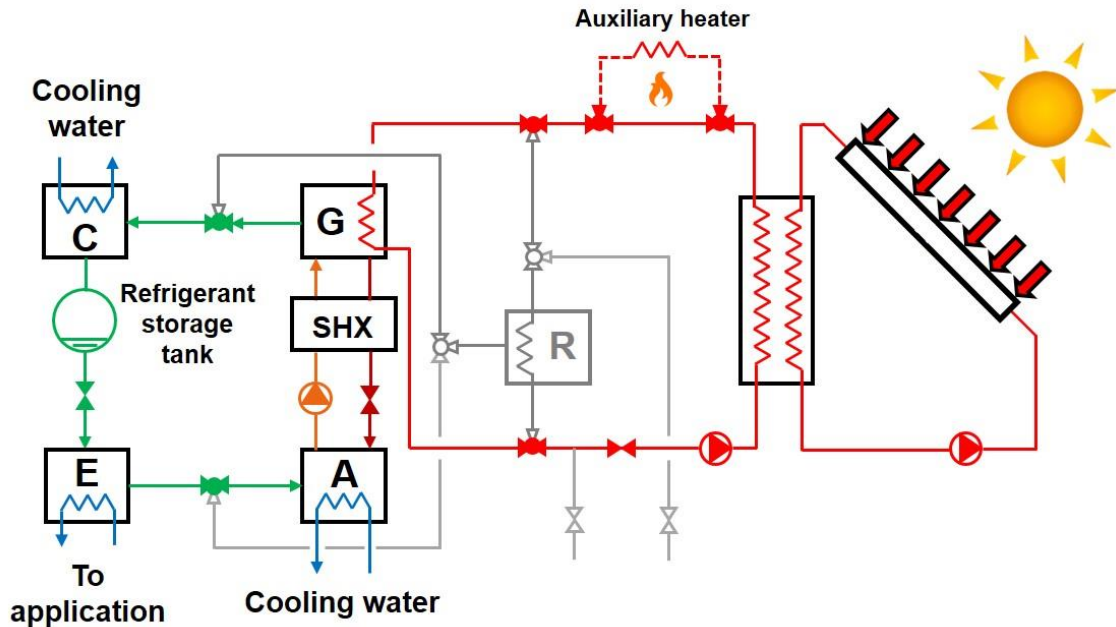


Figure 2.2. “ABS” operating mode represented on a Solar Hybrid Absorption Thermochemical Refrigeration System (SHATRS).

The configuration presented in Fig. 2.2 assumes non-autonomous operation of the system and therefore is provided with an auxiliary heater (driven by a non-renewable energy source, such as fossil fuels) which delivers driving heat to the system when the solar resource is not available. The condenser, absorber and reactor are provided with external flows of cooling water for heat dissipation, while the external flow in the evaporator collects the refrigeration effect (the cycle’s useful effect) and delivers it to whichever application the system is designed for.

With the system described in Fig. 2.2, the thermal energy collected during daytime by the solar thermal panels is delivered (via the solar loop) either to the generator for activation of the absorption subcycle, or to the reactor for activation of the thermochemical subsystem. Any surplus heat collected at the solar field is stored by the thermochemical subsystem, as described previously.

In “ABS” mode, the absorption subsystem proceeds as a conventional absorption chiller would (Fig. 2.3a).

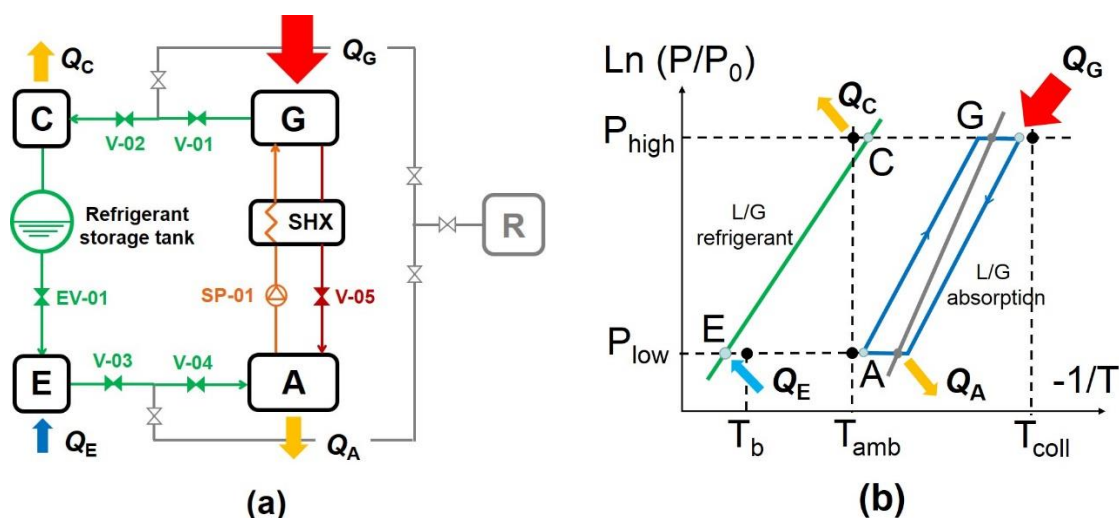


Figure 2.3. (a) “ABS” operating mode represented on the flow diagram of the Hybrid Absorption / Thermochemical Refrigeration System (HATRS); (b) “ABS” operating mode represented on the Clausius-Clapeyron diagram.

The heat supplied to the generator (Q_G) regenerates the absorbent and refrigerant vapor flows to the condenser, where it changes its phase from superheated vapor to saturated liquid, rejecting heat of condensation in the process (Q_C). This heat of condensation is collected and evacuated by cooling water. The refrigerant then undergoes isenthalpic expansion (EV-01).

During this isenthalpic expansion, a small fraction of refrigerant (usually 5% or lower) vaporizes and causes the refrigerant’s temperature to drop until the equilibrium temperature (T_{evap}) that corresponds to P_{EVAP} , according to the VLE of the pure refrigerant. After expansion, refrigerant flows into the evaporator, where it vaporizes to saturated vapor state, requiring a heat input (Q_E). This heat input is the useful effect of the refrigeration cycle, as it is removed from the stream that will deliver the cold to the application.

After the evaporator, the vaporized refrigerant flows into the absorber, where it is absorbed by the regenerated absorbent coming from the generator, and releases heat (Q_A) in the process. The mixture is then pumped again to the generator through a solution heat exchanger (SHX), and the cycle is completed. Fig. 2.3b shows the cycle on the Clausius-Clapeyron diagram.

In scenario #2 there is demand of cold, but no source heat available, and in addition, the energy stored (if there is) in the TCH subsystem is insufficient to satisfy the demand. In this situation another stable and permanently available

(and most likely, non-renewable) heat source is used. As in scenario #1, the ABS subsystem proceeds, while the TCH subsystem remains OFF. However, depending on the demand and sun irradiation profiles, this situation may be avoided if the system is designed for autonomous operation.

2.2.2.2 "TCH-charge" mode

There may be periods in which the solar resource is available but there is no cold demand (scenario #3). In these periods the operation of the ABS subsystem is not necessary (OFF), but the driving heat can still be utilized by the TCH subsystem to desorb refrigerant from the reactive salt and store it in liquid form (CHARGE).

At a given condensing temperature for the refrigerant, the operating pressure during this stage is imposed by the vapor/liquid equilibrium of pure refrigerant in the condenser. The heat provided by the high-temperature heat source to the reactor (Q_R) increases the temperature above the equilibrium temperature at the given pressure, thus activating the endothermic reaction, and refrigerant fluid in gaseous phase is desorbed from the reactor.

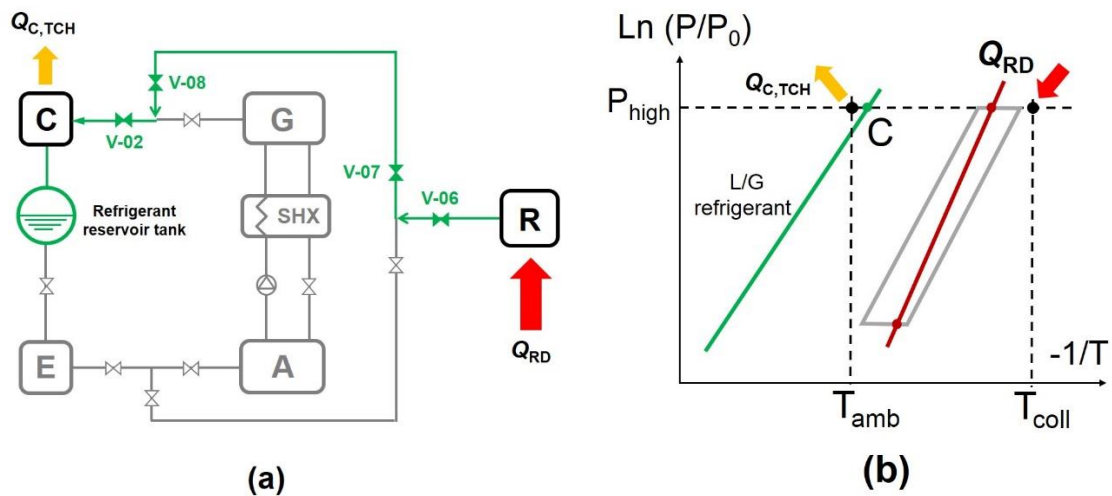


Figure 2.4. (a) "TCH-charge" mode shown on the basic configuration; (b) "TCH-charge" mode shown on the Clausius-Clapeyron diagram.

The refrigerant then flows to the condenser, where it condensates and remains stored in liquid state in the reservoir after the condenser's outlet. This stage is here referred as 'charge stage' (from the point of view of thermochemical storage) or 'decomposition phase' (from the point of view of the solid reactive composite). Thus, the solar energy provided to the system is transformed into (and stored as) chemical potential between the refrigerant and the salt, or otherwise called, 'refrigeration potential'. One important advantage

of this form of storage is that the liquefied refrigerant can be stored at ambient temperature, which means there are no concerns about thermal insulation. Figure 2.5 displays how this operating mode could be implemented in the SHATRS.

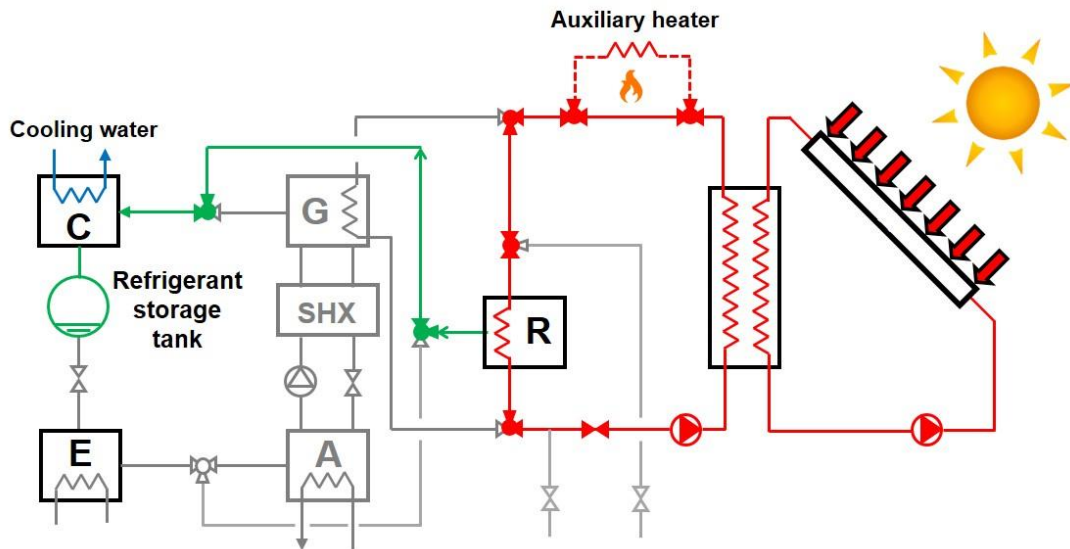


Figure 2.5. "TCH-charge" mode shown on the SHATRS.

2.2.2.3 "ABS + TCH-charge" mode

Scenario #4 refers to those periods in which the source heat is fairly more than sufficient (both in terms of heat and temperature level) to cover the demand of cold. In these situations the ABS subsystem is producing cold (ON) and the TCH subsystem is storing liquid refrigerant (CHARGE) as described in the "TCH-charge" mode (Fig. 2.6a).

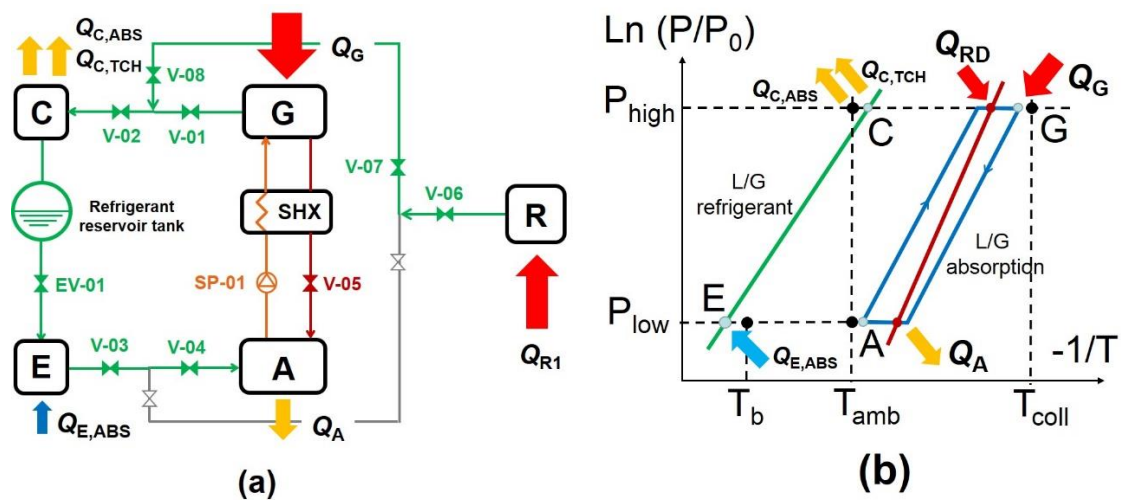


Figure 2.6. (a) "ABS + TCH-charge" mode shown in the basic configuration; (b) "ABS-TCH-charge" mode shown on the Clausius-Clapeyron diagram.

2.2.2.4 “TCH-discharge” mode

Scenario #5 from Table 2.1 indicates that when there is cooling demand but the source heat is either unavailable (e.g. solar resource during the night), insufficient or at too low temperature (e.g. solar resource early in the morning or late in the afternoon), the absorption subsystem alone cannot satisfy the demand, and remains inoperative (OFF). If there is stored refrigerant in the tank, the TCH subsystem proceeds in cold production (DISCHARGE) mode (Fig. 2.7a).

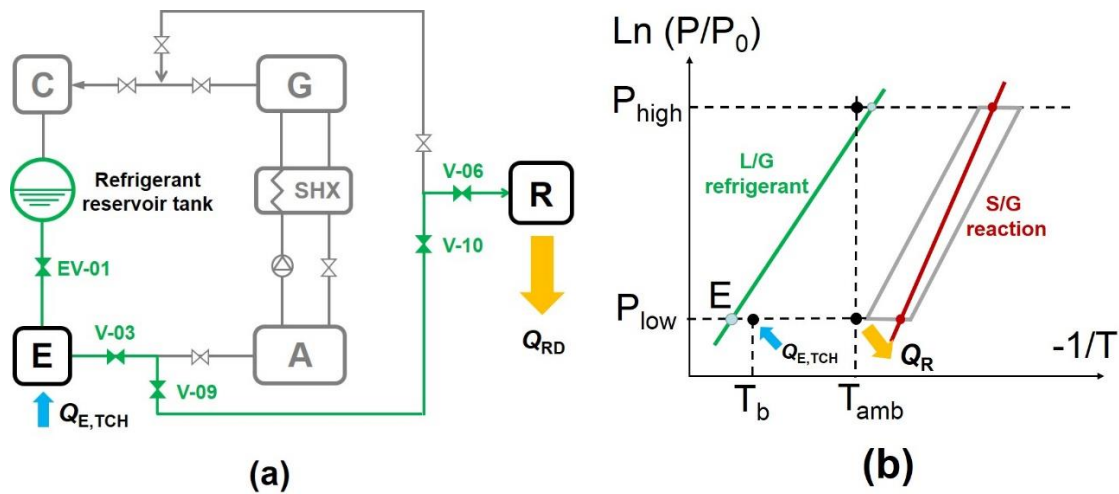


Figure 2.7. (a) “TCH-discharge” mode shown in the basic configuration; (b) “TCH-discharge” mode shown on the Clausius-Clapeyron diagram.

Liquid refrigerant is released from the tank and undergoes an expansion through the expansion valve (EV-01), dropping to evaporator pressure (P_{EVAP}). As explained previously, during this isenthalpic expansion, a small fraction of refrigerant (usually 5% or lower) vaporizes.

Upon entering the evaporator, all remaining liquid refrigerant vaporizes at T_{evap} and produces the cold ($Q_{E,TCH}$). This cold is collected by the fluid (usually water or glycol/water) circulating in the other side of the evaporator. This is one strong advantage of energy storage with thermochemical processes over sensible heat storage: the cold can be produced almost immediately when needed, just by releasing stored refrigerant.

During the production of cold, the evaporator and the thermochemical reactor are connected by the pipeline, and the pressure is imposed by the evaporator (Fig. 2.7b).

On the reactor’s side, refrigerant gas reacts with the solid salt in an exothermic process that releases heat of reaction (Q_R). From the point of view of

the solid composite inside the reactor, it is commonly known as 'synthesis phase', and from the point of view of energy storage in the system, this phase can be named 'discharge phase'.

The start of the exothermic reaction causes the reactor's temperature to rise quickly, potentially until the equilibrium temperature ($T_{eq,R}$) at this constraint pressure. Of course, due to the heat transfer limitation this heat (Q_R) is delivered to the environment at a lower temperature. Otherwise, if the heat was not dissipated and the reactor temperature remained at $T_{eq,R}$, the reaction would stop. To continue the process, the reactor must be cooled down. As a matter of fact the rate of reaction, and therefore the rate of cold production, can be (and is) controlled with the set temperature at which the reactor is being cooled down.

The difference between the equilibrium temperature and the composite's temperature is sometimes named 'equilibrium drop'. This equilibrium drop is the driving force of the thermochemical process, since it keeps the reaction active: the removal of moles of refrigerant gas in the pipeline creates a vacuum that forces more refrigerant to vaporize in the evaporator, thus continuing to generate the useful refrigeration effect (Q_{cold}) until the reaction is completed.

The amount of heat rejected at the reactor by the end of the process is practically the same as the amount needed to carry out the endothermic reaction during the decomposition phase. The only difference is that in this operating mode, a small part of this reaction heat is utilized by the system itself to raise the reactor's temperature from ambient temperature ($T_{amb,night}$) to the equilibrium temperature ($T_{eq,R}$).

Fig 2.8 shows how this mode would proceed in the SHATRS, during nighttime (or a cloudy day).

The valves in the solar loop are adjusted accordingly to operate as cooling loop for the reactor, and cooling water is pumped through the reactor's thermal jacket. This cooling water collects the reaction heat and dissipates it.

One way to dissipate this heat can be ground cooling [5]. Also, with proper design and operating conditions, the reactor can be air-cooled. In this case, the reaction heat collected by the cooling loop would be dissipated at the solar collector field, whose panels would be air-open, finally rejecting the heat to the ambient (at night, when the temperature is lower).

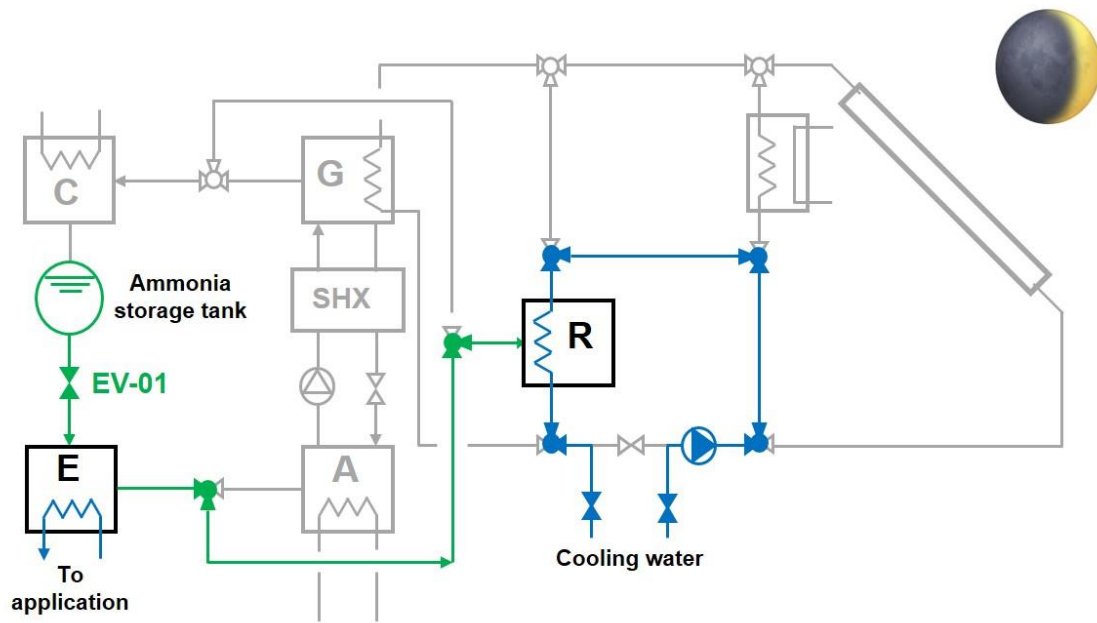


Figure 2.8. “TCH-discharge” mode on the SHATRS.

2.2.2.5 “ABS + TCH-discharge” mode

When there is cooling load and the absorption subsystem alone cannot satisfy it, but there is stored energy in the TCH subsystem (scenario #6), the TCH subsystem is operating in “DISCHARGE” mode along with the ABS operating continuously (Fig. 2.9).

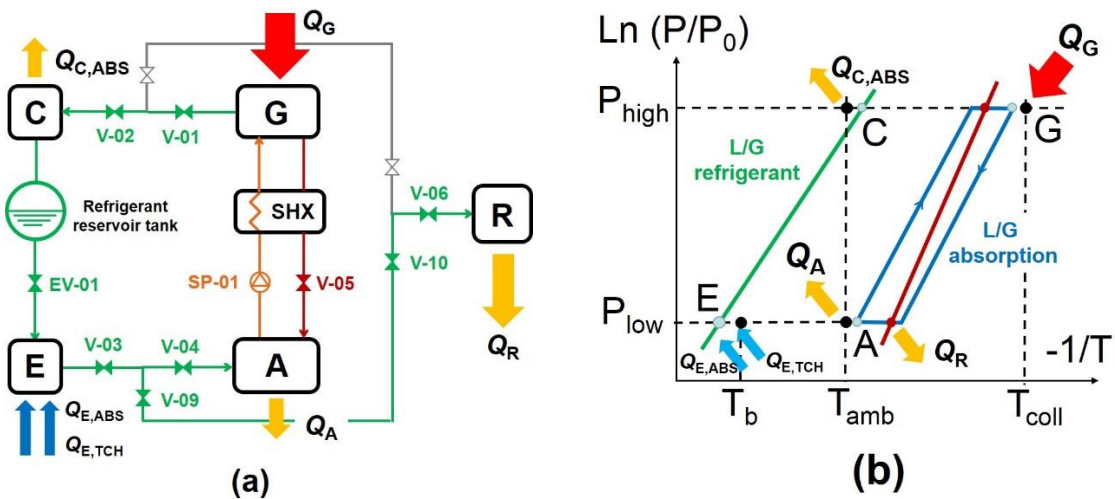


Figure 2.9. (a) “ABS + TCH-discharge” mode shown in the basic configuration; (b) “ABS + TCH-discharge” mode shown in the Clausius-Clapeyron diagram.

2.2.2.6 "OFF" mode

The simplest scenario (#7) takes place when there is no source heat available and there is no cold demand either; in such situation, neither the ABS nor the TCH subsystems would be required to operate. This scenario could take place in applications where cold demand is intermittent, like residential cooling.

In these periods, the reactor is disconnected from either the condenser or the evaporator. As a matter of fact, this mode can also be regarded as a transition from "TCH-charge" mode to "TCH-discharge" mode, or *vice versa*. During these transitions, valves are accordingly manipulated to change the circulation of the fluid in the solar loop, depending on which operating mode is to proceed next.

2.3. SYSTEM PRELIMINARY DESIGN

2.3.1 Working pair selection

There is sufficient literature on working pairs for both absorption refrigeration and thermochemical processes for refrigeration applications, with several promising working pairs in each case. However, the proper selection of suitable working pairs for this hybrid system is bound to some restrictions here discussed.

2.3.1.1 Discussion and pre-selection

First, the refrigerant is to be selected. Normally, two separate systems would be able to operate with different refrigerants, but in the hybrid system that we present here, both subsystems share the same condenser and evaporator. Thus, they should share the same refrigerant fluid as well, for the sake of compactness, simplicity, and economy.

Having decided to select the same refrigerant for both subsystems, it is time to decide which refrigerant.

For thermochemical systems, several choices are available for physical, thermochemical or composite sorption [6]. Regarding thermochemical sorption, conventional working pairs include: metal chloride/bromide/iodide-ammonia reactions, with driving temperatures ranging from 50 °C to 350 °C; metal oxides-oxygen/water/carbon dioxide reactions, with driving temperatures in the range of 150 °C - 1000 °C; and metal hydrides-hydrogen reactions, with driving temperatures between 110 °C and 400 °C.

The application is the first important aspect to have in mind. Each application requires certain temperature levels, especially for the cold produced, and this reduces the field of adequate refrigerants.

This study focuses on refrigeration (for applications like food conservation, ice making, deep-freezing...), which implies the production of cold under 0 °C (also called 'negative cold'). For this reason, ammonia as refrigerant is an interesting option, whereas water is usually preferable for other applications like air conditioning, with higher cold production temperatures. Therefore, ammonia was chosen over water as refrigerant for this study.

Nevertheless, water as refrigerant is not discarded for these systems either, since it would be viable in other applications and there are working fluids for both subsystems with water as refrigerant. In addition, water-based working fluids usually offer better thermal performance in general. In the case of water, absorbents like lithium bromide or lithium chloride, among others, can be used.

After the refrigerant is selected, a working pair must be chosen for each subsystem. That is, a sorbent salt for the absorption subsystem, and a reactive salt for the thermochemical subsystem.

Some candidates for ammonia-based working pairs in absorption refrigeration are ammonia/water ($\text{NH}_3/\text{H}_2\text{O}$), ammonia/lithium nitrate ($\text{NH}_3/\text{LiNO}_3$) and ammonia/sodium thiocyanate (NH_3/NaSCN) [7].

Ammonia-based working pairs in thermochemical systems include (but not limited to) metal chlorides [8], bromides or iodides, just to name a few. One of the most interesting ones is barium chloride (BaCl_2) [5], which has been used in several experimental studies [9]. Others are available, such as calcium chloride (CaCl_2) [10], strontium chloride (SrCl_2), or strontium bromide (SrBr_2).

To further reduce the field of eligible ammonia-based working pairs, two additional restrictions come into play.

The first one is the application, again. Although both the absorption and the thermochemical subsystems can achieve high driving temperatures with the adequate working pairs, their practical use in applications based on solar thermal energy is eventually limited by the type of solar collector. Here, we will consider the use of flat plate solar thermal collectors, which limit the heat source temperature to a maximum of approximately 100 °C.

Also related with the application, the location may influence the selection of working fluid. For the same application and cold production temperatures, a location with rather high ambient temperatures introduces limitations to the system's performance, and may accordingly lead to the use of another working

pair with a slightly higher driving heat temperatures, to compensate. However, for this study the application is not so precisely defined, therefore the location or the ambient temperature are not so strictly taken into account.

The second restriction is related to the system's configuration. As stated above, both subsystems share the same refrigerant. In some ammonia-based working pairs for absorption refrigeration, the ammonia may contain some traces of sorbent when entering the condenser.

This is especially true for the ammonia/water working pair. One of its characteristic traits is the presence of water at the generator outlet, since the rectification that is used after the generator outlet is not always completely efficient. This content in water (usually 10% or lower), if not properly removed before the evaporator, rises the vaporization temperature of the mixture, which may be unable to supply the cold at the demanded temperature.

This is already an issue in the design and operation of conventional ammonia/water absorption refrigeration cycles. Classically, this water content is minimized by applying at least one rectification stage at the generator outlet, before the condenser.

This solution allows to reduce the water content in ammonia to acceptable values (lower than 1%), but is not enough to remove it completely. And this causes the progressive accumulation of water in the evaporator, making a purge necessary from time to time. Further, the implementation of this solution reduces the thermal performance of ammonia/water cycles (since rectification needs some energy input) and their economic competitiveness (because proper rectification is costly).

When it comes to the hypothetical use of ammonia/water in hybrid absorption / thermochemical refrigeration systems, the risk goes beyond cold delivery temperature, periodic purges, reduced thermal performance, or cost amplification.

Moreover reactive salts commonly used in ammonia-based thermochemical refrigeration react also with water, and even preferentially to the ammonia. This is already a problem when these salts come in contact with atmospheric air, absorbing some of its humidity. As a matter of fact, these salts need to be dehydrated after implementation inside the reactor, right before charging the system with ammonia.

If the ammonia leaving the evaporator contains some traces of water, these may end up entering the reactor during the cold production phase on the thermochemical subsystem. Molecules of water are captured by molecules of

reactive salt and impede the formation of chemical bonds between the salt and the ammonia.

It is improbable to vaporize this water from the reactive composite on the next decomposition phase, and even if possible, the salt distribution inside the composite would be altered by the water solving the salt. Thus, it can be affirmed that the presence of water, even in small traces, in the ammonia flowing out of the evaporator would drastically reduce the performance of the thermochemical subsystem in the long run.

For all the reasons exposed above, only pure refrigerant should enter the condenser, or more precisely, only pure refrigerant can return to the thermochemical reactor. Ignoring this restraint would incur soon enough in incomplete reactions in the thermochemical subsystem, as well as the need of emptying and re-filling the reactor with new solid composite after not too many cycles.

For the absorption subsystem, this excludes the possibility of using the well-known ammonia/water working pair, despite the acceptable thermophysical properties and thermal performance of this mixture in absorption refrigeration. It might still be viable with an intense and costly rectification, but the overall machine would be much less attractive.

Instead, other interesting ammonia-based working pairs are available where the sorbent does not vaporize in the generator. This is the case of ammonia/lithium nitrate ($\text{NH}_3/\text{LiNO}_3$) and ammonia/sodium thiocyanate (NH_3/NaSCN).

With these mixtures, only pure ammonia circulates to the condenser/evaporator segment. According to the literature, ammonia/lithium nitrate shows slightly higher thermal performance and lower circulation ratios at lower generator temperatures, while ammonia/sodium thiocyanate shows better performance at higher generator temperatures [7]. Since the system's performance will be studied at conditions corresponding to solar applications (i.e. not a very high heat source temperature), the $\text{NH}_3/\text{LiNO}_3$ pair was preferred for the simulative studies.

Last but not least, environmental and safety-related considerations are always to be taken into account. From these standpoints, water is excellent as refrigerant: non-toxic, non-flammable, non-contaminating and non-expensive. Ammonia, despite posing some danger for human health, has still the advantages of being a "natural" refrigerant without any impact on ozone neither a greenhouse effect in the atmosphere.

All criteria applied above narrow the field of eligible working pairs to: $\text{NH}_3/\text{LiNO}_3$ and NH_3/NaSCN for the absorption subsystem; $\text{NH}_3/\text{BaCl}_2$, $\text{NH}_3/\text{PbBr}_2$, NH_3/LiCl , $\text{NH}_3/\text{NH}_4\text{Br}$, and $\text{NH}_3/\text{SnCl}_2$ for the thermochemical subsystem. Now, the selection proceeds to check cycle performance.

2.3.1.2 Analysis and selection

As seen in the previous section, even after considering several restrictions and discarding many working pairs, there are still some pairs to choose from.

At this point, the performance of every candidate working pair must be evaluated at least individually for each subsystem. In this study, a preliminary simulation of each subsystem is carried out with all candidate working pairs. Then, the most promising pair for the ABS subsystem and the most promising pair for the TCH subsystem are selected for simulation of the hybrid system.

A deeper level of analysis would be the simulation of the global hybrid system with each possible combination of working pairs. Nevertheless, if a particular working pair offers the highest COP over other candidates for the subsystem alone, it is logical to think that this pair is at least promising for the hybrid system. With this reasoning, and given the fact that this is only a preliminary study, the hybrid system was studied with the most performant working pairs from each subsystem according to the state of the art.

For cycle simulation, the operating conditions must be set. These conditions will determine the operation range of the system, and every working pair that can operate within this range is a candidate. Fig. 2.10 represents this step of the selection process on the Clausius-Clapeyron diagram.

For the sake of clarity, double axes are used in addition to the axes corresponding to the linearized form, in order to show clearly the temperature and pressure levels.

In this diagram, the blue continuous line represents the vapor/liquid equilibrium of pure ammonia. This line is common to both the ABS and the TCH subsystems.

The isosteres of the absorption subsystem are shown as continuous lines. The red continuous line represents the vapor/liquid equilibrium of the $\text{NH}_3/\text{LiNO}_3$ solution with higher concentration in ammonia (usually known as 'rich solution' or 'strong solution'), while the black continuous line accounts for the vapor/liquid equilibrium of the $\text{NH}_3/\text{LiNO}_3$ solution with lower concentration in ammonia (poor solution).

Thus, the absorption subsystem is made up of the combination of the three continuous lines (blue, black and red).

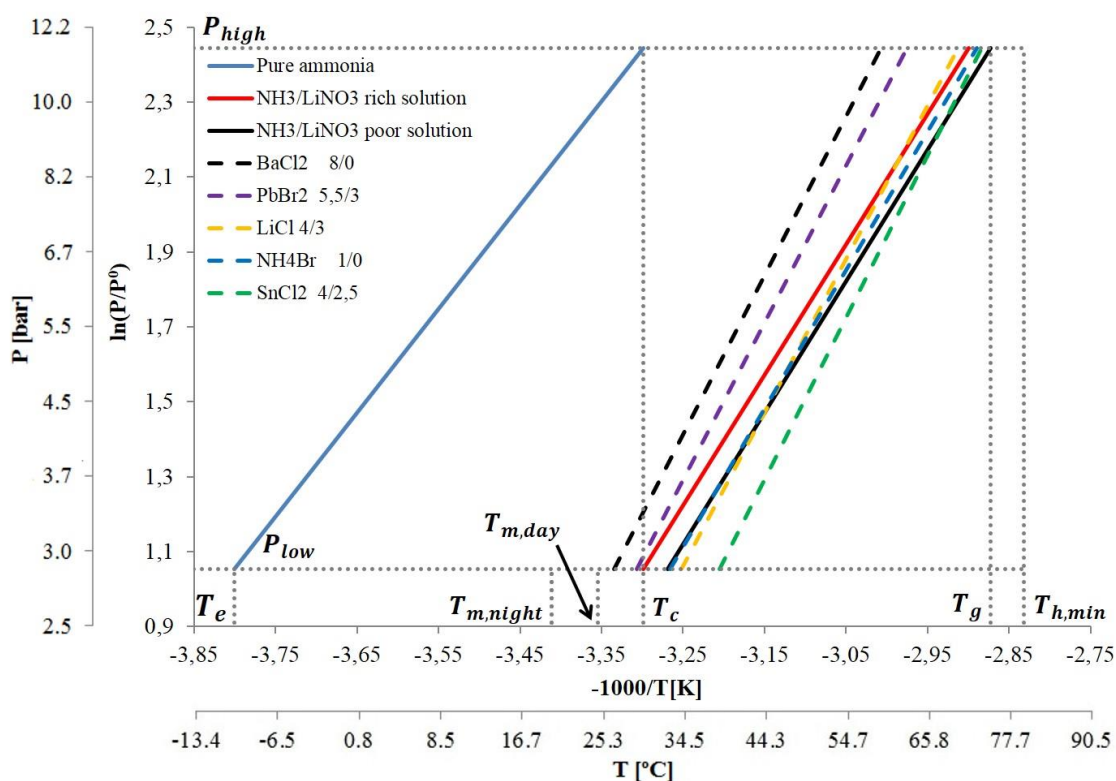


Figure 2.10. Clausius-Clapeyron diagram with some suitable reactive pairs for the TCH subsystem (with max/min stoichiometric coefficients) and an example of working pair for the ABS subsystem.

For the thermochemical subsystem, dashed lines display the solid/gas equilibrium of the reversible reaction for reactive pairs that are eligible in the specified operating conditions [8]. Each dashed line corresponds to one working pair: black for $\text{BaCl}_2/\text{NH}_3$; pink for $\text{PbBr}_2/\text{NH}_3$; yellow for LiCl/NH_3 ; blue for $\text{NH}_4\text{Br}/\text{NH}_3$; and green for $\text{SnCl}_2/\text{NH}_3$.

Thus, the thermochemical subsystem consists of the blue continuous line plus one of the dashed lines, to be selected.

As for the hybrid system, it consists of the blue, black and red continuous lines plus one of the dashed lines. Grey dotted lines are used to show relevant pressure and temperature levels for system design and pair selection.

As explained before, the temperature levels are imposed by the application. These temperature levels imply pressure levels, and the coupling of working pairs for ABS and TCH subsystems revolves around these temperature and pressure levels.

Firstly, the temperature at which the cold is needed (T_b) was assumed as $T_b = -5\text{ °C}$, which justifies the use of ammonia as refrigerant. Due to heat transfer, a minimum difference of $\Delta T = 5\text{ °C}$ between cold delivery temperature and cold production temperature was assumed, which sets an evaporator temperature of $T_e = -10\text{ °C}$.

This evaporator temperature sets a low operating pressure of $P_{low} = 2.8\text{ bar}$. This pressure corresponds to the evaporator/absorber segment of the ABS subsystem, as well as the synthesis phase (or cold production phase) of the TCH subsystem.

It is important that both working pairs, whichever they are, allow both subsystems to operate simultaneously, since, as described in the operating modes, they may be required to do so (scenario #6).

For the ABS subsystem, this means that at the given P_{low} the absorber temperature (T_{abs}) should be at least 5 °C higher than the ambient temperature during daytime ($T_{m,day}$), which was assumed as $T_{m,day} = 25\text{ °C}$, leading to $T_{abs,min} = 30\text{ °C}$. In conjunction with the given P_{low} , this sets a maximum value for the ammonia mass fraction in the rich solution ($x_{rich,max}^{NH_3}(P_{low}, T_{abs,min})$).

And for the TCH subsystem, the reactor temperature during synthesis phase (T_{rs}) should be at least 10 °C higher than the ambient temperature during nighttime ($T_{m,night}$), which was assumed as $T_{m,night} = 20\text{ °C}$, leading to $T_{rs,min} = 30\text{ °C}$. This temperature is unique for the given pressure and does not depend on any ammonia mass fraction.

As explained before, both ambient temperatures are determined by the location. Particularly, $T_{m,day} = 25\text{ °C}$ corresponds to a pressure of $P_{high} = 11.8\text{ bar}$, which is the operating pressure in the generator/condenser segment of the ABS subsystem, as well as in the decomposition phase (or refrigerant storage phase) of the TCH subsystem.

Another temperature level set by the application is the heat source temperature (T_h). As explained previously, flat plate solar thermal collectors can deliver heat at a temperature between $T_{h,min} = 80\text{ °C}$ and $T_{h,max} = 100\text{ °C}$. This implies that both subsystems must be able to operate, at least, when the heat source is at $T_{h,max}$, but even more recommended is that they should be able to operate when the heat source is at $T_{h,min}$.

And again, the condition of simultaneous operation is especially important here. While the “ABS + TCH-discharge” operating mode may or may not take place depending on the application and design, the “ABS + TCH-charge” operating mode is likely to occur in almost any application.

For the ABS subsystem this implies that at P_{high} , the maximum generator temperature ($T_{g,max}$) is $T_{g,max} = 95$ °C (if a minimum $\Delta T_{ex,g} = 5$ °C is assumed in the generator's heat exchanger). This condition sets a minimum value for the ammonia mass fraction in the poor solution, too ($x_{poor,min}^{NH_3}(P_{high}, T_{g,max})$).

And for the TCH subsystem, this implies that at P_{high} , the maximum reactor temperature during decomposition phase (T_{rd}) is $T_{rd,max} = 90$ °C (if a minimum $\Delta T_{ex,r} = 10$ °C is assumed in the reactor's thermal jacket). This maximum reactor temperature is unique for the given pressure and does not depend on any ammonia mass fraction.

All these considerations reflect the importance of choosing both working pairs carefully.

2.3.1.3 System operating conditions

A constant refrigeration demand of 5 kW in the daytime period and 3 kW in the nighttime period was assumed. The system was assumed to operate in daytime mode for $\Delta t_{day} = 9$ hours (typically from 09.00 to 18.00) and in nighttime mode for $\Delta t_{night} = 15$ hours (typically from 18.00 to 09.00). Assumed temperature levels are shown in Table 2.2.

Table 2.2. Operating conditions for the HATRS in the present study.

Common temperatures			
Solar loop hot fluid temperature ($T_{h,min}$), °C	80	Average daytime ambient temp. ($T_{m,day}$), °C	25
Evaporator temperature (T_{evap}), °C	-10	Avg. nighttime ambient temp. ($T_{m,night}$), °C	20
Absorption subsystem		Thermochemical subsystem	
Generator temperature (T_{gen}), °C	75	Reactor regeneration temperature ($T_{eq}(P_{high})$), °C	70
Condenser temperature (T_{cond}), °C	30	Cooling loop inlet temperature ($T_{cw,in}$), °C	20

2.3.2 Performance simulation

2.3.2.1 Hypotheses and assumptions

The absorption cycle was assumed to operate at steady state with no pressure drop along the pipes, and with isenthalpic expansion through any valves. Saturated liquid state was assumed for absorber and condenser outlets, as well as generator's solution outlet. Saturated vapor state was assumed for the ammonia flowing out of the evaporator. The ammonia vapor coming out of

the generator was assumed to be in equilibrium with the saturated state of the poor solution entering the generator.

Since valves were assumed isenthalpic, and no subcooling at the condenser's exit nor overheating at the evaporator's outlet was assumed, the low pressure (P_{low}) corresponds to the pressure of saturated ammonia vapor at T_e , and the high pressure (P_{high}) corresponds to the pressure of saturated ammonia vapor at T_c , and both were calculated through the expressions given by [11]. These two pressure levels are applicable to both the absorption and the thermochemical subsystems.

2.3.2.2 Simulation model

The operating conditions are shown in section 2.3.1.3.

T_e was assumed to be ΔT_{ex} degrees lower than the temperature at which the cold is needed, and T_c was assumed to be ΔT_{ex} degrees higher than the average daily environment temperature. A temperature difference of 5 °C between the two transferring fluids (ΔT_{ex}) was assumed for all external heat exchangers in this study.

$$P_{low} = P_{eq}(\text{sat. vap. ammonia}, T_{evap}) \quad (2.3)$$

$$P_{high} = P_{eq}(\text{sat. vap. ammonia}, T_{cond}) \quad (2.4)$$

For the evaporator, absorber and condenser, a simple energy balance was carried out (2.5). For the generator, the energy (2.5), materials (2.6) and salt mass (2.7) balances were applied.

$$\dot{Q} = \sum \dot{m}_{out} \cdot h_{out} - \sum \dot{m}_{in} \cdot h_{in} \quad (2.5)$$

$$\sum \dot{m}_{out} - \sum \dot{m}_{in} = 0 \quad (2.6)$$

$$\sum \dot{m}_{out} \cdot x_{out} - \sum \dot{m}_{in} \cdot x_{in} = 0 \quad (2.7)$$

The solution heat exchanger was calculated with an assumed effectiveness (ϵ_{SHX}) of 0.8:

$$\epsilon_{SHX} = \frac{(T_{hot,in} - T_{hot,out})}{(T_{hot,in} - T_{cold,in})} \quad (2.8)$$

The pump was calculated according to pressure change in the poor solution stream flowing through it, with an assumed pump isentropic efficiency (η_{pump}) of 0.7.

$$\dot{W}_{pump} = \frac{\dot{m}_{ws} \cdot v_{ws} \cdot (P_{high} - P_{low})}{\eta_{pump}} \quad (2.9)$$

The Coefficient Of Performance (COP) and solution circulation ratio (f) were used as indicators.

$$COP_{ABS} = \frac{\dot{Q}_{evap,day}}{(\dot{Q}_{gen} + \dot{W}_{pump})} \quad (2.10)$$

$$f = \frac{\dot{m}_{ss}}{\dot{m}_{ref,day}} \quad (2.11)$$

Properties of ammonia/lithium nitrate were given by [12] and [13].

The model for the thermochemical subsystem takes into account heat and mass transfer, and accordingly, relevant thermophysical properties (thermal conductivity, heat capacity, porosity...) of the involved compounds. Some parameters related to reactor geometry were considered. Nevertheless, as this is a preliminary study, heat and mass transfer phenomena inside the reactor were not characterized in detail. Models with a higher degree of detail can be found in other studies, e.g. [14]. A such detail model will be developed in the following chapter, but it is not necessary for this hybrid system in a first approximation.

For a fixed refrigeration power \dot{Q}_b , the molar flow of refrigerant gas (\dot{n}_g) depends on the enthalpy variation of the ammonia from condenser outlet to evaporator outlet (2.12). The number of moles of anhydrous salt in the solid composite (n_{sa}) was calculated thereafter, through reaction stoichiometry (2.13).

$$\dot{n}_g = \frac{\dot{Q}_{evap,night}}{h_{gsat,NH_3}(P_{low}) - h_{lsat,NH_3}(P_{high})} \quad (2.12)$$

$$n_{sa} = \frac{\dot{n}_g \cdot \Delta t_{night}}{\mu \cdot \Delta X} \quad (2.13)$$

ΔX (assumed 0.9 in this study) is the variation in the advancement degree of the synthesis reaction ($X = 0$ corresponds to completely discharged salt and $X = 1$ to completely charged salt).

The rejected heat at the reactor during the production of cold is related to the reaction's enthalpy. From this value, the heat required to increase the

temperature of ammonia from evaporator temperature to reactor low-pressure equilibrium temperature has to be deducted (2.14).

$$\dot{Q}_r = \dot{n}_g \cdot [\Delta h_r - \bar{C}_{p,(NH_3)} \cdot (T_{eq,r}(P_b) - T_{ev})] \quad (2.14)$$

The mean specific heat of ammonia gas ($\bar{C}_{p,(NH_3)}$) was evaluated with the expression given by [11] at the mean arithmetic temperature between $T_{eq,r}(P_b)$ and T_{ev} .

To improve mass and heat transfer during the process, the reactive salt is mixed with expanded natural graphite (ENG) [15]. Given the molar volume of the charged salt v_{s1} , obtained from [16], and the density of the ENG (ρ_{ENG}), and by fixing a value for the porosity of the solid composite at $X = 1$ (ε_1 , assumed 0.4) and the apparent density of the ENG ($\tilde{\rho}_{GNE}$, assumed $80 \text{ kg}\cdot\text{m}^{-3}$) inside the composite, the mass fraction of anhydrous salt in the composite (w_{sa}) is derived as [15]:

$$(1 - \varepsilon_1) = \tilde{\rho}_{GNE} \left[\frac{v_{s1}}{M_{sa}} \cdot \frac{w_{sa}}{(1-w_{sa})} + \frac{1}{\rho_{GNE}} \right] \quad (2.15)$$

Having calculated the mass fraction of anhydrous salt, and the mass of anhydrous salt (implicitly at eq. 14), the calculation of the mass of natural expanded graphite (m_{GNE}) is straightforward, as the solid composite is made up of only these two components. Then, the apparent volume of the composite is calculated (eq. 2.16).

$$\tilde{V}_c = \frac{m_{GNE}}{\tilde{\rho}_{GNE}} \quad (2.16)$$

Once the apparent volume of the composite is known, the composite thickness (e_c), the global heat transfer coefficient (U_p) and the exchanger surface ($S_{e,c}$) can be solved simultaneously (eqs. 2.17 to 2.19). An exchanger wall thickness (e_p) of 1 mm, and an equivalent convective heat transfer of $400 \text{ W}\cdot\text{m}^{-2}\cdot\text{K}^{-1}$ in the solid-wall region (h_{sw}) and $1000 \text{ W}\cdot\text{m}^{-2}\cdot\text{K}^{-1}$ in the wall-exchanger fluid (h_e) region were assumed.

$$\tilde{V}_c = e_c \cdot S_{e,c} \quad (2.17)$$

$$\frac{1}{U_p} = \frac{e_c}{2 \cdot \lambda_c} + \frac{1}{h_{sw}} + \frac{e_p}{\lambda_p} + \frac{1}{h_e} \quad (2.18)$$

$$S_{e,c} = \frac{\dot{Q}_r}{U_p \cdot (T_{eq}(P_b) - T_{cw,in})} \quad (2.19)$$

For graphite mass fractions in the composite equal to or higher than 0.20, the thermal conductivity of the composite (λ_c) was estimated according to eq. (20) [16].

$$\lambda_c \{W \cdot m^{-1} \cdot K^{-1}\} = 0.08 \cdot \tilde{\rho}_{GNE} \{kg \cdot m^{-3}\} \quad (2.20)$$

The total heat to be supplied to the reactor during the regeneration stage is calculated in eq. 2.21. The calculation takes into account the number of reacted moles of ammonia gas and the heat needed to increase reactor's temperature from ambient to activation of the endothermic reaction. The total mass of reactor takes into account the mass of solid composite (expanded graphite + anhydrous salt), the mass of ammonia present in the composite (as a function of the reaction's advancement degree), the mass of fluid m_h inside the reactor (assumed to be 40% of a shell-and-tube reactor's total volume), and the mass of steel from the reactor's structure (as function of wall surface and thickness, calculated above) (2.22).

$$Q_h^{net} = n_s \cdot \mu \cdot \Delta h_r \cdot \Delta X + \sum(m_i \cdot C_{p,i}) \cdot (T_h - T_m) \quad (2.21)$$

$$\sum(m_i \cdot C_{p,i}) = n_{sa} \cdot [C_{p,s1} \cdot X_i + C_{p,s0} \cdot (1 - X_i)] + m_{GNE} \cdot C_{p,GNE} + m_h \cdot C_{p,h} + m_{st} \cdot C_{p,st} \quad (2.22)$$

After calculating the net total cold production, the Coefficient Of Performance was finally quantified:

$$Q_{evap,night}^{net} = \dot{Q}_{evap,night} \cdot \Delta t_{night} \quad (2.23)$$

$$COP_{TCH} = \frac{Q_{evap,night}^{net}}{Q_h^{net}} \quad (2.24)$$

It is important to note that, while the COP_{ABS} is calculated in terms of power assuming steady state, the COP_{TCH} is calculated in terms of energy, because this system does not operate in steady state.

2.3.2.3 Preliminary sensitivity study

The sensitivity of the performance indicators with respect to some key operating temperatures was analyzed for both the absorption and the thermochemical subsystems. A nominal case is defined with standard values for each design variable and parameter, and in addition, for each parameter a minimum and maximum value is fixed.

For each parameter, calculations were done with the model from minimum to maximum values (including the nominal case) in fixed increment steps, as shown in Table 2.3.

The values selected for the study variables are within the typical range in the operation of absorption refrigeration cycles and thermochemical processes.

Table 2.3. Nominal case and max/min values for the parametric study.

Parameter	Units	Nominal case	Min. value	Step	Max. value
<i>Operating conditions</i>					
\dot{Q}_b	kW	5	1	1	10
Δt_b	h	2	0.5	0.5	5
$T_{G,ABS}$	°C	90	50	5	100
$T_{E,ABS}$	°C	0	-10	2	10
T_b	°C	0	-10	2	10
T_m	°C	20	14	2	26
$\Delta T_{e,ev}$	°C	10	5	5	15
<i>Composite implementation parameters (TCH subsystem)</i>					
$\tilde{\rho}_{ENG}$	kg/m ³	80	30	10	120
ε_1	-	0.4	0.2	0.1	0.5
h_{sw}	W·m ⁻² K ⁻¹	400	200	100	600
h_e	W·m ⁻² K ⁻¹	1000	500	500	1000
ΔX	-	0.9	0.8	0.1	0.9
e_p	m	0.001	0.001	0.001	0.002

2.3.2.4 Preliminary yearly simulation

Section 2.3.2.3 focuses on the performance study of individually the absorption subsystem and the thermochemical subsystem with those working pairs and operating conditions at which both can operate together.

This section focuses on the preliminary simulation of the hybrid system with a simplified model. The simulation scenario is the hybrid cycle being powered by a solar thermal system, and satisfying the cooling demand of a residence. Main parameters concerning the residence and the solar thermal system can be seen in Table 2.4.

The demand of cooling of this residence is estimated on an hourly basis through the degrees day method. This method has been proven to obtain very close-to-reality results among the simple methods [17], due to the considerable effect of the external environment temperature on the thermal demand.

According to this method, the monthly demand is expressed as a function of the specific monthly demand, $q_{need,m}$ (reference values available from real

measurements, specialized bibliography or simulation software [18]), and the residence's floor area (A_{floor}), and then normalized through the cooling degree days (CDD_m , CDD_d). CDD (eq. 2.25 and 2.26) are a function of the hourly ambient temperature ($T_{\text{amb},h}$) and the base temperature for cooling (T_b). A hourly utilization factor (α_h), a redistribution factor (k_d) and a weekend factor (β_{we}) were used to make hourly calculations for working days ($Q_{\text{need},\text{wd},h}$) (2.27) and weekends ($Q_{\text{need},\text{we},h}$) (2.28). Demand was assumed to be 50% higher during weekends [19].

Table 2.4. Weather- and application-related parameters for system simulation.

Location	Barcelona
Date	July
Building type	Single-family residence
Building surface (m²)	100
Monthly demand of cooling (MWh)	0.85
Base temperature of cooling (°C)	21
Solar collector type	Flat plate
Collector slope	45°
Collector useful area (m²/collector)	2.3624
Solar thermal system efficiency	0.5

$$CDD_m = \frac{\sum_{h=1}^{h=24} (T_{\text{amb},h} - T_b)}{24} \quad \text{for} \quad T_{\text{amb},h} > T_b \quad (2.25)$$

$$CDD_d = \frac{\sum_{h=1}^{h=24} (T_{\text{amb},h} - T_b)}{24} \quad \text{for} \quad T_{\text{amb},h} > T_b \quad (2.26)$$

$$Q_{\text{need},\text{wd},h} = \alpha_h \cdot k_d \cdot q_{\text{need},m} \cdot A_{\text{floor}} \cdot \frac{CDD_{\text{wd}}}{CDD_m} \quad (2.27)$$

$$Q_{\text{need},\text{we},h} = \alpha_h \cdot k_d \cdot \beta_{\text{we}} \cdot q_{\text{need},m} \cdot A_{\text{floor}} \cdot \frac{CDD_{\text{we}}}{CDD_m} \quad (2.28)$$

Information about hourly ambient temperature and solar irradiation for the selected location was processed to obtain the hourly solar irradiation on the collector field ($\dot{Q}_{\text{rad}}(t)$). With this value, and having into account the average global efficiency of the solar thermal system (η_{solar}), the hourly total driving heat input ($\dot{Q}_{\text{in}}(t)$) was determined (2.29).

$$\dot{Q}_{\text{in}}(t) = \dot{Q}_{\text{rad}}(t) \cdot \eta_{\text{solar}} \quad (2.29)$$

Then, calculations for each subcycle are made. The simulation procedure takes into consideration all cases described in Table 2.1. Given the input driving heat ($\dot{Q}_{\text{in}}(t)$) provided by the solar loop, the maximum deliverable amount of refrigeration effect by the absorption subcycle ($\dot{Q}_{E,\text{max}}^{\text{ABS}}(t) = \dot{Q}_{\text{in}}(t) \cdot \text{COP}_{\text{ABS}}$) is

compared to the demand of refrigeration ($\dot{Q}_{need}(t)$), and the hybrid cycle's operation mode is decided according to this criterion.

For the absorption subsystem a generator and evaporator temperatures of 90 °C and 5 °C, respectively, are assumed. Condenser and absorber temperatures are both taken as 35 °C. The system is assumed to be provided an auxiliary, stable heat source, to be used when the solar heat is insufficient to meet the demand, or when it is at too low temperature.

To determine whether or not the absorption subsystem proceeds and calculate the driving heat input to the generator, depending on whether or not the absorption subsystem alone can satisfy the demand of cold with the available input heat (2.30 or 2.31, respectively).

$$\dot{Q}_G(t) = \frac{\dot{Q}_{need}(t)}{COP_{ABS}} \quad \text{if } \dot{Q}_{E,max}^{ABS}(t) \geq \dot{Q}_{need}(t) \quad (2.30)$$

$$\dot{Q}_G(t) = \dot{Q}_{in}(t) \quad \text{if } \dot{Q}_{E,max}^{ABS}(t) < \dot{Q}_{need}(t) \quad (2.31)$$

Once the heat input to the generator is known, calculation of the useful cooling effect delivered at the evaporator by the absorption subcycle is straightforward (2.32).

$$\dot{Q}_E^{ABS}(t) = \dot{Q}_G(t) \cdot COP_{ABS} \quad (2.32)$$

Surplus heat produced by the solar system is derived to the thermochemical subcycle (2.33), causing some refrigerant to vaporize due to the reaction (2.34) and therefore storing some cooling capacity in form of liquefied refrigerant (2.35), which can be later utilized. When calculating the amount of refrigerant being vaporized at the reactor, a value is needed for the enthalpy of reaction (Δh_R); for reactions involving ammonia, a standard value of 40 kJ/(mole of NH₃) can be assumed as an approximation. Since all the demand is being covered by the absorption subcycle in this period, no cooling effect needs to be provided by the thermochemical subcycle (2.36).

$$\dot{Q}_R(t) = \dot{Q}_{in}(t) - \dot{Q}_G(t) \quad \text{if } \dot{Q}_{E,max}^{ABS}(t) > \dot{Q}_{need}(t) \quad (2.33)$$

$$\dot{m}_r^{TCH}(t) = \frac{\dot{Q}_R(t)}{\Delta h_R} \quad \text{if } \dot{Q}_{E,max}^{ABS}(t) > \dot{Q}_{need}(t) \quad (2.34)$$

$$m_r^{TCH}(t) = m_r^{TCH}(t-1) + \dot{m}_r^{TCH}(t) \cdot \Delta t \quad \text{if } \dot{Q}_{E,max}^{ABS}(t) > \dot{Q}_{need}(t) \quad (2.35)$$

$$\dot{Q}_E^{TCH}(t) = 0 \quad \text{if } \dot{Q}_{E,max}^{ABS}(t) > \dot{Q}_{need}(t) \quad (2.36)$$

The other way around, when the absorption subcycle alone cannot satisfy the demand, some cooling effect has to be provided by the thermochemical subsystem (2.37). Some of the stored refrigerant is vaporized (2.38), being therefore de-stored (2.39), and also rejecting heat at the reactor (2.40).

$$\dot{Q}_E^{TCH}(t) = \dot{Q}_{need}(t) - \dot{Q}_E^{ABS}(t) \quad \text{if } \dot{Q}_{E,max}^{ABS}(t) < \dot{Q}_{need}(t) \quad (2.37)$$

$$\dot{m}_r^{TCH}(t) = \frac{\dot{Q}_E^{TCH}(t)}{\Delta h_v} \quad \text{if } \dot{Q}_{E,max}^{ABS}(t) < \dot{Q}_{need}(t) \quad (2.38)$$

$$m_r^{TCH}(t) = m_r^{TCH}(t-1) - \dot{m}_r^{TCH}(t) \cdot \Delta t \quad \text{if } \dot{Q}_{E,max}^{ABS}(t) < \dot{Q}_{need}(t) \quad (2.39)$$

$$\dot{Q}_R(t) = \frac{\dot{Q}_E^{TCH}(t)}{COP_{TCH}} \quad \text{if } \dot{Q}_{E,max}^{ABS}(t) < \dot{Q}_{need}(t) \quad (2.40)$$

In those periods where the absorption subsystem satisfies the demand of cold and there is not sufficient surplus source heat, $\dot{Q}_R(t)$, $\dot{Q}_E^{TCH}(t)$ and $\dot{m}_r^{TCH}(t)$ become zero.

In any case it must be always verified that the total useful cooling effect delivered at the evaporator is the sum of that of the ABS subsystem and that of the TCH subsystem (2.41). If at some point the system cannot cover 100% of the demand, an auxiliary heat source is assumed (2.42).

$$\dot{Q}_E^{HYB}(t) = \dot{Q}_E^{ABS}(t) + \dot{Q}_E^{TCH}(t) \quad (2.41)$$

$$\dot{Q}_E^{TOT}(t) = \dot{Q}_E^{HYB}(t) + \dot{Q}_E^{AUX}(t) \quad (2.42)$$

The COP of the HYB system and the ABS and TCH subsystems for the studied operation period was defined as the relation between the total useful refrigeration effect delivered at the evaporator and the total driving heat input to the cycle (pump work being neglected), as it can be seen in (2.43).

$$COP_\xi = \frac{\int_{t=t_0^\xi}^{t=t_n^\xi} \dot{Q}_{E,\xi}(t) \cdot dt}{\int_{t=t_0^\xi}^{t=t_n^\xi} \dot{Q}_{in,\xi}(t) \cdot dt} \quad \{\xi = [HYB, ABS, TCH]\} \quad (2.43)$$

This definition of COP shows two main differences with respect to the common general definition for the COP. The first one and most remarkable is the fact that it deals in terms of total energy instead of energy flow rate. The reason for this variation is the intrinsically discontinuous and transient operation of this type of system, as a consequence of being driven by an intermittent heat source. Since the driving heat provided to the cycle will not be constant in time, and the required refrigeration effect will be varying with time for the application considered in this study (residential cooling), performance calculations must be done by integration over the defined operation period.

The term $\dot{Q}_{E,\xi}$ corresponds to the refrigeration effect at the evaporator that is provided by the cycle under consideration, that is, the absorption subcycle, the thermochemical subcycle, or the hybrid global cycle, being the latter the sum of the two previous ones. The term $\dot{Q}_{in,\xi}$ corresponds the driving heat input to the

cycle under consideration: for the absorption part, it is the heat input to the generator, Q_G ; for the thermochemical part, it is the heat input to the reactor, Q_R ; and for the global hybrid system, it is the sum of these two. The values $t = t_0^\xi$ and $t = t_n^\xi$ correspond to the integration time limits for each subsystem.

Although the COP shows performance by comparing the useful output to the heat input, the advantages of the hybrid system would not be visible without accounting for the increase in coverage of the demand of cold. A specific performance indicator, the Coefficient for Satisfaction of the Demand (CSD), is proposed for this system (2.44).

$$CSD_\xi = \frac{\int_{t=t_0^\xi}^{t=t_n^\xi} \dot{Q}_{need}(t) \cdot dt - \int_{t=t_0^\xi}^{t=t_n^\xi} \frac{[\dot{Q}_{need}(t) - \dot{Q}_{E,\xi}(t)]^2}{\dot{Q}_{need}(t)} \cdot dt}{\int_{t=t_0^\xi}^{t=t_n^\xi} \dot{Q}_{in,\xi}(t) \cdot dt} \quad \{\xi = [HYB, ABS]\} \quad (2.44)$$

$\dot{Q}_{need}(t)$ is the cooling power needed for the application. According to this definition, it results that $0 \leq CSD \leq COP$. If the cooling effect provided by the system ($\dot{Q}_{E,\xi}(t)$) equals the demand ($\dot{Q}_{need}(t)$), then $CSD = COP$. If the cooling effect is zero, then $CSD = 0$. In some manner, this indicator shows how, near to its nominal performance (COP), the system operates, according to which fraction of the load is satisfied. Other parameters similar to the CSD have been defined by other authors, for instance Cao et al. [20].

The CSD definition can also be normalized to obtain $0 \leq CSD \leq 1$ as an output, thus showing which fraction of the demand is satisfied (2.45).

$$CSD_{norm,\xi} = \frac{\int_{t=t_0^\xi}^{t=t_n^\xi} \dot{Q}_{need}(t) \cdot dt - \int_{t=t_0^\xi}^{t=t_n^\xi} \frac{[\dot{Q}_{need}(t) - \dot{Q}_{E,\xi}(t)]^2}{\dot{Q}_{need}(t)} \cdot dt}{\int_{t=t_0^\xi}^{t=t_n^\xi} \dot{Q}_{need}(t) \cdot dt} \quad \{\xi = [HYB, ABS]\} \quad (2.45)$$

This calculation procedure was applied for different working pairs (Table 2.5), and varying the number of solar thermal collectors.

Table 2.5. Working pairs considered in the simulations.

Option	Absorption subsystem	Thermochemical subsystem
A	H ₂ O / LiBr	H ₂ O / SrBr ₂
B	NH ₃ / LiNO ₃	NH ₃ / BaCl ₂
C	NH ₃ / NaSCN	NH ₃ / BaCl ₂

Properties of ammonia are obtained from [11], and properties of water are obtained from [21]. Correlations from [22] have been used for calculation of H₂O+LiBr properties. Vapor pressure data for NH₃+LiNO₃ are provided by [12],

and data for density and isobaric specific heat of this same working pair is available in [13]. Regarding the mixture NH_3+NaSCN , data from [23] is used for vapour pressure, density and isobaric specific heat. Correlations from [24] are used for specific enthalpy of $\text{NH}_3+\text{LiNO}_3$ as well as NH_3+NaSCN . All property correlations were implemented in a simulation code developed with the Engineering Equation Solver (EES) software.

2.4 RESULTS AND DISCUSSION

2.4.1 Absorption subsystem

For the absorption subsystem, Fig. 2.11 shows the dependence of its COP and its solution circulation ratio (f) as function of generator temperature, for selected evaporator temperatures and the $\text{NH}_3/\text{LiNO}_3$ working pair.

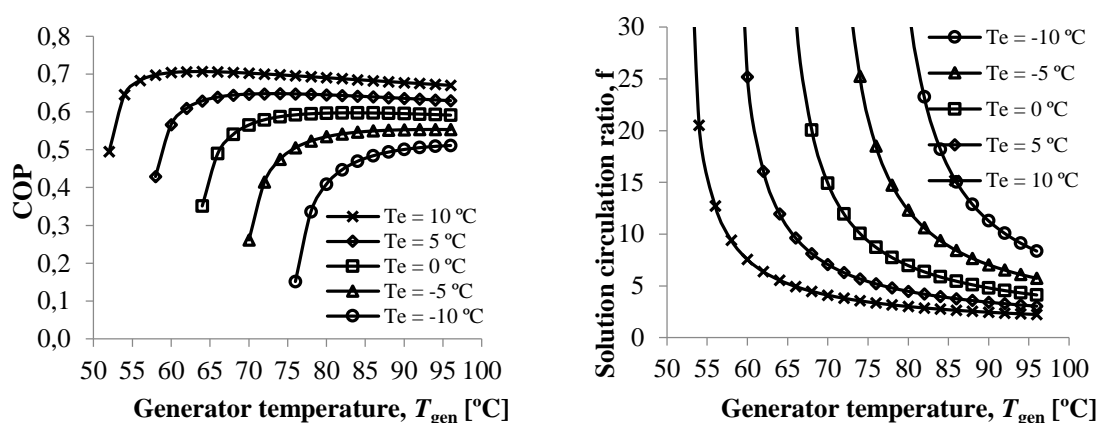


Figure 2.11. (a) Absorption subsystem's Coefficient Of Performance (COP) for selected generator and evaporator temperatures; (b) Solution circulation ratio (f) as a function of generator temperature for selected evaporator temperatures.

Results show that, under the selected design conditions, the absorption machine can operate at, or close to, its optimal COP and the corresponding value of f . A small risk of underperforming may be present if working at evaporator temperatures close to -10°C , if the temperature of the hot fluid for cycle activation is not high enough. It is important to avoid those operating conditions in which f reaches high values (above 10), since at those conditions, the power consumption from the solution pump increases considerably.

2.4.2 Thermochemical subsystem

For the thermochemical subsystem, Fig. 2.12a shows the evolution of COP with the evaporator temperature, for those working pairs that are identified as interesting in section 2.3.1.2.

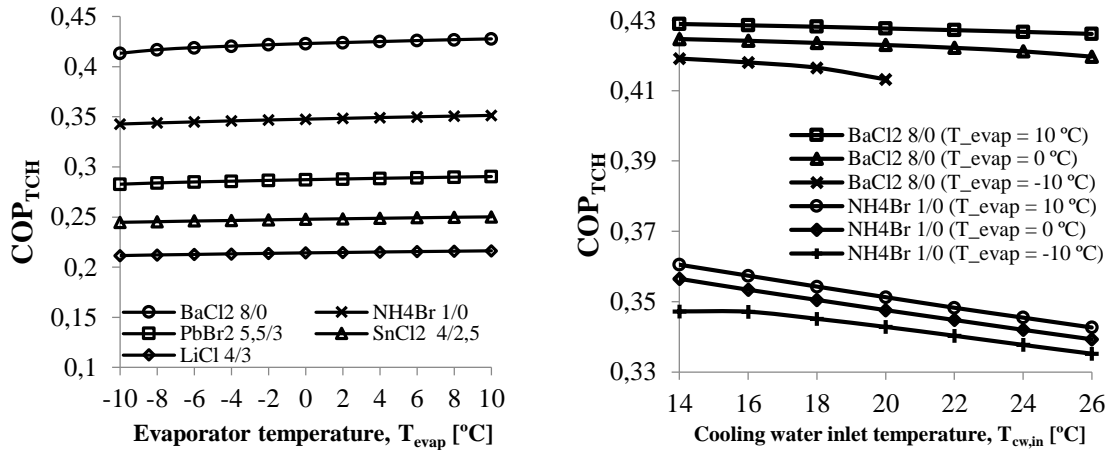


Figure 2.12. (a) Effect of evaporator temperature (T_{evap}) on the thermochemical subsystem's COP for selected pairs at a cooling water inlet temperature of $T_{cw,in} = 20$ °C; (b) Effect of cooling water's inlet temperature on the thermochemical subsystem's COP for the two most promising pairs at selected evaporator temperatures.

For an inlet temperature of $T_{cw,in} = 20$ °C for the cooling water, all reactive pairs perform with typical COP_{TCH} values for real ammonia-based thermochemical processes (i.e. between 0.2 and 0.45 approx.). According to these results, barium chloride and ammonium bromide are the two most promising salts to be used as reactive solid, with COP_{TCH} = 0.42 and COP_{TCH} = 0.35, respectively.

It is noted that, at the same heat source and cooling water temperatures, the evaporator temperature has little influence on the COP_{TCH}. This is in accordance with the characteristics of thermochemical processes.

As shown in Fig. 2.12b, the ammonia/barium chloride system suffers from high cooling water inlet temperatures when the evaporator temperature is -10 °C or close to that value. However, it is still the most promising system among all the considered ones.

After this preliminary study, the following figures (2.13 to 2.18) show the influence of operating conditions and composite implementation parameters on the storage-power and performance-power relationships of the thermochemical subsystem, for the NH₃/SrCl₂ (8-1) and NH₃/CaCl₂ (4-2) working pairs.

Figure 2.13 presents the relationship between energy storage density (D_e , displayed on the y-axis) and specific cooling power ($\dot{q}_{b,s}$, displayed on the x-axis) in the thermochemical subsystem, assuming that its working pair is $\text{NH}_3/\text{SrCl}_2$ and the design parameters are within the limit values shown in table 2.3. The energy storage density is defined with respect to the volume (in m^3) of solid reactive composite, which is directly related with the total volume of reactor. The specific cooling power is defined with respect to the total area (in m^2) of heat exchanger, which importantly influences the final price of the mentioned heat exchanger.

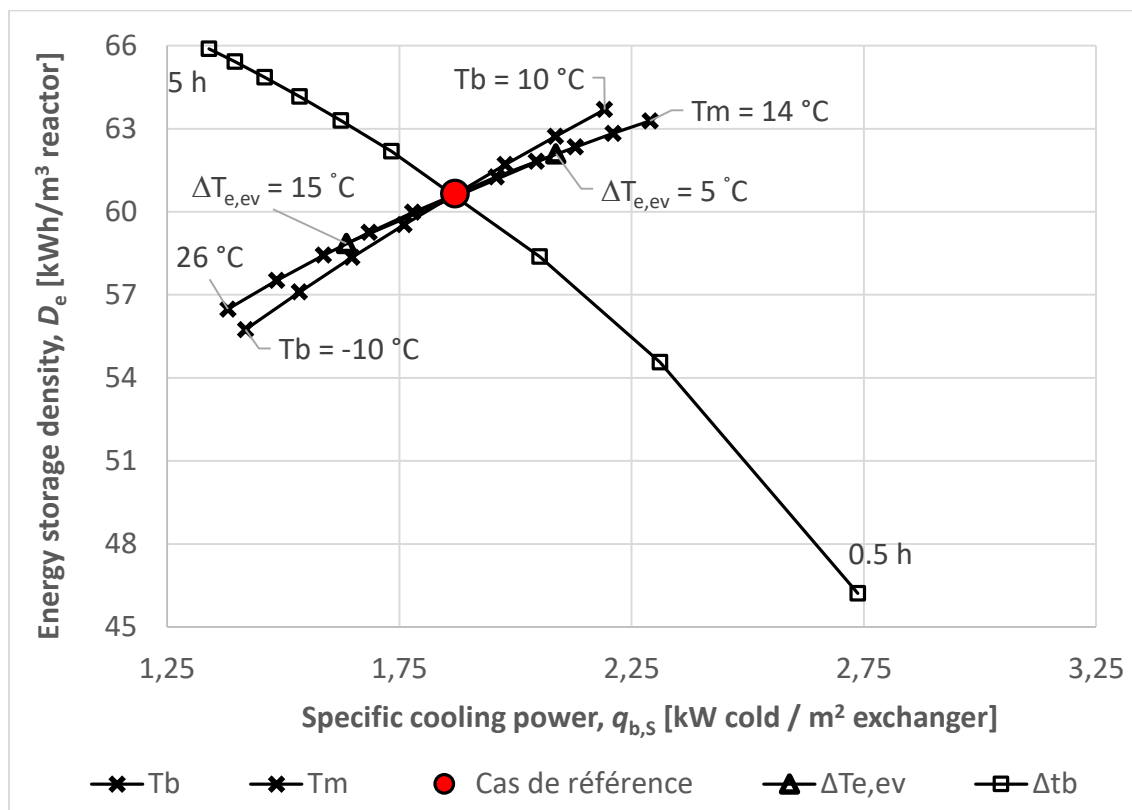


Figure 2.13. Evolution of the relationship between storage density and cooling power in an ammonia / strontium chloride thermochemical subsystem as a function of several operating conditions.

In this figure, the nominal case is clearly depicted with a red dot. In addition, the figure shows how this relationship evolves when varying the value of the following operating conditions: cold production temperature (T_b), heat sink temperature (T_m), evaporator pinch temperature ($\Delta T_{e,ev}$), and cold production time (Δt_b). The parameters vary one at a time, and the rest remain constant.

The variable T_b (represented with cross line) is directly related with the evaporator temperature (T_{ev}): T_{ev} increases when T_b increases, and it decreases when T_b decreases. The leftmost point corresponds to the minimum value ($T_b =$

-10 °C) that was considered in the study, and therefore to the minimum value of T_{ev} , too. In this case, both indicators have their lowest value with respect to T_b . Then, as T_b increases, the values of both D_e and $\dot{q}_{b,S}$ increase as well.

This evolution is logical and commonly known in refrigeration: the higher the temperature of cold production, the better the system's performance in general. This tendency is visible in the COP of refrigeration systems, and so it is in other performance indicators. The performance would further improve by further increasing the cold production temperature, but of course, there is an application-related limit to this evolution: this temperature is set by the demand.

A similar evolution is observed with respect to the heat sink temperature (T_m), but with this variable, the evolution is inverse: both D_e and $\dot{q}_{b,S}$ improve when T_m decreases, and the opposite happens then T_m increases. This evolution is also logical and well-known in tri-thermal refrigeration systems: the higher the heat sink temperature, the more the system suffers from lower performance. This is visible on the COP as well as other indicators such as those shown in Fig. 2.13.

The influence of $\Delta T_{e,ev}$ is also inverse to that of T_b , but it is bound to this variable. For a given value of T_b , a higher $\Delta T_{e,ev}$ implies a lower evaporator temperature. This means, as discussed above, that the general performance of the system decreases.

The influence of the cold production duration (Δt_b) is interesting. All other parameters discussed in this figure have a rather simple influence on the indicators (i.e. both indicators improve or worsen together when the parameter varies), but Δt_b is the only operating condition with which D_e and $\dot{q}_{b,S}$ evolve antagonistically.

With all other parameters at nominal case, an increase in the duration of the cold production leads to an increase in energy storage density. This is logical: for a fixed demand of cooling power, higher production times mean that the system has to be able to store that much energy, which requires higher amounts of reactive salt to be implemented inside the reactor. Since the mass fraction of ENG is fixed and considerably lower to that of reactive salt, this results in higher amount of energy per unit volume of reactor.

Conversely, smaller production times mean smaller amounts of salt to be implemented in the reactor. Thus, the energy density decreases, but in compensation, the cooling power increases. This happens because for lower amounts of salt, the ENG, thanks to its high porosity, leaves more 'empty space' within the reactive composite. This space allows the molecules of refrigerant

gas to flow more easily through the composite, so the system can supply the cold faster, resulting in higher cooling power.

Figure 2.14 shows again the relation between D_e and $\dot{q}_{b,S}$, but this time as a function of those parameters that are related to the implementation of the solid reactive composite inside the reactor: porosity (ϵ_1) and apparent density ($\tilde{\rho}_{GNE}$) of the expanded natural graphite; convective heat transfer between the reactive composite and the reactor's inner wall (h_{sw}) and between the reactor's outer wall and the heat transfer fluid (h_e); total advancement degree variation (ΔX) of the cold production phase; and reactor's wall thickness (e_p). Again, the nominal case is displayed as a red dot.

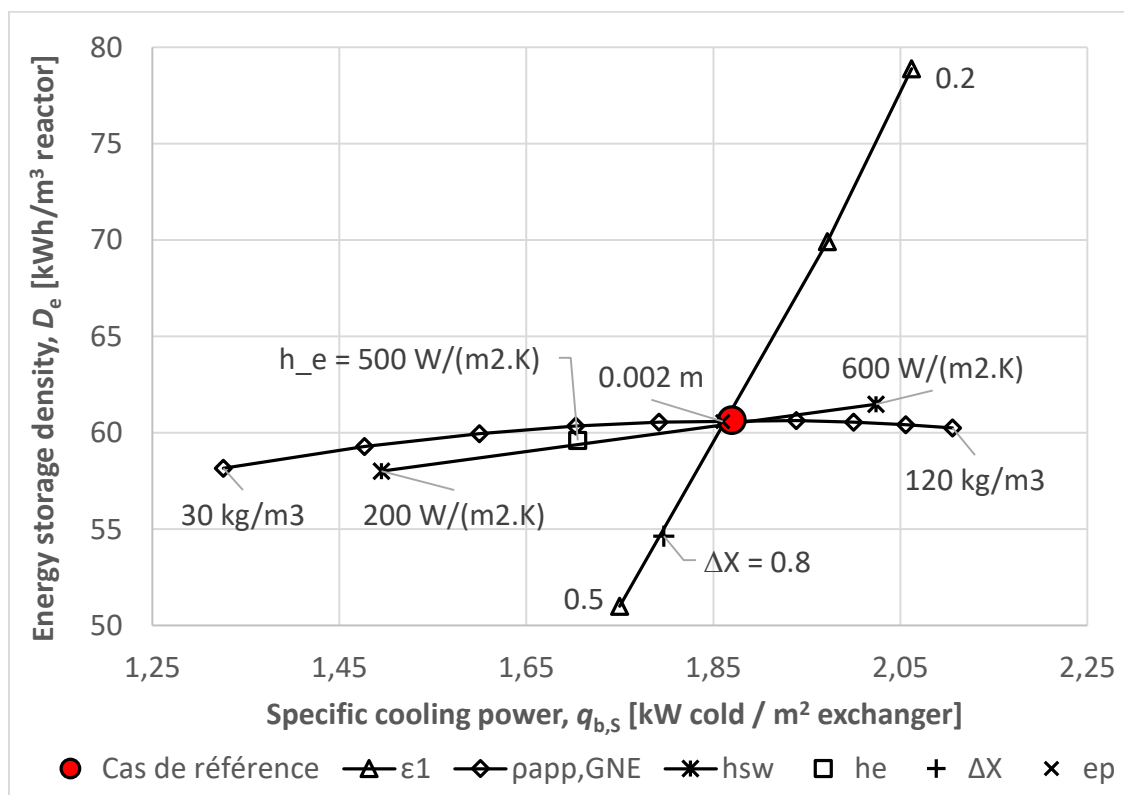


Figure 2.14. Evolution of the relationship between storage density and cooling power of the thermochemical subsystem as a function of composite implementation parameters, in the ammonia / strontium chloride system.

A noticeable influence is that of the porosity (ϵ_1) of the ENG. For a fixed demand of cold (which sets a fixed amount of reactive salt), a higher porosity of the ENG implies that there is more 'empty space' inside the reactor, resulting in greater reactor volume and heat exchanger area. Thus, higher porosity results in lower energy storage density and specific cooling power, and the opposite happens with lower porosity. This parameter has a notable influence on both indicators.

Nevertheless, the influence of ε_1 is not as simple as shown by Fig. 2.14. Mass transfer is neglected in the simulation model used for this study, and in addition, the model for heat transfer is simplified. With a more detailed model both for heat transfer and mass transfer, the curve showing the influence of ε_1 would probably be different, especially near the highest and lowest values of porosity.

Increased convective heat transfer between reactive composite and reactor's inner wall (h_{sw}) allows the heat of reaction to be supplied / evacuated at higher rates, thus requiring less exchanger area and notably improving $\dot{q}_{b,S}$. D_e also increases, but the influence is rather limited, since this parameter is not heavily heat transfer-dependent.

A very similar contribution is observed from the convective heat transfer between reactor's outlet wall and heat transfer fluid (h_e). An increase of 100% in the value of this parameter (from $500 \text{ W}\cdot\text{m}^{-2}\cdot\text{K}^{-1}$ to $1000 \text{ W}\cdot\text{m}^{-2}\cdot\text{K}^{-1}$) leads to an increase of 9.7 % in $\dot{q}_{b,S}$, while only a 1.7% increase in D_e . The reasons are basically the same as those discussed for h_{sw} . As a matter of fact, Fig. 2.14 shows almost the same slope for the contributions of both h_e and h_{sw} .

A similar case is that of the apparent density of ENG ($\tilde{\rho}_{ENG}$): this parameter has high influence on $\dot{q}_{b,S}$ but limited influence on D_e . Furthermore, with this parameter there is a very interesting maximum in D_e . The parameter $\tilde{\rho}_{ENG}$ directly influences conductive heat transfer through the charged (λ_{s1}) or discharged (λ_{s0}) salt, as ENG is a good heat transfer enhancer. When $\tilde{\rho}_{ENG}$ is low (a minimum of 30 kWh/m^3 -composite was considered), increasing it gives higher values of λ_{s1} and λ_{s0} , which means that less area of heat exchanger (S_{ech}) is needed, and therefore $\dot{q}_{b,S}$ becomes much higher. This area reduction results in slightly smaller apparent volume of composite (\tilde{V}_c), too, as similarly happens with h_{sw} . But there is a limit to this tendency. Given the high porosity of ENG, increased apparent density of this enhancer also implies increased 'empty volume' in the composite, which tends to increase the value of \tilde{V}_c . The increase in \tilde{V}_c caused by the volume occupied by the ENG grows at a higher rate than the decrease in \tilde{V}_c thanks to a smaller S_{ech} . There is a point where both contributions cancel each other (this is the maximum shown in Fig. 2.14), and from this point a further increase in $\tilde{\rho}_{ENG}$, while further increasing $\dot{q}_{b,S}$, starts having a negative impact on D_e . This evolution shows the importance of parametric studies to meet optimum design decisions. If the model had mass transfer into account, D_e would drop faster when increasing $\tilde{\rho}_{ENG}$.

The total variation in reaction advancement degree (ΔX) has, as expected, a non-negligible influence on D_e and a rather small influence on $\dot{q}_{b,S}$. Increasing this parameter from 0.8 to 0.9 shows a 10% increase in D_e and a 4% increase in

$\dot{q}_{b,s}$. This evolution is logical: a higher ΔX means that more reaction progress is achieved with the same amount of reactive salt. This automatically means more refrigerant reacting and more reaction heat, both resulting in higher energy density, and higher heat transferred per unit volume of composite and unit surface of exchanger.

The rather narrow study range of this parameter is justified by real operation of thermochemical processes. A $\Delta X = 0.9$ is attainable, but higher values are difficult to reach, especially in the mid-long term, due to some operation issues (salt agglomeration, altered uniformity of the composite, and other problems that arise after several cycles). If and when reachable, $\Delta X > 0.9$ tends to take too much operating time, which is impractical in real applications. On the opposite limit, $\Delta X = 0.8$ can be regarded as a minimum value for a performant thermochemical system. Lower ΔX usually means a non-expected problem (e.g. content of non-refrigerant molecules in the composite that impede complete reaction, or excessive salt fatigue after too much thermal cycling).

The last parameter left to discuss in Fig. 2.14 is the reactor's wall thickness (e_p). As shown, this parameter has almost no influence at all. Changing this value from 0.001 m to 0.002 m causes less than 1% decrease in both D_e and $\dot{q}_{b,s}$. The tendency is logical, since higher wall thickness means higher amount of steel, which increases the heat transfer limitation imposed by this material. However, as stated before, its influence is negligible and in addition, there are not many choices of wall thickness in a real setup.

Figure 2.15 shows, again for the $\text{NH}_3/\text{SrCl}_2$ working pair, the influence of the operating conditions on the performance-power relationship of the thermochemical subsystem. The x-axis ($\dot{q}_{b,s}$) and the operating conditions (T_b , T_m , $\Delta T_{e,ev}$ and Δt_b) are the same as in the previous figures, but this time the y-axis represents the system's COP.

Since the influence of these operating conditions on $\dot{q}_{b,s}$ has been already discussed (Fig. 2.13), only the influence on COP is left to evaluate.

The first circumstance to be noted is the weak influence of all studied operating conditions on the COP. The biggest variation observed in this indicator among all the study range was 5.5 %. This is not a surprise: as already discussed, thermochemical processes are based on the working pair's heat of reaction, and the refrigerant's latent heat of vaporization to a lesser degree. Any change in operating conditions or parameters has an impact mainly on heat transfer, sensible heat and latent heat, but not on heat of reaction. Therefore, high variations in COP were not expected here.

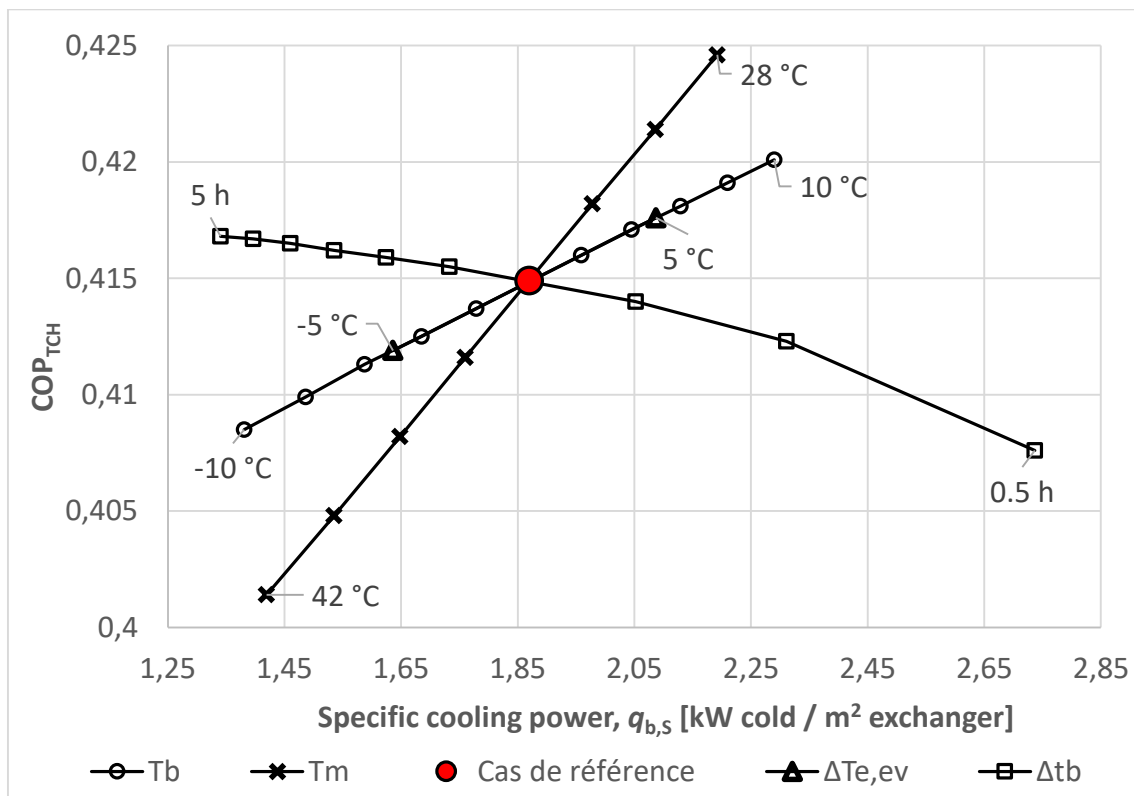


Figure 2.15. Evolution of the relationship between COP and cooling power of the thermochemical subsystem as a function of operating conditions, in the ammonia / strontium chloride system.

As for the tendencies, all of them are the expected ones: the COP increases with T_b and Δt_b , and decreases with T_m and $\Delta T_{e,ev}$. The reasons have been discussed previously (Fig. 2.13).

Figure 2.16 illustrates the same concept as figure 2.14, but this time the COP instead of the D_e is represented on the y-axis.

The effect of these composite implementation parameters on $\dot{q}_{b,s}$ has been already discussed in Fig. 2.14 and needs no further explanation. And again, the effect on the COP is minimal, for the reasons discussed in Fig. 2.15. The COP increases with an increase in those parameters related to heat transfer (h_{sw} , h_e) or to the heat of reaction (ΔX), while it decreases with an increase in those parameters that directly or indirectly pose limitations on heat or mass transfer (ϵ_1 and e_p). A bit more complex is its evolution with respect to $\tilde{\rho}_{ENG}$, showing a maximum like in the case of the $D_e - \dot{q}_{b,s}$ figure, this time around $\tilde{\rho}_{ENG} = 45 \text{ kg/m}^3$.

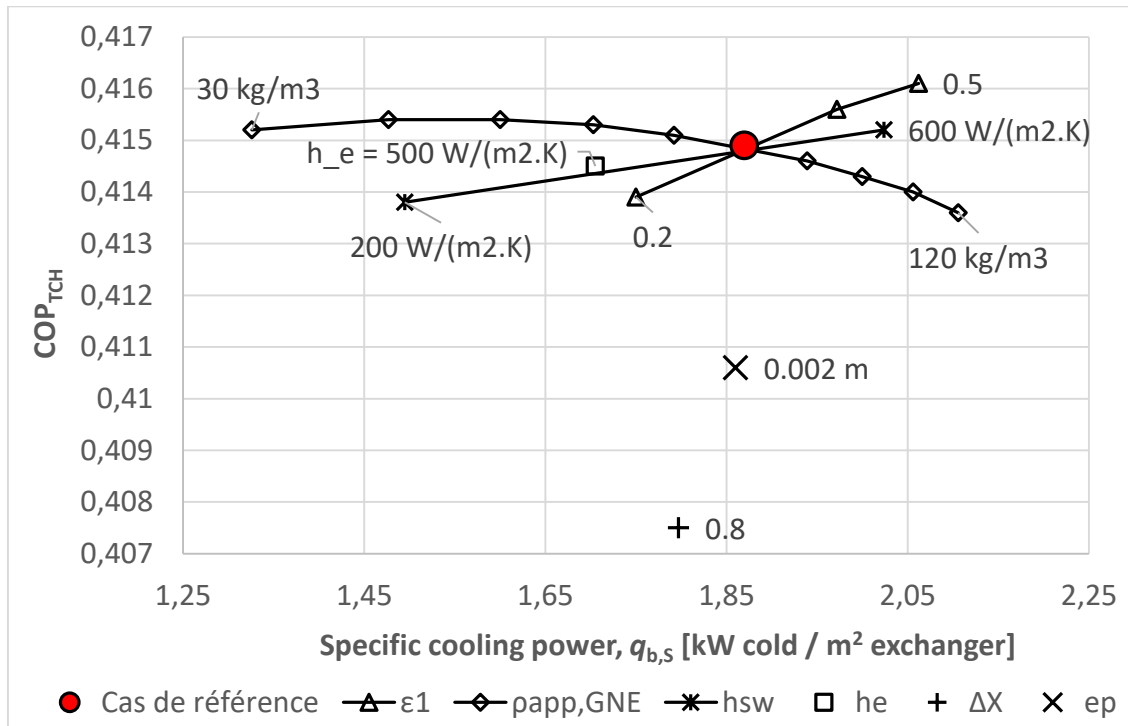


Figure 2.16. Evolution of the relationship between COP_{TCH} and cooling power of the thermochemical subsystem as a function of composite implementation parameters, in the ammonia / strontium chloride system.

The relatively higher influence (in comparison with all other parameters) of the ΔX on the COP is important to be noted. For any working pair, a simplified approach for COP calculation is to relate the refrigerant's enthalpy of vaporization to the enthalpy of reaction. In a slightly more detailed model, COP calculation accounts for the sensible heat needed to bring the whole reactor to operating temperature and maintain it. The heat absorbed (or rejected) by the reaction is usually large enough to overlook this sensible heat. But if the model takes it into account (such as the model used here), a variation in ΔX (parameter that represents the stoichiometry-related amount of reaction heat with respect to the maximum deliverable by the system) may reflect a slight variation in COP due to this sensible heat. This is the case in Fig 2.16.

Figure 2.17 shows the same indicators and operating conditions as Fig. 2.13, but this time for a different working pair: NH₃/CaCl₂. This figure allows to compare the same profiles with a different working pair and see the differences.

The evolution of the $D_e - \dot{q}_{b,s}$ relationship for all variables is the same as that shown in Fig. 2.13. Only the values are different: the ammonia/strontium chloride working pair has fairly higher values for these indicators. This is logical: the values of COP, energy density and cooling power are directly related to the stoichiometry, specifically the amount of moles of refrigerant that

can react for each mole of salt. For the $\text{NH}_3/\text{SrCl}_2$ working pair, this corresponds to 7 moles of NH_3 per mole of SrCl_2 , while for the $\text{NH}_3/\text{CaCl}_2$ it is 4 moles of NH_3 per mole of CaCl_2 . Therefore, the former is expected to deliver better thermal performance than the latter.

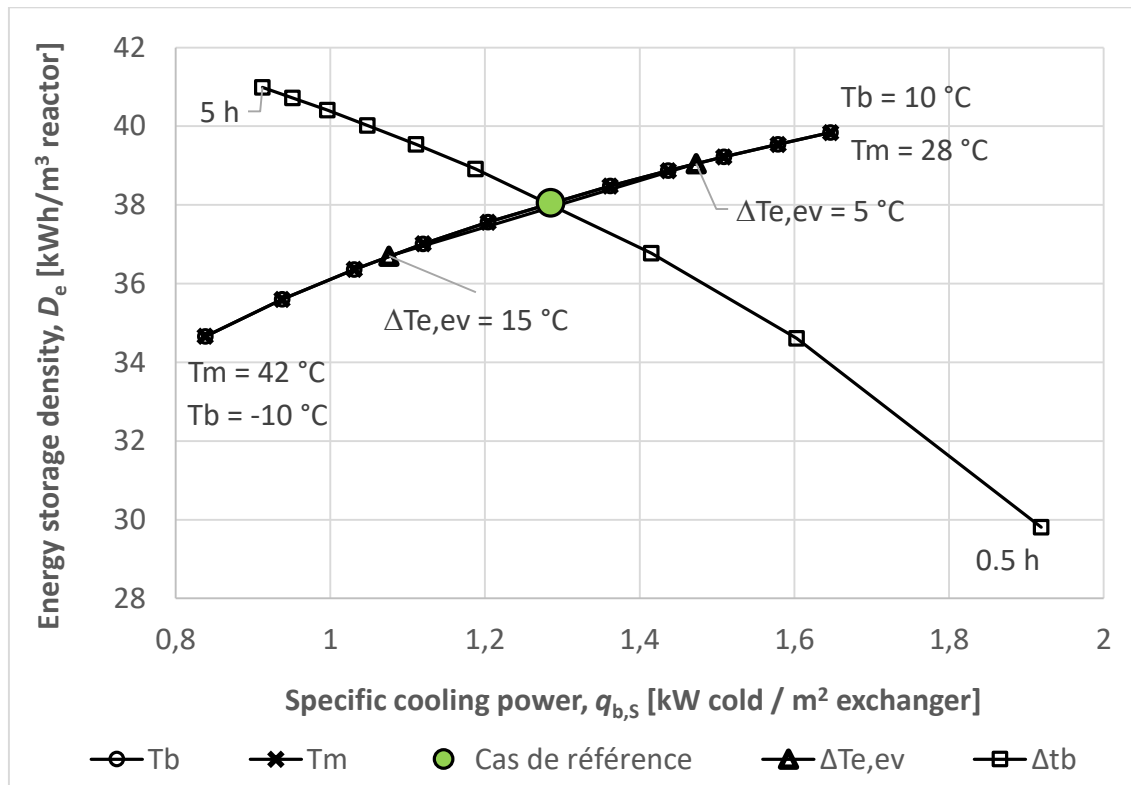


Figure 2.17. Evolution of the relationship between storage density and cooling power of the thermochemical subsystem as a function of operating conditions, in the ammonia / calcium chloride system.

To finish this preliminary parametric study of the thermochemical subsystem, Fig. 2.18 shows the COP - $\dot{q}_{b,s}$ relationship with respect to operating conditions with the $\text{NH}_3/\text{CaCl}_2$ working pair. In other words, this figure illustrates the same concept as Fig. 2.15 but with a different working pair.

Again, the profiles follow the same tendencies as in the $\text{NH}_3/\text{SrCl}_2$ working pair, with different values, for the reasons described in Fig. 2.17. Still, the influence of these parameters on the COP is rather small, as discussed in Fig. 2.15. The most important conclusion that can be extracted from figures 2.17 and 2.18 is that the choice of working pair has no noticeable impact on the tendencies followed by the indicators as response to the design parameters in this model.

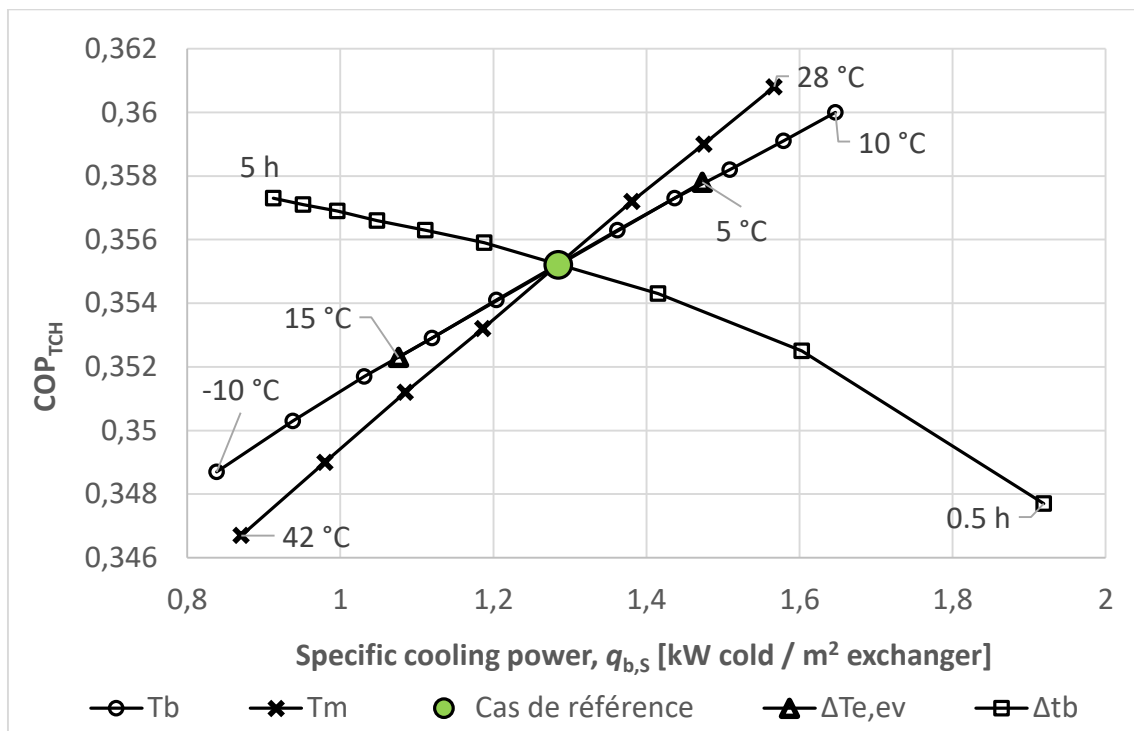


Figure 2.18. Evolution of the COP_{TCH} - cooling power relationship of the thermochemical subsystem as a function of operating conditions, in the ammonia / calcium chloride system.

Appendix A contains extended results of this preliminary parametric study with additional figures and reactive pairs.

2.4.3 Hybrid system preliminary yearly simulation

Fig. 2.19 shows the evolution of some study variables of the HATRS during 7 days of operation. In this scenario, the thermochemical subsystem has a maximum energy storage capacity of 5 kWh. From the 7 days that are shown, six of them correspond to sunny days, while the third one represents a cloudy or rainy day.

In those periods where the solar thermal system provides surplus heat, the amount of cooling capacity associated to liquid refrigerant in the storage tank increases until reaching its maximum. Then, when the solar resource is insufficient (see day 3), this stored energy drops. This represents the thermochemical subsystem in charge and discharge process.

Fig. 2.20 shows a zoomed view of the second day of simulation. The major part of solar energy produced by the panels takes place between 12:00 and 18:00. Accordingly, the demand of cold for the residential application increases during these hours, as this is how the CDD model used for the simulations

works. Since there is surplus heat provided by the solar thermal panel field, the cooling energy associated with the liquid ammonia stored by the TCH subsystem increases, until reaching its maximum of 9.5 kWh, and remains fully charged during peak hours of solar irradiation. A few hours later, at 17:00, when the solar resource starts to diminish, the TCH subsystem starts releasing stored ammonia to assist the ABS subsystem in satisfying the demand of cold.

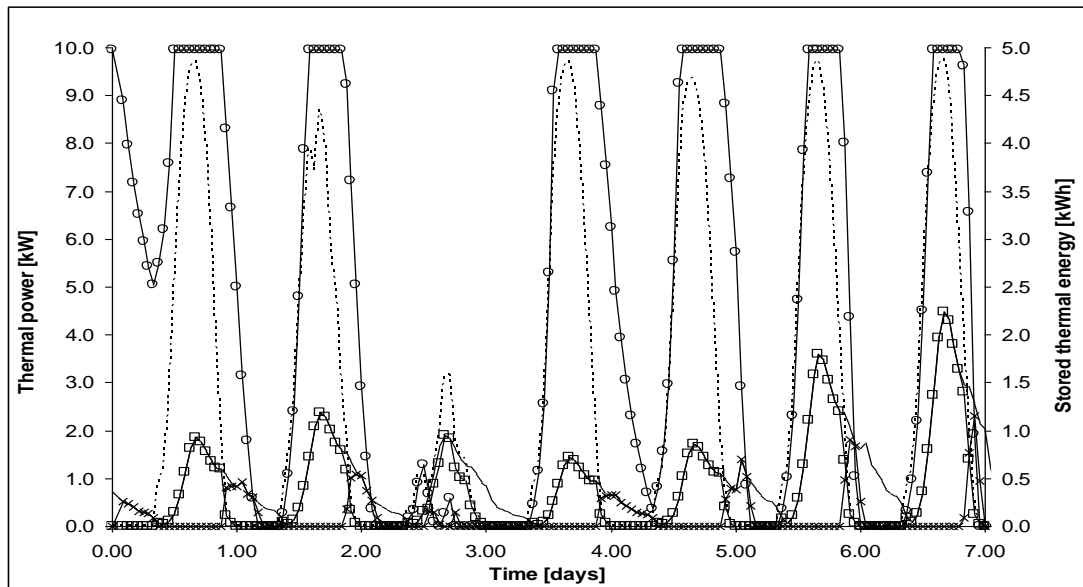


Figure 2.19. Driving heat provided by solar system (dotted line, left axis), demand of cooling (straight line, left axis), cooling provided by the absorption subsystem (squared line, left axis) and by the thermochemical subsystem (crossed line, left axis) and stored cooling capacity associated to liquid refrigerant at the reservoir (circle line, right axis); profiles for one week in the example case.

It can be noted that, while the ABS subsystem works when the solar thermal system produces heat, the thermochemical process comes into scene as soon as the absorption refrigeration effect cannot handle the demand.

Whether or not the hybrid system can fully satisfy the demand uninterruptedly depends on design, being the amount of refrigerant in the thermochemical subsystem (which is the only one providing storage function) and collector field area two relevant parameters.

Fig. 2.21a shows the influence of the number of solar thermal collectors (from one to ten) on the hybrid system's COP with three different working pair combinations in the ABS and TCH subsystems and two different amounts (in kg) of refrigerant available for storage in the TCH subsystem.

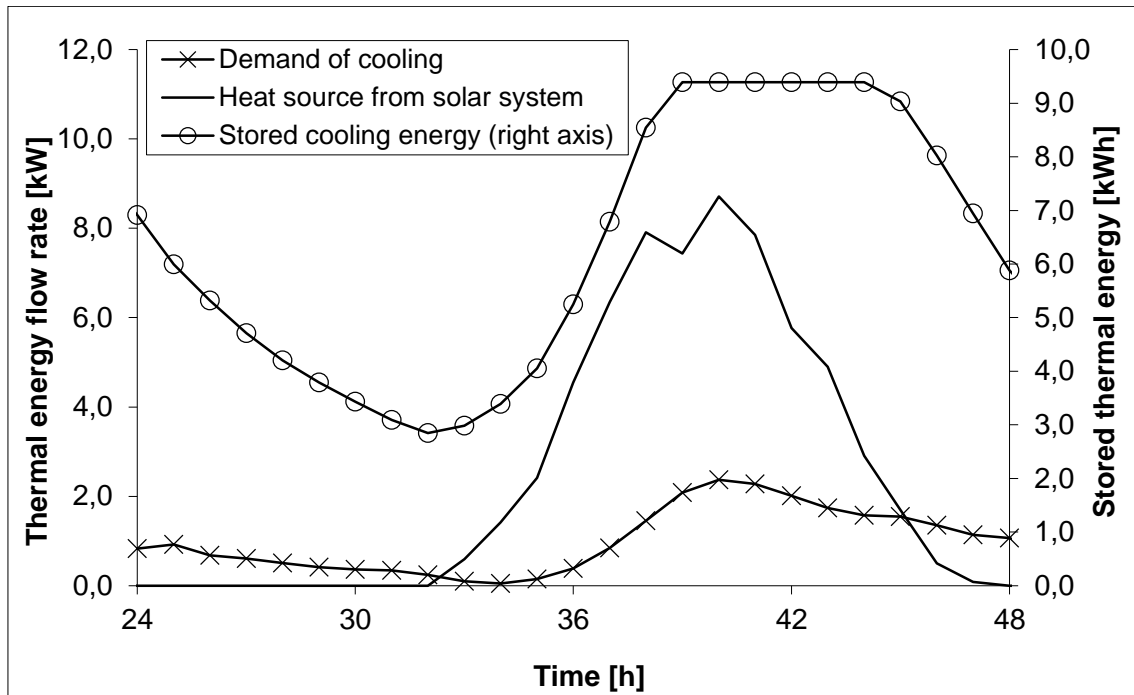


Figure 2.20. Second day of simulation of the SHATRS (zoomed from Fig. 2.19).

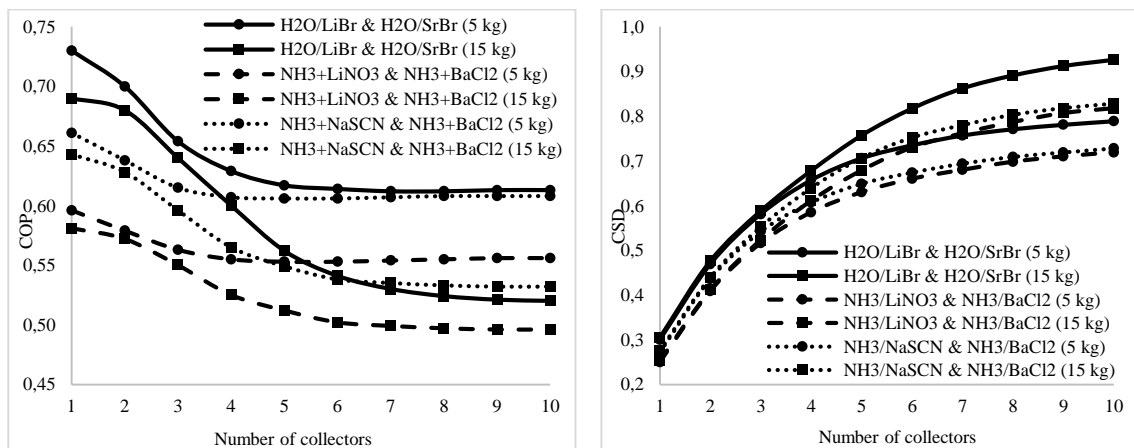


Figure 2.21. (a) Effect of number of solar thermal collectors on hybrid system's COP for different working pairs and mass of refrigerant (in kg) in the TCH subsystem; (b) Effect of the same parameters on the Coefficient of Satisfaction of the Demand (CSD).

As expected, COP_{HYB} decreases with every additional collector, from a value close to COP_{ABS} when only one collector is installed, to decreasing values each time closer to COP_{TCH} . This is logical since COP_{TCH} is lower than COP_{ABS} , and the amount of storable surplus energy increases with every additional collector, so the TCH gains more presence.

A similar effect occurs when more mass of refrigerant is available for storage at the TCH subsystem. Essentially, COP_{HYB} decreases whenever more driving heat is provided to the TCH subsystem.

It can also be observed that the decrease in COP_{HYB} is greater when a small number of collectors are being used, while the value remains almost flat after certain number of collectors. Profiles show that COP_{HYB} is also dependent on the working pair under use and the mass of refrigerant available for storage.

Fig. 2.21b shows the variation of CSD_{HYB} with increasing number of solar thermal collectors (from one to ten) for the same working pair combinations and mass of storable refrigerant as in Fig. 2.21a. As expected, CSD_{HYB} increases with increasing number of collectors, since a higher fraction of refrigeration needs can be covered by the system.

Similar to COP_{HYB} , the mass of refrigerant for storage in the thermochemical subsystem has an appreciable impact. In this case, however, the working pair under use in the absorption subsystem has not as big impact on CSD_{HYB} as on COP_{HYB} . The reason is simple: increasing the CSD depends mainly on the performance of the TCH, and not the ABS subsystem. Last, but not least, it can also be observed that for a small number of collectors, CSD_{HYB} is very similar in all cases under consideration.

2.5. CONCLUSIONS AND PERSPECTIVES

In this study, a novel solar-driven hybrid absorption/thermochemical refrigeration cycle is presented. Its working principle and main components are described, and its strengths and drawbacks are highlighted. In addition, a brief discussion on suitable working pairs is offered, followed by the description of a methodology for correct selection of suitable pairs, based on required temperature levels. The application of this methodology assuming typical operating conditions led to the identification of several suitable working pairs for each subsystem.

For the absorption subsystem, ammonia/lithium nitrate and ammonia/sodium thiocyanate were identified as suitable pairs in the described case, being ammonia/lithium nitrate finally selected, due to its higher COP at lower generation temperatures. For the thermochemical subsystem, operating with ammonia as refrigerant, ammonium bromide, barium chloride, lead(II) bromide, tin(II) chloride and lithium chloride were identified as suitable reactive salts. In terms of COP, ammonia/ammonium bromide and ammonia/barium chloride were the two most promising pairs for the thermochemical system.

The use of separate simulation models for the absorption and thermochemical subsystems allowed a first study of their performance at different operating conditions. It is concluded that there are combinations of working pairs with which both subsystems can operate simultaneously, and therefore, the hybrid system may be operationally viable.

2.6. REFERENCES

- [1] Sarbu I., Sebarchievici C. (2015). General review of solar-powered closed sorption refrigeration systems. *Energy Conversion and Management* 105, 403-422.
- [2] Mauran S., Lahmidi H., Goetz V. (2008). Solar heating and cooling by a thermochemical process. First experiments of a prototype storing 60kWh by a solid/gas reaction. *Solar Energy* 82(7), 623–636.
- [3] Touzain P. (1999). Thermodynamic values of ammonia-salts reactions for chemical sorption heat pumps. *Proceedings of the International Sorption Heat Pump Conference, München, Germany*, 225-236.
- [4] Fitó J., Mauran S., Stitou D., Mazet N., Coronas A. (2015). New solar hybrid absorption / thermochemical refrigeration cycle. *Proceedings of the ECOS2015 28th Int. Conference on Efficiency, Cost, Optimization, Simulation and Environmental Impact of Energy Systems, Pau, France, ISBN: 978-2-9555539-0-9*.
- [5] Stitou D., Mazet N., Mauran S. (2012). Experimental investigation of a Solid/Gas thermochemical storage process for solar air-conditioning. *Energy* 41(1), 261-270.
- [6] Li T.X., Wang R.Z., Li H. (2014). Progress in the development of solid-gas sorption refrigeration thermodynamic cycle driven by low-grade thermal energy. *Progr. Energy and Comb. Science* 40, 1-58.
- [7] Sun D.-W. (1998). Comparison of the performances of NH₃-H₂O, NH₃-LiNO₃ and NH₃-NaSCN absorption refrigeration systems. *Energy Conversion and Management* 39(5-6), 357-368.
- [8] Wang L.W., Wang R.Z., Oliveira R.G. (2009). A review on adsorption working pairs for refrigeration. *Renewable and Sustainable Energy Reviews* 13, 518-534.
- [9] Pons M., Anies G., Boudehenn F., Bourdoukan P., Castaing-Lasvignottes J., Evola G., Le Denn A., Le Pierrès N., Marc O., Mazet N., Stitou D., Lucas F. (2012). Performance comparison of six solar-powered air-conditioners operated in five places. *Energy* 46, 471-483.

- [10] Wang L.W., Wang R.Z., Wu J.Y., Wang K. (2004). Compound adsorbent for adsorption ice maker on fishing boats. *International Journal of Refrigeration* 27, 401-408.
- [11] Tillner-Roth R., Harms-Watzenberg F., Baehr H.D. (1993). Eine neue Fundamentalgleichung für Ammoniak. *DKV-Tagungsbericht* 20, 167-181.
- [12] Libotean S., Salavera D., Valles M., Esteve X., Coronas A. (2007). Vapor-Liquid Equilibrium of Ammonia + Lithium Nitrate + Water and Ammonia + Lithium Nitrate Solutions from (293.15 to 353.15) K. *J. Chem. Eng. Data* 52, 1050-1055.
- [13] Libotean S., Martín A., Salavera D., Valles M., Esteve X., Coronas A., 2008. Densities, Viscosities, and Heat Capacities of Ammonia + Lithium Nitrate and Ammonia + Lithium Nitrate + Water Solutions between (293.15 and 353.15) K. *J. Chem. Eng. Data* 53, 2383-2388.
- [14] Lahmidi H., Mauran S., Goetz V. (2006). Definition, test and simulation of a thermochemical storage process adapted to solar thermal systems. *Solar Energy* 80(7), 883-893.
- [15] Mauran S., Prades P., L'Haridon F., 1993. Heat and mass transfer in consolidated reacting beds for thermochemical systems. *Heat Recovery Systems & CHP*, 13(4), 315-319.
- [16] Mauran S., Bodiot D., Crozat G. (1983). Optimisation des densités énergétiques de systèmes de stockage chimique basés sur des réactions solide-gaz renversables. *Revue Phys. Appl.* 18, 107-112.
- [17] Heller, A. (2000). Demand modelling for central heating systems. Report R-040, Department of Buildings and Energy. Technical University of Denmark (DTU). ISBN: 87-7877-042-4.
- [18] Pedersen, L. (2007). Load modelling of buildings in mixed energy distribution systems [dissertation]. Trondheim, Norway: Norwegian University of Science and Technology NTNU; 2007.
- [19] López Villada, J. Integración de sistemas de refrigeración solar en redes de distrito de frío y de calor [dissertation]. Tarragona, Spain: Universitat Rovira i Virgili, 2010.
- [20] Cao S., Hasan A., Sirén K. (2013). On-site energy matching indices for buildings with energy conversion, storage and hybrid grid connections. *Energy and Buildings* 64, 423-438.
- [21] Harr L., Gallagher J.S., Kell G.S., NBS/NRC Steam Tables, Hemisphere Publishing Corp., 1984.
- [22] Patek J., Klomfar J. (2006). A computationally effective formulation of the thermodynamic properties of LiBr-H₂O from 273 to 500 K over full composition range. *Int. J. of Refrigeration* 29, 566-578.

- [23] Chaudhari S. K., Salavera D., Coronas A. (2011). Densities, Viscosities, Heat Capacities, and Vapor-Liquid Equilibria of Ammonia + Sodium Thiocyanate Solutions at Several Temperatures. *J. Chem. Eng. Data* 56, 2861-2869.
- [24] Garousi Farshi L., Infante Ferreira C. A., Mahmoudi S. M. S., Rosen M. A. (2014). First and second law analysis of ammonia/salt absorption refrigeration systems. *International Journal of Refrigeration* 40, 111-121.

CHAPTER 3

Solar hybrid compression / thermochemical refrigeration system

3.1 INTRODUCTION AND OBJECTIVES

Chapter 2 discussed all concerns related to the hybridization of thermochemical processes with solar thermal absorption refrigeration. The resulting hybrid absorption / thermochemical refrigeration system (HATRS) is designed to operate solely with thermal energy, and a heat source temperature of about 100 °C.

Sometimes, the temperature of the heat source is not high enough to activate either the thermochemical process or the absorption counterpart. In solar-driven systems, this can happen either at the beginning or towards the end of the day.

In addition, there are several utilizable waste heat sources in the industry, but their temperature levels are usually well below 100 °C, which makes these heat sources non-utilizable in the HATRS unless some adaptations are applied to the systems.

First, other working pairs should be selected with the adequate activation temperature at the given pressure levels. If the system is to operate with waste heat at, for example, 40 °C, the well-performant ammonia / barium chloride pair must then be discarded, since for the common condenser temperatures in refrigeration, this pair has a decomposition temperature of at least 60 °C.

Other pairs could be selected, but they would have lower COP values, as well as operating issues that may still be unknown to the state of the art of thermochemical systems, given the rather reduced experimental data in real operation. If the thermochemical reactor is to reach the same operating pressure as the condenser, then the range of selectable working pairs is strict and rather small.

Instead, another solution can be chosen. If the refrigerant gas leaving the reactor undergoes a compression process before entering the condenser, the pressure range for the decomposition phase can be well widened. Given the

typical condenser pressure of about 11 bar at real operating conditions, and a vapor compressor operating at a compression ratio of 3, this leads to a reactor pressure of about 3.5 bar. And this opens the door to using working pairs that would have an activation temperature above 40 °C at 11 bar, but below that temperature at 3.5 bar. Ammonia / barium chloride falls into this category.

To reach continuous cold production, the system can be completed with a few additional instrumentation to compose a compression refrigeration subcycle. This broadens the field of usable technologies for hybridization with thermochemical processes, especially given that compression refrigeration is a mature technology, with many years of development and already implemented in real applications.

This concept is also interesting for solar applications. The compressor can be driven by electricity generated from solar photovoltaic (PV) panels [1]. These are also a mature technology with competitive costs both in construction and materials [2], and these costs are expected to decrease further [1].

In the resulting hybrid system, the energy storage function is provided by the thermochemical process. This rises a critical point in comparison to the state of the art, since classically, an off-grid compression refrigeration system powered by solar energy would be equipped with electrical batteries. These are also a mature and reliable technology, and in many cases it is probably safer and cleaner to store electricity rather than storing liquid refrigerant.

However, there are still some attractive points to choosing thermochemical storage over electric batteries. In electric storage, electricity has to be released from the batteries to activate the compressor and then the cold is produced. This implies some issues related to inertia, that should be taken into account. Meanwhile, in energy storage based on thermochemical processes, it is not electricity that is stored, but liquid refrigerant. And this liquid refrigerant remains ready for expansion and cold production, which implies less concerns about inertia. Further, this liquid is stored at ambient temperature without adding any noticeable drawback to the system's cost or performance.

Moreover, electricity storage in batteries is not free from drawbacks, either. Batteries cannot store the same amount of energy indefinitely, and when not in use, they tend to discharge gradually. Also, their full storage capacity is usually not available since it is not recommended to fully charge or discharge them. Thus, it is necessary to take into account the depth of discharge.

In contrast, thermochemical processes allow, as discussed in the previous chapters, energy storage for the mid- and even long-term with negligible heat losses, for cooling [3], refrigeration or heating applications [4]. This, plus their relatively high energy density (which leads to smaller equipment size), are two

major advantages thanks to which thermochemical processes can become economically competitive in the near future.

Whether or not the implementation of a thermochemical process for the storage function compensates economically (in the present) in comparison to the use of batteries, and under which scenarios, are highly interesting matters that are not covered in the scope of this Chapter, but may inspire future investigations.

This Chapter proposes a hybrid refrigeration system consisting of a compression refrigeration cycle hybridized with a thermochemical process. The system is electrically driven and benefits from the technologic maturity of compression refrigeration, plus the promising strengths of thermochemical processes applied to energy storage. Also, another configuration is presented in the form of a solar hybrid compression / thermochemical refrigeration system (SHCTRS), which adds the use of solar energy to its possibilities and the low cost of PV technology to its interest.

The main objectives of this Chapter are:

- To present the concept of the system. To this purpose, a flow diagram with the basic components of the system, in its most simple configuration, is presented. The thermodynamic cycle is also represented on the Clausius-Clapeyron diagram.
- To discuss the possibility of activation with thermal energy at ambient temperature. Due to the presence of a compression stage in between the decomposition phase at the reactor and the condensation of refrigeration, it is possible to reduce the temperature of the source heat to a point, eventually, where the system can be activated with heat at ambient temperature. However, this temperature reduction is not obvious and must be at least quantitatively discussed. In this Chapter a flow diagram is presented to depict how the system should be configured for this objective.
- To present a quasi-steady simulation model that allows to predict the evolution of the reaction's advancement degree and the reactor's pressure with time. This is important because as a monovariant system, the pressure will indicate the temperature, and it is important to know the temperature to be aware of the equilibrium drop.
- To test the sensitivity of the model predictions to variation in several design variables and parameters. This mainly includes: the equilibrium drop, the composite's permeability and thermal conductivity.

The sections below describe the developed hybrid systems as well as their main components, their operating modes, choice of working fluid, static dimensioning, preliminary simulation, quasi-steady simulation, and preliminary sensitivity study of the simulation model.

3.2 SYSTEM DESCRIPTION

3.2.1. Components

Figure 3.1 illustrates the simplest concept of the proposed system. Fig. 3.1a shows the flow diagram. The system consists of a thermochemical reactor, a mechanical vapor compressor, a condenser, a refrigerant storage tank, an expansion valve and an evaporator as main components. It can be regarded as conventional compression refrigeration cycle with the addition of a storage tank and a reactor, or conversely, as a thermochemical process with the addition of vapor compression between the reactor's outlet and the condenser's inlet, and an evaporator to complete a continuous cycle.

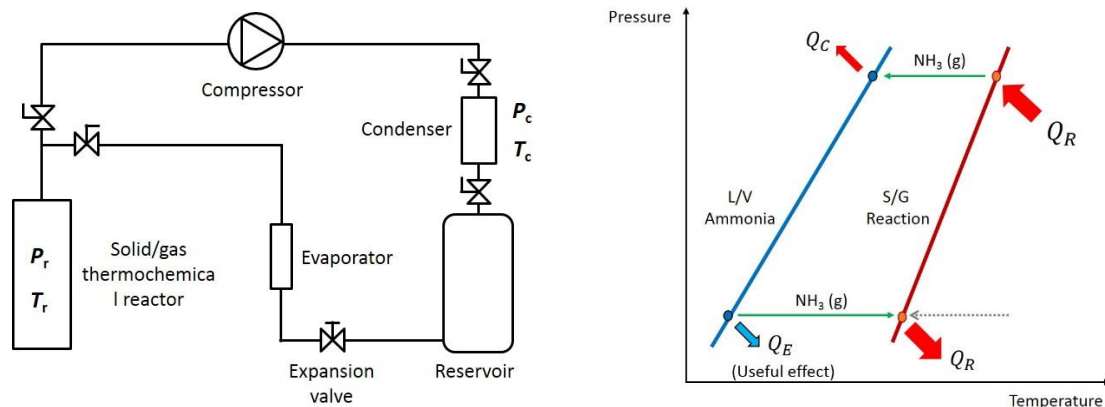


Figure 3.1. (a) Basic configuration of the hybrid compression / thermochemical refrigeration system (HCTRS); (b) HCTRS on the Clausius-Clapeyron diagram.

In the flow diagram, some valves are also displayed. These could be regarded as the minimum number of valves that would be required to run the process smoothly, since their function is to differentiate between the operating modes. However, for real operation, more valves are necessary for practical reasons. Refer to the setup description in Chapter 4 for further description.

Fig. 3.1b shows how the process looks like on the Clausius-Clapeyron diagram. The x-axis represents temperature, and the y-axis represents pressure in logarithmic form. The blue line ("L/V Refrigerant") represents the vapor/liquid equilibrium for the refrigerant, while the red line ("S/G Reaction")

represents the equilibrium of the solid/gas reaction taking place between the refrigerant gas and the solid reactive composite.

The system has three pressure levels. The low pressure level corresponds to the evaporator pressure (P_{evap}), which is dictated by the temperature of the refrigerant inside the evaporator (T_{evap}). This pressure is the same as the reactor pressure during the synthesis phase ($P_{\text{R,syn}}$), since both components are connected during this stage.

The high pressure level corresponds to the condenser pressure (P_{cond}), which is dictated by the temperature of the refrigerant inside the condenser (T_{cond}). Without the compressor, this pressure would be the same as that of the reactor during the decomposition phase ($P_{\text{R,dec}}$), since both components are connected in this stage. However, the presence of the compressor leads to the existence of a third pressure level.

This third pressure level corresponds to the reactor's pressure during the compression-assisted decomposition phase ($P_{\text{R,dec}^*}$). Depending on the temperature of the available heat source, this pressure can be adjusted to utilize that source heat. This adjustment must respect always the limitations of a real compressor, mainly the maximum admissible compression ratio, the minimum suction pressure and the maximum discharge pressure.

This third pressure level might be misleadingly labelled as an 'intermediate' pressure level, since it may sometimes (or even oftentimes) fall between the high and low pressure levels. As a matter of fact, from an operational point of view, this pressure level is the same as the reaction's equilibrium pressure at the given temperature at the very beginning of the compression-assisted decomposition phase. Right after the start of the decomposition, it is expected to drop initially, and to continue decaying slowly during the remainder of the process.

Further, the novelty of this system is the possibility of activating the decomposition phase with heat source temperatures as low as possible, *even at ambient temperature*. The latter possibility (that will be explained later in this Chapter) will most likely imply, as demonstrated in Chapter 4, to lower the reactor's pressure during compression-assisted decomposition at a level *even below the evaporator pressure during synthesis*.

The target level of this pressure is unsure, as it depends on the temperature of the source heat that has to be utilized, or otherwise said, it depends strongly on the application. In addition, its dynamic profile may be rather 'unstable', depending on the presence or absence of a control strategy and its accuracy.

These arguments, plus the fact that this pressure level may equal the high pressure level at the very beginning of a decomposition, and the fact that it can become even lower than the low pressure level itself, imply that from the conceptual point of view it would be more adequate to consider it as a 'floating' pressure level.

As for the temperature levels of this system, they can be classified into one low temperature level, two intermediate temperature levels, and one 'floating' temperature level.

The low temperature level corresponds to the cold production temperature, which is dictated by the demand. One of the two intermediate temperature levels is, as in conventional compression refrigeration cycles, the cooling water temperature, which is suitable for collecting both the condenser heat and the reaction heat during synthesis phase. The second intermediate temperature refers to the reactor's temperature during synthesis phase. This temperature is expected to be higher than the condenser temperature, although not high enough to be regarded as a 'high' temperature level.

The 'floating' temperature level corresponds, accordingly to the 'floating' pressure level, to the reaction's equilibrium temperature during the compression-assisted decomposition phase.

As a difference of this system with respect to the HATRS, the isosteres of the absorption subsystem are not present anymore. This somewhat simplifies the thermodynamic design of this system, since there are fewer degrees of freedom (no rich or poor solution concentration to set).

Another difference with respect to the HATRS is that, while the HATRS can operate solely with thermal energy sources, the HCTRS always requires an input of both electric and thermal energy. However, in this system the temperature of the heat source is lower in comparison to the HATRS.

In addition, with appropriate adaptation, the heat that is rejected by the thermochemical reactor during the synthesis phase could be used, for low-temperature application purposes, such as DHW production.

Fig. 3.2 shows how the system can be coupled to solar-PV panels to form a solar-driven hybrid compression / thermochemical refrigeration system (SHCTRS).

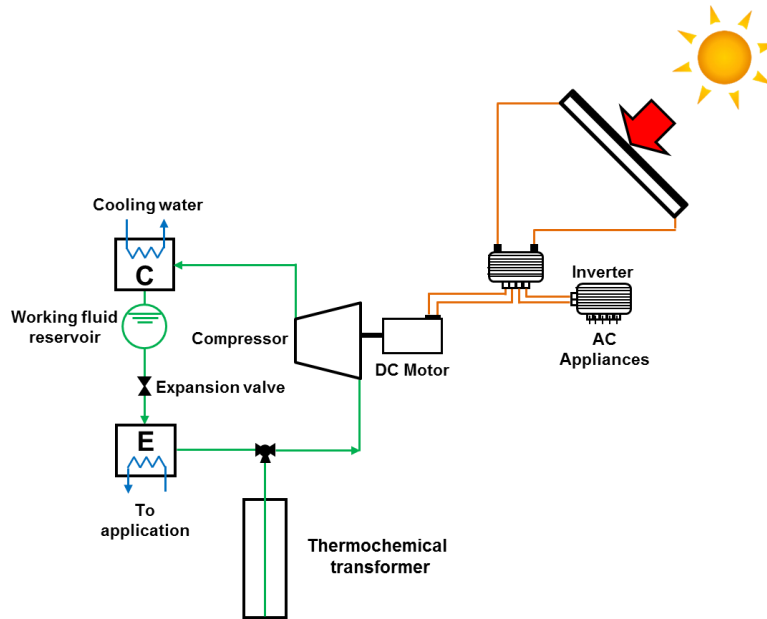


Figure 3.2. Diagram of the solar PV-driven hybrid compression thermochemical refrigeration system (SHCTRS).

3.2.2. Operating modes

Although the two main applications that we propose here differ in the origin of its driving energy, the basic idea is the same: to use the resource when it is most favorable to use it (i.e. use solar energy when it is present –in the case of solar-PV HCTRS–, or grid-delivered electricity when it is cheapest –in the case of grid-driven HCTRS–).

Given that the demand of cold is usually continuous and constant, it is the electricity profile that dictates which operating mode proceeds. In the case of solar application, this is fixed by the solar irradiation profiles, while for the case of grid-driven application, this is fixed by the price variations in the electricity.

The operating modes are depicted for the basic configuration and discussed for both the solar-PV and the grid-based configurations.

3.2.2.1 “COMP” mode

Since compression refrigeration has better COP (higher than 1) than thermochemical refrigeration (with a maximum COP around 0.5), it is preferably used when the energy source is present. Thus, this mode proceeds when the solar resource produces enough electricity to run the system, or when the electricity from the grid is cheapest (or in any case, when it is not at its peak price).

Table 3.1. Description of operating modes in the SHCTRS.

#	W_{PV}	Q_{demand}	COMP	Demand satisfied by COMP?	TCH	Mode	Notes
1	>0	>0	ON	Y	OFF	COMP	Source satisfies demand, no surplus.
2	=0	>0	ON*	N	OFF	COMP	Demand, no source, no stored refrigerant: Auxiliary source.
3	>0	=0	OFF	Surplus	CHARGE	TCH-charge	Source, no demand, store refrigerant.
4	>0	>0	ON	Surplus	CHARGE	COMP + TCH-charge	Source surplus: store refrigerant.
5	=0	>0	OFF	N	DISCHARGE	TCH-discharge	Demand, no source: release refrigerant.
6	>0	>0	ON	N	DISCHARGE	COMP + TCH-discharge	Source is insufficient: release refrigerant.
7	=0	=0	OFF	=0	OFF	OFF	No source, no demand, systems off.

The flow diagram from Fig 3.3a depicts how this mode proceeds in the simple configuration. Basically, the hybrid system in this mode operates as a conventional compression refrigeration system. Refrigerant circulates in a constant mass flow rate (regardless of the amount of refrigerant stored inside the tank) and sufficient to satisfy the demand of cold.

This cold is produced by the refrigerant vaporizing inside the evaporator and right after the expansion that transitions from high pressure to low pressure (evaporator pressure, P_{evap}). After the evaporator, the refrigerant is suctioned by the compressor, which increases its pressure to the high pressure level (condenser pressure, P_{cond}). Once inside the condenser, the refrigerant gas exchanges heat with the cooling fluid and changes to liquid phase, rejecting condensation heat (Q_c) in the process. Then, the liquefied refrigerant enters the storage tank and the cycle is completed.

During this mode the TCH subsystem does not proceed, and for this reason its S/G equilibrium line is not displayed on the Clausius-Clapeyron diagram.

3.2.2.2 "TCH-charge" mode

In those cases in which there is no demand of cold but it is still favorable to use the driving energy, the "TCH-charge" mode proceeds (Fig. 3.4). This scenario may occur only if the demand of cold is intermittent (which is rather

unusual), and there is a period in which the source heat is available, the electric energy is either available from the solar resource or in its lowest price, and there is no demand of cold.

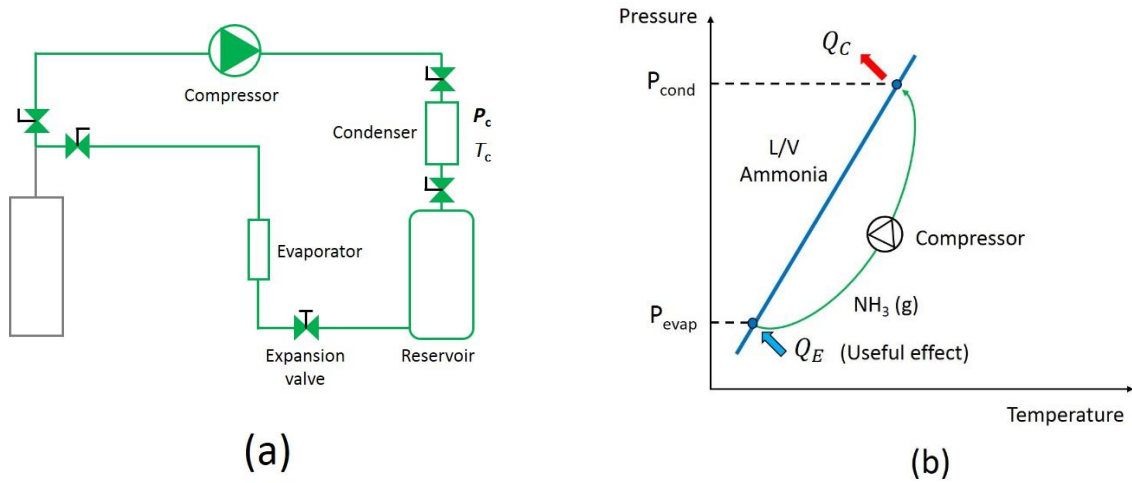


Figure 3.3. (a) “COMP” mode on the flow diagram of the HCTRS; (b) “COMP” mode on the Clausius-Clapeyron diagram.

In this mode, the available electricity is used to operate the compressor, and since there is no demand of cold, the available source heat is provided to the thermochemical reactor to activate the decomposition phase and store refrigerant inside the tank. The evaporator does not operate. All this mode occurs at the ‘floating’ pressure level.

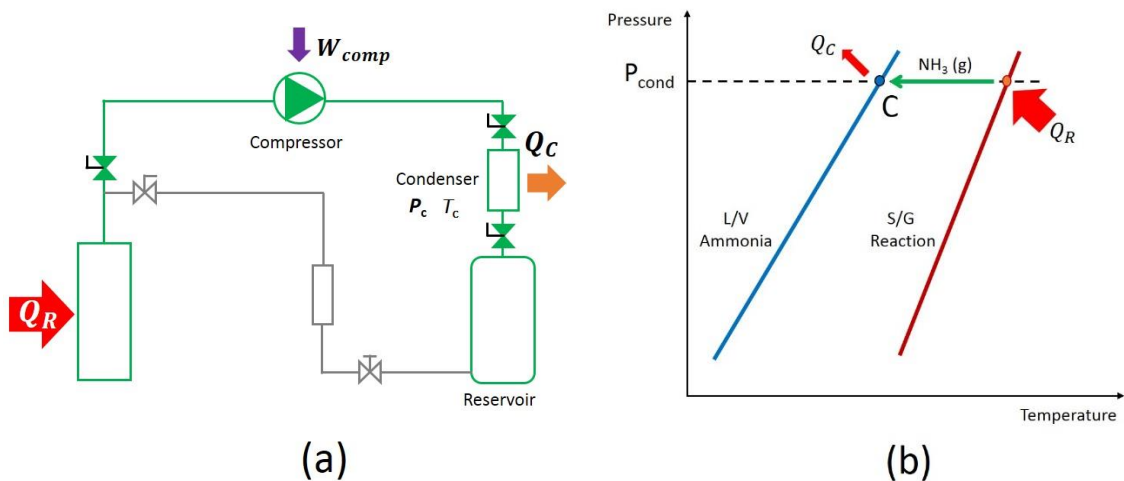


Figure 3.4. (a) “TCH-charge” mode on the flow diagram of the HCTRS; (b) “TCH-charge” mode on the Clausius-Clapeyron diagram.

3.2.2.3 “COMP + TCH-charge” mode

This operating mode is especially useful in those applications in which the system operates with electricity from the grid. This mode can be applied during those periods of the day in which the price of electricity is at its lowest point. It is then used to produce the refrigerant that will be stored and later used, when the price of electricity is at its peak.

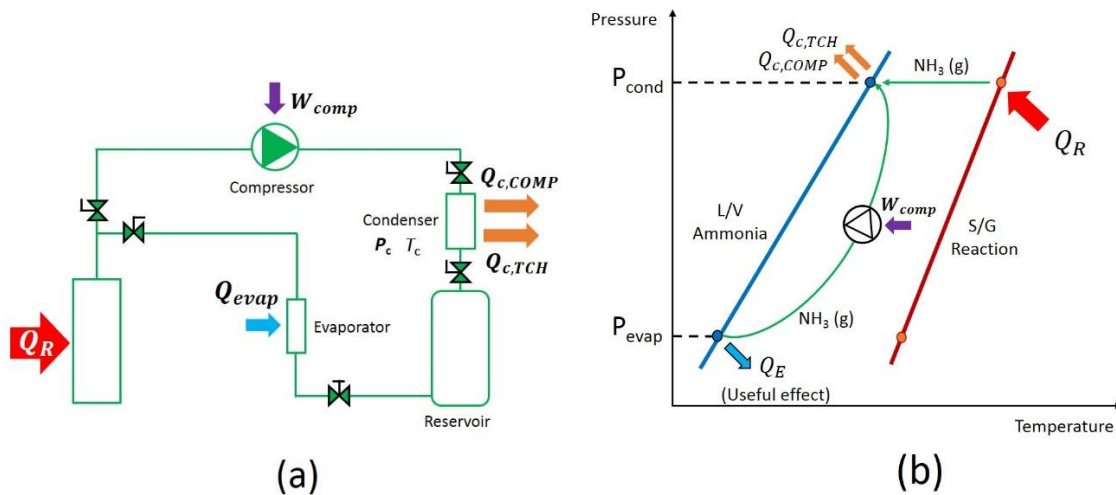


Figure 3.5. (a) “COMP + TCH-charge” mode on the flow diagram of the HCTRS; (b) “COMP + TCH-charge” mode on the Clausius-Clapeyron diagram.

3.2.2.4 “TCH-discharge” mode

This mode is especially proficient in those periods in which there is demand of cold but the source is either not available (for instance in off-grid solar-driven refrigeration applications) or too expensive (for on-grid systems, when the price of electricity is at its highest point).

It is expected to proceed rather frequently (i.e. at least once daily) in both solar-PV applications and a grid-based applications. In the solar-PV application, it is useful during the night, were the solar resource is unavailable but still there is demand of cold (as many of the conceivable applications have an uninterrupted demand). In a grid-based application, during those periods of the day in which the price of electricity is highest (which is classically during the night, although in those countries in which the night tariff applies, it corresponds to daytime).

This mode requires no electricity or source heat input at all. It simply consists in releasing refrigerant from the reservoir and expanding it to evaporator pressure, at which it will supply the cold inside the evaporator.

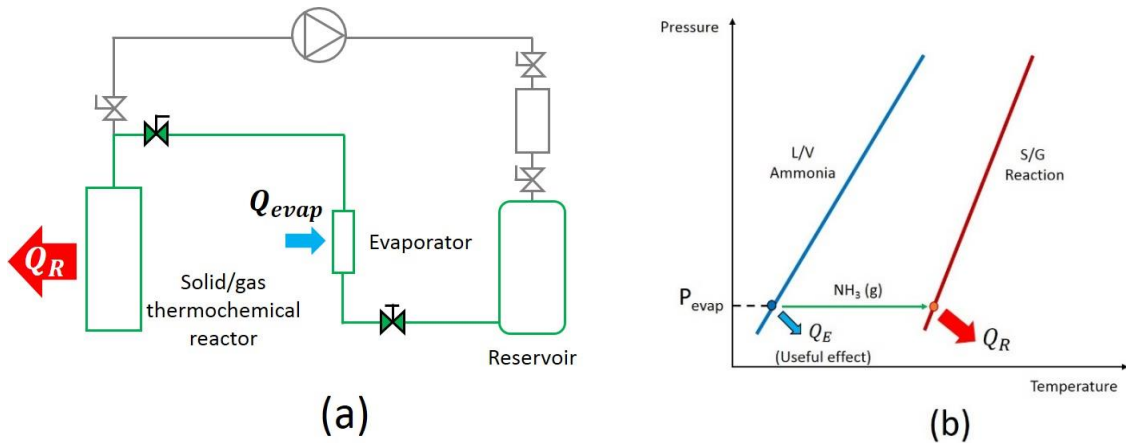


Figure 3.6. (a) “TCH-discharge” mode on the flow diagram of the HCTRS; (b) “TCH-discharge” mode on the Clausius-Clapeyron diagram.

Thanks to the thermochemical process, the energy storage saves one step of energy conversion during the discharge stage. This reduces the inertia of the system in comparison with electricity storage in batteries. As for storage dimensioning, no big concerns should be raised around the size of the thermochemical reactor, thanks to the high energy density of such processes. Moreover in solar applications, this mode will most likely proceed during the night, where the demand of cold tends to be lower since the ambient temperature is lower than during the day.

3.2.2.5 “COMP + TCH-discharge” mode

If the system dimensioning is done carefully, this mode is not expected to proceed frequently, or at all. This is especially true for grid-based applications, in which any peak of cold demand should be easily addressed by supplying more electricity from the grid to the compressor.

However, in off-grid solar-powered applications, it may still be necessary to assist the compression subsystem during unexpectedly high peak-demand periods in which solar irradiation does not suffice.

In this operating mode, both the compression and the thermochemical subsystem are operating, the latter in “discharge” mode, or otherwise stated, in reaction of decomposition.

A constant flow rate of refrigerant is circulating through the compression subsystem as described in the “COMP” operating mode (refer to section 3.2.2.1), requiring an input of electric energy to the compressor (W_{comp}) and rejecting condensation heat at the condenser (Q_{cond}).

Simultaneously, the refrigerant stored in the tank is being released and circulated to the thermochemical reactor, rejecting the heat from the exothermal

reaction, as described in the “TCH-discharge” operating mode (refer to section 3.2.2.4).

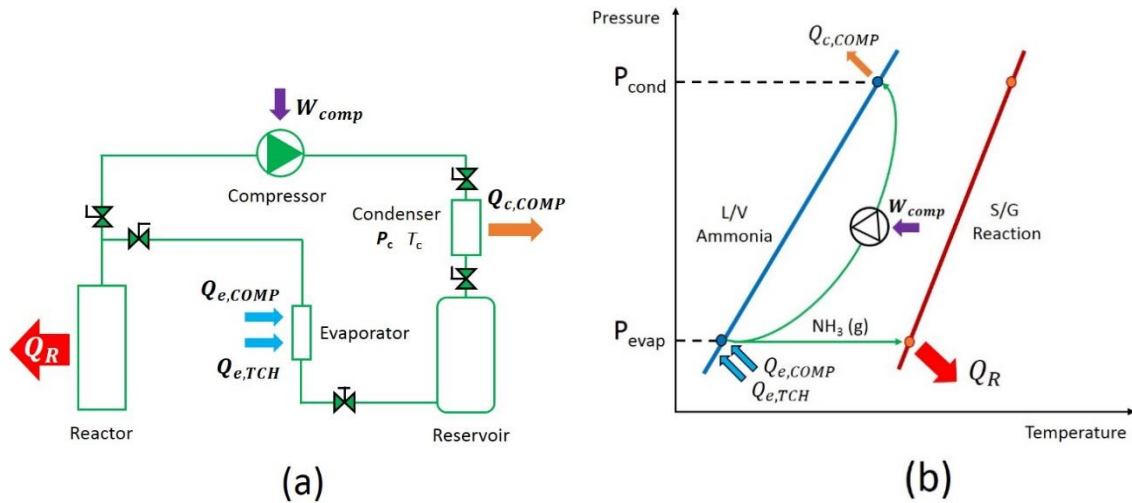


Figure 3.7. (a) “COMP + TCH-discharge” mode on the flow diagram of the HCTRS; (b) “COMP + TCH-discharge” mode on the Clausius-Clapeyron diagram.

As a consequence, the system has a double refrigeration effect from both the compression subsystem ($Q_{e,COMP}$) and the thermochemical process ($Q_{e,TCH}$).

3.2.2.6 “OFF” mode

In this operating mode, none of the components are operating and the refrigerant fluid remains in its most part either stored inside the tank or absorbed inside the thermochemical reactor. All valves are closed.

This mode is also expected to not be frequent, since the application will most likely require continuous cold production. Nevertheless, for the sake of completion, it is included in this description.

3.3. SYSTEM PRELIMINARY DESIGN

The preliminary design and performance simulation of the system was carried out by means of a simplified, steady-state simulation model implemented in the *Engineering Equation Solver* software.

3.3.1. Working pair selection

The selection of working pair in this system is simpler than in the HATRS, mainly because the compression subsystem works simply with pure refrigerant

(there is no sorbent pair). This reduces the selection process to just choosing a refrigerant fluid and a reactive salt for the thermochemical subsystem.

Given that almost the same application is considered for both the HATRS and the HCTRS, this implies that the operating conditions and temperature levels are more or less the same for both systems.

As discussed in Chapter 2, for refrigeration applications, which usually require cold production temperatures under 0 °C, ammonia is a reasonable and performing choice that also runs in compression refrigeration, with satisfactory results.

Another simplification with respect to the HATRS is the fact that no particular concerns exist about the hypothetical presence of small fractions of sorbent in the refrigerant leaving the evaporator, which may negatively affect the thermochemical reaction.

However, another new concern does exist in this same line of thought. It is related to the presence of a vapor compressor, and it refers to the use of oil. Many of the compressor types that exist in the market and that would be suitable for the construction of this system use oil for lubrication purposes. The presence of oil in the refrigerant leaving the evaporator, if this oil reaches the thermochemical reaction, may negatively affect the reaction's development the same way as the presence of a sorbent would.

Therefore, either a good oil separation stage must be included in a real setup based on this system, or an oil-free compressor (e.g. a membrane compressor) has to be chosen.

3.3.2. Application and operating conditions

The design is strongly affected by the application. The application sets important parameters such as reactor volume, mass flow rates, equipment size, average and maximum power consumption, area of solar panels, etc. For the preliminary design of the HCTRS, a rough approximation was used as application.

A continuous demand of cold of $\dot{Q}_{cond}^{day} = 5 \text{ kW}$ was assumed for the daytime period (a $\Delta t_{day} = 9 \text{ h}$, i.e. from 9.00 to 18.00) and a continuous demand of cold of $\dot{Q}_{cond}^{day} = 1 \text{ kW}$ was assumed for the nighttime period (a $\Delta t_{day} = 15 \text{ h}$, i.e. from 18.00 to 9.00). From the daily demand of cold, the required ammonia mass flow was calculated as:

$$m_{NH_3}^{day} = \frac{\dot{Q}_{cond}^{day}}{\lambda_{NH_3}^{vap}} \quad (3.1)$$

Then, the static dimensioning of the system was carried out. In addition to the static dimensioning, a brief performance study was carried out at several evaporation and condensation temperatures, within the common operating range of these systems in refrigeration applications.

The simulation of this system was later improved with the quasi-steady simulation model implemented in Matlab[®] (refer to section 3.4).

3.3.3. Considerations about the compressor

When determining the size and capacity of the compressor that has to be used for this system, the important parameters to have in mind are: the pressure ratio, the minimum suction and maximum discharge pressures, and the flow rate of refrigerant gas.

The maximum discharge pressure of a commercial compressor depends mainly on its setup and the construction materials. From the point of view of the process, if the system works with ammonia as refrigerant the maximum pressure that will be needed at the compressor's discharge will be the equilibrium pressure of pure ammonia at condenser temperature. In refrigeration, this condenser temperature can normally be up to 40 °C, which corresponds to a pressure of around 13 bar. Commercial compressors exist that can admit such discharge pressures.

The minimum reactor pressures in the compression-assisted decomposition influence the pressure ratio for a given discharge pressure. Depending on the coupling between the compressor and the thermochemical reactor, the operating pressure during the decomposition phase may become lower than 1 bar. In that case, it is recommendable to run a compressor that can operate in such suction pressure.

In addition to suction and discharge pressures, the pressure ratio is also to be taken into account. If it is not too higher than 3, then the compression stage between decomposition reaction and refrigerant condensation can be carried with one single compressor. For instance, for ammonia / barium chloride working pair and a heat source temperature above 40 °C, this will be the case.

From the hypotheses that a good oil / refrigerant separation is reached, different compressor types are viable, being the scroll compressor maybe one of the most interesting ones. If it is preferred to completely avoid issues related to oil / refrigeration separation, then a membrane compressor can be selected.

3.3.4. Equilibrium drop

One important parameter that influences the speed of a thermochemical process in the equilibrium drop (Fig. 3.8b). It is defined as the difference between the reaction's equilibrium temperature at the given operating pressure, and the temperature of the heat exchange fluid.

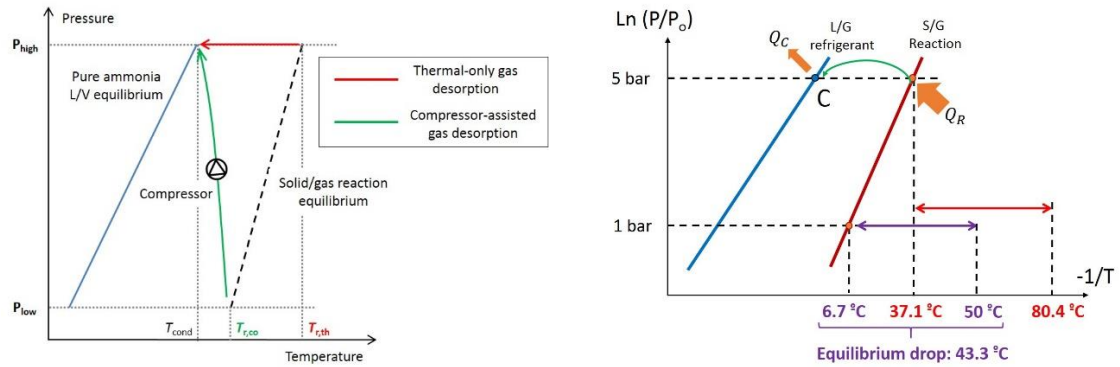


Figure 3.8. (a) Graphical demonstration of the equilibrium drop reduction due to the vapor compression; (b) Numerical example of the equilibrium drop.

The bigger the equilibrium drop, the faster the reaction. This concept is especially important in the compression-assisted decomposition, where the operating pressure, and therefore the equilibrium temperature, can be significantly reduced. With a given heat source temperature, this implies that the equilibrium drop can be dramatically increased. So, will other parameters and operating conditions remaining the same, faster reactions are expected in compression-assisted decomposition with respect to thermal-only decomposition.

3.4. QUASI-STEADY SIMULATION MODEL

A quasi-steady model is developed to simulate the reaction's progress as a function of several design conditions. The model presented here is an adaptation from an original model that was already existing at, and developed by, the Promes laboratory. Only certain parts of the original model were adapted for the model to take into account the influence of the compressor on reactor's pressure. The main model hypotheses, parameters, variables and results are described.

3.4.1. Hypotheses and assumptions

Fig. 3.9a shows a lateral view of the basic design that was chosen for the thermochemical reactor. Its geometry is cylindrical with an external heat transfer coating (depicted as an area of red wavy lines).

Inside the reactor, two areas can be distinguished. The grey-green area represents the solid reactive composite, which consists of a mixture of the reactive salt and an enhancer of heat and mass transfer. When this area is almost completely green, it represents the fully charged salt (i.e. the salt after having absorbed as much –or nearly as much– refrigerant gas as it can absorb). When this area is almost completely grey, it represents the fully discharged salt (i.e. the salt after all –or almost all– refrigerant has been desorbed from it).

Any representation of the solid composite with both a green and a grey area represents an intermediate point between fully charged and fully discharged salt. The three images in Fig. 3.9a represent the progress of the thermochemical reaction. From left to right, they represent a decomposition phase, where heat is supplied to the composite, refrigerant is gradually desorbed from the salt and leaves the reactor in gas form through the innermost channel (a small diameter duct that works as a gas diffusor).

If the same images are watched from right to left, they represent a synthesis phase, where refrigerant gas enters the thermochemical reactor and reacts with the salt, in an exothermic process (thus, the heat transfer fluid in the coating would collect heat from the reactor instead of supplying it, and it should be represented rather with blue lines than red lines).

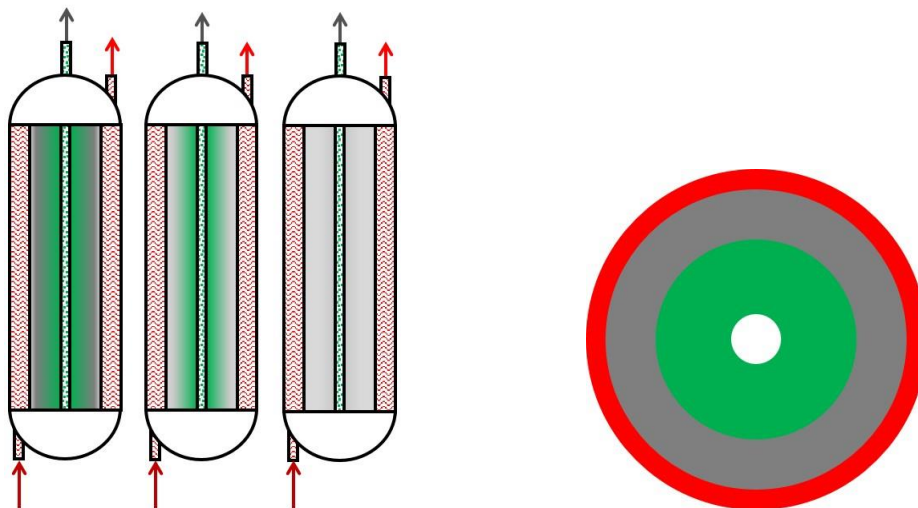


Figure 3.9. (a) View of the thermochemical reactor during the decomposition phase. (b) Front view of the solid reactive composite during the reaction progress.

Fig. 3.9b shows a cross-section view of the reactor during the reaction progress. The same four radial areas from Fig. 3.9a are represented in it: the outmost, red ring represents the heat transfer fluid supplying heat to the solid composite. The intermediate, grey ring represents solid composite with no refrigerant absorbed in it: in a decomposition phase it is salt that has already reacted, while in synthesis phase it is salt that is yet to react.

The inner, green ring represents solid composite with refrigerant absorbed in it. Conversely to the grey area, in a decomposition phase this green area corresponds to salt that is yet to react, while in a synthesis phase it represents salt that has already reacted. Finally, the innermost, white ring represents the gas diffusor.

This configuration is not the unique possible one, and several others exist in literature, both for simulative [5] and experimental studies.

If the composition and distribution of the solid reactive composite is perfectly uniform in the axial direction, the temperature difference between the inlet and outlet of the heat transfer fluid is small enough, and the reactor's length is at least 5 times its diameter, then both the heat and mass transfers can be neglected in the axial direction.

This hypothesis results in a 'reactive front' advancing in the radial direction. The existence of this reaction front has been proved experimentally, and later stated and used in simulative studies. With the abovementioned hypotheses and simplifications, all operating conditions are constant along the axial direction in this front.

As a matter of fact, depending on heat and mass transfer limitations, two reactive fronts exist in reality: one of them related to heat transfer and that will be named 'thermal front', and the other one related to mass transfer and that will be named 'mass front'.

The thermal front is generated by the heat transfer limitations within the reactive composite. In beginning of both the synthesis and the decomposition phases, this front appears in the outmost radius of the reactive composite, since this is the first area to start exchanging thermal energy with the heat transfer fluid from the external coating.

During the reaction progress, this front advances inwards through the reactive composite. Depending on the conditions of the experiment, the front may or may not reach the innermost radius (usually not, unless mass transfer is completely non-limiting). Thus, at any given moment during the reaction, this front is located at an exact radial position inside the reactive composite. The

presence of this front implies the existence of a temperature gradient in the radial direction from the front to the outmost radius.

The mass front is generated by the mass transfer limitations within the reactive composite. In beginning of both the synthesis and the decomposition phases, this front appears in the innermost radius of the reactive composite, since this is the first area to start receiving refrigerant gas and therefore starting to react.

During the reaction progress, this front advances outwards through the reactive composite. Depending on the conditions of the experiment, the front may or may not reach the innermost radius (usually not, unless heat transfer is completely non-limiting). Thus, at any given moment during the reaction, this front is located at an exact radial position inside the reactive composite. The presence of this front implies the existence of a pressure gradient in the radial direction from the front to the innermost radius.

As explained above, each one of the two reactive fronts could reach the opposite radius to that of its origination, if the other front did not exist (this happens if the mass or heat limitations that originate the fronts are negligible). However, in reality, most of the times both fronts do exist, because both heat and mass transfer limitations exist. Therefore, the two fronts advance and, when the reaction is completed, they finally coincide in the same radial position.

The exact radius in which the reactive fronts find each other depends strongly on the conditions of the experiment. If mass transfer limitations are stronger than heat transfer limitations, then the 'mass front' advances further than the 'heat front', resulting that they find each other in a position that is closer to the outmost radius than to the innermost radius. The opposite situation happens if heat transfer limitations are stronger than mass transfer limitations.

Therefore, an accurate simulation model must take into account both heat and mass transfers, unless one of the two can be neglected. For instance, if the operating pressure and the composite's permeability are high enough, mass transfer limitations can be neglected. This simplification may be applied in the synthesis phase and especially in the decomposition phase without compressor. However, in compression-assisted decomposition, the operating pressure inside the reactor is low enough to make mass transfer limitations relevant.

The model described in this section takes into account heat and mass transfer. However, it gives the option to neglect the influence of mass transfer limitations through the solid composite, and also to neglect some aspects of heat transfer limitations. This is applicable especially during the synthesis phase and during the decomposition phase when it is not assisted with the compressor.

As a conclusion, the main model hypotheses and assumptions are:

- The mass fractions of reactive salt and inert enhancer, as well as the distribution of layers of inert enhancer, are uniform in all the solid composite.
- The relation between reactor's length and diameter (L/D) is at least 5.
- The difference between the temperature of the heat transfer fluid at the inlet and outlet of the reactor's coating is lower than 2 K.
- Accumulation terms (sensible heat of the solid reactive composite, and mass of ammonia gas inside the porous volume) are neglected.
- Two reactive fronts exist: one is bound to mass transfer limitations, it is formed in the innermost radius of the solid composite and advances outwards; the other one is bound to heat transfer limitations, it is formed in the outmost radius of the solid composite and advances inwards.
- Steady state is assumed at both reaction fronts, based on equation (2.2) for the ammonia/barium chloride reactive pair.

The sections below describe the design variables and parameters, study variables, sensitivity analysis and results that are consequence of these hypotheses and assumptions.

3.4.2. Variables and parameters

The parameters that influence the reaction's progress can be classified into two main categories: parameters related to composite implementation, and parameters related to operating conditions.

Table 3.2. Nominal case and minimum / maximum values of the design parameters and variables.

Parameter	Units	Min	Nominal case	Max.
λ_0	W/(m·K)	0.85	2.00	5.00
λ_1	W/(m·K)	0.85	= λ_0	5.00
k_0	m ²	10 ⁻¹⁶	10 ⁻¹⁵	10 ⁻¹⁴
k_1	m ²	10 ⁻¹⁶	= k_0	10 ⁻¹⁴
ΔT_{eq}	K	10	15	20
h_{sw}	W/(m ² ·K)	300	500	1000

Table 3.2 introduces the design parameters and variables that will be considered in the sensitivity analysis of the simulation model. For each parameter the nominal, minimum and maximum values are shown.

3.4.3. Model equations

The thermal conductivity of the solid reactive composite is estimated according to the model in [6], which is applicable if the apparent density of the ENG ($\tilde{\rho}_{GNE}$) is higher than 50 kg/m³. First, the effective axial conductivity of ENG is estimated through the correlation from [6] (eq. 3.2).

$$\lambda_b = \lambda_{b0} \cdot \left(\frac{\tilde{\rho}_{GNE}}{50} \right)^{(4/3+0.17)} \quad (3.2)$$

In eq. (3.1), λ_{b0} corresponds to the thermal conductivity of isotropic ENG at a $\tilde{\rho}_{GNE}$ of 50 kg/m³.

Then, the volumetric fraction of the fully discharged and fully charged salt (f_{s0} and f_{s1} , respectively) was estimated at $X = 0$ and $X = 1$ through equations (3.3) and (3.4).

$$f_{s0} = \frac{\frac{\tilde{\rho}_{GNE}}{M_{s0}}}{v_{s0} \cdot (1-eps_{g0})} \cdot \frac{w_{s0}}{(1-w_{s0})} \quad (3.3)$$

$$f_{s1} = \frac{\frac{\tilde{\rho}_{GNE}}{M_{s1}}}{v_{s1} \cdot (1-eps_{g1})} \cdot \frac{w_{s1}}{(1-w_{s1})} \quad (3.4)$$

The estimated values of λ_b , f_{s0} and f_{s1} were then used for the calculation of the effective axial conductivity of the solid reactive composite at $X = 0$ and $X = 1$ (eq. 3.5 and 3.6, respectively).

$$\lambda_0 = \frac{\lambda_b}{(1+\alpha \cdot f_{s0})^2} \quad (3.5)$$

$$\lambda_1 = \frac{\lambda_b}{(1+\alpha \cdot f_{s1})^2} \quad (3.6)$$

For the calculations related to mass transfer, the model proceeds first with the estimation of the permeability and the coefficients of Klinkenberg. For the calculation of the permeability, first the effective apparent density of ENG is calculated both at $X = 0$ and $X = 1$ (eq. 3.7 and 3.8, respectively) by having into account the porosity of the grain.

$$\tilde{\rho}_{be0} = \frac{1}{\frac{1}{\tilde{\rho}_{GNE}} - \frac{w_s}{1-w_s}} \cdot \frac{v_{s0}}{M_{sa} \cdot (1-eps_{g0})} \quad (3.7)$$

$$\tilde{\rho}_{be1} = \frac{1}{\frac{1}{\tilde{\rho}_{GNE}} - \frac{w_s}{1-w_s}} \cdot \frac{v_{s1}}{M_{sa} \cdot (1-eps_{g1})} \quad (3.8)$$

With the values of $\tilde{\rho}_{be0}$ and $\tilde{\rho}_{be1}$, the permeability of the solid reactive composite is estimated through the correlation from [7] applied at $X = 0$ and $X = 1$ (eq. 3.9 and 3.10, respectively).

$$k_0 = 10^{(-5.24 - 3.83 \cdot \log(\tilde{\rho}_{be0}))} \quad (3.9)$$

$$k_1 = 10^{(-5.24 - 3.83 \cdot \log(\tilde{\rho}_{be1}))} \quad (3.10)$$

And the Klinkenberg coefficients are estimated through the correlations from [5] at $X = 0$ and $X = 1$ (eq. 3.11 and 3.12, respectively).

$$b_0 = 1.507 \cdot 10^{-9} \cdot k_0^{-0.9461} \quad (3.11)$$

$$b_1 = 1.507 \cdot 10^{-9} \cdot k_1^{-0.9461} \quad (3.12)$$

After these initial estimations for heat and mass transfer, the main calculation routine proceeds. The iterations are carried out over the value of X (reaction advancement degree) from $X = 1$ to $X = 0$ for the decomposition phase or, conversely, from $X = 0$ to $X = 1$ for the synthesis phase. At each iteration, the operating pressure (P_C) and the temperature of the reactive front (T_{f2}) are calculated from the definition of the global reaction rate n_3 (eq. 3.15) taking into account the partial rates n_1 and n_2 , which are limited by mass diffusion (3.13) and heat transfer (3.14) respectively. Radial geometry was considered.

$$n_1 = \frac{2 \cdot \lambda_1 \cdot (T_{f1} - T_{f2})}{D_{e,c} \cdot (r_{sw}^2 - r_{dif}^2) \cdot \log\left(\frac{r_{f2}}{r_{f1}}\right)} \quad (3.13)$$

$$n_2 = \frac{\Delta h \cdot k_1 \cdot (P_{f1}^2 - P_{f2}^2) + 2 \cdot b_1 \cdot (P_{f1} - P_{f2})}{\mu \cdot R \cdot T_C \cdot D_{e,c} \cdot (r_{sw}^2 - r_{dif}^2) \cdot \log\left(\frac{r_{f2}}{r_{f1}}\right)} \quad (3.14)$$

$$n_3 = n_1 + n_2 \quad (3.15)$$

For the vapor compressor, a simplified model was used in which the molar flow of gas at the suction is a function of the required pressure difference (eq. 3.16).

$$\dot{V}_a = a_{comp} \cdot \Delta P^2 + b_{comp} \cdot \Delta P + c_{comp} \quad (3.16)$$

Equation (3.16), along with the iterative recalculation of reactor pressure at each calculation step, are the main contributions of the author of this thesis to the original 2-front reaction model that was already pre-existing at, and created by, the Promes laboratory. The Matlab codes used for process simulation with this model are available in Appendix B.

The model is built so that at the end of the calculations, a vector of just 100 values of X is kept. This vector consist of the two extremes $X = 0$ and $X = 1$, plus 98 more values of X in between, in arithmetically equal increments.

3.5. SIMULATION RESULTS AND DISCUSSION

The difference in the progression of the reaction's advancement degree (X) and the reactor pressure along reaction time is represented graphically. Profiles are shown to depict the influence of the equilibrium drop (ΔT_{eq}), permeability of the reactive composite (k_0 and k_1) and thermal conductivity of the reactive composite (λ_0 and λ_1) on the reaction's advancement degree (X) – time (t) curve (hereinafter named 'X-t curve').

3.5.1. Reactor pressure and reaction advancement degree

Since the first aim of the simulation model is to predict the reaction's advancement degree (X) and the reactor pressure (P) with respect to time, the X-t and P-t curves were obtained in two opposite configurations: power-oriented (Fig. 3.10a) and storage-oriented (Fig. 3.10b).

Fig 3.10a corresponds to the configuration named 'power-oriented'. This configuration corresponds to low values of energy storage density (D_e of about 50-100 kWh/m³) and rather high values of apparent density of expanded natural graphite ($\tilde{\rho}_{app,ENG}$ of about 150 kg/m³).

In the power-oriented configuration, the lower density of reactive salt, plus the higher presence of ENG with its porosity, creates more 'empty space' inside the composite for the molecules of gas to flow through. Therefore, the refrigerant that is desorbed from the reactive salt can leave the solid composite at higher speeds than in a 'storage-oriented' configuration.

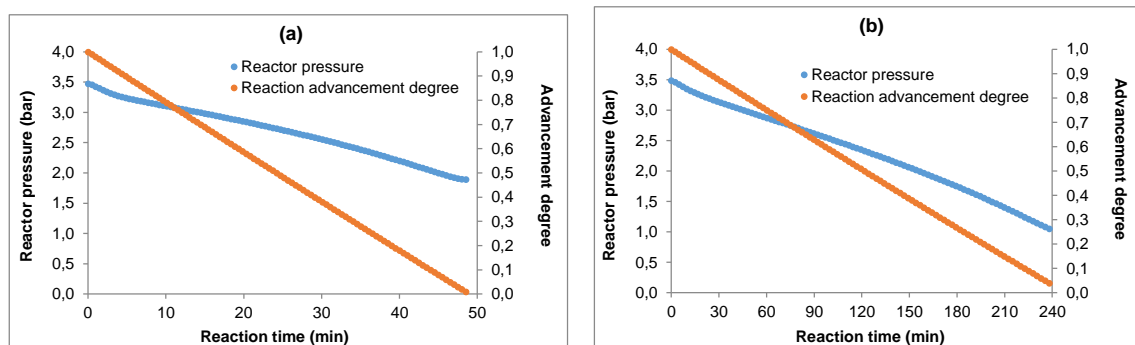


Figure 3.10. (a) Evolution of reactor pressure and reaction's advancement degree during decomposition phase in power-oriented configuration; (b) Evolution of reactor pressure and reaction advancement degree during decomposition phase in storage-oriented configuration.

This circumstance has two noticeable consequences on the X-t and P-t curves of reaction. First, the reaction ends well sooner (lower value of final time in the X-t curve) than in the storage-oriented configuration. Second, since the reactor

can deliver higher flow rates of refrigerant, the pressure decay inside the reactor (which is consequence of the coupling with the compressor) is lower, and thus the reactor pressure at the end of reaction is higher than in the case of a storage-oriented configuration.

3.5.2. Influence of thermal conductivity

Fig. 3.11 shows profiles of the $X-t$ curve for different values of λ_0 and λ_1 being the rest of design variables and parameters at their nominal values. As expected, the speed of the process improves with an improvement in the composite's thermal conductivity. The red continuous line shows the $X-t$ curve with the values of λ_0 and λ_1 calculated through the correlation from [7].

3.5.3. Influence of permeability

Fig. 3.12 shows profiles of the $X-t$ curve for different values of k_0 and k_1 being the rest of design variables and parameters at their nominal values. As expected, the speed of the process improves with an improvement in the composite permeability. The green continuous line shows the $X-t$ curve with the values of k_0 and k_1 calculated through the correlation from [6].

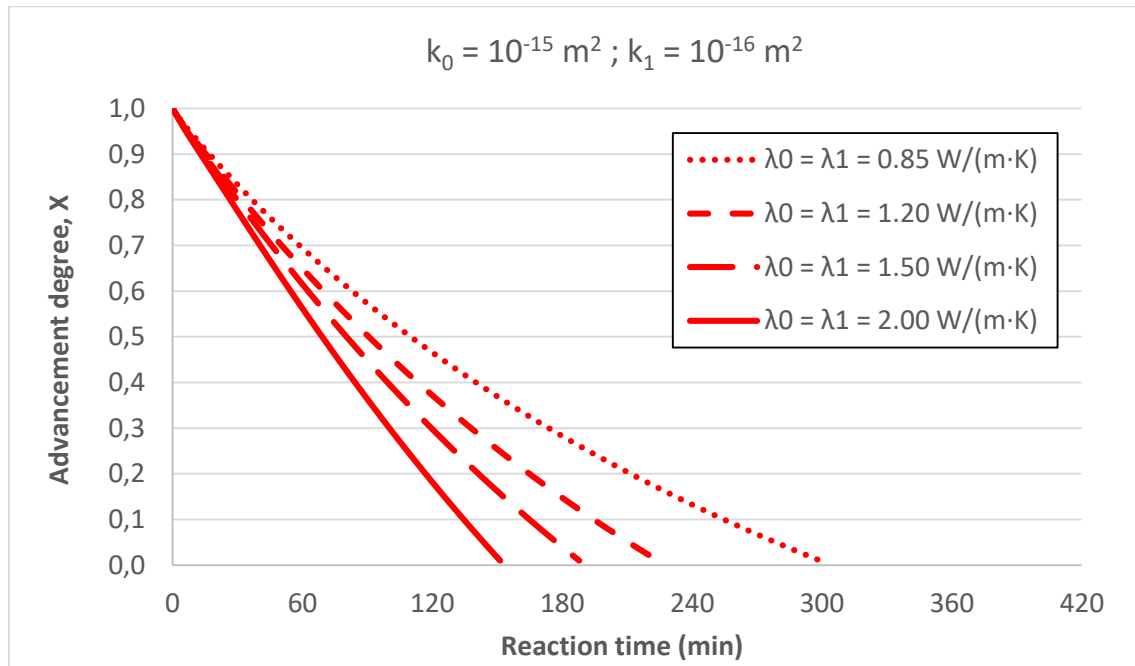


Figure 3.11. Evolution of the reaction's advancement degree during decomposition phase without compressor for different values of thermal conductivity of the charged and discharged salt (λ_0 and λ_1 , respectively).

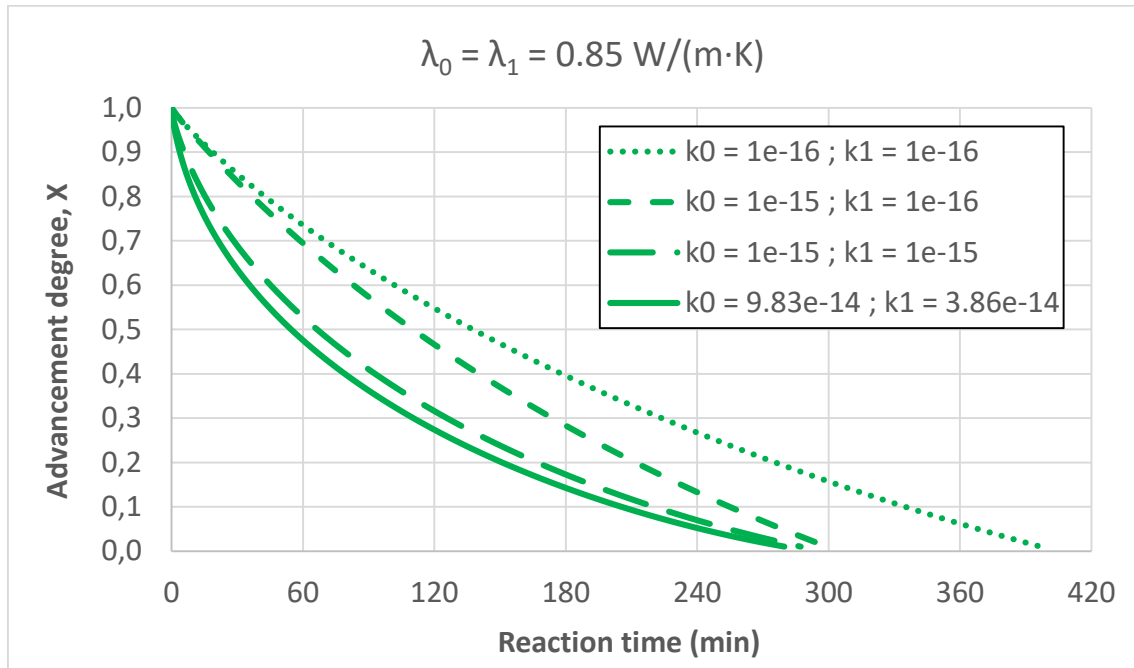


Figure 3.12. Evolution of the reaction's advancement degree during decomposition phase without compressor for different values of permeability (k) of the charged and discharged salt.

3.6. CONCLUSIONS AND PERSPECTIVES

The hybrid compression / thermochemical refrigeration system (HCTRS) and the solar hybrid compression / thermochemical refrigeration system (SHCTRS) are presented. Both concepts are depicted in its simplest configuration on a flow diagram, and their thermodynamic constraints are introduced and discussed on the Clausius-Clapeyron diagram.

The operational autonomy of both systems and competitive cost of most of its components are identified as their strong features. Meanwhile, the technological underdevelopment (TRL of about 3.5) of thermochemical processes is identified as one weak point of the hybrid systems. Nevertheless, the promising strengths of thermochemical processes are expected to compensate their current weaknesses in the present.

The economic (or even exergo-economic) comparison of these hybrid systems with other state-of-the-art solutions remains unclear and a highly interesting perspective for future work.

The main components are identified and a brief discussion is offered about working pair selection and choice of compressor, having into account all restrictions described when introducing the system. It is concluded that, for refrigeration applications, ammonia is an option to have in mind, since it has

been successfully used both in compression refrigeration and thermochemical processes.

A quasi-steady simulative study is carried out for the reaction taking place, with a special focus on the decomposition phase when it is assisted with the compressor and when it is not. It is found that heat transfer limitations are to be permanently taken into account for process simulation, while mass transfer limitations can be negligible if the product between the operating pressure and the reactive composite's permeability is high enough. This is usually the case in the non-assisted decomposition phase, and sometimes in the synthesis phase. However, in the compression-assisted decomposition phase, mass transfer limitations will usually be non-negligible, due to the low operating pressures.

3.7. REFERENCES

- [1] Bilgili, M. (2011). Hourly simulation and performance of solar electric-vapor compression refrigeration system. *Solar Energy* 85, 2720-2731.
- [2] Kim, D. S., & Infante Ferreira, C. A. (2008). Solar refrigeration options - a state-of-the-art review. *International Journal of Refrigeration*, 31(1), 3–15.
- [3] Stitou D., Mazet N., Mauran S. (2012). Experimental investigation of a solid/gas thermochemical storage process for solar air-conditioning. *Energy* 41(1), 261-270.
- [4] Mauran, S., Prades, P., L'Haridon, F. (1993). Heat and mass transfer in consolidated reacting beds for thermochemical systems. *Heat Recovery Systems & CHP*, 13(4), 315-319.
- [5] Lahmidi H., Mauran S., Goetz V. (2006). Definition, test and simulation of a thermochemical storage process adapted to solar thermal systems. *Solar Energy* 80, 883-893.
- [6] Olivès, Régis. Doctoral thesis. Université de Perpignan Via Domitia, France, 2005.
- [7] Michel B., Mazet N., Mauran S., Stitou D., Xu J. (2012). Thermochemical process for seasonal storage of solar energy: Characterization and modeling of a high density reactive bed. *Energy* 47 (1), pp. 553-563.

"This page intentionally left blank"

CHAPTER 4

Experimental study of the compression-assisted decomposition phase in the hybrid compression / thermochemical refrigeration system

4.1. INTRODUCTION AND OBJECTIVES

The simulations and parametric study carried out in Chapter 3 state that the hybrid system based on compression refrigeration and thermochemical storage is interesting for further study.

Moreover, the simulation model developed in Chapter 3 needs experimental validation before stating its reliability. This is especially true during the decomposition phase, in which the vapor compressor plays a major role.

Consequently, an experimental study followed the simulative study. A prototype was built to carry out the operation of a hybrid thermochemical/compression refrigeration system (HTCRS).

The main objectives of this experimental study are:

- To *prove the experimental feasibility* of the hybrid thermochemical/compression refrigeration system. In other words, prove that the operation of this system is viable, and that the presence of the compressor actually reduces the activation temperature.
- To *validate the quasi-steady simulation model* developed for this system and described in Chapter 3. To reach this objective, the results of selected experiments were compared to results obtained from simulations with the abovementioned model at the same operating conditions. This step included the calibration of the model's main parameters. The deviation of the simulation results with respect to the experimental results was quantified.
- To *study the behavior of this system* (especially inside the thermochemical reactor) during the decomposition phase. To meet this objective, thermocouples were used to obtain temperature profiles inside

the reactor. These temperature profiles will be analyzed to describe accurately the heat transfer and indirectly the mass transfer within the fixed bed during the reaction.

This chapter is a rather detailed description of the steps followed in this experimental study, from design to results. The most significant information is offered about the methodology followed (design, dimensioning, data treatment), the setup (components, main specs, operating modes) and commissioning (main and auxiliary procedures), and the results (analysis and model validation).

4.2. METHODOLOGY

The construction of this experimental setup involved several decisions and design choices. Some of them referred to the system's size, components, sensors, etc.: these are detailed in section 4.2.1.3, "Dimensioning". Other decisions referred to operating conditions (temperature and pressure levels): these are detailed in section 4.2.1.1, "Application".

4.2.1. System design

The setup presented in this Chapter was built during the elaboration of this doctoral thesis for the purpose of carrying out the experimental studies here described.

The design is a collaboration between the CREVER Group of Applied Thermal Engineering (from the Universitat Rovira i Virgili, Spain) and the PROMES laboratory (Procédés, Matériaux et Énergie Solaire) from Perpignan, France, linked to the Centre National de la Recherche Scientifique (CNRS, France) and the Université de Perpignan Via Domitia (UPVD, Perpignan, France).

The construction was done almost entirely (under the supervision of the Promes laboratory) at the Pilot Plant 2 of the Campus Sescelades (Avinguda dels Països Catalans 26, 43007 Tarragona, Spain), which belongs to the facilities of the CREVER Group at the Rovira i Virgili University. Nevertheless, the procedure to fill the thermochemical reactor with solid composite was carried out at the facilities of the PROMES laboratory.

Some of the components were already available at these facilities; other components are a contribution of the PROMES laboratory; and some of the components were acquired during the design phase.

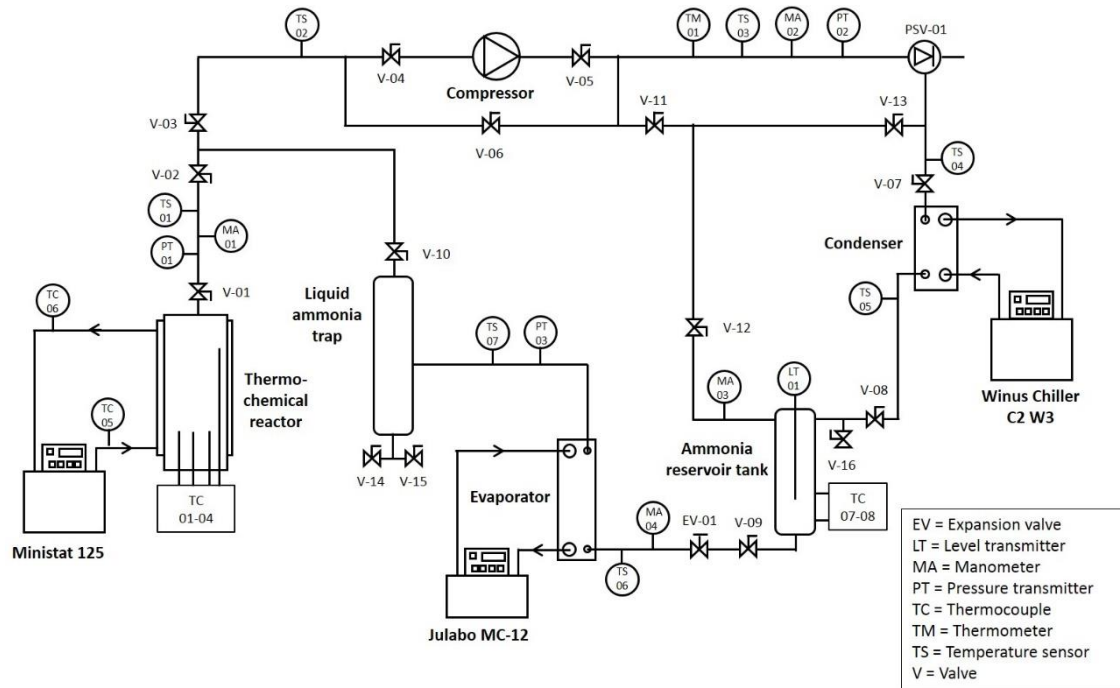


Figure 4.1. Flow diagram of the experimental setup of the hybrid thermochemical / compression refrigeration system.

4.2.1.1. Application

Thermochemical storage, as well as any other form of energy storage, exists with the purpose of covering a certain demand of useful effect (in this case, refrigeration) for a certain amount of time (which sets the autonomy of the system) when the energy source (in this case, solar energy) is not available.

Although our experiments did not focus on any particular case study, the aim was clearly to simulate the scenario of a refrigeration system driven by solar energy. Further, the idea is to propose a system that can operate with flat plate solar collectors. This decision sets a maximum value of about 100 °C for the heat source temperature (T_{hs}).

As for the temperature at which the cold is produced, the idea is to present a system for refrigeration rather than air conditioning. This usually implies the production of negative cold (temperatures below 0 °C), which discards the use of water as refrigerant. As discussed previously in this thesis, ammonia is one of the best choices for cold production at negative temperatures, and has several working pairs in thermochemical systems.

4.2.1.2. Working pair

In thermochemical systems based on reversible solid/gas reaction, each working pair has its own stoichiometry. This means that for a given mass of refrigerant, the mass of reactive salt varies from one pair to another, and the other way around.

Once the amount of refrigerant is set by the application (and any other decision criteria that may apply), the amount of reactive salt is calculated through the stoichiometry.

In thermochemical systems, the ammonia/barium chloride working pair has been studied experimentally and is well known to deliver the highest COP values.

4.2.1.3. Dimensioning

The dimensioning of the system started by deciding the amount of ammonia to be contained in it.

A SS316 vessel was already available to be used as reservoir tank for liquid ammonia. Further, a capacitive sensor was already available for measuring and recording the level of liquid inside the tank. Therefore, the maximum capacity of the reservoir tank, as well as the minimum and maximum level that the sensor can register, were two constraints to be taken into account while deciding the mass of ammonia in the system.

Two additional restraints existed for the maximum amount of ammonia in the system. First, according to the Spanish regulations [1], a pressurized vessel charged with ammonia may contain up to 5 kg of this substance without requiring special (i.e. costly and time-consuming) regulations. Second, the product between the total volume of the setup and its maximum operating pressure must be equal to or lower than 80000 atm/L, if no special regulations are to be fulfilled [1].

These two constraints set the design of the setup to a rather small-size machine. Since small scale experiments usually yield similar results to big-scale experiments, and given that the main objective of this study is to investigate the feasibility and behavior of the system regardless of its size, the design was adapted to these regulations.

With all considerations explained above, a final value of 2 kg of ammonia in the system was selected. Having fixed the value of this design variable, the required number of moles of barium chloride salt (n_{BaCl_2}), and therefore the

total mass of this salt (m_{BaCl_2}) inside the reactor for the full reaction to take place is calculated through the reaction's stoichiometry as shown in eq. 4.1.

$$m_{BaCl_2} = \frac{m_{NH_3}/M_{NH_3}}{\nu \cdot \Delta X} \cdot M_{BaCl_2} \quad (4.1)$$

ΔX represents the total variation in the reaction's advancement degree (X), being the value of X comprised between $X = 1.0$ (salt fully charged with ammonia) and $X = 0.0$ (salt fully discharged). $\Delta X = 0.8$ is a reasonable and realistic assumption for thermochemical systems that have gone through several cycles. The stoichiometric coefficient ν has been introduced by equation 2.1 and its value depends on the reaction.

According to calculations, a mass of barium chloride of 3,821 kg corresponds to a full reaction with the 2 kg of ammonia that had previously been fixed.

Since the thermochemical system is monovariant, when either the temperature or the pressure of the reactor is set, the other is automatically fixed. Thus, knowing the activation temperature (T_R), the reactor's pressure (P_R) was calculated. This pressure corresponds to the compressor aspiration pressure as well. The temperature of the ammonia gas at the suction ($T_{NH_3,suc}$) is lower than its temperature inside the reactor, due to heat dissipation.

The definition of the compressor's isentropic efficiency (η_{Comp}) can be used to estimate the properties of the ammonia gas at the compressor outlet (eq. 4.2).

$$\eta = \frac{h_{2s} - h_1}{h_2 - h_1} \quad (4.2)$$

With h_1 and h_2 the enthalpy of ammonia gas at the inlet and outlet of the compressor, respectively, and h_{2s} the enthalpy of ammonia gas at the compressor outlet assuming isentropic compression.

The temperature of ammonia gas at the compressor outlet (T_{out,NH_3}^{comp}) depends mainly on the pressure ratio (P_R). The inlet pressure (P_{in}^{comp}) depends directly on the temperature inside the reactor (T_R), and the outlet pressure (P_{out}^{comp}) depends directly on the temperature of the ammonia inside the condenser (T_{Cond}).

The compressor discharge temperature should be below an acceptable limit (i.e. less than 120 °C, for material resistance issues) in most of the operating conditions considered here. No serious issues related to high discharge temperatures are expected during the real operation of the setup.

The maximum mass flow of ammonia gas ($\dot{m}_{NH_3,max}$) can be calculated through eq. 4.3.

$$\dot{m}_{NH_3,max} = \dot{V}_{NH_3,max} \cdot \rho_{disch}^{NH_3(g)}(T_{disch}^{NH_3(g)}, P_{disch}^{NH_3(g)}) \quad (4.3)$$

Where $\dot{V}_{NH_3,max}$ is the maximum volumetric flow of ammonia at the compressor's discharge, which is given by the manufacturer, $\rho_{disch}^{NH_3(g)}$ is the density of ammonia gas at the compressor's discharge, calculated as a function of its pressure ($P_{disch}^{NH_3(g)}$) and temperature ($T_{disch}^{NH_3(g)}$).

For the reasons stated above about the monovariant reaction, the ammonia flow displaced by the compressor during the experiments depends ultimately on two design variables: the reactor temperature and the condenser temperature during the decomposition phase.

Once the ammonia mass flow is known as a function of the compression ratio, the expected duration of the experiment (Δt_R) is straightforwardly calculated (eq. 4.4).

$$\Delta t_R = \frac{m_{NH_3}}{\dot{m}_{NH_3}} \quad (4.4)$$

Experiment durations of about 4 hours were targeted. This duration meets a compromise between solid acquisition of data and an acceptable number of experiments.

The estimated required heating power of thermal bath TB-01 is related to the ammonia gas flow through the enthalpy of reaction, as shown in eq. (4.5).

$$\dot{Q}_{TB1} = \frac{\dot{m}_{NH_3}}{MW_{NH_3}} \cdot \Delta h_r \quad (4.5)$$

Table 4.1. Minimum and maximum values of several design variables for experimental setup dimensioning.

T_R	Δt	m_{NH_3}	m_{BaCl_2}	Q_{TB}
$^{\circ}C$	h	kg	kg	kW
40	2.5	0.36	0.69	0.90
85	5.5	9.99	19.08	12.46

Table 4.2. Max/min values of main reaction-related design parameters.

Variable	Min.	Max.	Units
Energy density (D_e)	50	250	kWh/m ³
Apparent density of ENG ($\rho_{app,GNE}$)	80	200	kg/m ³
Reactor temperature during decomposition phase (T_{RD})	40	85	$^{\circ}C$
Reactor temperature during synthesis phase (T_{RS})	5	15	$^{\circ}C$
Expected experiment duration (Δt)	2.5	5.5	h

4.2.2. Experimental design

The experiments must be as representative of real operation scenarios as possible. As stated above, the design of this setup depended on some restrictions.

From the point of view of the compressor, the two pressure levels (reactor pressure –low pressure- and condenser pressure –high pressure-) are important values. The pressure ratio has an influence on the mass flow rate that the compressor can deliver: this affects the duration of the experiment and may affect the control of the aspiration pressure.

As stated in previous chapters, thermochemical systems are defined as monovariant, meaning that when either the pressure or the temperature is fixed, the other one is automatically fixed. Therefore, a range of activation temperatures are covered in the experiments, in order to cover a certain range of pressures. This means that the reactor temperature (T_R) is one of the design variable in the experiments, and this temperature is controlled through the set point temperature of the thermal bath (T_{TB1}) that is connected to the reactor's jacket, that is, the "*Ministat 125*".

As for the pressure at the condenser (P_{COND}), each pressure corresponds to one unique equilibrium temperature in pure substances. Since the refrigerant is pure ammonia, controlling the condensation temperature (T_{COND}) is enough to control the pressure inside the condenser, and consequently, the discharge pressure at the compressor. This temperature is controlled through the set point temperature of the thermal bath that is connected to the condenser (T_{TB2}), that is, the "*Winus C2-W3*".

Table 4.3 shows a list of all experiments carried out within the frame of this doctoral thesis.

4.2.3. Data treatment

The main information to be derived from the experimental data obtained in this study is:

- **Advancement degree (X) vs time (t) curves** of reaction from each experiment.
- **Temperature (T) vs time (t) profiles** at several points inside the solid reactive composite.
- **Coefficient Of Performance (COP)** in each experiment.

- **Maximum and average Specific Cooling Power (SCP)** in each experiment.
- **X-t curves** indicate whether or not full reaction is achieved and in how much time. Further, the derivate function of these curves (dX/dt) provides useful information about the system kinetics, and assists in comparing whether or not the process with compressor is faster or slower than the process without compressor.

Table 4.3. List of experiments carried out and their operating conditions.

#	Experiment	Date	P_c	$T_{eq,NH_3} (P_c)$	$T_{eq,R} (P_c)$	T_c	ΔT_{eq}	P_{cond}
			bar	°C	°C	°C	°C	bar
S1	Synthesis	25/05/2017	3.5	-5.4	29.8	5.0	-24.8	-
D1	Decomposition	02/06/2017	7.2	14.6	45.0	68.0	+23.0	7.2
S1	Synthesis	05/06/2017	3.5	-5.4	29.8	5.0	-24.8	-
D2	Decomposition	07/06/2017	7.2	14.6	45.0	68.0	+23.0	7.2
S3	Synthesis	08/06/2017	3.5	-5.4	29.8	5.0	-24.8	-
D3	Decomposition	12/06/2017	7.2	14.6	45.0	68.0	+23.0	7.2
S4	Synthesis	14/06/2017	3.5	-5.4	29.8	9.0	-20.8	-
D4	Decomposition	15/06/2017	3.5	-5.4	29.8	40.0	+10.2	3.5
S5	Synthesis	22/06/2017	5.0	4.1	37.1	5.0	-32.1	-
D5	Decomposition*	26/06/2017	1.0	-33.6	6.7	50.0*	+43.3	5.0
S6	Synthesis	28/06/2017	5.0	4.1	37.1	9.0	-28.1	-
D6	Decomposition	05/07/2017	5.0	4.1	37.1	80.0	+42.9	5.0
S7	Synthesis	06/07/2017	5.0	4.1	37.1	9.0	-28.1	-
D7	Decomposition*	14/07/2017	1.0	-33.6	6.7	50.0	+43.3	3.7
S8	Synthesis	17/07/2017	4.0	-1.9	32.5	9.0	-23.5	-
D8	Decomposition*	18/07/2017	1.0	-33.6	6.7	50.0	+43.3	4.4

These curves are easily obtained if the mass of ammonia inside the solid composite is known at several moments during the experimentation. However, it is not obvious to know this mass. Instead, it is easier to know how much mass of ammonia enters or leaves the reactor.

In this study, this measurement relies on the level transmitter placed inside the reservoir tank of liquid ammonia. This measuring device reads the level of liquid inside the tank with acceptable accuracy. With proper calibration, the total volume of ammonia can be derived from the level. Then, a simple calculation with the density converts the volume into mass. To know the density of ammonia at every moment inside the tank, two thermocouples were used at different heights of the tank.

T-t profiles are useful in knowing the thermal behavior of the solid composite during the reaction progress. The variations in temperature inside the composite are directly linked to variations in pressure, given the

monovariant nature of the thermochemical process. This relation will be illustrated later on in this Chapter. They also help in knowing whether or not mass transfer is limiting. Also, these profiles would be quite useful in validating the quasi-steady model developed for this system in Chapter 3.

The production of these temperature profiles is straightforward in these experiments, since 4 thermocouples were introduced inside the solid composite at different radial positions. A simple plot of the readings from these thermocouples offers any information that is needed.

4.3. SETUP DESCRIPTION

The setup described in this chapter is relatively small-sized. With proper valve manipulation, it allows to carry out experiments of the decomposition phase of the thermochemical system, or the synthesis phase, or to operate a compression refrigeration cycle continuously. As for the decomposition phase, it can be done either with solely thermal activation, or assisting the process with the compressor, which is the novelty of this study.

4.3.1. Components

Fig 4.2 shows a picture of the setup before insulation. The setup is made up of: one thermochemical reactor (R-01); an electrically driven mechanical vapor compressor (C-01); a liquid ammonia storage reservoir (RS-01); two flat plate heat exchangers, one working as a condenser (CD-01) and the other one working as an evaporator (E-01); three thermal baths (TB-01 to TB-03); an indicator of liquid ammonia level inside the reservoir (LI-01); a set of valves (V-01 to V-15), and a set of temperature (T-01 to T-07) and pressure (P-01 to P-03) indicators, a pressure regulator used as expansion valve (EV-01), and a thermometer (TM-01).

For the sake of safety, the setup was permanently placed inside a protective chamber (Fig. 4.3). This chamber surrounds the whole setup (with the exception of the thermal baths) and protects any user from ammonia gas leakage.

The roof of this confinement chamber is equipped with a ventilator connected to an alarm.

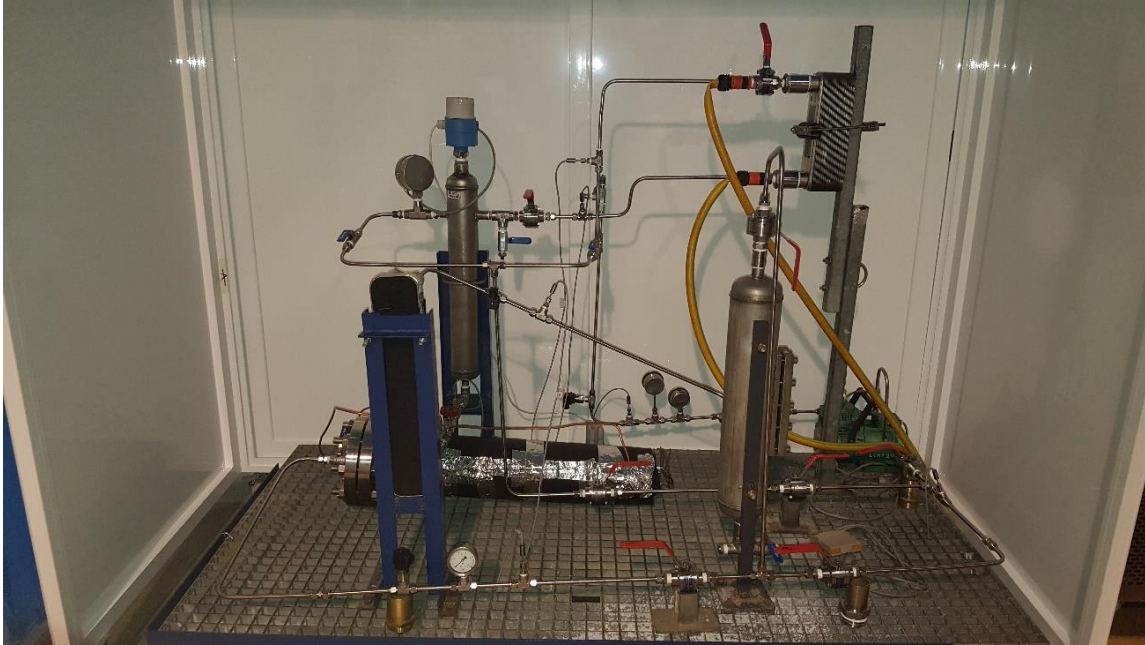


Figure 4.2. Picture of the experimental setup before insulation.

The setup allows experimentation using the compressor to activate the process, or experiments bypassing the compressor and activating the process thermally only.

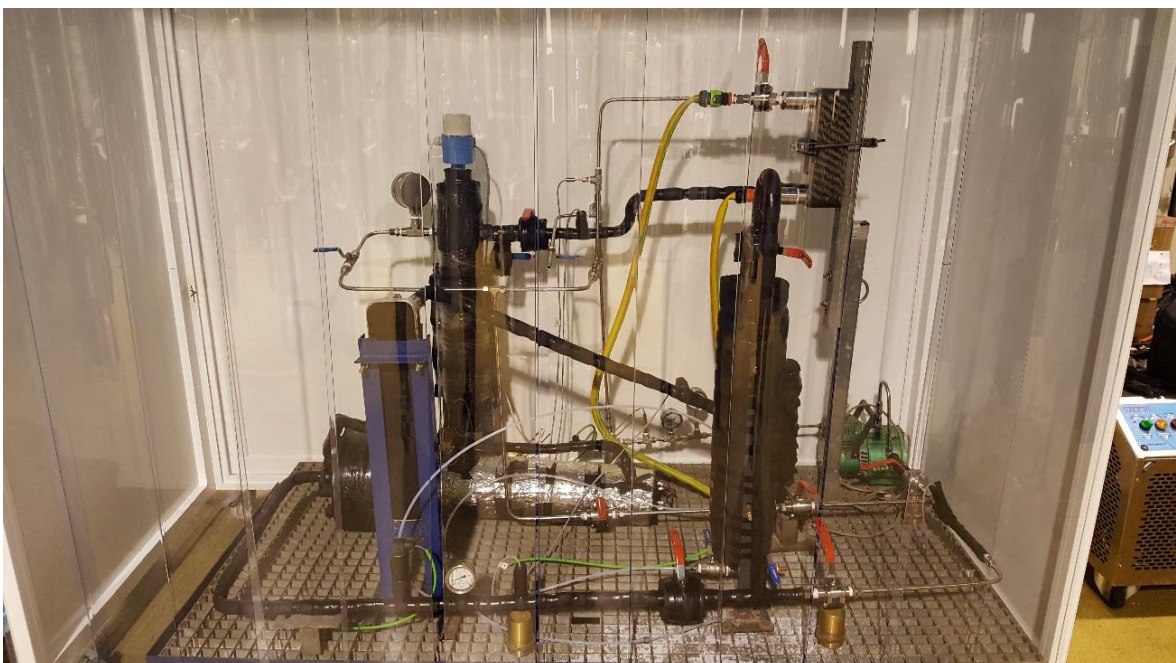


Figure 4.3. Picture of the experimental setup after insulation.

4.3.1.1 Thermochemical reactor

Fig 4.4 shows the diagram and picture of the thermochemical reactor used in the setup. This reactor is made out of stainless steel 316, to ensure its resistance to ammonia. It is an 800 mm-long cylinder with an internal diameter of 108.2 mm, with a flange at the top and a flat, 2 cm-thick bottom.

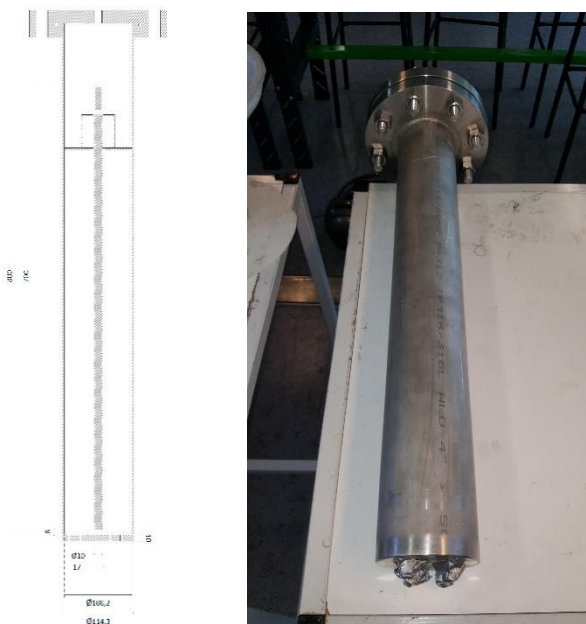


Figure 4.4. (a) Diagram of the thermochemical reactor; (b) Picture of the thermochemical reactor before thermal jacket and insulation.

The upper end is also flat, but its closing consists of a flange. The sealing of this flange is flat and made up of EPDM.

The bottom is flat and has four perforations to introduce thermocouples in the inside. A flat bottom was preferred over a curved one to facilitate the introduction of the thermocouples.

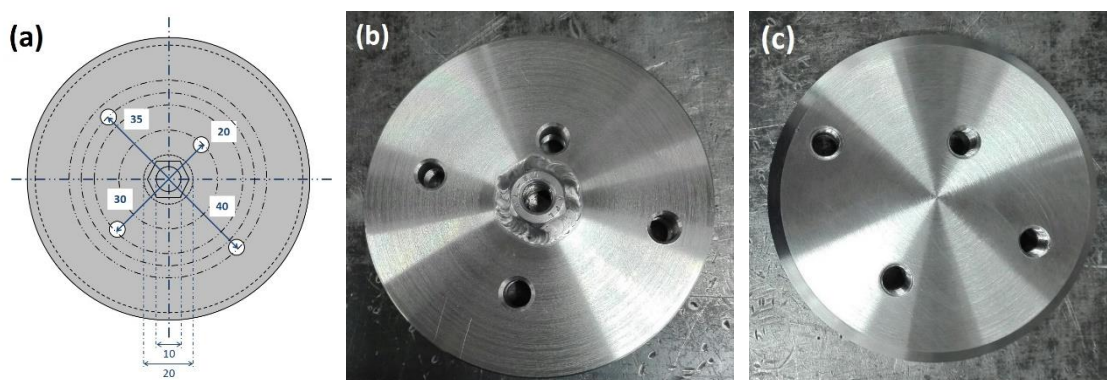


Figure 4.5. (a) Diagram of the reactor's bottom (dimensions in mm); (b) Reactor's bottom (inner part with welded nut); (c) Reactor's bottom (outer part).

Inside the reactor, there is a threaded rod made of stainless steel. This rod has a diameter of 10 mm and is 640 mm long, and it is screwed into a 10 mm-deep perforation within the reactor's bottom. To allow for better stability of this rod, a screw of the same diameter is welded to the reactor's bottom, so the rod is screwed through about 12 mm of screw plus 10 mm of perforation at the bottom.

A disc made of stainless steel 316 is screwed at the upper part of the threaded rod (Fig. 4.6a). The function of this disc is to confine the reactive composite inside the reactor.

As stated previously, the thermochemical reaction needs to exchange heat with an external source. For this experimental study, this is done with the circulation of a heat transfer fluid through a thermal jacket placed in the outside of the reactor. This jacket consists of a copper tube rolled up around the reactor's external surface, as shown in Fig. 4.7a. The tube has an external diameter of 6 mm, and around 35 meters of this tube were used to complete the thermal jacket around the reactor. A conductive paste was introduced between the tube and the outer wall of the reactor to improve as well as possible the heat transfer.

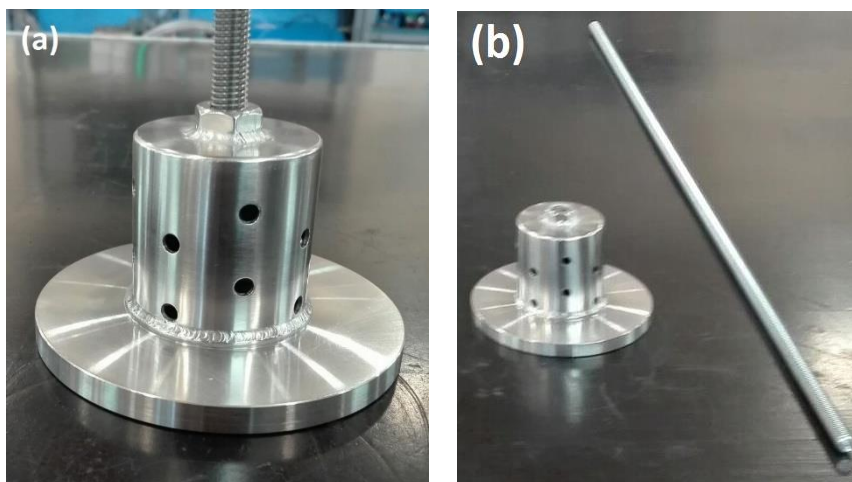


Figure 4.6. (a) SS316 confinement disc screwed into the SS316 threaded rod; (b) SS316 confine disc and full-length SS316 threaded rod.

The inlet and outlet of this jacket are connected to a thermal bath that provides either heat or cold to the heat transfer fluid, depending on whether the exothermic or the endothermic reaction takes place.

4.3.1.2 Solid composite

Inside the reactor there is a solid composite made up of a salt and an inert material which acts as a heat transfer enhancer. Inside the reactors there are also three thermocouples, to obtain a temperature profile of the solid composite during the reaction progress.

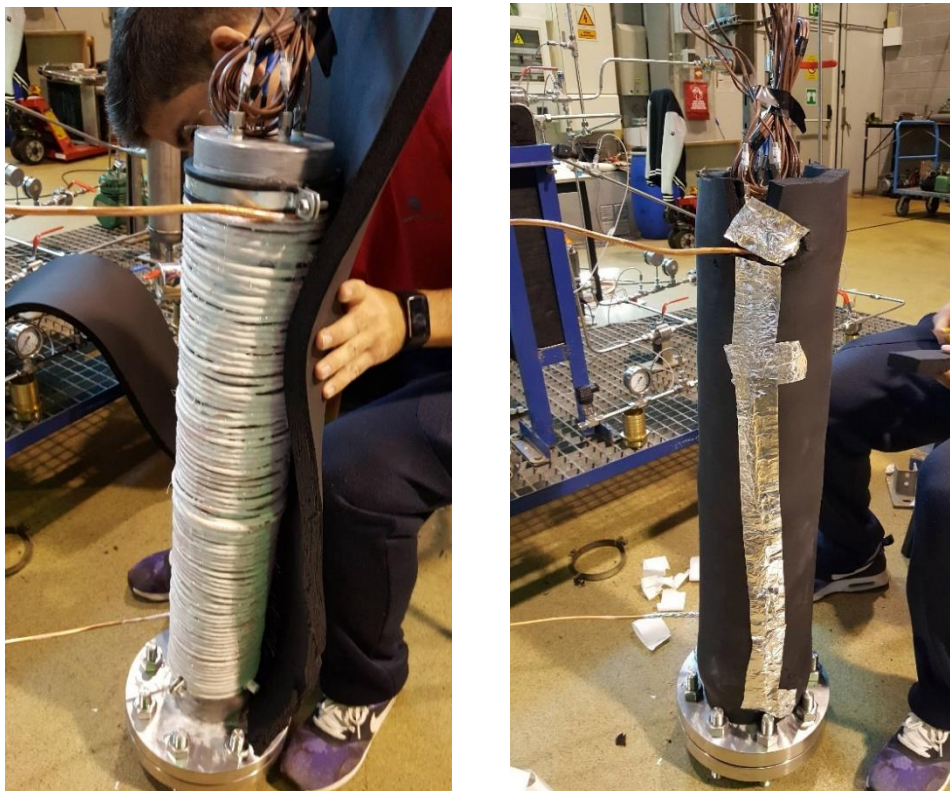


Figure 4.7. (a) Reactor's thermal jacket under construction; (b) Reactor's thermal jacket after construction.

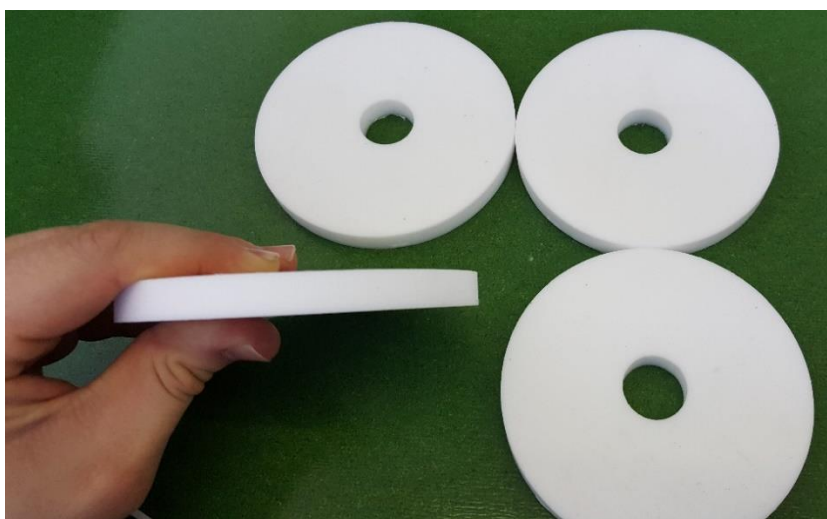


Figure 4.8. Teflon disks for thermal confinement of the solid composite.

In addition, there is a fourth thermocouple, placed in a different depth into the composite. The objective of this fourth thermocouple is to obtain temperature readings from a different length of immersion, which can be later compared with the other thermocouples to see whether or not there longitudinal heat transfer inside the reactor.

4.3.1.3 Vapor compressor

As discussed in the previous chapter, the compressor must be oil-free. As a consequence, a membrane compressor was selected for this experimental setup. Its most relevant specifications are provided in Fig. 4.9b.

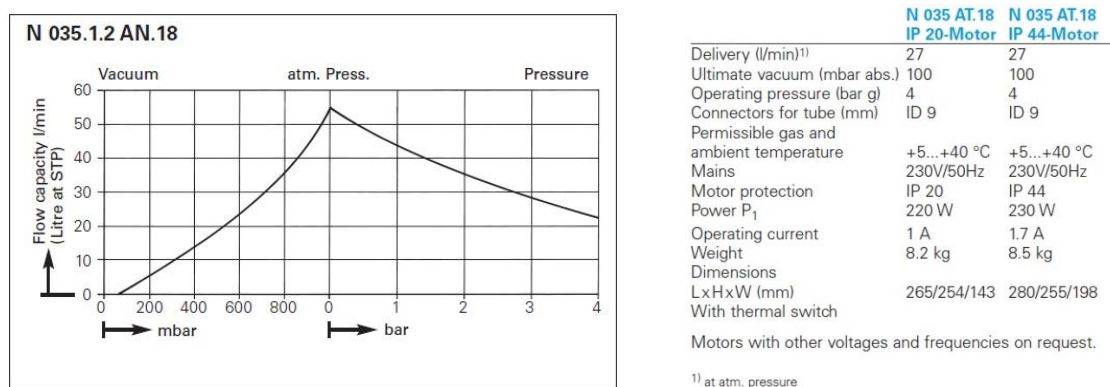


Figure 4.9. (a) Compressor's characteristic curve [2]; (b) Compressor's technical specifications [2].

4.3.1.4 Ammonia reservoir tank and level indicator

The reservoir tank contains liquid ammonia during the decomposition and synthesis phases, as well as the periods between the end of a decomposition experiment and the beginning of the next synthesis experiment.

The importance of this component lies on the fact that it determines the maximum amount of ammonia that the setup can contain. Whereas the thermochemical reactor was especially designed and dimensioned for this setup, the vessel that is used as ammonia reservoir tank was an already available component. For this reason, the calculation of the minimum and maximum mass of barium chloride salt inside the thermochemical reactor revolved around the capacity of the reservoir tank.

The reservoir tank is made out of stainless steel 316 and has a total capacity of 4 L. It is provided four openings: in the upper end, it has a 3/4" threaded connection for the level indicator; about 200 mm under the upper connection, it has two lateral 1/2" connections, one at each side; and at the bottom it has another 1/2" connection, which is used as outlet of liquid ammonia.

The level indicator is a capacitive sensor of liquid ammonia [3]. It is introduced to the reservoir tank through the upper connection.

4.3.1.5 Condenser and evaporator

Two flat plate heat exchangers were used as condenser and evaporator in this setup. These two components were already available at the facilities from the CREVER research group at the Universitat Rovira i Virgili. The manufacturer is Alfa Laval [4]. Both heat exchangers are oversized with respect to the need of the setup.

The condenser has two ½" threaded connections internally connected between them, and two ¾" threaded connections also internally connected between them. The ½" connections were used for the SS316 tube carrying ammonia, while the ¾" connections were used for the hose carrying the working fluid from the external bath "Winus C2-W3". The connections were done so that the condenser operates in counter flow.

The evaporator has two ½" threaded connections internally connected between them, and two 1" threaded connections also internally connected between them. As done in the case of the condenser, the ½" connections were used for the SS316 tube carrying ammonia, while the 1" connections were used for a hose coming from the external thermal bath "Julabo MC12". Similarly to the case of the condenser, the connections were done so that the evaporator operates in counter flow.

4.3.1.6 Thermal baths

A total of three thermal baths are connected to the setup through external connections.

The thermal bath named "Ministat 125" is connected to the external jacket from the thermochemical reactor. The manufacturer is Huber, and according to the specs, this bath has a maximum heating power of 1 kW at a maximum delivery temperature of 150 °C, and a maximum cooling power of 300 W at 20 °C [5].

The thermal bath named "Julabo MC12" is connected to the evaporator. Its manufacturer is Julabo, and according to the specs, it provides heating with a maximum power of 1000 W (it does not provide cooling) [6].

The thermal bath named "Winus C2-W3" is connected to the condenser. This bath provides cooling with a maximum power of 1.5 kW, and does not provide heating [7]. The temperature at which the cold is delivered depends on the

working fluid. For this study, a glycol/water refrigerant with a 20 % of glycol was used. This refrigerant has a freezing point of $-9\text{ }^{\circ}\text{C}$.

From the three thermal baths available for this study, the “Ministat 125” is the only one that has both heating and cooling functions. Moreover, the thermochemical reactor needs heat during the decomposition phase, while it needs to be cooled down during the synthesis phase. These two circumstances made the “Ministat 125” the best choice of thermal bath for the reactor even if its cooling power may be limiting for the process during the synthesis reaction (exothermic).

Otherwise, a circuit with several valves would have been necessary, creating a “hose network” to allow to choose which bath to connect to which component. This option was discarded for the sake of simplicity.

4.3.1.7 Data acquisition unit

A data logger from Agilent® (model 34901A) was used as data acquisition unit [8]. This unit admits up to 3 multiplexers, although only two of them were used for the experiments. These are 20-channel multiplexer (2/4-wire) modules from Keysight®. Each one of the two multiplexers has 18 connections for voltage signal, and 2 connections for intensity signal.

The first multiplexer receives voltage signals from all thermocouples (a total of 8 signals), plus intensity signals from 2 pressure sensors. The second multiplexer receives voltage signals from all PT-100 sensors (a total of 7 signals), 1 intensity signal from the remaining pressure sensor, and 1 intensity signal from the level sensor. The unit includes a software to collect all the data on a computer.

4.3.1.8 Other components

In addition to the main components, the system has several measurement devices and several valves to facilitate the transition from one operation mode to another (see Fig 4.1 for their localization in the experimental device).

As for temperature measurement, type T thermocouples were used inside the thermochemical reactor (TC-01 to TC-04), at the inlet (TC-05) and outlet (TC-06) of the heat transfer fluid from the reactor’s thermal jacket, and at mid-height (T-07) and the bottom (TC-08) of the ammonia reservoir tank.

For the rest of the setup, PT-100 sensors were used at: the reactor outlet (T-01); the compressor inlet (T-02) and outlet (T-03); the condenser inlet (T-04) and outlet (T-05); the evaporator inlet (T-06) and outlet (T-07). In addition, a

thermometer was placed at the compressor outlet, to monitor the temperature of the ammonia gas after the compressor.

For pressure measurement and recording, four manometers (MA-01 to MA-04) and three pressure sensors (P-01 to P-03) are used.

Sensor P-01 is used to record the pressure in the reactor (by keeping valve V-01 open and valve V-02 closed). Sensor P-02 records the pressure at the compressor outlet, and sensor P-03 records the evaporator pressure during the synthesis phase.

Manometer MA-01 is used to keep track of the reactor's pressure. This is especially important during the decomposition phase when not assisted with the compressor, since the activation temperatures are higher and the operating pressure may be relatively high before initiating the process. Manometer MA-02 is useful to monitor the pressure at the compressor outlet. Manometer MA-03 allows to know at any time the pressure inside the reservoir tank. This is especially important when the setup is not operating and the reservoir tank reaches ambient temperature. Finally, manometer MA-04 is highly useful during the synthesis phase. This manometer helps to keep track of the pressure at the outlet of the expansion device while manually regulating it at the beginning of the experiments.

Several floating ball valves were appropriately placed to enable a quick switch from one operation mode to another. Valve V-01 is placed at the reactor inlet/outlet channel, and its importance is notable. This valve allows to retain the ammonia inside the reactor while increasing the reactor's temperature, or simply while switching operation modes.

Valves V-02, V-03 and V-10 allow to differentiate between the decomposition phase (where V-02 and V-03 are open and V-10 is closed) and the synthesis phase (where V-02 and V-10 are open while V-03 is closed).

Valves V-04, V-05 and V-06 allow to differentiate between the compressor-assisted decomposition phase (where V-06 remains closed and V-04 and V-05 are open) and a decomposition phase driven by thermal energy only, without the compressor (where valves V-04 and V-05 remain closed and V-06 stays open).

Valve V-07 allows to separate the system between the decomposition / compression segment and the condensation / storage segment. This is important in some cases where, due to operational reasons, it is required to reduce the temperature (or consequently, the pressure) of the liquid ammonia inside the reservoir tank, without varying the pressure at the remaining parts of the setup.

This valve is also useful while charging ammonia into the system, since ammonia charges are done by introducing ammonia gas and condensing it. Especially at the end of this procedure, closing valve V-07 is important to keep the condenser from condensing more ammonia into the tank or reducing the system's pressure.

Valves V-08, V-09 and V-12 confine the liquid ammonia inside the reservoir tank. This is highly important at any time in the setup, since there is always liquid ammonia inside the reservoir tank. It mainly contains just a small amount (when the reactive salt is fully charged with ammonia after the synthesis phase), or it may be close to its full capacity (when the reactive salt is fully discharged after finishing the decomposition phase).

Valve V-DE consists of a pressure regulator, which is used as an expansion device for the cycle. Its maximum output pressure is 7 bar.

Valves V-11 and V-13 allow, along with valve V-12, to equilibrate the pressure between the reservoir tank and the condenser, or between the compressor's inlet and outlet, if needed. Valves V-14 and V-15 were placed to facilitate the procedures of making vacuum in the setup and charging ammonia into it. These valves can also help evacuate some liquid ammonia that may be retained inside the liquid trap. Finally, valve V-16 was used during the procedure of leak testing. In addition, this valve allows to directly charge liquid ammonia into the reservoir, if this procedure is needed.

Some of the valves are unidirectional, which helps protect some important parts of the setup. The sealing of these unidirectional valves is made out of EPDM.

4.3.2. Main operating modes and procedures

4.3.2.1. Compression-assisted decomposition phase

The decomposition phase in the presence of the compressor is the most important operating mode in this setup, since all useful results for this study are obtained from this procedure.

The term "compression-assisted" refers to the fact that the decomposition phase is feasible without a compressor (that is, using thermal energy only). The compressor assists in reducing the operating pressure inside the reactor during the decomposition phase.

Fig. 4.10 depicts the decomposition phase on the setup's flow diagram. During this phase, the chemical bonds between the NH_3 and the BaCl_2 are

broken by supplying heat to the solid composite. For this purpose, the thermal bath “Ministat 125” supplies heat to the thermochemical reactor, increasing the temperature of the solid composite slightly above the equilibrium temperature.

Then, ammonia gas is rejected from the solid reactive bed. This ammonia gas enters the vapor compressor, which increases the pressure up to the condenser pressure. Given the presence of the compressor, the ammonia gas at the suction side is at a lower pressure than it would be in the absence of a compressor.

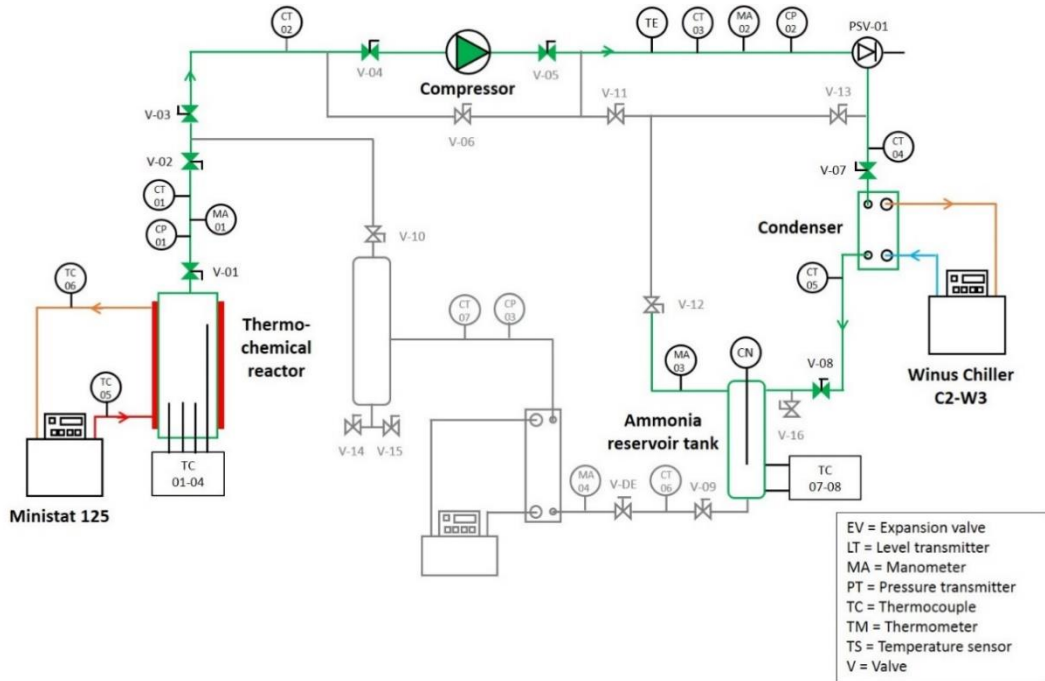


Figure 4.10. Flow diagram of the decomposition phase assisted with vapor compression.

After the compressor, the ammonia enters the condenser, where it changes from vapor phase to liquid phase, rejecting condensation heat. This heat is evacuated by the refrigerant connected to the thermal bath “Winus C2-W3”.

After condensing, the ammonia enters the reservoir tank, where it is stored until the synthesis phase is carried out. The increase in liquid level is recorded by the level sensor. Knowing the initial composition inside the reactor, and assuming that the liquid ammonia retained within the condenser is more or less constant during this phase, we can deduce the reaction advancement at any time.

4.3.2.2. Synthesis phase

The synthesis phase is the operation mode in which the system delivers the useful effect (i.e. production of cold). This cold is produced by the ammonia that is stored in liquid state inside the reservoir tank.

For this purpose, this ammonia is released from the tank and its pressure is reduced by means of the expansion valve EV-01. This expansion causes a small fraction of this liquid to vaporize and reduces the temperature of the ammonia, until approximately the temperature at which the cold must be delivered.

Then, after having vaporized inside the evaporator, the ammonia (now in gas phase) returns to the thermochemical reactor, where it reacts with the barium chloride salt in an exothermic reaction. The heat rejected by the reaction is evacuated by the heat transfer fluid that circulates through the reactor's jacket.

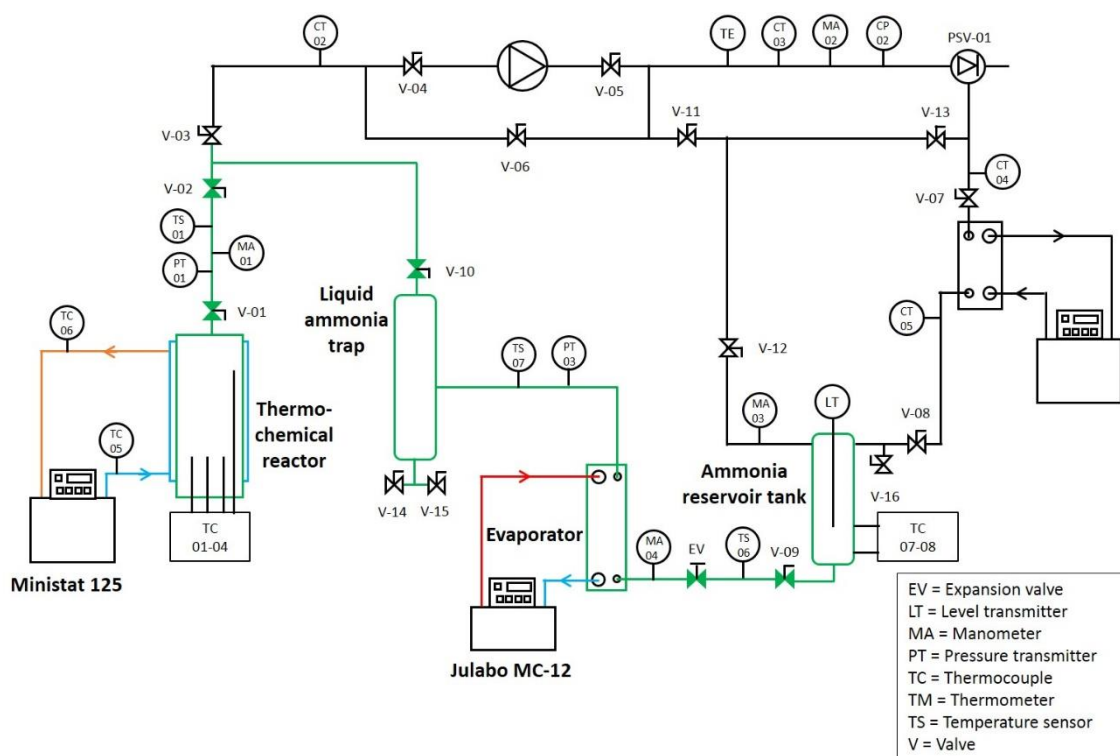


Figure 4.11. Flow diagram of the setup during the synthesis phase.

4.3.2.3. Non-assisted decomposition phase

One of the objectives of this study is to evaluate the advantages of using a compressor during the decomposition phase. This evaluation wouldn't be possible unless some decomposition phases without compressor are carried out.

More precisely, one of the objectives is to compare the temperatures inside the reactor (and their evolution) when using and not using the compressor.

Here, the term “thermal-only” is used just to note that other experiments with decomposition exist in which electrical energy is needed as well (due to the presence of the compressor).

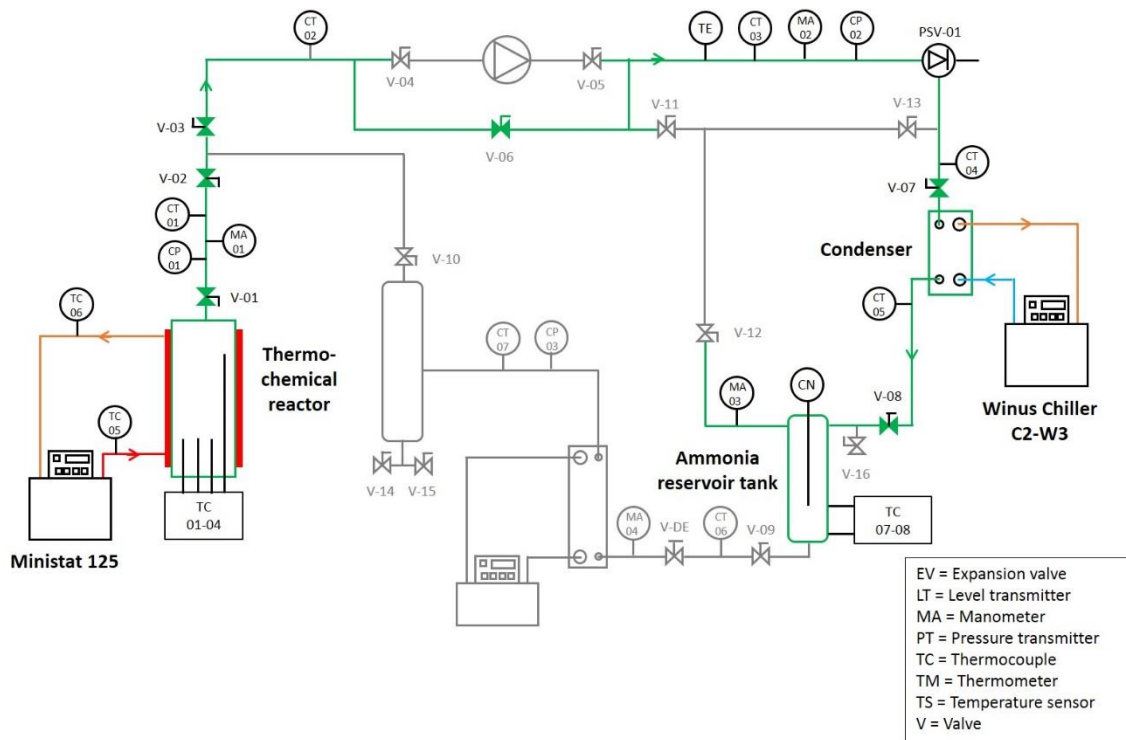


Figure 4.12. Flow diagram of the setup during the thermal-only decomposition phase.

4.3.2.4 Compression refrigeration subcycle (unused)

With adequate valve settings, this setup can operate as a conventional, continuous, compression refrigeration cycle.

Although this procedure does not provide, by itself, any advancement with respect to the state of the art, the possibility of carrying it out leaves some options open to the experimental testing of the hybrid compression / thermochemical refrigeration system.

With proper experiment design and procedure, the operation of the hybrid system could be simulated experimentally. For instance, the vapor compression subcycle would represent the operation of the global system in those periods in which the solar resource is enough to meet the demand of cold.

Then, at a given time, a heating of the thermochemical reactor, and the subsequent opening of valve V-02 would represent a period of surplus in the solar resource. The ammonia desorbed from the salt would be stored in the tank. Then, some minutes later, the thermochemical reactor could be cooled down, and the ammonia previously stored could be redirected to the reactor. This would represent those operation periods in which the solar resource is not enough to meet the demand, and the thermochemical storage is necessary to reach the production.

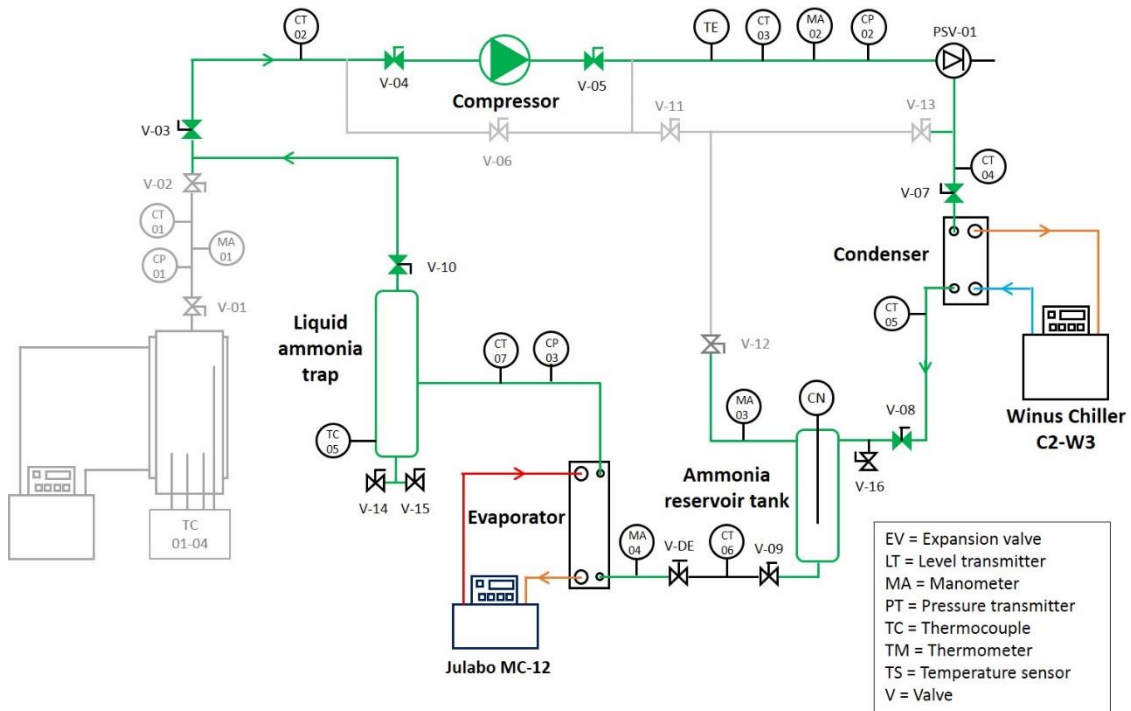


Figure 4.13. Flow diagram of the setup during operation of the compression refrigeration subcycle.

4.3.3. Auxiliary procedures

4.3.3.1. Sensor calibration

The PT100 temperature probes were calibrated by means of a calibrator and a reference probe. This procedure was also used to calculate the compensation for the deviation in the readings from the thermocouples.

The pressure transmitters were calibrated with respect to a reference transmitter, too.

The level transmitter was calibrated *in-situ* with water, previously to any charge of ammonia into the system.

4.3.3.2. *Leak tests*

The leak tests were performed by pressurizing the system up to 7 bar with air from the atmosphere with the help of an air compressor. These tests consisted of two main procedures. On the first stage, the bubble method was applied with soapy water to look for major-to-moderate leaks.

After solving these, minor leaks were found through another procedure. The system was pressurized (again up to 7 bar) and then, some valves were closed, dividing the setup into some segments, each one with a pressure transmitter. The pressure measured by each transmitter was written down and compared with the value registered by the same transmitter 24 hours later. All connections were re-checked in those segments with a 5% or higher decrease in pressure. The detailed procedure can be found in [9].

4.3.3.3. *Composite preparation and charge into the reactor*

The preparation of the solid reactive composite and its charge into the reactor is a specialized procedure that belongs to the expertise of the PROMES laboratory. Therefore, this procedure was carried out at their facilities during the 20th and 21st of February, 2017. The reactor was moved from Tarragona to Perpignan, and the substances (barium chloride salt and ENG) were provided by the PROMES laboratory. After finishing the procedure, the reactor (now charged) was moved back from Perpignan to Tarragona.

Previously to this procedure, the barium chloride salt was dehydrated inside an oven at high temperature.

Then, target values were set for the energy density (D_e) and the apparent density of the ENG (ρ_{app}^{ENG}). These values were 100 kWh/m³ and 100 kg/m³ respectively (referred to the volume of the solid composite). From here, a simple calculation gave the amount of BaCl₂ and ENG to be introduced in the reactor. These values were 1316.0 g and 536.0 g, respectively.

The ENG has the particularity of a great porosity, and as a consequence, a very small density at its powder state without constraint: 3.10 kg/m³. This value of density means that the abovementioned mass of ENG would occupy a volume of 0.173 m³. However, the reactor's useful capacity is $5.364 \cdot 10^{-3}$ m³. This implies that the targeted amount of ENG could not be introduced in the reactor in one unique step.

Further, there was another limiting condition: the capacity of the recipient used to carry the composite from the preparation table to the reactor. Its capacity was about $5 \cdot 10^{-3}$ m³, which means that a maximum of about 15.5 g of ENG could be carried at a time. Therefore, the reactive composite was charged

into the reactor in 40 steps, introducing 32.9 g of BaCl₂ and 13.4 g of ENG at every step.

Moreover, at every step the composite had to be compacted from its initial volume to a smaller volume, in order to reach the targeted D_e and the ρ_{app}^{GNE} . Since human force was not enough to attain this compacting, a specific tool was used. This was the most time-consuming circumstance of this procedure, and it was carried out carefully, in order to reach as much uniformity as possible in the solid composite.

In each step, the mass of BaCl₂ and GNE was weighted and noted down. At the end of the procedure, the D_e and the ρ_{app}^{GNE} were recalculated from the experimental measurements. The values were 105.4 kWh/m³ and 100.1 kg/m³ respectively, having a deviation of 5.4 % and 0.1 % with respect to the targeted values, which was considered acceptable.

4.3.3.4. Salt dehydration

The BaCl₂ was dehydrated again before charging any ammonia into the system. This procedure was necessary because during the preparation of the solid composite –which took long enough–, the salt was in contact with atmospheric air. This salt happens to be quite hygroscopic, and this contact with the air's humidity was enough for it to capture some water.

For this procedure, a vacuum pump was connected to the setup as shown in Fig. 4.14. There was also a trap surrounded with liquid nitrogen, in order to condensate any content of water suctioned by the pump. With the “Ministat 125” thermal bath, the reactor's temperature was increased to 80 °C. This temperature, in addition to the vacuum pump, was enough to dehydrate the salt within a few hours. A total of 10.5 g of water was retired.

To check if all water had been indeed retired from salt, valve V-01 was closed and reactor temperature was kept at 80 °C. Then, the pressure was monitored for a few hours to check whether or not there was an increase. This increase, if it appears, means there is still some water in the composite, since at the same temperature the vapor pressure of pure water is higher than that of water in equilibrium with the salt. This verification was done at 80 °C for the sake of time-saving (any pressure increase is noticeable sooner at higher temperatures).

4.3.3.5 Charge of ammonia

When the solid composite is introduced in the system for the first time, it is completely empty of ammonia (i.e. it is fully discharged). Thus, the first reaction to carry out is a synthesis.

As explained above in this Chapter, the ammonia for the synthesis reaction comes from the reservoir tank. This means that, before the first experiment, ammonia has to be charged in the system and stored in liquid phase inside the tank.

For this purpose, a bottle of ammonia was connected to the system through valve V-14. Ammonia gas was introduced in the system, condensed in the condenser, and finally stored in the reservoir tank.

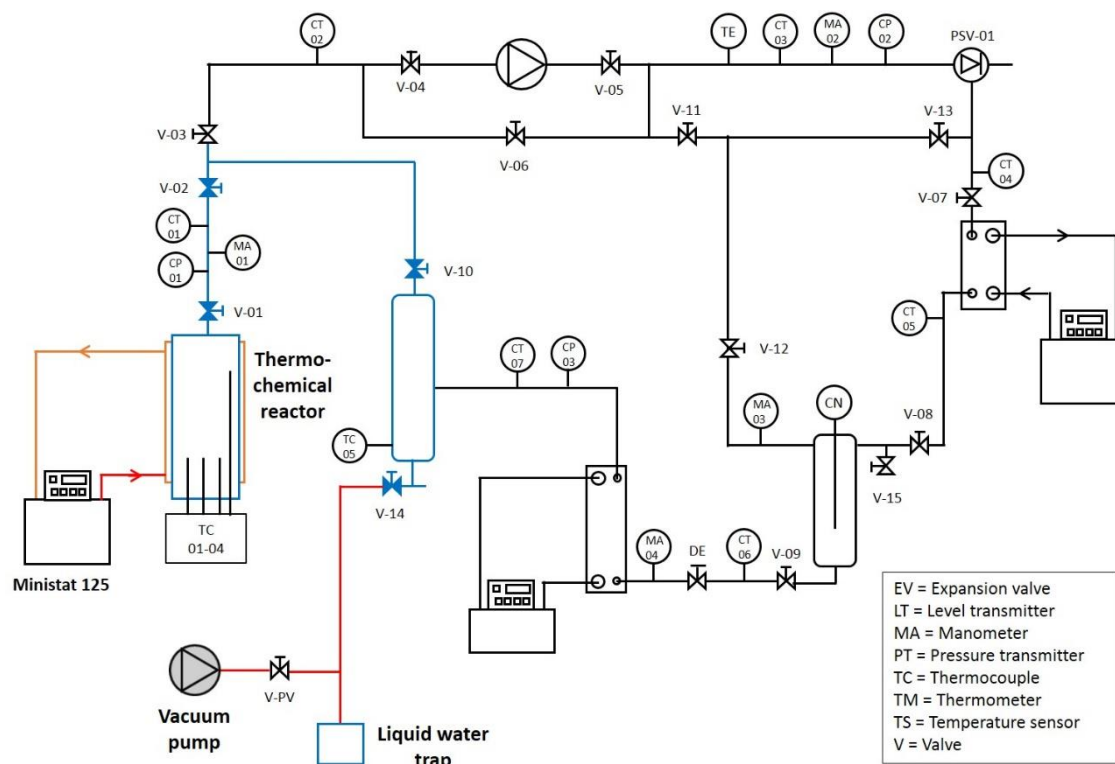


Figure 4.14. Flow diagram of the setup during the salt dehydration procedure.

The total mass of ammonia introduced was calculated from the readings of a weight scale under the bottle. This value was also compared with the readings of the level transmitter, to verify again that the calibration of this sensor was correct. The detailed procedure is described in [9].

4.4. RESULTS AND DISCUSSION

4.4.1. Analysis of results

Fig. 4.16 shows the most important data obtained from the first experiment with compression-assisted decomposition. This figure shows the evolution of the reactor and condenser pressures along the reaction. Also, this figure shows

the evolution of the temperatures recorded by the thermocouples inside the solid composite.

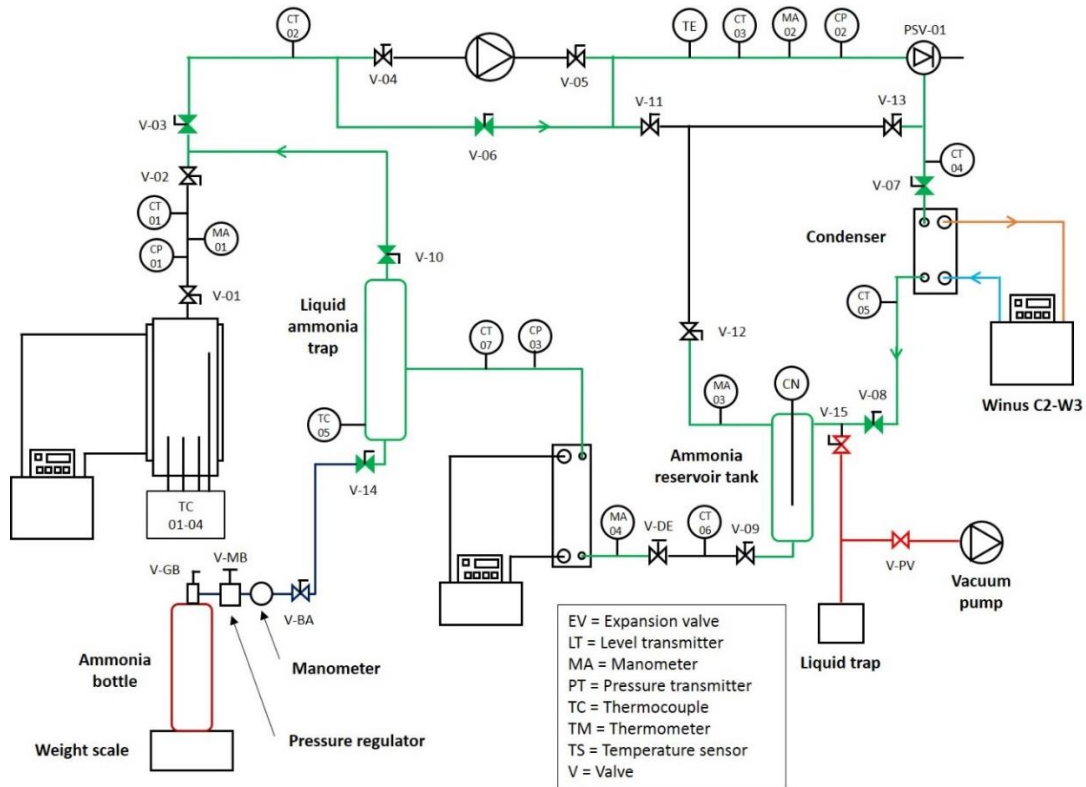


Figure 4.15. Flow diagram of the setup during the ammonia charge procedure.

As shown by Fig. 4.16, the pressure inside the reactor is around 5 bar before opening valve V-01. Then, this pressure drops quickly to around 1 bar due to the compressor. At the same time, reactor temperatures drop from 50 °C to 10 °C. After the first 10 minutes of experiment, the reactor pressure stays more or less constant (with no valve being manipulated) around 1 bar until the end of the reaction. This probably means that at these operating conditions, the suction pressure is self-regulated.

The condenser pressure remains constant during all the experiment with the exception of the first hour, but the variations in this first hour are caused by a change in the set point of the bath “Winus C2-W3”. This set temperature was slightly reduced to facilitate a lower pressure ratio at the compressor, which would allow a higher mass flow rate of ammonia to be compressed.

Fig. 4.17 shows the $X-t$ curve obtained for this experiment. Two main differences were noted in relation to other experiences with this setup. First, according to the data the reaction never reaches $X = 0.0$. As a matter of fact, it never reaches below $X = 0.3$ (assuming that it was at $X = 1.0$ at the beginning of the experience).

This lack of complete reaction may be caused by a wrong estimation of the number of moles of ammonia that were in the solid composite at the beginning of the experiment.

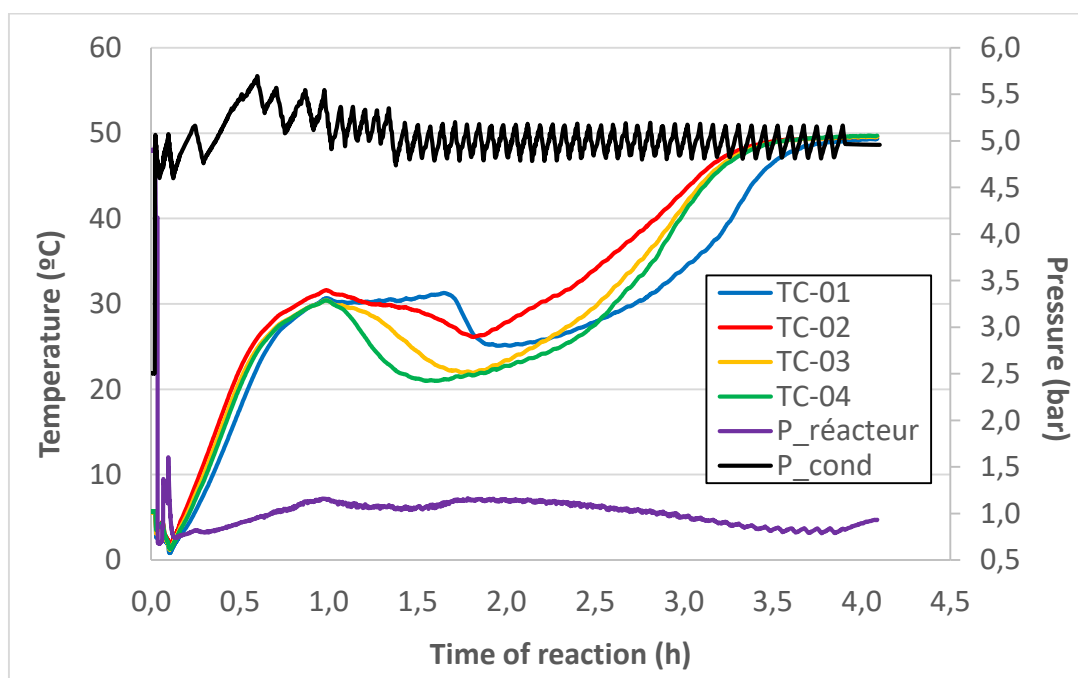


Figure 4.16. Pressure and temperature profiles of the first experience with compression-assisted decomposition.

The pressure and temperature readings from the second experiment with compression-assisted decomposition are shown in Fig. 4.18.

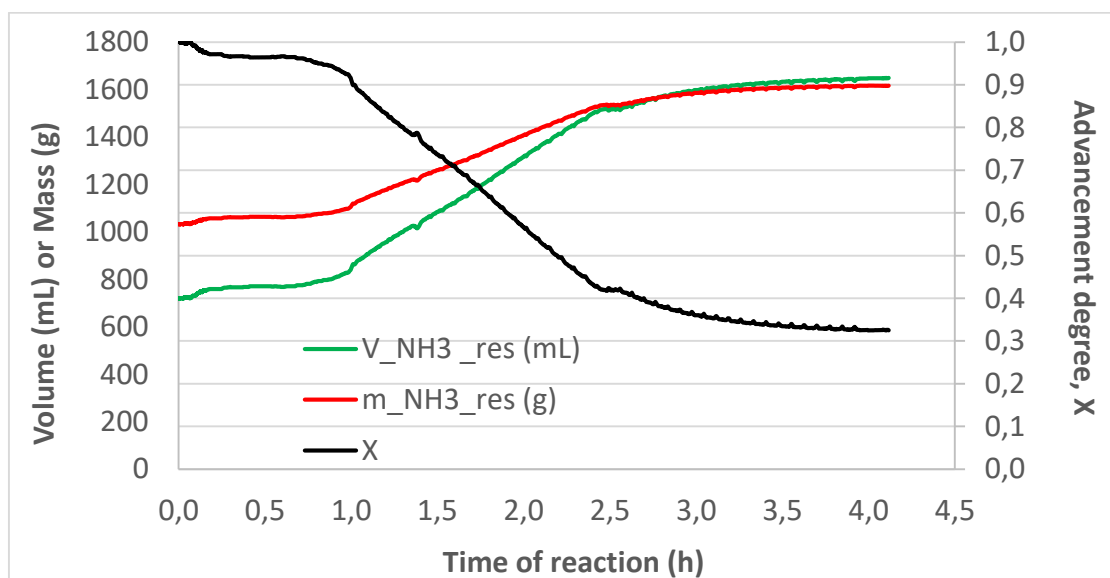


Figure 4.17. X-t curve obtained from the first experience with compression-assisted decomposition.

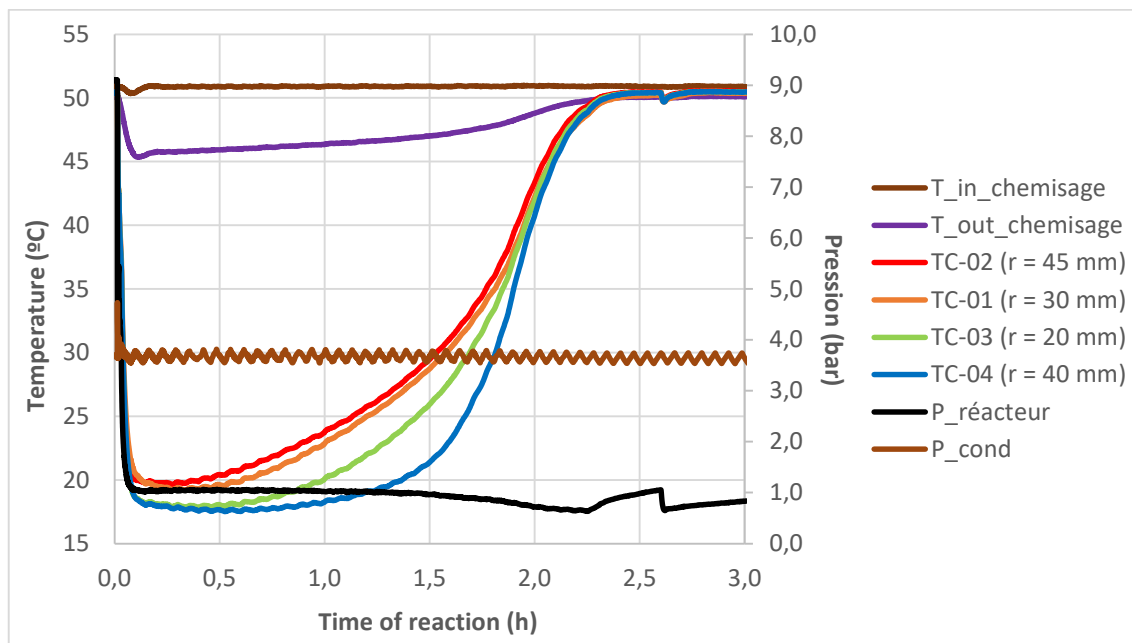


Figure 4.18. Pressure and temperature profiles of the second experience with compression-assisted decomposition.

In this second experience, the temperature inside the reactor was at its set point (50 °C) since the beginning. The initial phase of the experience shows a steep decrease in all four temperatures inside the solid composite, typical from the “adiabatic phase” (Fig. 4.19). Then, as the reaction progresses, these temperatures increase gradually and, after 2.5 hours of experiment approximately, they return to the initial temperature of 50 °C.

Again, the pressure inside the reactor (which corresponds to the suction pressure at the compressor) remains almost constant around 1 bar during all the experiment after the first few minutes. As it can be seen in the graph, this pressure was about 9 bar at the beginning of the experiment. Then, right after opening valve V-01, this pressure drops during the “adiabatic phase”.

The condenser pressure remains with a constant oscillation around 3.7 bar approximately, which corresponds to an equilibrium temperature of -4.5 °C for pure ammonia. This time, the set temperature of the thermal bath “Winus C2-W3” was kept constant, but the regulation of temperature is of ON/OFF type, that explains the pressure oscillation.

Fig. 4.18 also shows the inlet and outlet temperatures of the heat transfer fluid that circulates through the reactor’s thermal jacket. As seen in the figure, both temperature were around 50 °C before initiating the experiment. Then, upon the start of the reaction, the outlet temperature drops until almost 45 °C, and gradually increases back to its initial value during the remainder of the

experiment. This evolution is synchronized with that of the four temperatures inside the solid composite.

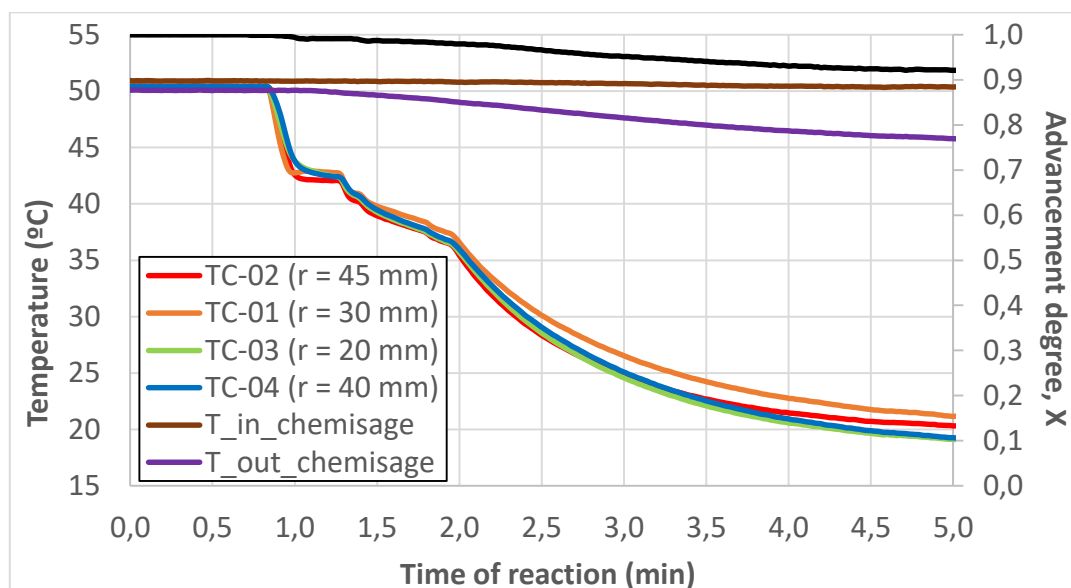


Figure 4.19. Pressure and temperature profiles during the first 5 minutes of the second experience with compression-assisted decomposition.

Fig. 4.20 shows the evolution of the reaction's advancement degree (X) and reactor pressure (right axis) with respect to reaction time for compression-assisted decomposition (experiment D5). For the sake of comparison, the figure also shows the $X-t$ curve from a non-assisted decomposition phase (experiment D6) with a very similar equilibrium drop to that of experiment D5 (see Table 4.3). The fact that in experiment D5 the same equilibrium drop as in experiment D6 was achieved with a lower heat source temperature (50 °C at D5 in front of 80 °C at D6) is noteworthy, since it arguably proves the interesting concept that is presented with the SHCTRS.

Fig. 4.21 can be seen as an 'historical record' of all experiments carried out in this study, in the form of a global $X-t$ curve (black line). This figure accounts for net reaction time only, neglecting the interludes between experiments. The evolution of mass of ammonia inside the reactor (calculated from level of liquid inside the storage tank) is also shown to reflect correspondence with the $X-t$ curve. The global $X-t$ curve plotted in this figure is based on the hypothesis that at the beginning of each experiment, the total mass of ammonia inside the thermochemical reactor equals the mass of ammonia calculated at the end of the immediately previous experiment. The fact that X reaches values above 1 proves that, for reasons that are currently being investigated, this hypothesis is not applicable, so all $X-t$ curves shown in this Chapter were 'normalized' ($X = 0$ at the beginning of each synthesis and $X = 1$ at the beginning of each decomposition).

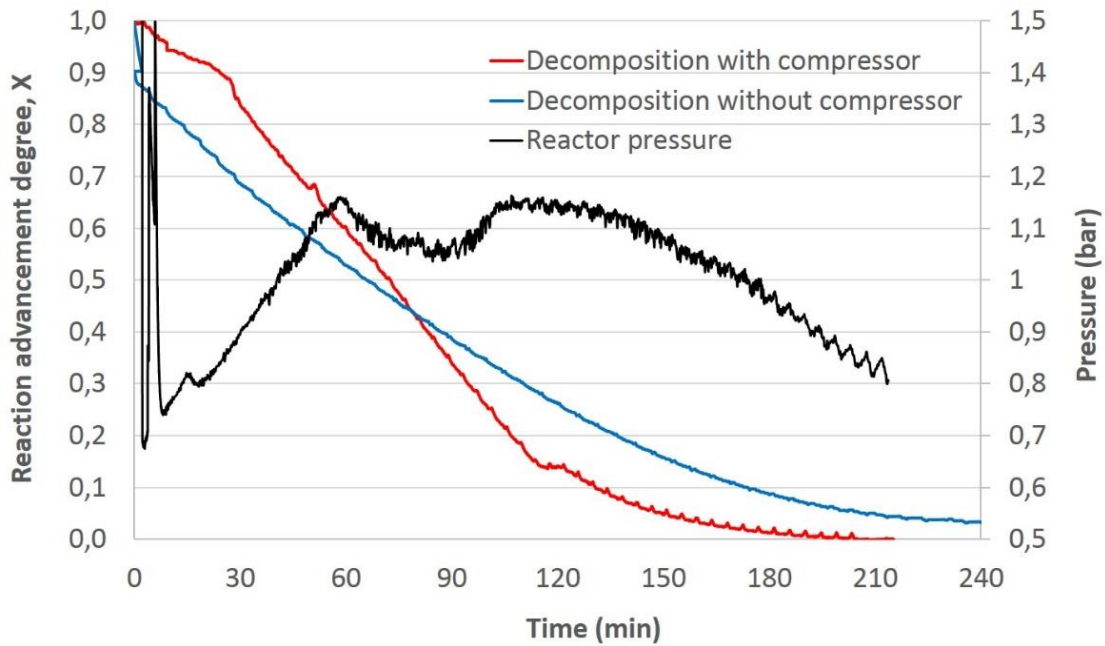


Figure 4.20. Comparison of $X-t$ curves during compression-assisted decomposition and non-assisted decomposition. Evolution of reactor pressure during compression-assisted decomposition.

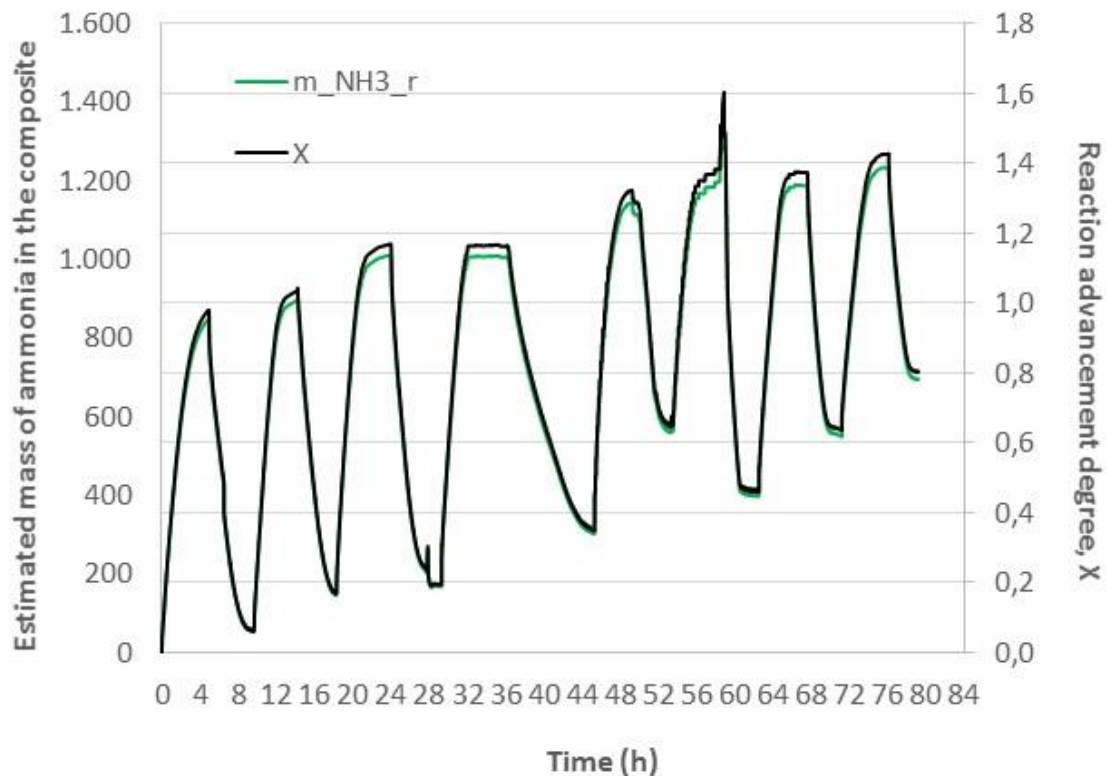


Figure 4.21. Evolution of the estimated mass of ammonia in the solid composite along all the experiments carried out with the setup.

4.4.2. Model validation

The results from the experiments were used to validate the simulation model. This validation consisted on adjusting the parameters of the model and check if, after adjusting, the model can predict the outcome of the experiments accurately enough.

4.4.2.1 *Criteria*

The procedure consisted in adjusting some parameters related to the solid composite with the data from one of the experiments, to later compare the predictions, already with the adjusted parameters, for other experiments. The steps followed were:

- Adjustment of the values of thermal conductivity of the reactive composite (λ_0 for the discharged salt and λ_1 for the charged salt), to fit the predicted $X-t$ curve with the experimental $X-t$ curve in the experiment D2 by the least squares method.
- After parameter adjustment, confrontation of predicted and experimental $X-t$ curves for experiments D4, D6, S4, S2 and S5. Evaluation of the maximum deviation in the predicted results.
- After validation for the synthesis phase and the non-assisted decomposition phase, confrontation of predicted and experimental $X-t$ curves for experiments D7 and D8 (compression-assisted decomposition phases).

Table 4.4. Parameters adjusted for model validation.

Parameter	Units	Min	Nominal case	Max
λ_0	W/(m·K)	0.7	2.0	6.0
λ_1	W/(m·K)	0.7	= λ_0	6.0
k_0	m ²	10 ⁻¹⁶	10 ⁻¹⁵	10 ⁻¹⁴
k_1	m ²	10 ⁻¹⁶	10 ⁻¹⁵	10 ⁻¹⁴
h_w	W/(m ² ·K)	100	300	500

The parameter h_w corresponds to a global heat transfer coefficient from the heat exchange fluid that circulates inside the reactor's coating, to the reactive composite. Its value was estimated (eq. 4.6) having into account: convective

heat transfer from the heat exchange fluid to the copper wall of the coating (h_{FC}); conductive heat transfer through the copper wall (λ_{Cu} along e_{Cu}); convective heat transfer from the coating's external, copper wall to the reactor's external, stainless steel wall ($h_{Cu-Inox}$), improved thanks to the thermal glue; conductive heat transfer through the stainless steel wall (λ_{Inox} along e_{Inox}); and convective heat transfer from the inner stainless steel wall to the solid reactive composite (h_{sw}).

$$\frac{1}{h_w} = \frac{1}{h_{FC}} + \frac{e_{Cu}}{\lambda_{Cu}} + \frac{1}{h_{Cu-Inox}} + \frac{e_{Inox}}{\lambda_{Inox}} + \frac{1}{h_{sw}} \quad (4.6)$$

The values used for each parameter are shown in table 4.5. Each parameter has a value that corresponds to a 'nominal case', and most of the parameters have a maximum and minimum value (except wall thicknesses, which are fixed by the real materials that were used in the setup).

Table 4.5. Nominal, minimum and maximum values of parameters used for estimation of the overall heat transfer coefficient composite-coating (h_w).

Parameter	Units	Min	Nominal case	Max
h_{FC}	W/(m ² ·K)	1000	1500	2000
h_{sw}	W/(m ² ·K)	200	350	800
$h_{Cu-Inox}$	W/(m ² ·K)	100	150	200
λ_{Inox}	W/(m·K)	15	20	25
e_{Inox}	m	-	0.002	-
λ_{Cu}	W/(m·K)	350	370	390
e_{Cu}	m	-	0.001	-

4.4.2.2 Parameter adjustment

With all parameters from tables 4.4 and 4.5 at nominal case, the values of thermal conductivity of the fully discharged and fully charged salt (λ_0 and λ_1 , respectively) were adjusted to fit the predicted curve of advancement degree (X) vs reaction time (t_r) with the experimental curve. As this is a preliminary model validation, and given that both parameters usually have close values, it was assumed that $\lambda_0 = \lambda_1$ for the sake of simplicity.

Figure 4.22 shows some of the evolutions that were obtained during parameter adjustment. The values of $\lambda_0 = \lambda_1$ ranged from 0.75 W/(m·K) to 1.15 W/(m·K). The higher those values, the faster the reaction. This tendency is

logical, since a higher thermal conductivity reduces heat transfer limitations in the process. Further reducing the value of thermal conductivity would make no sense since $0.75 \text{ W}/(\text{m}\cdot\text{K})$ is already a low value for this composite (especially because of the presence of expanded natural graphite, which improves heat transfer). Further increasing λ_0 and λ_1 above $1.15 \text{ W}/(\text{m}\cdot\text{K})$ is possible, but the predicted $X-t$ curve would continue to separate from the experimental curve.

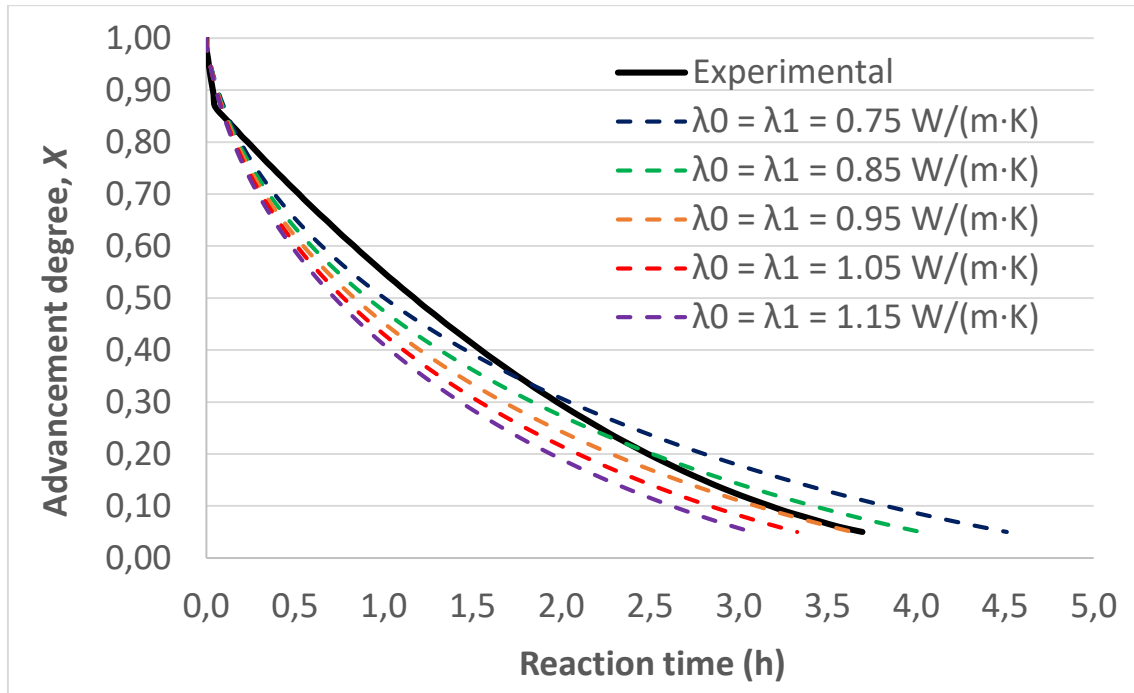


Figure 4.22. Comparison of predicted $X-t$ curves for parameters at nominal case and several values of $\lambda_0 = \lambda_1$ with data from experiment D2 (non-assisted decomposition phase).

Therefore, it was considered that the value of $\lambda_0 = \lambda_1$ that best fits the experimental curve lies somewhere between $0.75 \text{ W}/(\text{m}\cdot\text{K})$ to $1.15 \text{ W}/(\text{m}\cdot\text{K})$. Figure 4.23 confirms this hypothesis mathematically. It shows the results of the least squares method (applied on the reaction time in minutes at a series of X values) for several values of $\lambda_0 = \lambda_1$ ranging from $0.75 \text{ W}/(\text{m}\cdot\text{K})$ to $1.15 \text{ W}/(\text{m}\cdot\text{K})$. A minimum is clearly observed in this range, precisely at $\lambda_0 = \lambda_1 = 0.85 \text{ W}/(\text{m}\cdot\text{K})$. Therefore, this value was finally taken as optimal for the strategy and hypotheses that were applied.

To confirm the suitability of $\lambda_0 = \lambda_1 = 0.85 \text{ W}/(\text{m}\cdot\text{K})$, the predicted $X-t$ curve was confronted to the experimental curve with this value and for the minimum, average and maximum values of T_c . Indeed, the model considers that the stress temperature T_c applied to the wall of the exchanger is constant and uniform. In practice, however, there is a notable difference in temperature between the inlet

and the outlet of the heat transfer fluid, a difference which, moreover, varies over time. Figure 4.24 shows the result of this verification. The black line represents the experimental curve, while the red lines represent predicted curves with the extreme temperature values (inlet and outlet) of the heat transfer fluid plus the mean value.

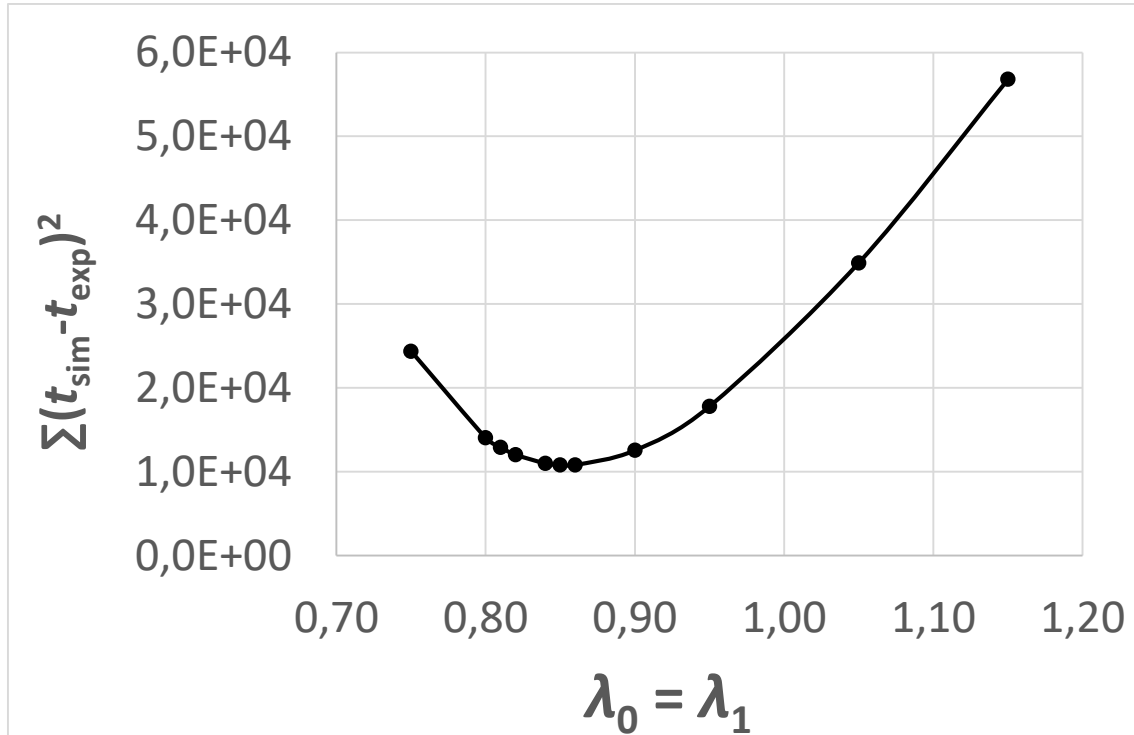


Figure 4.23. Adjustment of parameters $\lambda_0 = \lambda_1$ by the least squares method for experiment D2.

The predictions seem to adjust to the experimental data acceptably, and most of the experimental points are inside, or at least close to the prediction range. After this check the value of $\lambda_0 = \lambda_1 = 0.85 \text{ W}/(\text{m}\cdot\text{K})$ is taken as valid, and parameter adjustment is considered finished.

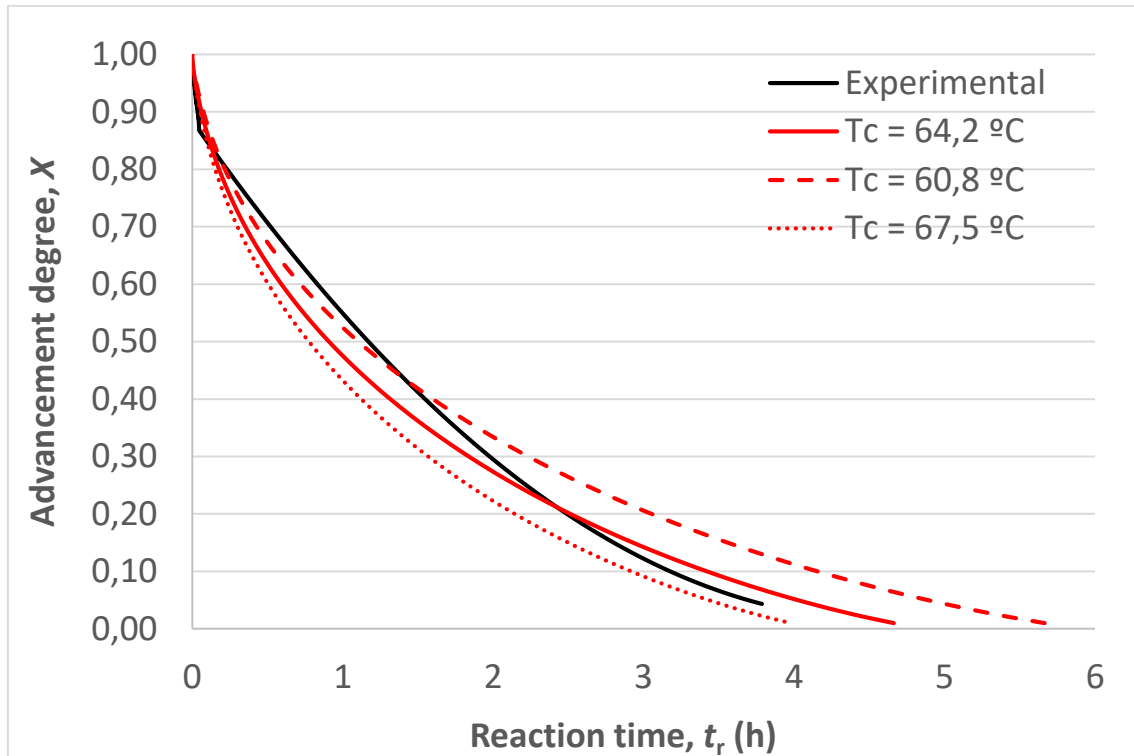


Figure 4.24. Verification of parameter adjustment for decomposition D2.

4.4.2.3 Model-Experiments confrontation

Fig. 4.25 shows the comparison between the simulated $X-t$ curve (with always the three curves corresponding to the inlet, mean and outlet temperature of the heat transfer fluid) and the experimental curve for experiment D4, which corresponds again to a decomposition phase not assisted with compression. The black dashed line represents the experimental curve, while the red lines represent predicted curves through simulation with all parameters at nominal values, with the exception of λ_0 and λ_1 , for which the adjusted values were used ($0.85 \text{ W} \cdot \text{m}^{-1} \cdot \text{K}^{-1}$ for each of the two), and the coating temperature (T_c), for which a maximum, average and minimum value was experimentally used.

The maximum value of T_c ($42.5 \text{ }^\circ\text{C}$) corresponds to the highest temperature that was recorded by the thermocouple placed at the inlet of the reactor's thermal coating, while the minimum value ($34.0 \text{ }^\circ\text{C}$) corresponds to the lowest temperature recorded by the thermocouple at the coating's outlet, and the $38.3 \text{ }^\circ\text{C}$ is just an average between the two. This choice of values provides a range of $X-t$ curves that covers from the fastest to the slowest reaction.

The red continuous line is the predicted $X-t$ curve for the average value $T_c = 38.3 \text{ }^\circ\text{C}$. As seen in the figure, at these conditions the reaction ends sooner than

the real one. The same applies to the $X-t$ curve for $T_c = 42.5\text{ }^\circ\text{C}$, which ends even sooner, since the equilibrium drop is greater. Nevertheless, the $X-t$ prediction for $T_c = 34.0\text{ }^\circ\text{C}$ (which is slower because of the smaller ΔT_{eq}) seems to fit the experimental data more accurately than the other two, despite overestimating the reaction time towards the end of the experiment.

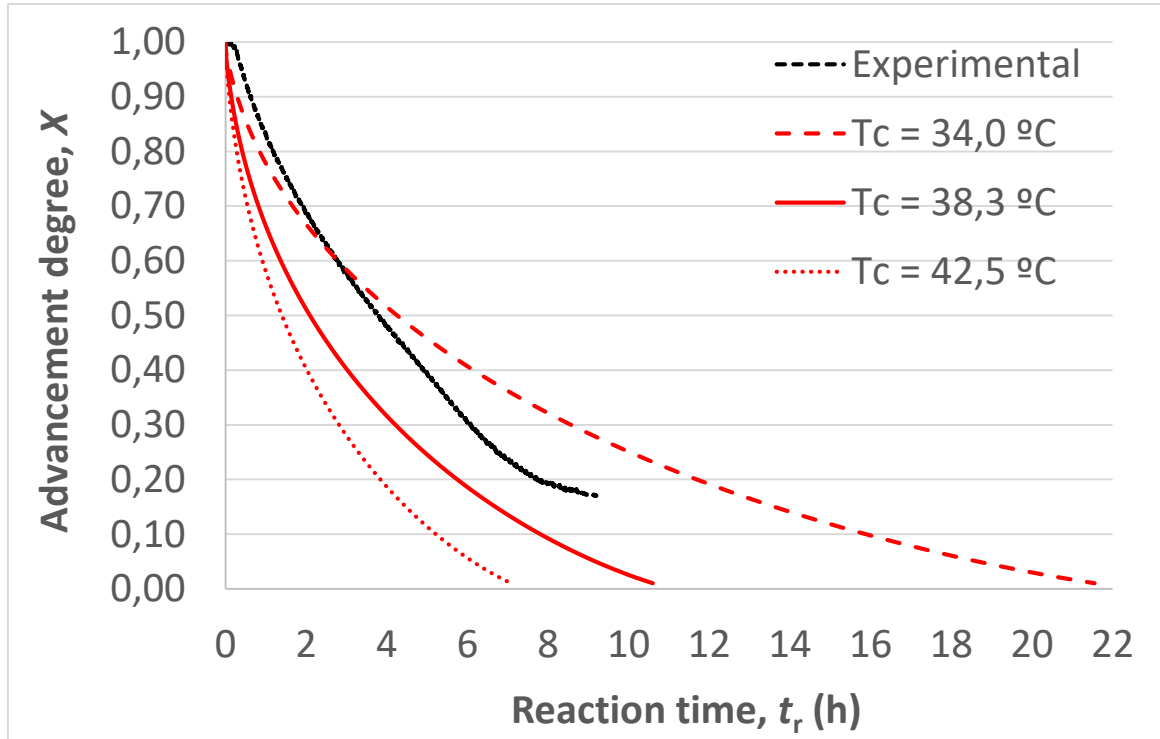


Figure 4.25. Confrontation of experimental and predicted $X-t$ curves for experiment D4 (non-assisted decomposition phase).

The experimental curve concludes at $X = 0.18$ with a total reaction time of 9 hours. For this same X , the predicted reaction times are 4 hours, 6 hours and 12 hours, which indicates a deviation of -55.6 %, -33.3 % and 33.3 %, respectively. Overall, it can be stated that for this reaction, with the applied set of parameters, the model tends to slightly underestimate the reaction time for a given advancement degree.

Fig. 4.26 shows the same data confrontation applied to experiment D6, which is also a non-assisted decomposition phase like D4. Again, the black line represents experimental data, while the red lines represent predictions with parameters at nominal case, same adjusted values of λ_0 and λ_1 and different values of T_c (inlet, mean and outlet of the jacket).

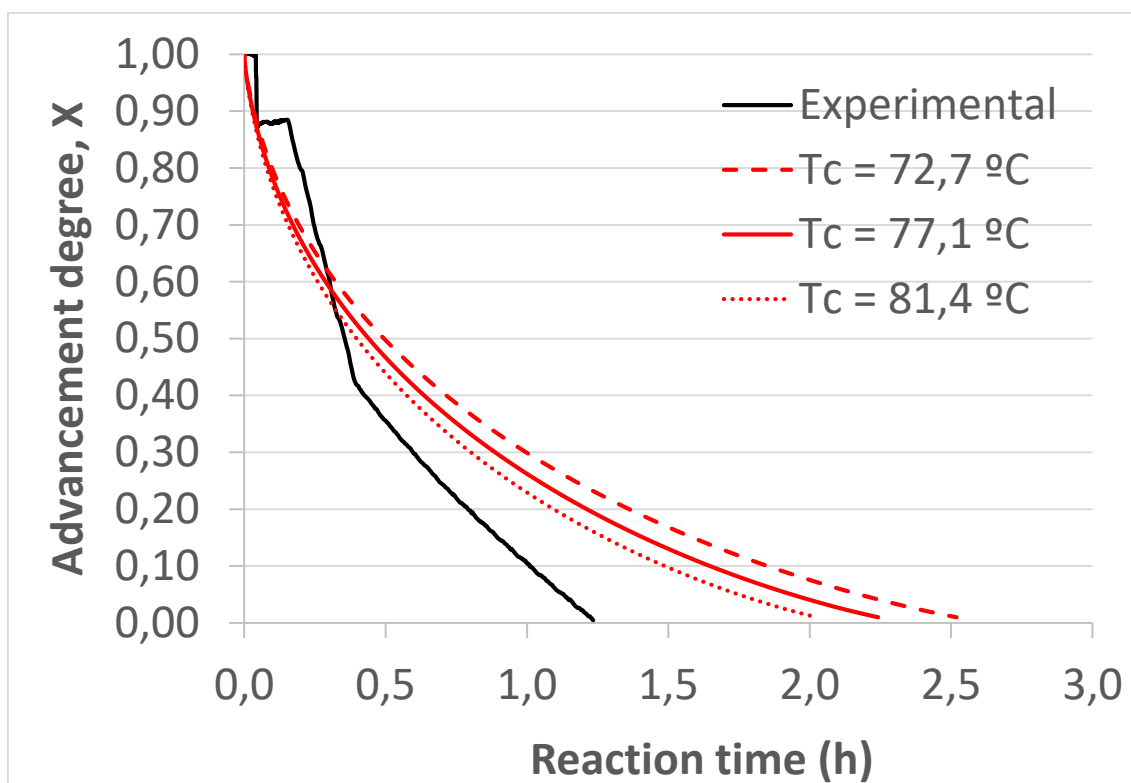


Figure 4.26. Confrontation of experimental and predicted $X-t$ curves for experiment D6 (non-assisted decomposition phase).

Conversely to the previous confrontation, the model tends to overestimate the reaction time for a given advancement degree, especially towards the end of the reaction. The exception to this is the reaction's beginning, where the three predictions are more or less accurate with respect to the experiment.

It can be also noted that in this reaction, which is notably faster than the previous one, the range of prediction as a function of T_c is quite narrower, while for each of the two confrontations, the difference between maximum and minimum T_c is practically the same (8.5 °C for D4 and 8.7 °C for D6). This tendency is logical: the higher the T_c , the less relevant becomes its variation.

The fact that the deviations become greater towards the end of the reaction may indicate that a more accurate adjustment could be done by using independent values for λ_0 and λ_1 , and especially, re-adjusting λ_0 . Since this is a decomposition, at the first stages of the experiment the parameter λ_1 is dominant, while λ_0 becomes more important at a later stage, where the deviations are observed. If the predicted reaction is faster than the experimental, then λ_0 should be diminished for better adjustment, and in the opposite case it should be increased. However, this option was not considered in the present validation.

In addition, the fact that in this experiment the predicted reaction times are overestimated, while in the previous experiment they are underestimated, may support the idea that there is no systematic deviation in the model predictions.

Figures 4.27 and 4.28 illustrate the parameter validation for the slowest and the fastest non-assisted decomposition phases, respectively. Having checked these two cases, it can be affirmed that the model can predict the $X-t$ curve of non-assisted decomposition phases with rather acceptable accuracy, at least within the experimental range of this study. A tendency is observed in which the model slightly overestimates reaction times in the fastest reactions, and underestimates reaction times in the slowest reactions. Further, better accuracy can probably be reached with a more detailed, calculation-intensive adjustment method, although such procedure is out of the scope of this study.

After these considerations, the validation can proceed to the synthesis phase. Fig. 4.27 shows data confrontation applied to experiment S5. This is probably the experiment in which predictions with the nominal set of parameters fit the experimental curve most accurately.

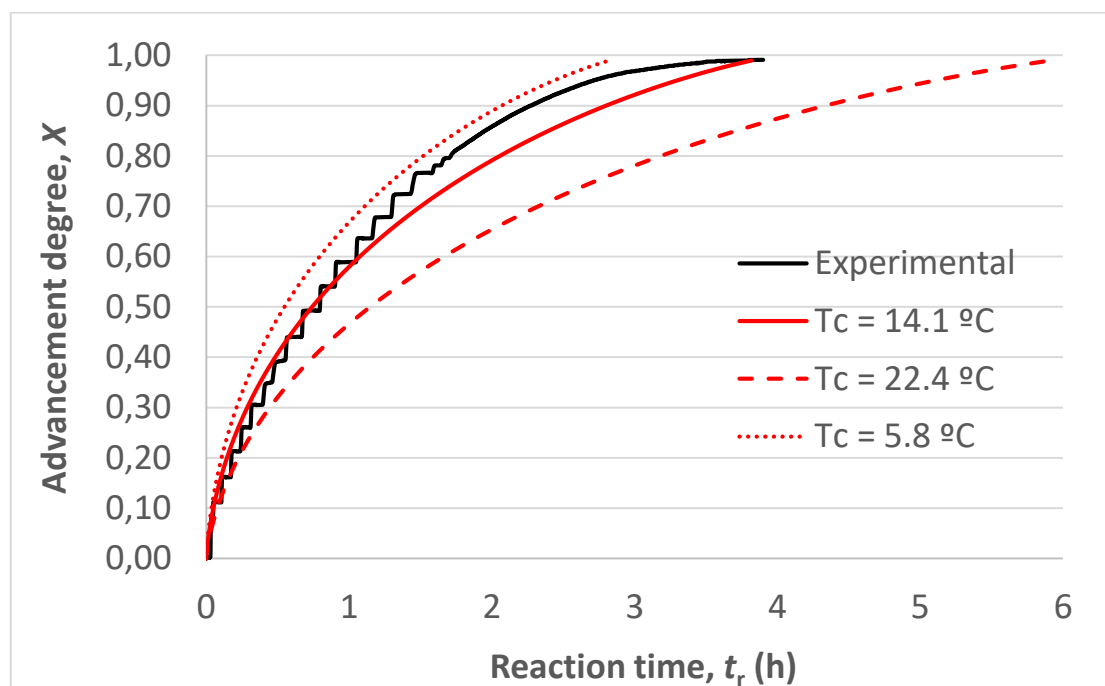


Figure 4.27. Confrontation of experimental and predicted $X-t$ curves for experiment S5 (synthesis phase).

Although during the second half of reaction there is a deviation, the slopes during the first half of reaction are almost the same in both curves, and the final reaction times are practically equal. If the two additional predictions with highest and lowest equilibrium drop are taken into account, this is the only

experiment in which every single point of the experimental $X-t$ curve (with few exceptions at the very beginning of the reaction) falls within the model's prediction range. Having into account that this is a synthesis phase, while parameter adjustment was done on a decomposition phase, this fact is remarkable.

Despite not fitting so accurately, predictions for synthesis S2 (Fig. 4.28) are also quite acceptable. While in S5 the slopes of predicted curves with average and minimum T_c are very similar to the experimental curve, here a different situation is noted.

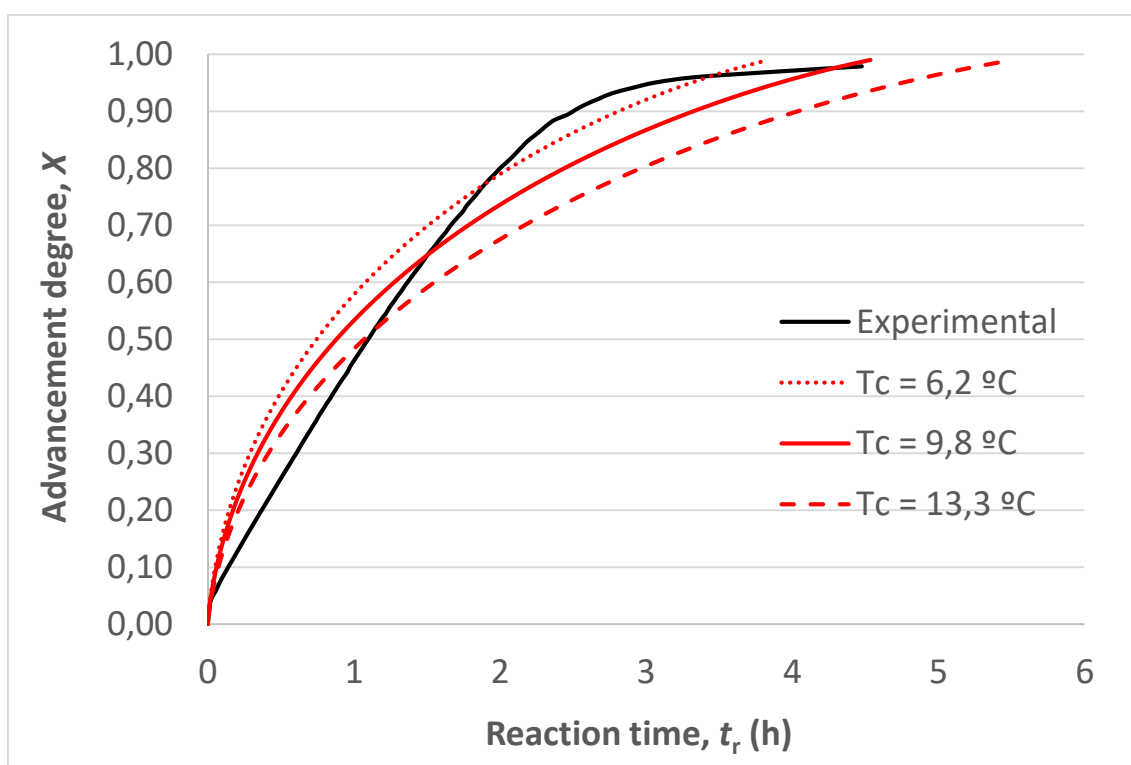


Figure 4.28. Confrontation of experimental and predicted $X-t$ curves for experiment S2 (synthesis phase).

During approximately the first half of reaction, all predictions seem to underestimate reaction times, as seen in previous data confrontations. Then, at the second half of reaction, the difference in slope seems to reverse, and all predictions overestimate reaction times, except towards the end of reaction.

Curve fitting in synthesis S4 is less accurate than in other synthesis phases (Fig. 4.29). In this case, predictions deviate from experimental data during the second half of reaction, reaching more than 100% deviation at the end of reaction.

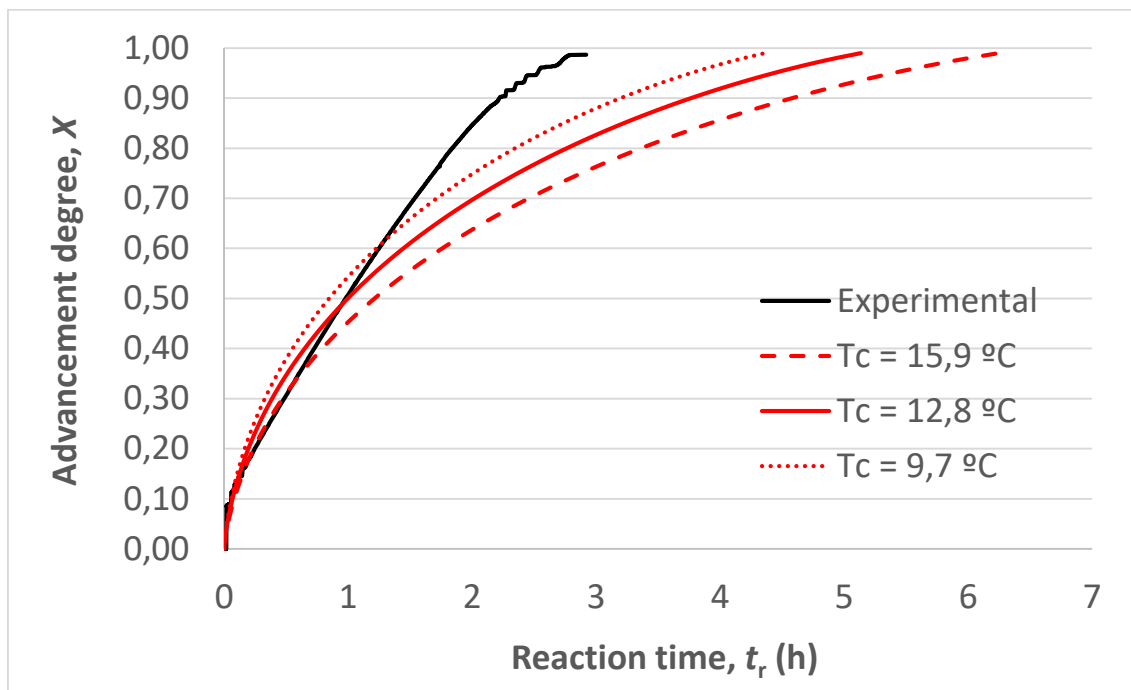


Figure 4.29. Confrontation of experimental and predicted $X-t$ curves for experiment S4 (synthesis phase).

This data corresponds to the experiment in which the reactor's thermal bath was less limiting, given its 9 °C set temperature, which is higher than the 5 °C set temperature of the other synthesis experiments. This probably explains why predictions for other syntheses adjust accurately to the experimental data, while in this experience they do not. If the thermal bath is the only reason for this, then it might be stated that the model with this set of parameters has a tendency to overestimate reaction times towards the end of the synthesis phase.

Fig. 4.30 shows data confrontation for experiment D7, which is a compression-assisted decomposition phase. At first glance, two circumstances are observed: first, the experimental $X-t$ curve stagnates at about $X = 0.25$, which means that the reaction does not reach completion; second, prediction deviate considerably from the experimental data.

The fact that there is no complete reaction may be caused by the condensation of pure ammonia at some parts of the reactive composite during synthesis S5, in which the operating pressure at the reactor was rather close to the condensation temperature of pure ammonia at the given pressure. This phenomenon may have occurred and affected later experiments.

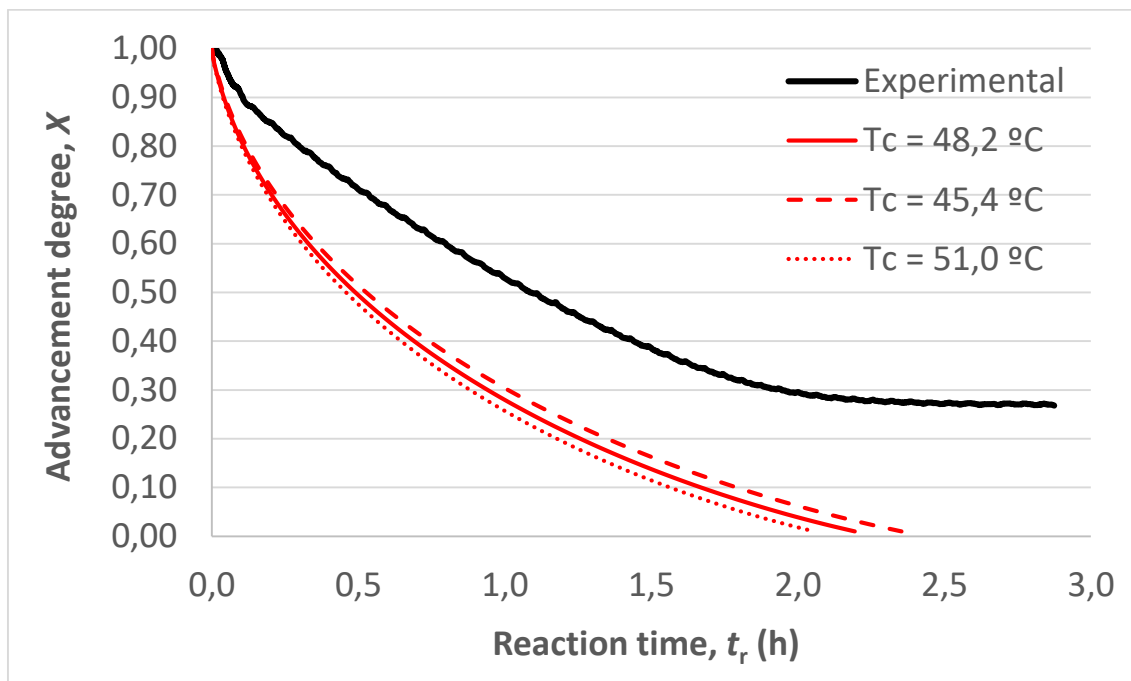


Figure 4.30. Confrontation of experimental and predicted $X-t$ curves for experiment D7 (compression-assisted decomposition phase).

The deviation in model predictions is probably caused by the low reactor pressure during this experiment. In this experiment, the pressure becomes low (1 bar) in comparison with the other experiments. At this pressure, mass transfer limitations probably become non-negligible, which may explain that the actual reaction is slower than the predicted ones.

Finally, figure 4.31 shows data confrontation for experiment D8, which is another compression-assisted decomposition phase. The same two circumstances as in experiment D7 are observed. The reasons for these deviations are discussed above.

A more precise model validation would involve temperature profiles, multi-parameter optimization (which would require the application of a more powerful method such as Simplex), and adjustment for not only one experiment, but all of them.

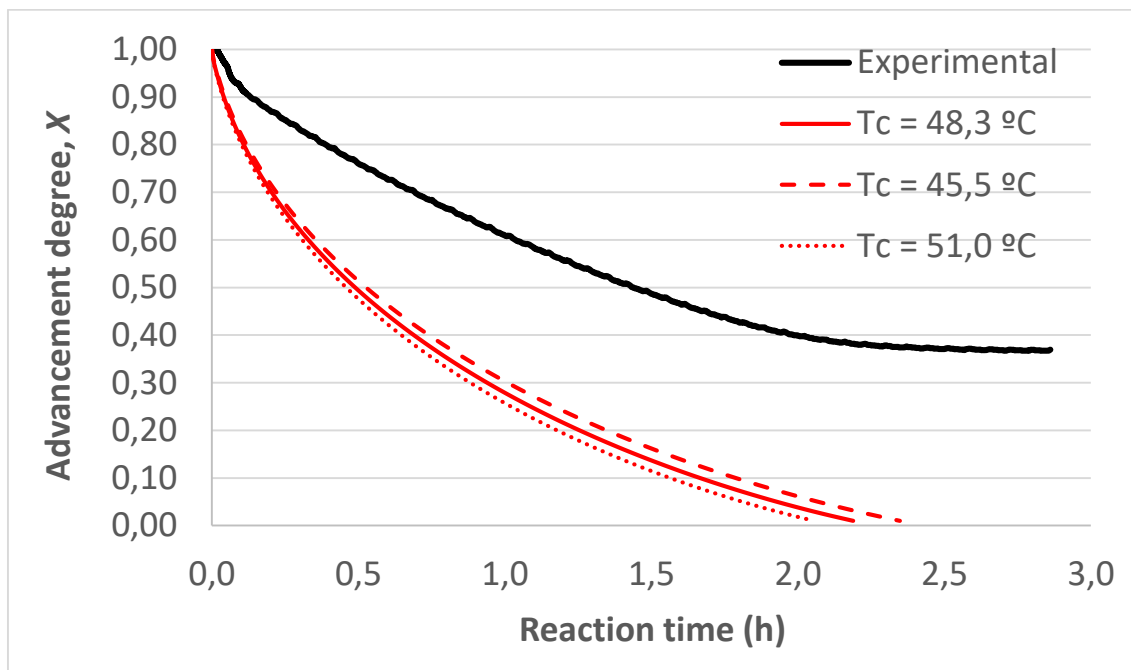


Figure 4.31. Confrontation of experimental and predicted $X-t$ curves for experiment D8 (compression-assisted decomposition phase).

4.5. CONCLUSIONS AND PERSPECTIVES

According to the experimental results obtained for this system, a first conclusion may be that the system is, at least from the prototype perspective, viable.

From the subsequent validations, it is concluded that the 2-front reaction model developed for this system in Chapter 3 is accurate enough to obtain a rough estimate of experiment durations and temperature profiles of the compression-assisted decomposition phase.

Interesting perspectives can be: the acquisition of another compressor that can reach discharge temperatures up to 10 bar, since this pressure would allow to carry out studies at more realistic condenser temperatures; the evaluation of the performance of this system in front of a real application, which would fix values of specific cooling capacities and others; and some technical improvements in the setup to improve data acquisition and treatment.

4.6. REFERENCES

- [1] Real Decreto 108/2016, de 18 de marzo, por el que se establecen los requisitos esenciales de seguridad para la comercialización de los recipientes a presión simples. Ministerio de Industria, Energía y Turismo, "BOE" núm. 70, de 22 de marzo de 2016. Spain.
- [2] KNF Series N 035 AT.18 Operating manual. KNF Neuberger.
- [3] Multicap T-DC Level Probes Operating Manual. Endress + Hauser.
- [4] AlfaNova 52 / AlfaNova HP 52 Operating Manual. Alfa Laval.
- [5] Huber Ministat 125 Operating Manual. Huber.
- [6] Julabo MC12 Operating Manual. Julabo.
- [7] Winus Chiller C2 W3 Operating Manual. Winus.
- [8] Agilent® 34901A Operating Manual. Keysight Technologies.
- [9] E. F. Urresta, A. Coronas: *Experimental study of the thermochemical process of a refrigeration system using NH₃/BaCl₂*. Master thesis. Universitat Rovira i Virgili, Tarragona, Spain, 2017.

“This page intentionally left blank”

CHAPTER 5

General Conclusion and Future Outlook

5.1 GENERAL CONCLUSION

From the study of the hybrid absorption / thermochemical refrigeration system, it can be concluded that the hybrid system has better utilization of solar energy than a solar absorption refrigeration system without any form of energy storage. The COP of the hybrid system is always between that of the ABS subsystem and that of the TCH subsystem. As the presence of the TCH subsystem increases (for instance by increasing the mass of stored refrigerant or the area of solar collector field), the COP of the hybrid system approaches to that of the TCH subsystem. As a compensation, the solar coverage increases. Therefore, the final design for a given application should reach a compromise between performance and coverage.

The COP is not the only parameter to monitor the system. The cooling power and the energy density of storage are two relevant parameters that have been studied in this thesis as well. Results show that some design variables (like the heat sink temperature and the cold production temperature) and some design parameters (like composite porosity and heat transfer) have a direct and simple influence on these two performance parameters, i.e. both of them increase or decrease together. From the point of view of these variables and parameters, optimization of the system is rather simple. However, other variables, like the duration of the cold production phase, have an inverse influence on the indicators: cooling power can be increased, at the expenses of energy storage. These variables are in need of finding a compromise between the two parameters and are more interesting for system optimization. One special case is the apparent density of the inert heat transfer enhancer (in this case expanded natural graphite, ENG). For this parameter, there is a region in which increasing its value improves both the storage density and the cooling power, until reaching a maximum for the storage density, with a further decrease. The fact that there is a maximum point with respect to this parameter makes it quite interesting towards optimal design. Nevertheless, the study was preliminary and did not take mass transfer into account, in which case the results would be more complex and difficult to interpret and optimize.

Although not the same parametric study was applied in the ABS/TCH hybrid system as in the COMP/TCH hybrid system, the main conclusions from the former (increased solar coverage, and the tendencies of performance indicators with respect to design) are likely to be applicable to the latter, since the core idea behind both systems is the same.

In addition, the parametric study of the COMP/TCH hybrid system provides more detail on the influence of the composite's permeability and thermal conductivity, confirming the tendencies observed preliminarily in the ABS/TCH system.

From the experimental study of the compression-assisted decomposition phase, it is verified that the compressor in the COMP/TCH allows to reduce the activation temperature of the reaction, which leaves the door open for utilization of low-grade heat sources. It is also concluded that, with proper adjustment, the 2-front quasi-steady simulation model can predict the reaction curve with rather acceptable accuracy, although a more complete parameter adjustment should be carried out.

5.2 FUTURE OUTLOOK

Several interesting research lines are open for this topic. From the conceptual point of view, advanced ABS/TCH systems can be designed which use heat sources with medium or high temperature. Such designs increase the complexity of the system, requiring double- or triple effect and different working pairs in the ABS subsystem, and the use of different working pairs in the TCH subsystem than those described in this thesis. At these temperature levels, the concept of heat integration within the system becomes highly interesting. Reaction heat or high-pressure condensation heat might be recovered and utilized for the low-pressure generator, for instance.

Both the simulative and experimental studies can be further improved. More detailed simulation models can be developed for both the HATRS and the HCTRS, and more complete parametric studies can be conducted (e.g. through the method of Morris and Sobold). For the experimental study, one of the first improvable aspects should be the acquisition of a compressor (or the implementation of a chain of compressors) that would allow to operate the system at a higher discharge pressure. This would make the experiments more representative of a real application, because of the high vapor pressure of the ammonia at real condensing temperatures. Another interesting idea could be to try different types of compressors and evaluate how each one responds to the system.

To evaluate the potentialities of these hybrid systems in a fair manner, first a more realistic case study should be carried out for an application. Then, the general performance of the systems should be compared to other options for the same applications and operating conditions. This comparison would require a precise definition of indicators to compare all the systems on a same, unbiased basis. These studies could be culminated with an exergo-economic evaluation, if the development of these systems makes it that far.

"This page intentionally left blank"

Appendix A: EES code and additional results of the parametric study of the hybrid absorption / thermochemical refrigeration system

A.1 EES CODE FOR THE ABSORPTION SUBSYSTEM

"NOMENCLATURE"

{1 = From Absorber to P-1}
{2 = From P-1 to SHX}
{3 = From SHX to G}
{4 = From G to SHX}
{5 = From SHX to V-1}
{6 = From V-1 to Absorber}
{7 = From G to TV-1}
{8 = From TV-1 to Condenser}
{9 = From Condenser to Reservoir}
{10 = From Reservoir to V-2}
{11 = From V-2 to Evaporator}
{12 = From Evaporator to TV-2}
{13 = From TV-2 to Absorber}

"INPUT DATA"

T_E = 5
T_C = 35
T_A = 35
{T_G = 104,8}
Eff_SHX = 0.64
m[7] = 1
{Qd = 0,7}
Q[9] = 0
Q[12] = 1

"SET PRESSURES"

P_high=Pressure(Water,T=T_C,x=0)
P_low=Pressure(Water,T=T_E,x=0)

"SET TEMPERATURES"

T[1] = T_A
T[4] = T_G
T[12] = T_E
T[9] = T_C
T[8] = T[7]
T[13] = T[12]
T[10] = T[9]

w[1] = x_LiBrH2O(T[1],P[1])
w[4] = x_LiBrH2O(T[4],P[4])

T[7] = T_LiBrH2O(P[7],w[3])

"SOLUTION HEAT EXCHANGER"

$$\text{Eff_SHX} = (T[4] - T[5]) / (T[4] - T[2])$$

$$Q_hot = m[4] * (h[4] - h[5])$$

$$Q_cold = m[3] * (h[3] - h[2])$$

$$Q_hot - Q_cold = 0$$

{Check}

$$C_{hot} = m[4] * (h[4] - h[5]) / (T[4] - T[5])$$

$$C_{cold} = m[2] * (h[3] - h[2]) / (T[3] - T[2])$$

"ABSORBER"

$$m[6] + m[13] = m[1]$$

$$m[6] * w[6] + m[13] * w[13] = m[1] * w[1]$$

$$m[6] * h[6] + m[13] * h[13] - m[1] * h[1] - Q_a = 0$$

"DESORBER"

$$m[3] * h[3] - m[4] * h[4] - m[7] * h[7] + Q_d = 0$$

"CONDENSER"

$$m[8] * h[8] - m[9] * h[9] - Q_c = 0$$

"EVAPORATOR"

$$m[11] * h[11] - m[12] * h[12] + Q_e = 0$$

"OVERALL ENERGY BALANCE"

$$\text{ENE_BAL} = Q_d + Q_e - Q_c - Q_a + W_P$$

"PUMP P-1"

$$h[2] = h[1] + W_P / m[1]$$

$$T[2] = T[1]$$

$$W_P = m[1] * v_1 * (P[2] - P[1])$$

$$v_1 = 1 / \rho_1$$

$$\rho_1 = \rho_{\text{LiBrH}_2\text{O}}(T[1], w[1])$$

"VALVE V-1"

$$h[6] = h[5]$$

"SOLUTION CIRCULATION RATIO"

$$F = w[4] / (w[4] - w[3])$$

"COMPUTE COP"

$$\text{COP} = Q_e / (Q_d + W_P)$$

"COMPUTE EXERGY EFFICIENCY"

$$T_0 = -5$$

$$\text{Ex_eff} = (Q_e * (1 - (T_0 + 273.15) / (T_E + 273.15))) / (Q_d * (1 - (T_0 + 273.15) / (T_G + 273.15)) + W_P) * 100$$

"COMPUTE THERMODYNAMIC PROPERTIES"

$$h[1] = h_{\text{LiBrH}_2\text{O}}(T[1], w[1])$$

$$h[3] = h_{\text{LiBrH}_2\text{O}}(T[3], w[3])$$

$$h[4] = h_{\text{LiBrH}_2\text{O}}(T[4], w[4])$$

$$h[5] = h_{\text{LiBrH}_2\text{O}}(T[5], w[5])$$

$$\text{CALL } Q_{\text{LiBrH}_2\text{O}}(h[6], P[6], w[6]: Q[6], T[6], x6lb)$$

$$T_{6\text{sat}} = T_{\text{LiBrH}_2\text{O}}(P[6], w[6])$$

$$h[7] = \text{Enthalpy}(\text{Water}, T=T[7], P=P[7])$$

$$Q[7] = \text{Quality}(\text{Water}, T=T[7], h=h[7])$$

$$T_{\text{sat}}[7] = T_{\text{sat}}(\text{Water}, P=P[7])$$

$$h[8] = h[7]$$

$$Q[8] = Q[7]$$

h[9] = Enthalpy(Water,T=T[9],x=Q[9])
h[10] = Enthalpy(Water,T=T[10],x=Q[10])
h[11] = h[10]
T[11] = Temperature(Water,h=h[11],P=P[11])
Q[11] = Quality(Water,T=T[11],h=h[11])
h[12] = Enthalpy(Water,T=T[12],x=Q[12])
h[13] = Enthalpy(Water,T=T[13],x=Q[13])

"TRIVIAL BALANCES"

m[2] = m[1]
m[3] = m[2]
m[5] = m[6]
m[4] = m[5]
m[8] = m[7]
m[9] = m[8]
m[10] = m[9]
m[11] = m[10]
m[12] = m[11]
m[13] = m[12]
w[2] = w[1]
w[3] = w[2]
w[5] = w[4]
w[6] = w[5]
w[7] = 0
w[8] = 0
w[9] = 0
w[10] = 0
w[11] = 0
w[12] = 0
w[13] = 0

"SET PRESSURES"

P[1] = P_low
P[2] = P_high
P[3] = P_high
T3sat = T_LiBrH2O(P[3],w[3])
P[4] = P_high
P[5] = P_high
P[6] = P_low
P[7] = P_high
P[8] = P_high
P[9] = P_high
P[10] = P_high
P[11] = P_low
P[12] = P_low
P[13] = P_low

"SET VAPOR QUALITY"

Q[1] = 0
Q[4] = 0
Q[10] = Q[9]
Q[13] = Q[12]
{CALL Q_LiBrH2O(h[3];P[3];w[3]: Q[3];T3b; x3lb)}

A.2 EES CODE FOR THE THERMOCHEMICAL SUBSYSTEM

" PARAMETERS OF THE STUDY "

```
Q_dot_b = 3 "kW"  
{T_b = 0 "°C"  
T_m = 30 "°C"}  
T_h = 70 "°C"  
DELTAT_e_ev = 5 "°C"  
DELTA_t_b = 15 * 3600 "s"  
epsilon_1 = 0,4  
rho_app_GNE = 80 "kg/m3"  
h_sw = 400 "W/(m2*K)"  
h_e = 1000 "W/(m2*K)"  
DELTAX = 0,9  
e_p = 0,0026 "m"  
v_NH3_molar = Volume(Ammonia;T=T_b;x=0)
```

" CHOICE OF REACTIVE PAIR "

```
"----- <NH4Br> + NH3 <=> <NH4Br · NH3> -----"  
DELTAh_0 = 33271 "kJ/kmol NH3" "NH4Br 1/0"  
DELTA_s_0 = 117,777 "kJ/(kmol·K)" "NH4Br 1/0"  
v_s1 = 0,06870735 "m3/kmol <NH4Br·NH3>"  
M_s = 97,94 "kg/kmol NH4Br"  
p = 0 "NH4Br 1/0"  
v = 1 "NH4Br 1/0"  
  
"----- <BaCl2> + 8 NH3 <=> <BaCl2 · 8 NH3> -----"  
{DELTAh_0 = 38250 "kJ/kmol NH3"  
DELTA_s_0 = 136.657 "kJ/(kmol·K)"  
v_s1 = 0.215 "m3/kmol <BaCl2·8NH3>"  
M_s = 208.233 "kg/kmol BaCl2"  
p = 0  
v = 8}  
  
"----- <PbBr2 · 3 NH3> + 2,5 NH3 <=> <PbBr2 · 5,5 NH3> -----"  
{DELTAh_0 = 37665 "kJ/kmol NH3" "PbBr2 5,5/3"  
DELTA_s_0 = 133.677 "kJ/(kmol·K)" "PbBr2 5,5/3"  
v_s1 = 0.2109755 "m3/kmol <PbBr2·5,5NH3>"  
M_s = 367.01 "kg/kmol PbBr2"  
p = 3 "PbBr2 5,5/3"  
v = 2.5 "PbBr2 5,5/3"}  
  
"----- <SnCl2 · 2,5 NH3> + 1,5 NH3 <=> <SnCl2 · 4 NH3> -----"  
{DELTAh_0 = 38921 "kJ/kmol NH3" "SnCl2 4/2,5"  
DELTA_s_0 = 133.877 "kJ/(kmol·K)" "SnCl2 4/2,5"  
v_s1 = 0.16215949 "m3/kmol <SnCl2·4NH3>"  
M_s = 189.6 "kg/kmol SnCl2"  
p = 2.5 "SnCl2 4/2,5"  
v = 1.5 "SnCl2 4/2,5"}  
  
"----- <LiCl · 3 NH3> + NH3 <=> <LiCl · 4 NH3> -----"  
{DELTAh_0 = 36828 "kJ/kmol NH3" "LiCl 4/3"  
DELTA_s_0 = 128.877 "kJ/(kmol·K)" "LiCl 4/3"  
v_s1 = 0.13402019 "m3/kmol <NH4Br·NH3>"  
M_s = 42.394 "kg/kmol LiCl"  
p = 3 "LiCl 4/3"  
v = 1 "LiCl 4/3"}  
  
"----- <CaCl2 · 4 NH3> + 4 NH3 <=> <CaCl2 · 8 NH3> -----"  
{DELTAh_0 = 41013 "kJ/kmol NH3" "CaCl2 8/4"  
DELTA_s_0 = 134.377 "kJ/(kmol·K)" "CaCl2 8/4"
```

$v_{s1} = 0.207 \text{ "m}^3/\text{kmol } \langle \text{CaCl}_2 \cdot 8\text{NH}_3 \rangle$
 $M_s = 110.98 \text{ "kg/kmol CaCl}_2$
 $p = 4 \text{ "CaCl}_2 \text{ 8/4"}$
 $v = 4 \text{ "CaCl}_2 \text{ 8/4"}$
 $\text{"----- } \langle \text{CaCl}_2 \cdot 2 \text{ NH}_3 \rangle + 2 \text{ NH}_3 \rightleftharpoons \langle \text{CaCl}_2 \cdot 4 \text{ NH}_3 \rangle \text{ -----"}$
 $\{\text{DELTA}h_0 = 42269 \text{ "kJ/kmol NH}_3 \text{ "CaCl}_2 \text{ 4/2"}$
 $\text{DELTA}s_0 = 133.977 \text{ "kJ/(kmol}\cdot\text{K)" "CaCl}_2 \text{ 4/2"}$
 $v_{s1} = 0.128 \text{ "m}^3/\text{kmol } \langle \text{CaCl}_2 \cdot 4\text{NH}_3 \rangle$
 $M_s = 110.98 \text{ "kg/kmol CaCl}_2$
 $p = 2 \text{ "CaCl}_2 \text{ 4/2"}$
 $v = 2 \text{ "CaCl}_2 \text{ 4/2"}$

"MODEL"

$Q_{b_net} = Q_{dot_b} \cdot \text{DELTA}t_b \text{ "kJ = kW}\cdot\text{s"}$

$T_{ev} = T_b - \text{DELTA}T_{e_ev} \text{ "}^\circ\text{C} = \text{ }^\circ\text{C} - \text{ }^\circ\text{C"}$
 $P_b = \text{Pressure}(\text{Ammonia}; T=T_{ev}; x=1) \text{ "bar"}$

$P_h = \text{Pressure}(\text{Ammonia}; T=T_m; x=1)$

$h_{gsatPb} = \text{Enthalpy}(\text{Ammonia}; P=P_b; x=1)$
 $h_{lsatPh} = \text{Enthalpy}(\text{Ammonia}; P=P_h; x=0)$

$n_{dot_g} = Q_{dot_b} / (h_{gsatPb} - h_{lsatPh}) \text{ "kmol/s = kW / kJ/kmol"}$

$\ln(P_b/P_0) = -\text{DELTA}h_0 / (R \cdot (T_{eq_Pb} + 273,15)) + \text{DELTA}s_0 / R \text{ "Equilibrium temperature [}^\circ\text{C] of the reaction as a function of pressure [bar]"}$

$P_0 = 1 \text{ "bar"}$

$R = 8,3144 \text{ "kJ/(kmol}\cdot\text{K)"}$

$T_{m_eq_ev} = (T_{eq_Pb} + T_{ev}) / 2 \text{ " }^\circ\text{C} = \text{ }^\circ\text{C} + \text{ }^\circ\text{C"}$

$C_{p_NH3eqev} = C_p(\text{Ammonia}; T=T_{m_eq_ev}; x=1) \text{ "kJ/(kmol}\cdot\text{K)" "Specific heat of ammonia at the average temperature between } T_{eq_Pb} \text{ and the evaporator temperature"}$

$Q_{dot_r} = n_{dot_g} \cdot (\text{DELTA}h_0 - C_{p_NH3eqev} \cdot (T_{eq_Pb} - T_{ev})) \text{ "kW = kmol/s} \cdot (\text{kJ/kmol} - \text{kJ/(kmol}\cdot\text{K)} \cdot \text{ }^\circ\text{C} - \text{ }^\circ\text{C)"}$

$\rho_{GNE} = 2250 \text{ "kg/m}^3$

$(1 - \epsilon_{1}) = \rho_{app_GNE} \cdot (v_{s1}/M_s \cdot w_s / (1 - w_s) + 1/\rho_{GNE}) \text{ "<adim> = kg/m}^3 \cdot ((\text{m}^3/\text{kmol}) / \text{kg/kmol} + 1/(\text{kg/m}^3)) \text{ "}$

$n_g = n_{dot_g} \cdot \text{DELTA}t_b \text{ "kmol = kmol/s} \cdot \text{ s"}$

$n_s = n_g / (\text{DELTA}x \cdot v) \text{ "kmol = kmol/(<adim>} \cdot \text{ <adim>)"}$

$m_{sa} = n_s \cdot M_s \text{ "kg = kmol} \cdot \text{ kg/kmol"}$

$w_s = m_{sa} / (m_{sa} + m_{GNE})$

$\rho_{app_GNE} = m_{GNE} / V_{app_c} \text{ "kg/m}^3 = \text{kg} / \text{m}^3$

$V_{app_c} = e_r \cdot S_{ech} \text{ "m}^3 = \text{m} \cdot \text{m}^2$

$Q_{dot_r} \cdot 1000 \text{ [W/kW]} = U_p \cdot S_{ech} \cdot (T_{eq_Pb} - T_m) \text{ "W / m}^2 = \text{W} / (\text{m}^2 \cdot \text{K)} \cdot \text{ }^\circ\text{C} - \text{ }^\circ\text{C"}$

$1/U_p = (e_r/2)/\lambda_{r_p} + 1/h_{sw} + e_p/\lambda_{p_p} + 1/h_e \text{ "1 / (W/(m}^2 \cdot \text{K)} = \text{m} / (\text{W/(m}^2 \cdot \text{K)} + 1 / (\text{W/(m}^2 \cdot \text{K)} + \text{m} / (\text{W/(m}^2 \cdot \text{K)} + 1 / (\text{W/(m}^2 \cdot \text{K)})) \text{ "}$

$\lambda_{r_p} = 0,08 \text{ [W}\cdot\text{m}^2/\text{kg}\cdot\text{K]} \cdot \rho_{app_GNE} \text{ "W/(m}^2 \cdot \text{K)} = \text{W}\cdot\text{m}^2/(\text{kg}\cdot\text{K)} \cdot \text{ kg/m}^3$

$\lambda_{p_p} = 17 \text{ "W/m}\cdot\text{K" } \{15-20\}$

$C_{p_s} = 70 \text{ "kJ/(kmol}\cdot\text{K)"}$
 $C_{p_NH3l} = Cp(\text{Ammonia}; T=T_m; x=0) \text{ "kJ/(kmol}\cdot\text{K)"}$ "Specific heat of liquid ammonia at T_m "
 $C_{p_s0} = C_{p_s} + p^*C_{p_NH3l} \text{ "kJ/(kmol}\cdot\text{K) = kJ/(kmol}\cdot\text{K) + <adim>*kJ/(kmol}\cdot\text{K)"}$ "Specific heat of the reactive composite when the salt is charged"
 $C_{p_s1} = C_{p_s0} + v^*C_{p_NH3l} \text{ "kJ/(kmol}\cdot\text{K) = kJ/(kmol}\cdot\text{K) + <adim>*kJ/(kmol}\cdot\text{K)"}$ " Specific heat of the reactive composite when the salt is discharged"

$X_i = (1-DELTAx)/2$

$\rho_{acier} = 8000 \text{ "kg/m}^3\text{"}$
 $m_{acier} = S_{ech} * e_p * \rho_{acier} \text{ "kg = m}^2 * m * \text{kg/m}^3\text{"}$
 $\{m_{acier} = m_{sa} * 2\}$
 $C_{p_acier} = 0,490 \text{ "kJ/kg}\cdot\text{K}"$ "On fixe dans (490 - 530) J/kg*K"
 $C_{p_GNE} = 0,800 \text{ "kJ/kg}\cdot\text{K}"$ "Chaleur spécifique du graphite"

$mC_{p_sum} = n_s * (C_{p_s1} * X_i + C_{p_s0} * (1-X_i)) + m_{GNE} * C_{p_GNE} + m_{acier} * C_{p_acier} + m_{eau} * cp_{eau} \text{ "kJ/K = kmol * (kJ/(kmol}\cdot\text{K}) * <adim> + kJ/(kmol}\cdot\text{K}) * <adim>) + kg * kJ/(kg}\cdot\text{K) + kg * kJ/(kg}\cdot\text{K)"}$

$\{T_h = T_{eq_Ph} + (T_{eq_Pb} - T_m)\}$

$Q_h = n_s * v * DELTAh_0 * DELTAX + mC_{p_sum} * (T_h - T_m)$
 $\{Q_h = n_s * v * DELTAh_0 * DELTAX + mC_{p_sum} * (T_{eq_Ph} - T_m)\}$
 $\text{"kJ = kmol * <adim> * kJ/kmol * <adim> + kJ/K * (}^\circ\text{C - }^\circ\text{C)"}$

$V_{eau} = V_{app_c} / 0,6 * 0,4$
 $\rho_{eau_molar} = \text{Density}(\text{Water}; T=T_m; x=0)$
 $MW_{eau} = \text{MolarMass}(\text{Water})$
 $\rho_{eau} = \rho_{eau_molar} * MW_{eau}$
 $m_{eau} = V_{eau} * \rho_{eau}$
 $cp_{eau_molar} = \text{SpecHeat}(\text{Water}; T=T_m; x=0)$
 $cp_{eau} = cp_{eau_molar} / MW_{eau}$

$Q_{h_sens} = mC_{p_sum} * (T_h - T_m)$
 $pp_{qsens} = Q_{h_sens} / Q_h * 100$

$\ln(P_h/P_0) = -DELTAh_0 / (R * (T_{eq_Ph} + 273,15)) + DELTAs_0 / R$

$COP_{TCH} = Q_{b_net} / Q_h \text{ "<adim> = kJ / kJ"}$

$e_d = 0,005 \text{ "m"}$ "thickness of the diffuser"
 $e_e = 0,005 \text{ "m"}$ "thickness of the heat exchanger's wall"
 $\zeta = 0,9$
 $V_{app_r} = S_{ech} * (e_r + e_d + e_e) / \zeta$
 $De = (Q_{b_net} / 3600 \text{ [kJ/kWh]}) / V_{app_r} \text{ "kWh/m}^3\text{"}$ "Energy density of the reactive composite"

$q_{dot_b_v} = Q_{dot_b} / V_{app_r}$
 $q_{dot_b_s} = Q_{dot_b} / S_{ech}$

$ss_r = m_{acier} / m_{sa} \text{ "Steel-to-anhydrous salt mass ratio, kg/kg" "<adim>"}$

$MW = \text{MolarMass}(\text{Ammonia})$
 $m_{nh3} = n_g * MW$

A.3 ADDITIONAL RESULTS OF THE PARAMETRIC STUDY

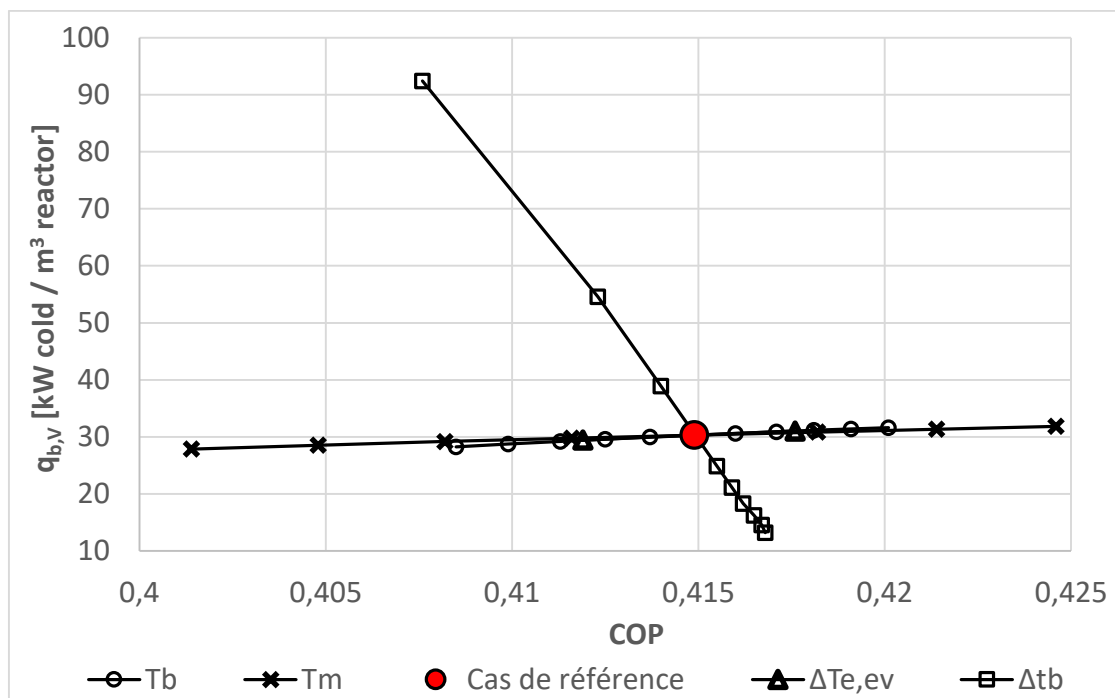


Figure A.1. Evolution of the relationship between COP and cooling power (per unit volume) of the thermochemical subsystem as a function of operating conditions, with the ammonia / strontium chloride reactive pair.

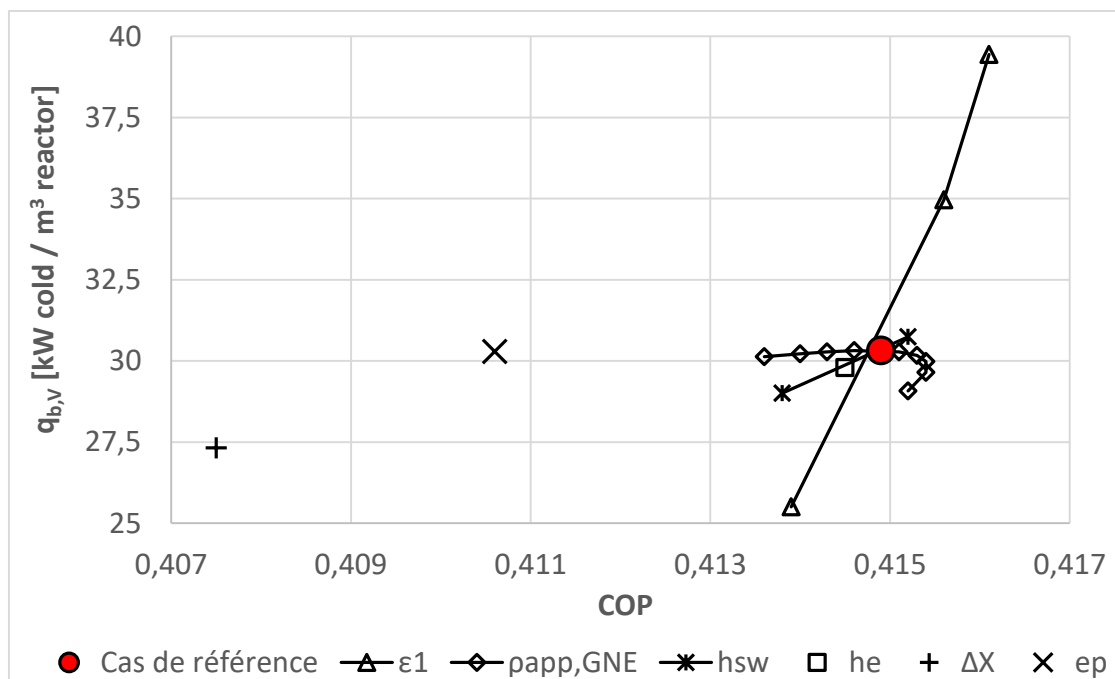


Figure A.2. Evolution of the relationship between COP and cooling power (per unit volume) of the thermochemical subsystem as a function of composite implementation parameters, with the ammonia / strontium chloride reactive pair.

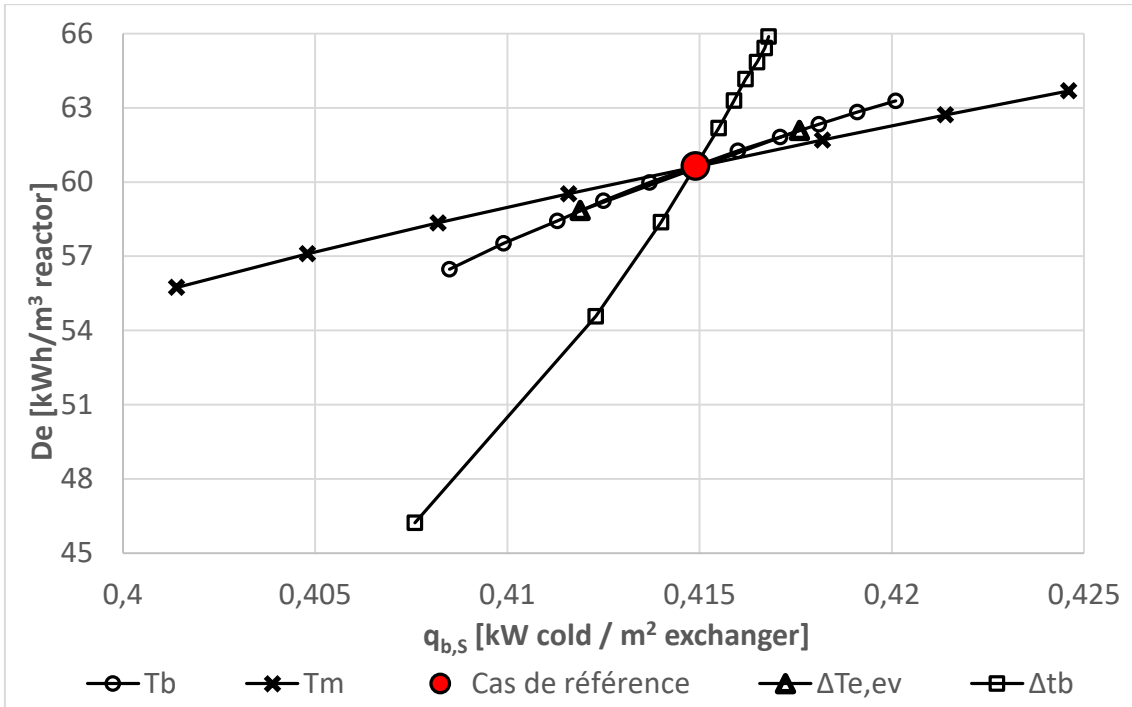


Figure A.3. Evolution of the relationship between energy storage density and cooling power (per unit surface) of the thermochemical subsystem as a function of operating conditions, with the ammonia / strontium chloride reactive pair.

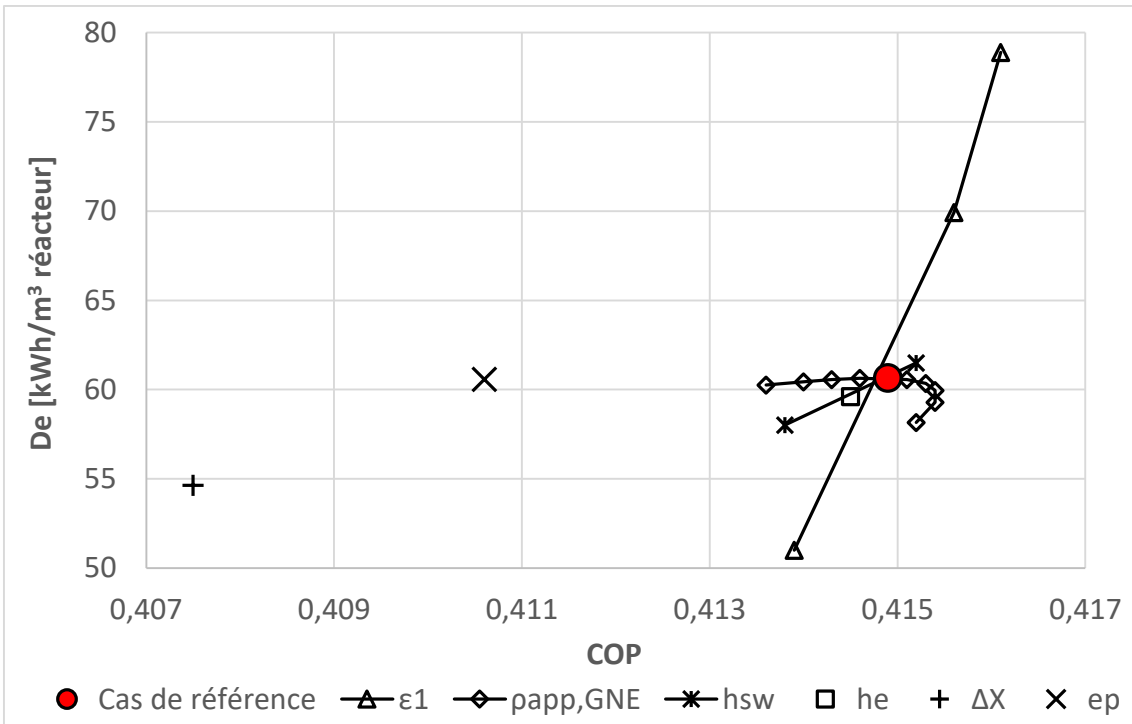


Figure A.4. Evolution of the relationship between energy storage density and COP of the thermochemical subsystem as a function of composite implementation parameters, with the ammonia / strontium chloride reactive pair.

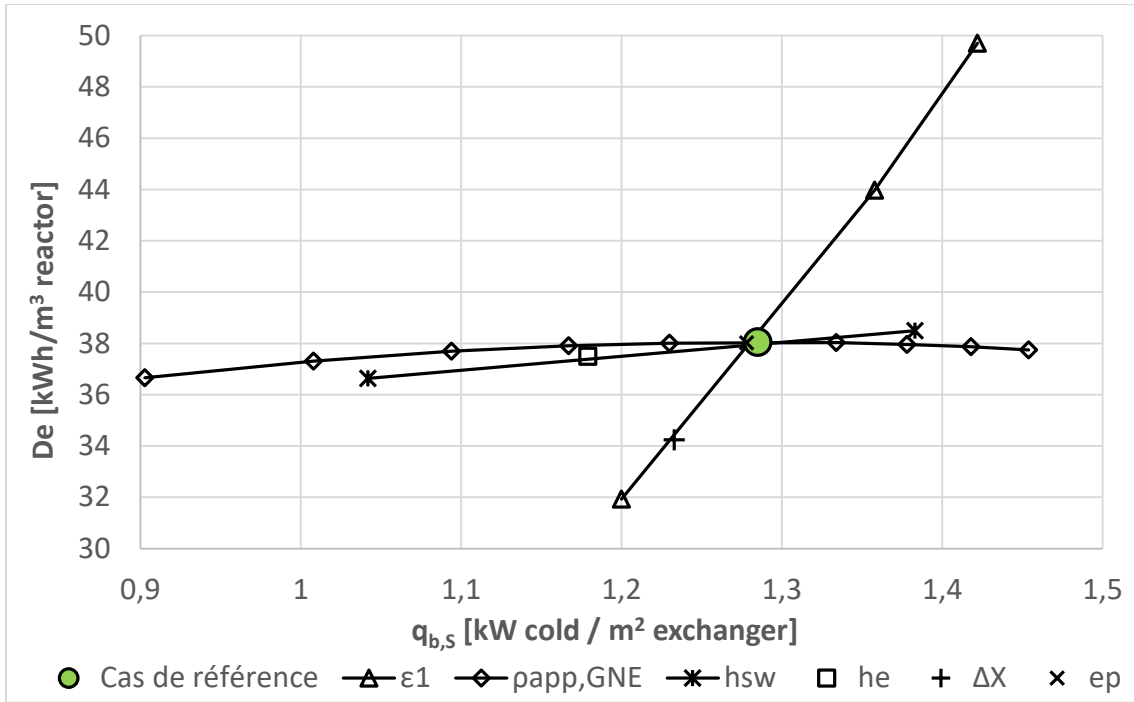


Figure A.5. Evolution of the relationship between energy storage density and cooling power (per unit surface) of the thermochemical subsystem as a function of composite implementation parameters, with the ammonia / calcium chloride (8-4) reactive pair.

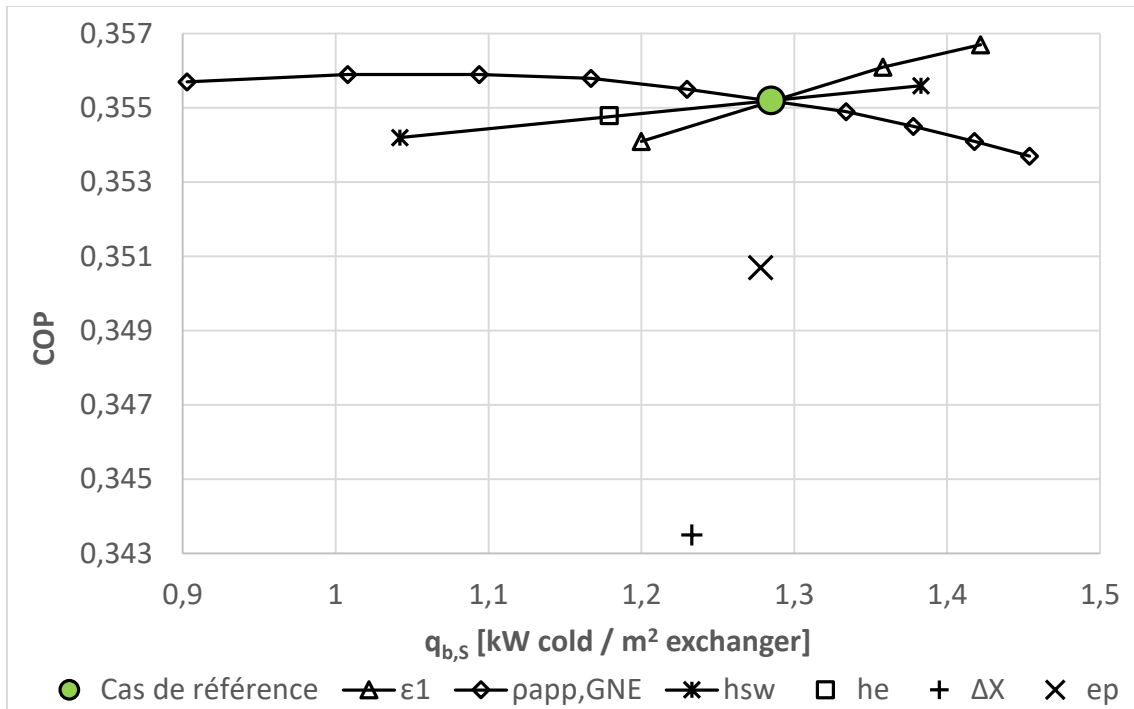


Figure A.6. Evolution of the relationship between COP and cooling power (per unit surface) of the thermochemical subsystem as a function of composite implementation parameters, with the ammonia / calcium chloride (8-4) reactive pair.

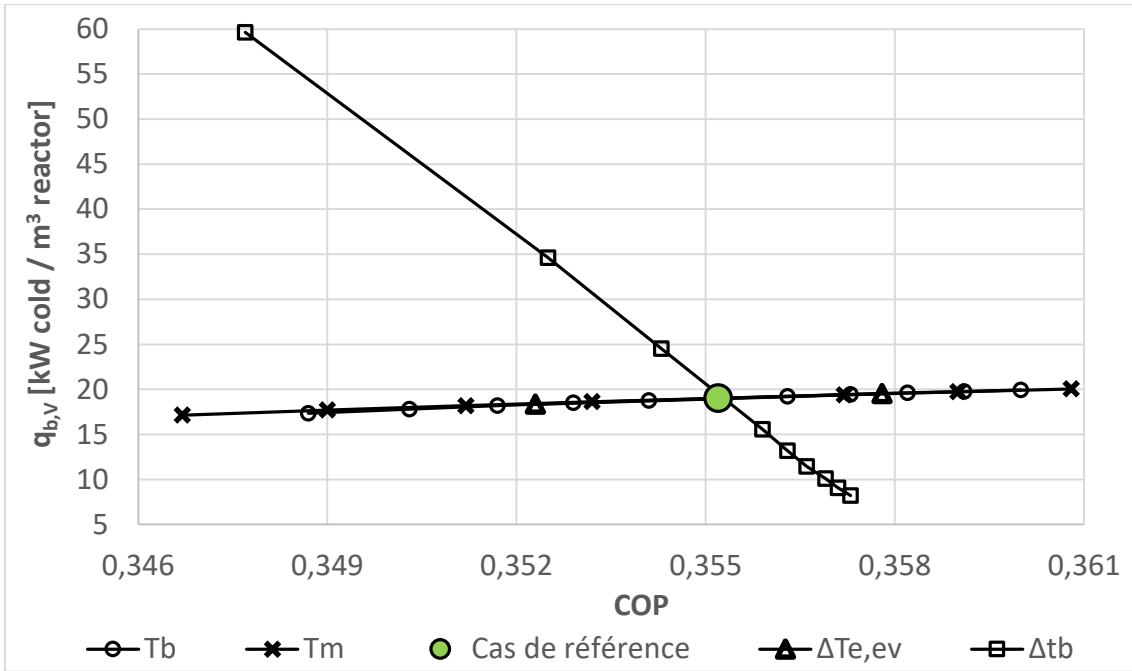


Figure A.7. Evolution of the relationship between COP and cooling power (per unit volume) of the thermochemical subsystem as a function of operating conditions, with the ammonia / calcium chloride (8-4) reactive pair.

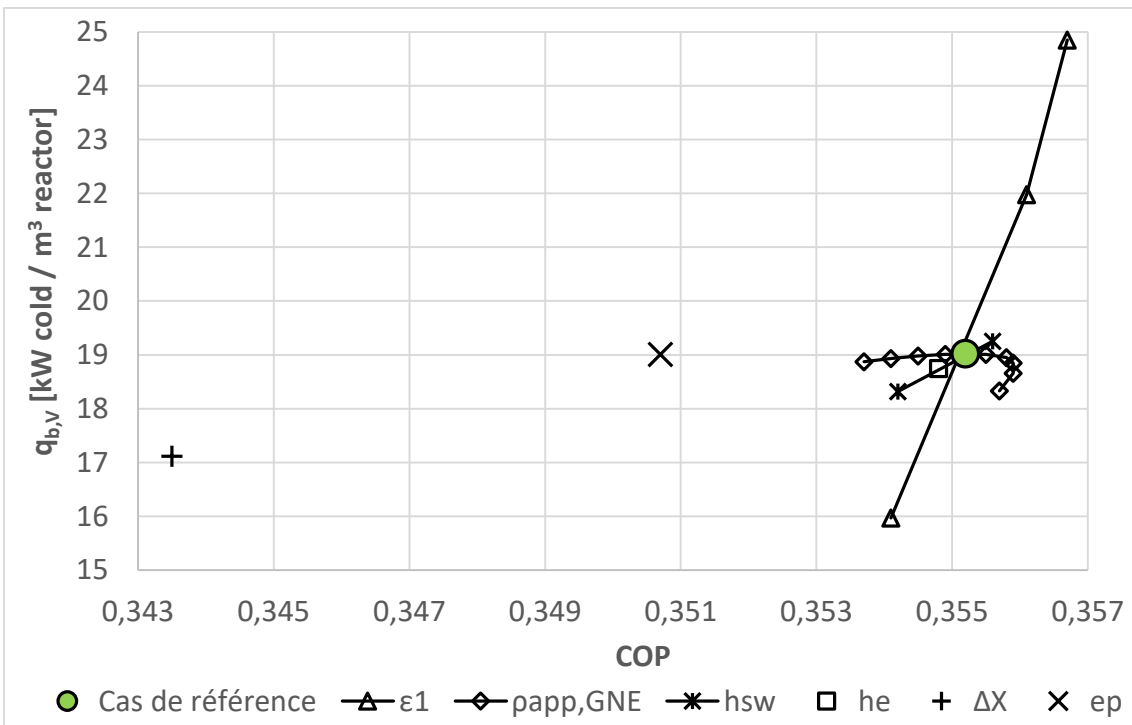


Figure A.8. Evolution of the relationship between COP and cooling power (per unit volume) of the thermochemical subsystem as a function of composite implementation parameters, with the ammonia / calcium chloride (8-4) reactive pair.

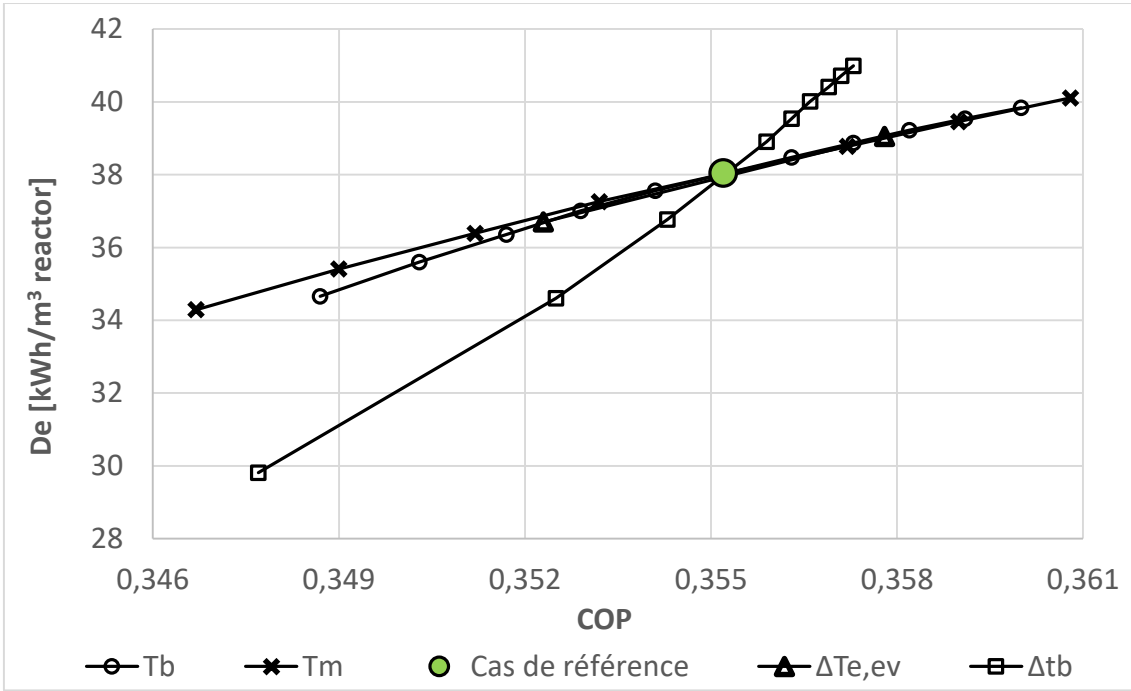


Figure A.9. Evolution of the relationship between COP and energy storage density of the thermochemical subsystem as a function of operating conditions, with the ammonia / calcium chloride (8-4) reactive pair.

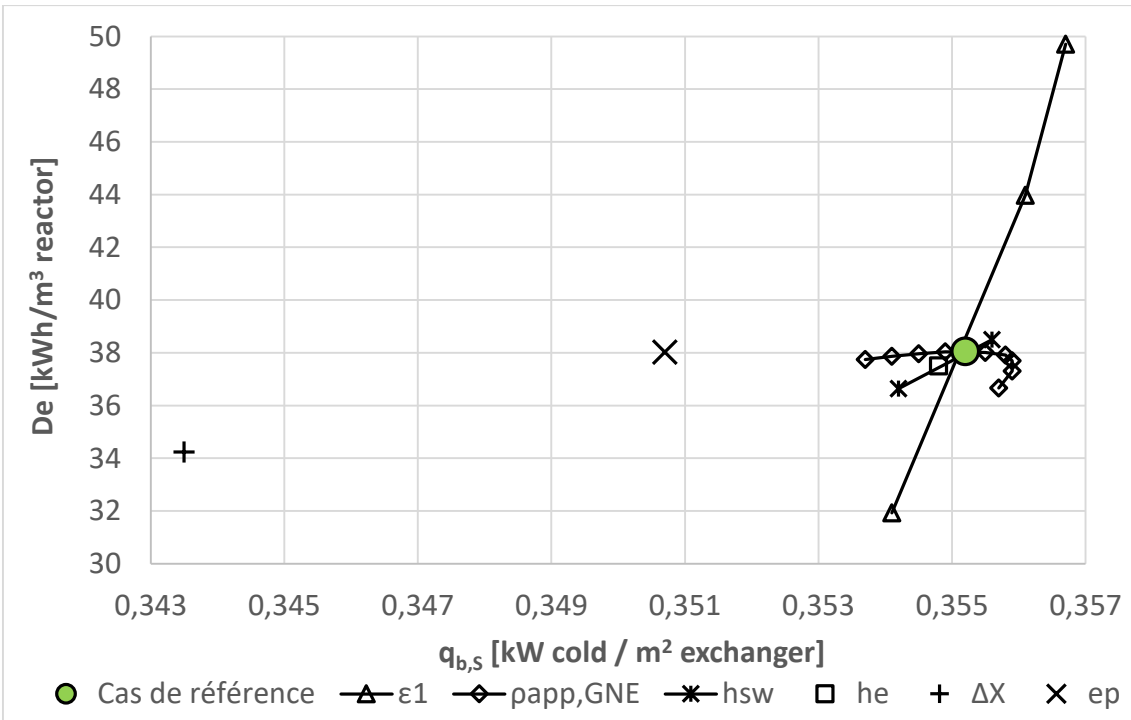


Figure A.10. Evolution of the relationship between energy storage density and cooling power (per unit surface) of the thermochemical subsystem as a function of composite implementation parameters, with the ammonia / calcium chloride (8-4) reactive pair.

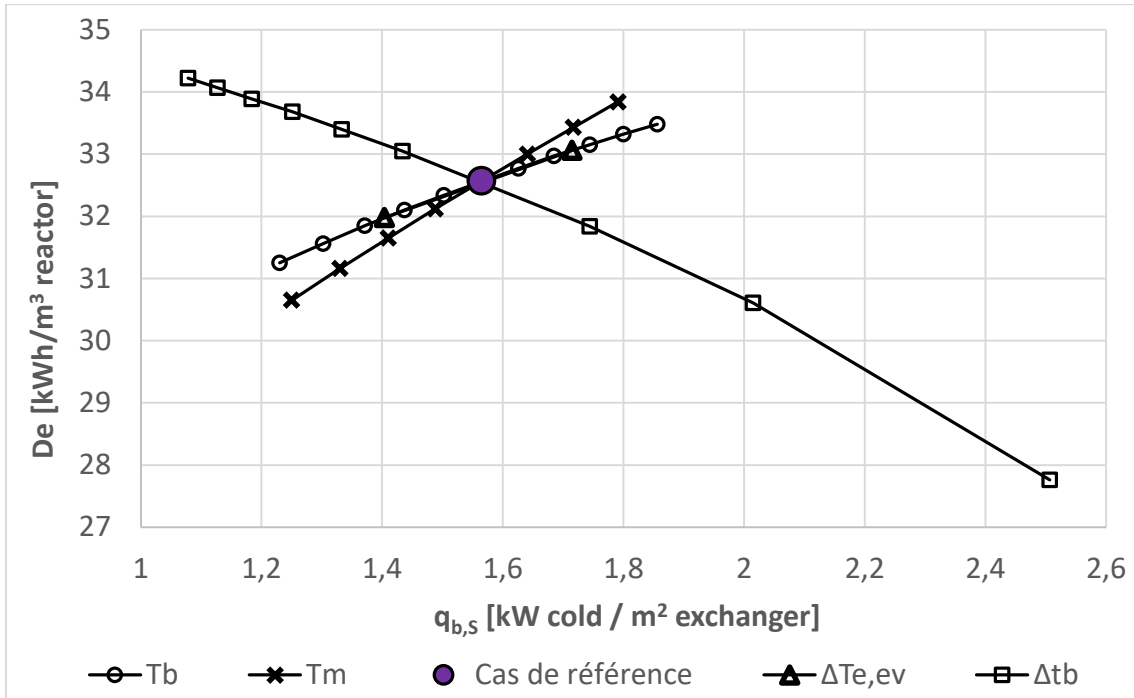


Figure A.11. Evolution of the relationship between energy storage density and cooling power (per unit surface) of the thermochemical subsystem as a function of operating conditions, with the ammonia / calcium chloride (4-2) reactive pair.

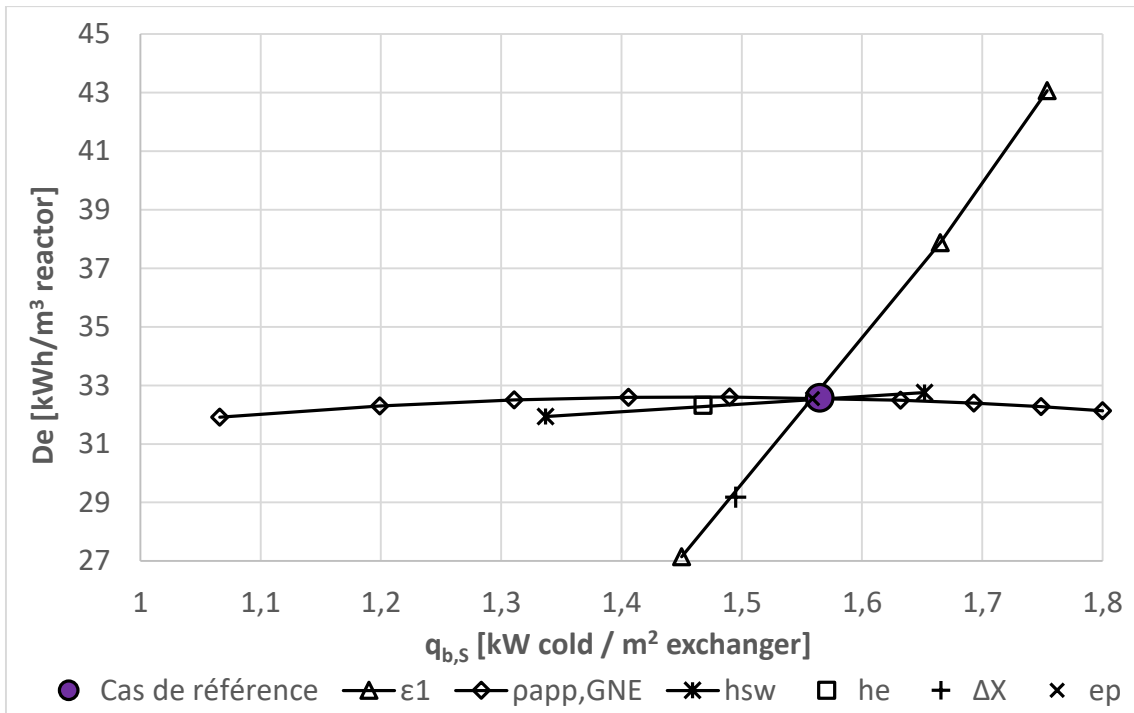


Figure A.12. Evolution of the relationship between energy storage density and cooling power (per unit surface) of the thermochemical subsystem as a function of composite implementation parameters, with the ammonia / calcium chloride (4-2) reactive pair.

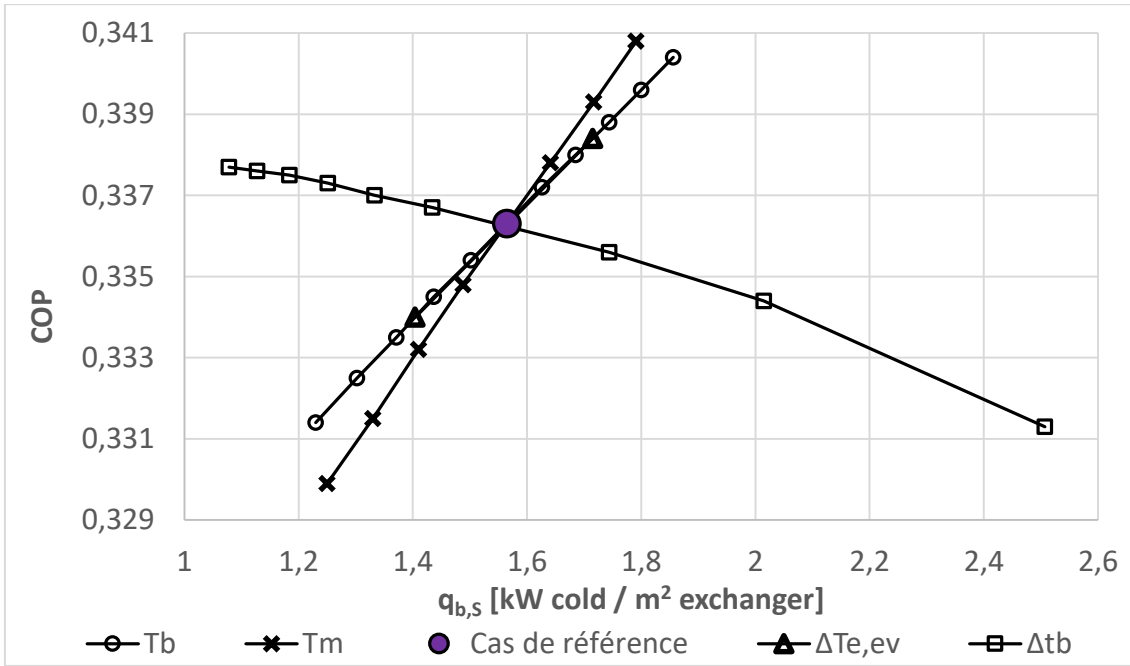


Figure A.13. Evolution of the relationship between COP and cooling power (per unit surface) of the thermochemical subsystem as a function of operating conditions, with the ammonia / calcium chloride (4-2) reactive pair.

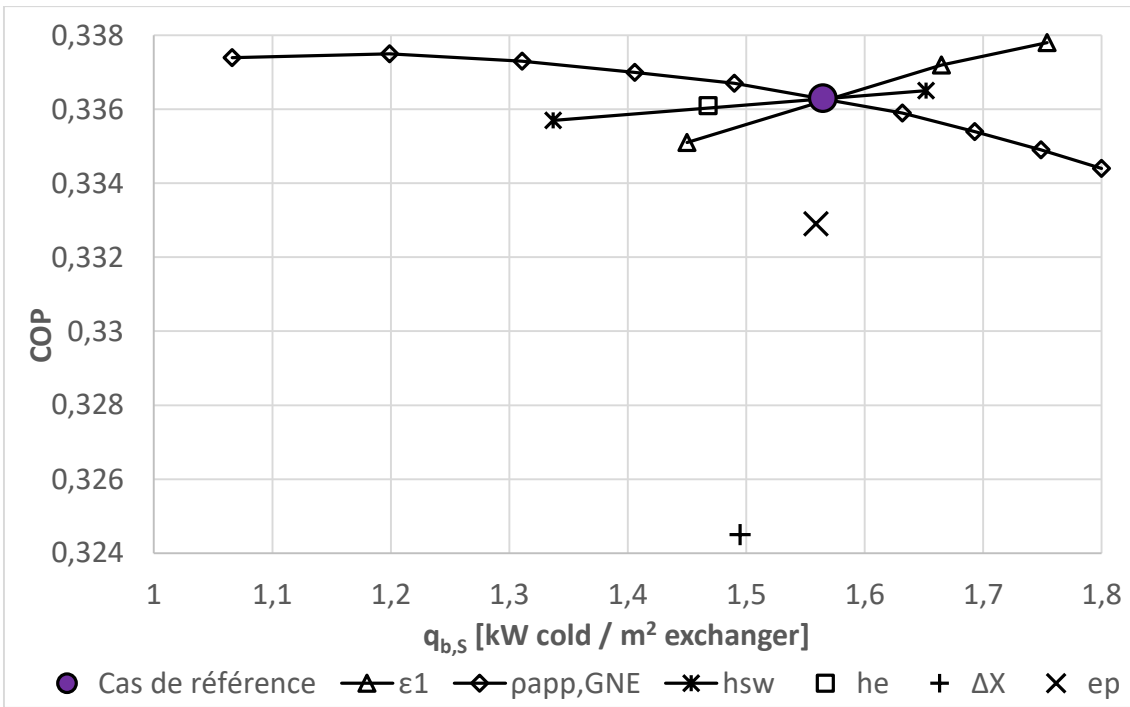


Figure A.14. Evolution of the relationship between COP and cooling power (per unit surface) of the thermochemical subsystem as a function of composite implementation parameters, with the ammonia / calcium chloride (4-2) reactive pair.

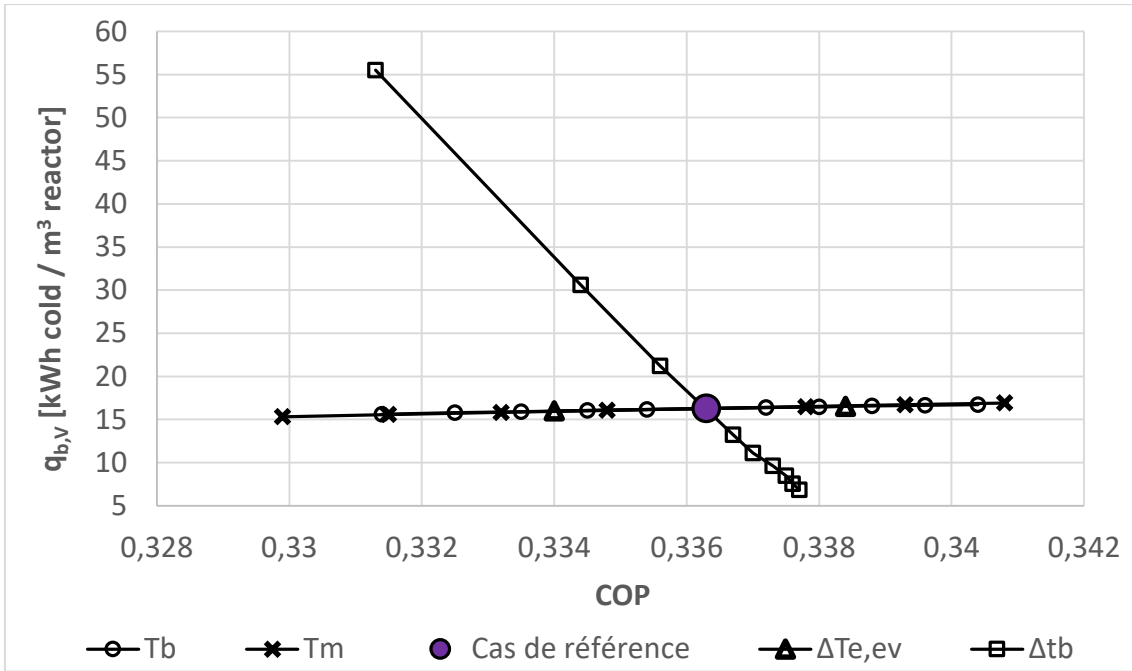


Figure A.15. Evolution of the relationship between COP and cooling power (per unit volume) of the thermochemical subsystem as a function of operating conditions, with the ammonia / calcium chloride (4-2) reactive pair.

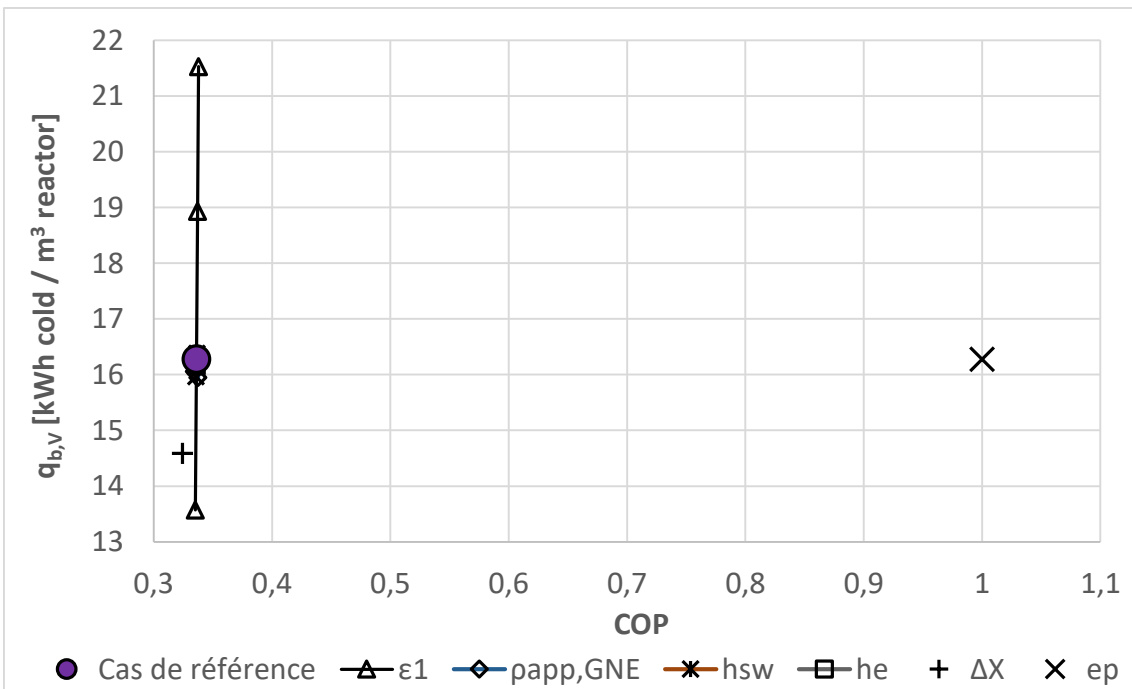


Figure A.16. Evolution of the relationship between COP and cooling power (per unit volume) of the thermochemical subsystem as a function of composite implementation parameters, with the ammonia / calcium chloride (4-2) reactive pair.

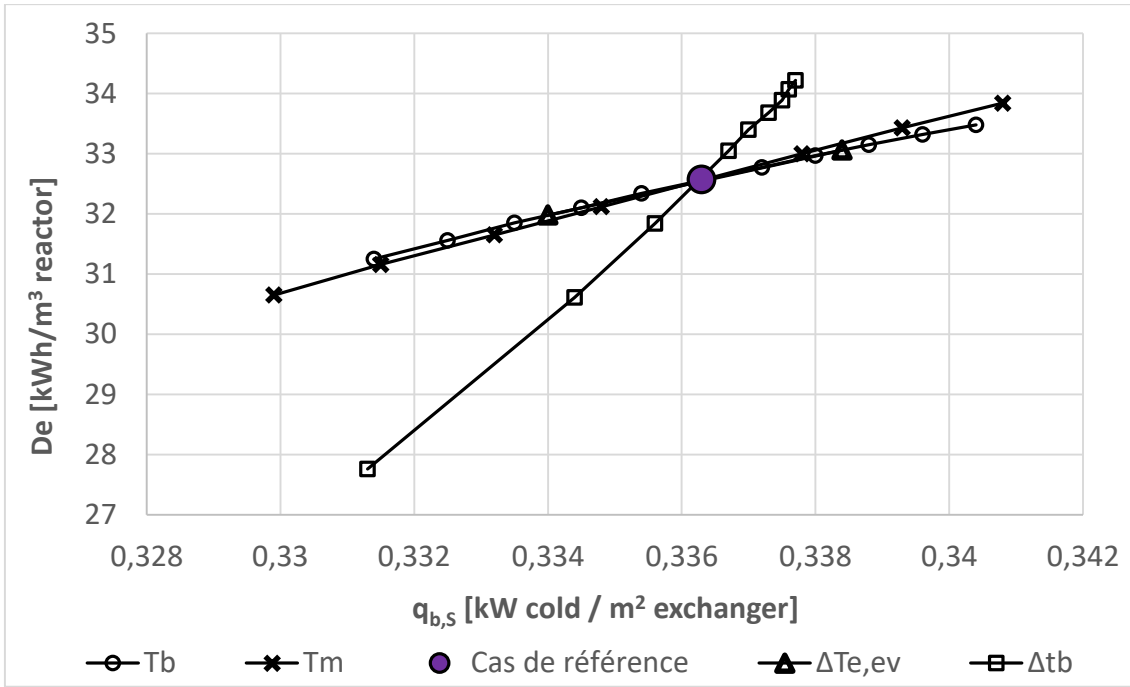


Figure A.17. Evolution of the relationship between energy storage density and cooling power (per unit surface) of the thermochemical subsystem as a function of operating conditions, with the ammonia / calcium chloride (4-2) reactive pair.

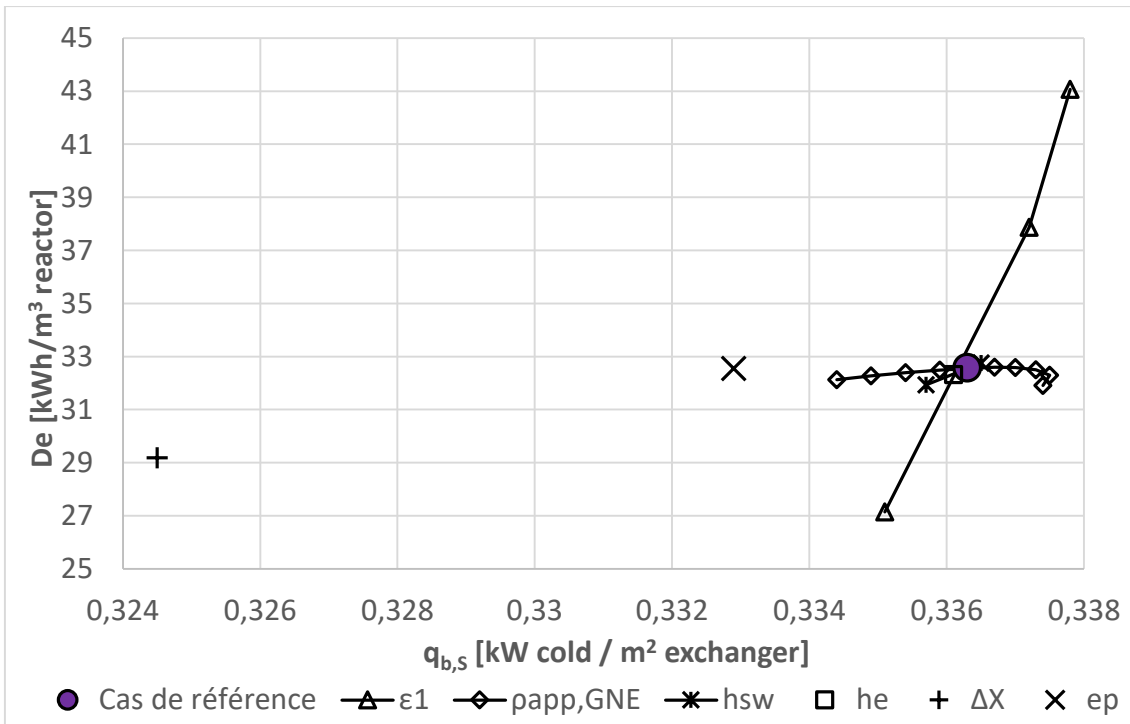


Figure A.18. Evolution of the relationship between energy storage density and cooling power (per unit surface) of the thermochemical subsystem as a function of composite implementation parameters, with the ammonia / calcium chloride (4-2) reactive pair.

"This page intentionally left blank"

Appendix B: Matlab codes for simulation of the synthesis and decomposition phases of the hybrid compression / thermochemical refrigeration system

B.1 CODE FOR SIMULATION OF THE COMPRESSION-ASSISTED DECOMPOSITION PHASE

```
%Auteur: Sylvain MAURAN
%Date sur cahier laboratoire: 4 avril 2012
%modèle à 2 fronts raides en décomposition, lit à épaisseur constante
et coordonnées cylindriques
%réaction : <BaCl2.8NH3> ==> <BaCl2> + 8 NH3
%Prise en compte du coefficient de Klinkenberg pour le transfert de
masse
tic
clc
clear all
format long g
%%%%%%%%%%%%%%%%%%%%%%%%%%%%%%%%%%%%%%%%%%%%%%%%%%%%%%%%%%%%%%%%%%%%%%%%
% Mise en oeuvre du composite
Dec=100;          % densité énergétique du composite en kWh/m3
dg=100;          % masse volumique apparente du GNE dans le composite
en kg/m3
rsw=.1102/2;     % rayon interne du tube réacteur en mètre, c-à-d du
centre diffuseur jusqu'à l'interface sel/paroi échangeur
rdif=.01/2;     % rayon externe du diffuseur en mètre, c-à-d du centre
diffuseur jusqu'à l'interface sel/paroi diffuseur
hco=.6;         % en m; hauteur du composite (influe sur ns et débit
sortant)
Dec=Dec*3600000; % en J/m3

%%%%%%%%%%%%%%%%%%%%%%%%%%%%%%%%%%%%%%%%%%%%%%%%%%%%%%%%%%%%%%%%%%%%%%%%
% Contraintes thermodynamiques
Tc=51.0;        % température de contrainte du réacteur en °C
Tc=Tc+273.15;  % température de contrainte du réacteur en K
Pc=9.1;        % Pression de contrainte du réacteur en bar
Pc=Pc*100000;  % Pression de contrainte du réacteur en Pa
Tcond=15;      % °C; Température du condenseur.

%%%%%%%%%%%%%%%%%%%%%%%%%%%%%%%%%%%%%%%%%%%%%%%%%%%%%%%%%%%%%%%%%%%%%%%%
% Définition des paramètres et constantes
ng0=0;         % nombre de moles de gaz fixées par mole de sel à X=0
ng=8;         % nombre de moles de gaz échangées par mole de sel
Msa=.20823;    % masse molaire du sel anhydre <BaCl2> en kg/mol
Mg=0.017031;  % masse molaire du gaz (NH3) en kg/mol
Ms0=Msa+ng0*Mg; % masse molaire du sel à X=0 en kg/mol
Ms1=Ms0+ng*Mg; % masse molaire du sel à X=1 <Ca(OH)2> en kg/mol
CpGNE=846;    % en J/(kg*K), Capacité calorifique du GNE (originelle
846 J/(kg*K))
```

```

Cps0=75.930;      % en J/(mol-s*K), Capacité calorifique molaire du sel
à X=0 (originelle 75.930 J/(mol-s*K))
Cps1=77.730;      % en J/(mol-s*K), Capacité calorifique molaire du sel
à X=1 (originelle 77.730 J/(mol-s*K))
R=8.3144;         % constante GP en J/mol/K
dh=38250;         % enthalpie de la réaction en J/mol de NH3.
ds=136.657;       % entropie de la réaction en J/mol/K [F. Schaube,
Thermochimica acta, mars 2012]
dhg=23366;        % En J/mol-G, Enthalpie de vaporisation de l'ammoniac
dsg=97.587;       % En J/(mol-G.K), Entropie de vaporisation (avec
P/P°)
Teq=dh/(ds-R*log(Pc/1e5)); % température d'équilibre (en K) de la
réaction solide/gaz pour la pression de contrainte
Tcart=Tc-Teq;     % °C; Écart à l'équilibre.
mu=1e-6*(0.0403*(Tc+Teq)/2-2.6835); % viscosité vapeur d'eau en Pa.s.
Peq=1e5*(exp(-dh/(R*Tc)+ds/R)); % pression d'équilibre de la réaction
en Pa
Pcond=exp(dsg/R-dhg/(R*(273.15+Tcond))); % En bar, pression au
condenseur
nse=Dec*pi*(rsw^2-rdif^2)*hco/(ng*dh); % nombre de moles de sel dans
réacteur
%mu=1e-6*(0.0403*(Tc+Teq)/2-2.6835); % viscosité vapeur d'eau en Pa.s.
% Régression linéaire entre 300 et 900K à partir de data de Refprop
V9.0. Par simplification on considère la vapeur d'eau à T constant
(égale à la moyenne de Tc et Teq)
vsa=Msa/3917;     % volume molaire du sel anhydre <BaCl2> en
m3/mol,déduite de la masse volumique moyenne donnée dans Handbook
vs0=vsa;         % volume molaire du sel à X=0 en m3/mol
vs1=0.0002258;   % volume molaire du sel à X=1 en m3/mol,déduite de la
masse volumique donnée dans Handbook
epsga=0.000001;  % porosité du grain de sel anhydre. Valeur à déduire
expérimentalement par le pycnomètre à Hélium
epsg0=1/(1+vs0/vsa*(1/epsga-1)); % porosité du grain de sel à X=0.
Le volume poreux du grain est constant.
epsg1=1/(1+vs1/vsa*(1/epsga-1)); % porosité du grain de sel à X=1.
Le volume poreux du grain est constant.
ws=1/(1+ng*dh*dg/(Dec*Msa)); % taux massique de sel anhydre
dans le composite
ws0=1/(1+Msa/Ms0*(1/ws-1)); % taux massique de sel à X=0
ws1=1/(1+Msa/Ms1*(1/ws-1)); % taux massique de sel à X=1
Cpc0=(1-ws0)*CpGNE+ws0*Cps0/Ms0; % en J/(kg*K), Capacité
calorifique du composite à X=0
Cpc1=(1-ws1)*CpGNE+ws1*Cps1/Ms1; % en J/(kg*K), Capacité
calorifique du composite à X=1

%%%%%%%%%%%%%%%%%%%%%%%%%%%%%%%%%%%%%%%%%%%%%%%%%%%%%%%%%%%%%%%%%%%%%%%%
% Transferts thermiques
hsw=358; % coefficient d'échange à la paroi en W/m2/K % hsw=1000
%variante coeff. non limitant
% Estimation conductivités en transfert radial, c-à-d perpendiculaire
à la direction de compression du composite GNE/sel. Modèle de Olives,
valable si dg>50 kg/m3
alpha=0.8; % coeff dans corrélation de Régis (thèse)
lambdab0=2.7; % conductivité du GNE isotrope à dg =50kg/m3 en
W/(m.K)
lambdab=lambdab0*(dg/50)^(4/3+0.17); % conductivité axiale
effective du GNE, corrélation de Régis (eq 2.56 thèse)

```



```

fs0=dg/(Ms0/vs0*(1-eps0))*(ws0/(1-ws0)); % fraction volumique du
sel à X=0 dans le composite. Le volume apparent du grain de sel tient
compte de sa porosité (eq 2.60 thèse)
fs1=dg/(Ms1/vs1*(1-eps1))*(ws1/(1-ws1)); % fraction volumique du
sel à X=1 dans le composite
lambda0=lambdab/(1+alpha*fs0)^2; % en W/m.K, conductivité
axiale effective du composite à X=0, corrélation de Régis (eq 2.59
thèse)
lambda1=lambdab/(1+alpha*fs1)^2; % en W/m.K, conductivité
axiale effective du composite à X=1, corrélation de Régis
lambda0=0.85; %variante transfert thermique non limitant. Mais
inapplicable avec le critère de convergence choisi sur Tf2
lambda1=0.85; %variante transfert thermique non limitant. Mais
inapplicable avec le critère de convergence choisi sur Tf2

%%%%%%%%%%%%%%%%%%%%%%%%%%%%%%%%%%%%%%%%%%%%%%%%%%%%%%%%%%%%%%%%%%%%%%%%
% Estimation perméabilités et coefficients de Klinkenberg
robe0=1/(1/dg-(ws/(1-ws))*vs0/(Msa*(1-eps0))); % masse volumique
apparente effective en kg/m3 du GNE dans composite à X=0. Le volume
apparent du grain de sel tient compte de sa porosité
robe1=1/(1/dg-(ws/(1-ws))*vs1/(Msa*(1-eps1))); % masse volumique
apparente effective en kg/m3 du GNE dans composite à X=1
k0=10^(-5.24-3.83*log10(robe0)); % permeabilite du composite à X=0
en m2, corrélation de SM [Solar Energy 2006]. Problème: cette
corrélation a été établie dans la direction axiale (qui serait
inférieure à la perméabilité radiale) mais avec des densités
% de GNE faibles (<60 kg/m3) pour lesquelles le composite est
quasi isotrope. Eq 20 de thèse H. Lahmidi.
k1=10^(-5.24-3.83*log10(robe1)); %permeabilite du composite à X=1
en m2, corrélation de SM.
%k0=1e-15; %variante si TM négligé 1e-10
%k1=1e-15; %variante si TM négligé 1e-10
b0=1.507e-9*k0^-.9461; % coeff Klinkenberg du composite
à X=0 en Pa. Eq 19 de thèse H. Lahmidi.
b1=1.507e-9*k1^-.9461; % coeff Klinkenberg du composite
à X=1 en Pa.
b0=0; %variante si coeff Klinkenberg négligé
b1=0; %variante si coeff Klinkenberg négligé

%%%%%%%%%%%%%%%%%%%%%%%%%%%%%%%%%%%%%%%%%%%%%%%%%%%%%%%%%%%%%%%%%%%%%%%%
%Itération sur X (noté x) par pas de dx variable jusqu'à convergence
sur temps de réaction t à X=0.99
dtr99=1;
dx=.02; % Pas de taux de réaction (originel: .02)
k=1; % initialisation du nombre de boucles nécessaires jusqu'à
convergence
temps99(1)=0;
while (dtr99>.01) % Originel: (dtr99>.01)
% Initialisation
t=0; % temps
x1=1; % taux de réaction initial du front "de masse"
x2=1; % taux de réaction initial du front "de chaleur"
x=1; % taux de réaction global initial
deltat=0; % incrément de temps
Tf2=Tc; % Température initiale au front de chaleur
Tsw=Tc; % Température initiale à la paroi de l'échangeur
en contact avec le sel
Pc=8*100000; % Pa

```

```

Pf1=Pc;           % Pression initiale au front de masse
rf1=rdif;        % Position initiale du front de masse
rf2=rsw;         % Position initiale du front de chaleur
Tf1=dh/(ds-R*log(Pf1/1e5));           % Température au front de
masse
Pf2=1e5*(exp(-dh/(R*Tf2)+ds/R));      % Pression de vapeur au front
de chaleur
n1=2*lambda1*(Tf1-Tf2)/(Dec*(rsw*rsw-rdif*rdif)*log(rf2/rf1));
%dX1/dt c-à-d vitesse de réaction au front de masse
n2=dh*k1*((Pf1^2-Pf2^2)+2*b1*(Pf1-Pf2))/(mu*R*Tc*Dec*(rsw*rsw-
rdif*rdif)*log(rf2/rf1)); %dX2/dt c-à-d vitesse de réaction au front
de chaleur
n3=n1+n2;          %dX/dt vitesse de réaction totale au taux de
réaction X
Tempfront2=Tc;    % température retenue ici pour le front de chaleur
temps(1)=t;
avancement(1)=x;
avancement1(1)=x1;
avancement2(1)=x2;
pressionc(1)=Pc;
Tfront2(1)=dh/(ds-R*log(Pc*1e-5));
dx=dx/2;          % delta X à la lère boucle k égal à 0.01
k=k+1;
jdiscret=1;
jj=99*2^(k-2)+1; %Astuce pour n'enregistrer finalement que 100
valeurs de t(X) quelque soit le dX final après k boucles
for j=2:jj
x1=x1-n1*dx/n3;
x2=x2-n2*dx/n3;
x=x-dx;
if x > 0.925
Pc=948359.031704*x^4-
3599569.222806*x^3+5123146.895739*x^2-3240516.243712*x+768588.233100;
%bar
else Pc=1; %bar
end
Pc=Pc*1e5; %Pa
rf1=(rdif^2+(1-x1)*(rsw^2-rdif^2))^0.5;
rf2=(rsw^2-(1-x2)*(rsw^2-rdif^2))^0.5;

Tsw=(lambda0*Tf2/log(rsw/rf2)+hsw*rsw*Tc)/(lambda0/log(rsw/rf2)+hsw*rs
w);
DTf2=10;         %initialisation du critère de convergence sur la
température calculée au front de chaleur par itération
i=1;
imax=100;

%%%%%%%%%%%%%%%%%%%%%%%%%%%%%%%%%%%%%%%%%%%%%%%%%%%%%%%%%%%%%%%%%%%%%%%%
%Itération pour convergence par méthode de Newton-
Raphson
while (DTf2>1e-8) % Original: 1e-9
i=i+1;
%disp(i)
if i > imax
disp('problème de convergence sur Tf2')
break
end
T2=Tf2(i-1); %changement de nom nécessaire pour le
calcul symbolique

```

```

% syms T2 dh ds R Tc Tsw Pc mu lambda0 lambda1 k0 k1
b0 b1 rf1 rf2 rdif rsw; %Calcul symbolique effectué une fois
Pf2=1e5*(exp(-dh/(R*T2)+ds/R)); %Pression d'équilibre
pour la température du front de chaleur au pas précédent avec
Tf2(1)=Tc, valeur par défaut quand k=1
c=2*mu*lambda0*R*Tc*(T2-
Tsw)*log(rf1/rdif)/(dh*k0*log(rsw/rf2))-Pc*(Pc+2*b0);
Pf1=-b0+(b0^2-c)^(0.5); % racine positive de
l'équation du 2nd degré en Pf1
Tf1=dh/(ds-R*log(Pf1*1e-5));
Tf2i=Tf1-dh*log(rf2/rf1)*(k0*((Pc^2-Pf1^2)+2*b0*(Pc-
Pf1))/log(rf1/rdif)-k1*((Pf1^2-Pf2^2)+2*b1*(Pf1-
Pf2))/log(rf2/rf1))/(2*mu*R*Tc*lambda1); % autre façon de calculer Tf2
fct=T2-Tf2i; %fonction à dériver
% derivef=diff(fct,T2) % Calcul symbolique effectué
une fois et dont le résultat est reproduit et affecté à la variable
derivef2

%
derivef2=(dh*log(rf2/rf1)*((k1*(2*b1*((100000*dh*exp(ds/R -
dh/(R*T2)))/(R*T2^2) +
(R*Tc*lambda0*mu*log(rf1/rdif))/(dh*k0*log(rsw/rf2)*(Pc*(Pc + 2*b0) +
b0^2 - (2*R*Tc*lambda0*mu*log(rf1/rdif)*(T2 -
Tsw))/(dh*k0*log(rsw/rf2)))^(1/2))) + (20000000000*dh*exp((2*ds)/R -
(2*dh)/(R*T2)))/(R*T2^2) - (2*R*Tc*lambda0*mu*log(rf1/rdif)*(b0 -
(Pc*(Pc + 2*b0) + b0^2 - (2*R*Tc*lambda0*mu*log(rf1/rdif)*(T2 -
Tsw))/(dh*k0*log(rsw/rf2)))^(1/2)))/(dh*k0*log(rsw/rf2)*(Pc*(Pc +
2*b0) + b0^2 - (2*R*Tc*lambda0*mu*log(rf1/rdif)*(T2 -
Tsw))/(dh*k0*log(rsw/rf2)))^(1/2))))/log(rf2/rf1) +
(k0*((2*R*Tc*b0*lambda0*mu*log(rf1/rdif))/(dh*k0*log(rsw/rf2)*(Pc*(Pc
+ 2*b0) + b0^2 - (2*R*Tc*lambda0*mu*log(rf1/rdif)*(T2 -
Tsw))/(dh*k0*log(rsw/rf2)))^(1/2)) -
(2*R*Tc*lambda0*mu*log(rf1/rdif)*(b0 - (Pc*(Pc + 2*b0) + b0^2 -
(2*R*Tc*lambda0*mu*log(rf1/rdif)*(T2 -
Tsw))/(dh*k0*log(rsw/rf2)))^(1/2)))/(dh*k0*log(rsw/rf2)*(Pc*(Pc +
2*b0) + b0^2 - (2*R*Tc*lambda0*mu*log(rf1/rdif)*(T2 -
Tsw))/(dh*k0*log(rsw/rf2)))^(1/2))))/log(rf1/rdif)))/(2*R*Tc*lambda1*m
u) - (R^2*Tc*lambda0*mu*log(rf1/rdif))/(100000*k0*log(rsw/rf2)*(ds -
R*log((Pc*(Pc + 2*b0) + b0^2 - (2*R*Tc*lambda0*mu*log(rf1/rdif)*(T2 -
Tsw))/(dh*k0*log(rsw/rf2)))^(1/2)/100000 - b0/100000))^2*(b0/100000 -
(Pc*(Pc + 2*b0) + b0^2 - (2*R*Tc*lambda0*mu*log(rf1/rdif)*(T2 -
Tsw))/(dh*k0*log(rsw/rf2)))^(1/2)/100000)*(Pc*(Pc + 2*b0) + b0^2 -
(2*R*Tc*lambda0*mu*log(rf1/rdif)*(T2 -
Tsw))/(dh*k0*log(rsw/rf2)))^(1/2)) + 1
reduc=(Pc*(Pc + 2*b0) + b0^2 -
(2*R*Tc*lambda0*mu*log(rf1/rdif)*(T2 -
Tsw))/(dh*k0*log(rsw/rf2)))^(1/2); % ce terme n'apparaissait pas dans
le développement de derivef donné par Matlab; c'est moi qui est trouvé
ce facteur commun sur le modèle de ce que j'avais dans le précédent
programme où la dérivation avait été faite par MuPad
derivef2=(dh*log(rf2/rf1)*((k1*(2*b1*((1e5*dh*exp(ds/R
- dh/(R*T2)))/(R*T2^2) +
(R*Tc*lambda0*mu*log(rf1/rdif))/(dh*k0*log(rsw/rf2)*reduc)) +
(2e10*dh*exp((2*ds)/R - (2*dh)/(R*T2)))/(R*T2^2) -
(2*R*Tc*lambda0*mu*log(rf1/rdif)*(b0 -
reduc))/(dh*k0*log(rsw/rf2)*reduc))/log(rf2/rf1) +
(k0*((2*R*Tc*b0*lambda0*mu*log(rf1/rdif))/(dh*k0*log(rsw/rf2)*reduc) -
(2*R*Tc*lambda0*mu*log(rf1/rdif)*(b0 -
reduc))/(dh*k0*log(rsw/rf2)*reduc))/log(rf1/rdif)))/(2*R*Tc*lambda1*m

```

```

u) - (R^2*Tc*lambda0*mu*log(rf1/rdif))/(1e5*k0*log(rsw/rf2)*(ds -
R*log(reduc/1e5 - b0/1e5))^2*(b0/1e5 - reduc/1e5)*reduc) + 1;
    Tf2(i)=T2-fct/derivesf2;
    DTf2=abs(Tf2(i)-T2); % test de convergence : écart
absolu sur Tf2 en °C
    %disp(DTf2)
end

%%%%%%%%%%%%%%%%%%%%%%%%%%%%%%%%%%%%%%%%%%%%%%%%%%%%%%%%%%%%%%%%%%%%%%%%
Tempfront2=Tf2(i);
Pf2=1e5*(exp(-dh/(R*Tempfront2)+ds/R));
c=2*mu*lambda0*R*Tc*(Tempfront2-
Tsw)*log(rf1/rdif)/(dh*k0*log(rsw/rf2))-Pc*(Pc+2*b0);
Pf1=-b0+(b0^2-c)^(0.5);
Tf1=dh/(ds-R*log(Pf1*1e-5));
n1=2*lambda1*(Tf1-Tempfront2)/(Dec*(rsw*rsw-
rdif*rdif)*log(rf2/rf1));
n2=dh*k1*((Pf1^2-Pf2^2)+2*b1*(Pf1-
Pf2))/(mu*R*Tc*Dec*(rsw*rsw-rdif*rdif)*log(rf2/rf1));
n3=n1+n2; % dX/dt vitesse de réaction totale
au taux de réaction X
%na0_point=-nse1*ng*n3; % mol-NH3/s; Débit molaire de gaz
aspiré par le compresseur
%Va0_point=na0_point*R*(0+273.15)/101325; % m3/s
%Va0_point=Va0_point*60*1e3; % L/min
%DP_comp=(-b_comp-(b_comp^2-4*a_comp*(c_comp-
Va0_point))^0.5)/(2*a_comp); % bar
%Pc=Pcond-DP_comp; % bar
%Pc=Pc*1e5; % Pa
%difPc=abs(Pc/1e5-Pcpre/1e5)/abs(Pc/1e5);
%end
deltat=-dx/(n3*60); % incrément de temps en minute pour le
pas dx choisi
t=t+deltat;
Tfront2(j)=Tf2(i);
if (j==2^(k-2)*jdiscret+1)
jdiscret=jdiscret+1 ;
temps(jdiscret)=t ;
avancement(jdiscret)=x;
disp(avancement(jdiscret))
avancement1(jdiscret)=x1;
avancement2(jdiscret)=x2;
pressionc(jdiscret)=Pc;
limhsw(jdiscret)=abs((Tsw-Tc)/(Tempfront2-Tc));
end
Tf2=Tempfront2;
end
temps99(k)=temps(jdiscret);
dtr99=abs(temps99(k)-temps99(k-1))/temps99(k); % test de
convergence : écart relatif sur t à X=.99
if (k>5)
disp('Convergence sur dx difficile : k>5')
break
end
end
end
vec_tout(:,1)=temps';
vec_tout(:,2)=avancement';
vec_tout(:,3)=pressionc'/1e5;
disp(' nombre de boucles pour convergence sur dx : k')

```

```

k
    if (k>5)
        disp(' convergence sur dx difficile : k>5')
    end
toc

```

B.2 CODE FOR SIMULATION OF THE SYNTHESIS PHASE

```

%Auteur: Sylvain MAURAN
%Date sur cahier laboratoire: 27 mars 2012
%modèle à 2 fronts raides en synthèse, lit à épaisseur constante et
coordonnées cylindriques
%réaction : <CaO> + (H2O) ==> <Ca(OH)2>
%Prise en compte du coefficient de Klinkenberg pour le transfert de
masse

clc
clear all

%%%%%%%%%%%%%%%%%%%%%%%%%%%%%%%%%%%%%%%%%%%%%%%%%%%%%%%%%%%%%%%%%%%%%%%%
% Mise en oeuvre du composite
Dec=100;          % densité énergétique du composite en kWh/m3
dg=100;          % masse volumique apparente du GNE dans le composite
en kg/m3
rsw=.1102/2;     % rayon interne du tube réacteur en mètre, c-à-d du
centre diffuseur jusqu'à l'interface sel/paroi échangeur
rdif=0.01/2;    % rayon externe du diffuseur en mètre, c-à-d du
centre diffuseur jusqu'à l'interface sel/paroi diffuseur
hco=0.6;        % en m; hauteur du composite (influe sur ns et débit
sortant)
Dec=Dec*3600000; % en J/m3

%%%%%%%%%%%%%%%%%%%%%%%%%%%%%%%%%%%%%%%%%%%%%%%%%%%%%%%%%%%%%%%%%%%%%%%%
% Contraintes thermodynamiques
Tc=5.8;         % température de contrainte du réacteur en °C
Pc=5.1;         % Pression de contrainte du réacteur en bar
Tc=Tc+273.15;  % température de contrainte du réacteur en K
Pc=Pc*100000;  % Pression de contrainte du réacteur en Pa

%%%%%%%%%%%%%%%%%%%%%%%%%%%%%%%%%%%%%%%%%%%%%%%%%%%%%%%%%%%%%%%%%%%%%%%%
% Définition des paramètres et constantes
ng0=0;         % nombre de moles de gaz fixées par mole de sel à X=0
ng=8;         % nombre de moles de gaz échangées par mole de sel
Msa=.20823;    % masse molaire du sel anhydre <BaCl2> en kg/mol
Mg=0.017031;  % masse molaire du gaz (NH3) en kg/mol
Ms0=Msa+ng0*Mg; % masse molaire du sel à X=0 en kg/mol
Ms1=Ms0+ng*Mg; % masse molaire du sel à X=1 <Ca(OH)2> en kg/mol
CpGNE=846;    % en J/(kg*K), Capacité calorifique du GNE (originelle
846 J/(kg*K))
Cps0=75.930;  % en J/(mol-s*K), Capacité calorifique molaire du sel
à X=0 (originelle 75.930 J/(mol-s*K))
Cps1=77.730;  % en J/(mol-s*K), Capacité calorifique molaire du sel
à X=1 (originelle 77.730 J/(mol-s*K))
R=8.3144;    % constante GP en J/mol/K
dh=38250;    % enthalpie de la réaction en J/mol de NH3.
ds=136.657;  % entropie de la réaction en J/mol/K [F. Schaubé,
Thermochimica acta, mars 2012]
dhg=23366;   % En J/mol-G, Enthalpie de vaporisation de l'ammoniac

```

```

dsg=97.587;          % En J/(mol-G.K), Entropie de vaporisation (avec
P/P°)
Teq=dh/(ds-R*log(Pc/1e5))-273.15; % température d'équilibre (en C) de
la réaction solide/gaz pour la pression de contrainte
mu=1e-6*(0.0403*(Tc+Teq)/2-2.6835); % viscosité vapeur d'eau en Pa.s.
Peq=1e5*(exp(-dh/(R*Tc)+ds/R)); % pression d'équilibre de la réaction
en Pa
nse1=Dec*pi*(rsw^2-rdif^2)*hco/(ng*dh); % nombre de moles de sel dans
réacteur
%Teq=dh/(ds-R*log(Pc/1e5)); % température d'équilibre (en K) de la
réaction solide/gaz pour la pression de contrainte
%mu=1e-6*(0.0403*(Tc+Teq)/2-2.6835); % viscosité vapeur d'eau en Pa.s.
% Régression linéaire entre 300 et 900K à partir de
data de Refprop V9.0. Par simplification on considère la vapeur d'eau
à T constant (égale à la moyenne de Tc et Teq)
vsa=Msa/3917; % volume molaire du sel anhydre <BaCl2> en
m3/mol, déduite de la masse volumique moyenne donnée dans Handbook
vs0=vsa; % volume molaire du sel à X=0 en m3/mol
vs1=0.0002258; % volume molaire du sel à X=1 en m3/mol, déduite de la
masse volumique donnée dans Handbook
epsga=0.000001; % porosité du grain de sel anhydre. Valeur à déduire
expérimentalement par le pycnomètre à Hélium
epsg0=1/(1+vs0/vsa*(1/epsga-1)); % porosité du grain de sel à X=0.
Le volume poreux du grain est constant.
epsg1=1/(1+vs1/vsa*(1/epsga-1)); % porosité du grain de sel à X=1.
Le volume poreux du grain est constant.
ws=1/(1+ng*dh*dg/(Dec*Msa)); % taux massique de sel anhydre
dans le composite
ws0=1/(1+Msa/Ms0*(1/ws-1)); % taux massique de sel à X=0
ws1=1/(1+Msa/Ms1*(1/ws-1)); % taux massique de sel à X=1
Cpc0=(1-ws0)*CpGNE+ws0*Cps0/Ms0; % en J/(kg*K), Capacité
calorifique du composite à X=0
Cpc1=(1-ws1)*CpGNE+ws1*Cps1/Ms1; % en J/(kg*K), Capacité
calorifique du composite à X=1

%%%%%%%%%%%%%%%%%%%%%%%%%%%%%%%%%%%%%%%%%%%%%%%%%%%%%%%%%%%%%%%%%%%%%%%%
% Transferts thermiques
hsw=358; % coefficient d'échange à la paroi en W/m2/K
% hsw=1000 % variante coeff. non limitant

% Estimation conductivités en transfert radial, c-à-d perpendiculaire
à la direction de compression du composite GNE/sel. Modèle de Olives,
valable si dg>50 kg/m3
alpha=0.8; % coeff dans corrélation de Régis (thèse)
lambdab0=2.7; % conductivité du GNE isotrope à dg =50kg/m3 en
W/(m.K)
lambdab=lambdab0*(dg/50)^(4/3+0.17); % conductivité axiale
effective du GNE, corrélation de Régis (eq 2.56 thèse)
fs0=dg/(Ms0/vs0*(1-epsg0))*(ws0/(1-ws0)); % fraction volumique du
sel à X=0 dans le composite. Le volume apparent du grain de sel tient
compte de sa porosité (eq 2.60 thèse)
fs1=dg/(Ms1/vs1*(1-epsg1))*(ws1/(1-ws1)); % fraction volumique du
sel à X=1 dans le composite
lambda0=lambdab/(1+alpha*fs0)^2; % en W/m.K, conductivité
axiale effective du composite à X=0, corrélation de Régis (eq 2.59
thèse)
lambda1=lambdab/(1+alpha*fs1)^2; % en W/m.K, conductivité
axiale effective du composite à X=1, corrélation de Régis
lambda0=0.85;

```

```

lambda1=lambda0;
%lambda0=10 %variante transfert thermique non limitant. Mais
inapplicable avec le critère de convergence choisi sur Tf2
%lambda1=10 %variante transfert thermique non limitant. Mais
inapplicable avec le critère de convergence choisi sur Tf2

%%%%%%%%%%%%%%%%%%%%%%%%%%%%%%%%%%%%%%%%%%%%%%%%%%%%%%%%%%%%%%%%%%%%%%%%
% Estimation perméabilités et coefficients de Klinkenberg
robe0=1/(1/dg-(ws/(1-ws))*vs0/(Msa*(1-eps0))); % masse volumique
apparente effective en kg/m3 du GNE dans composite à X=0. Le volume
apparent du grain de sel tient compte de sa porosité
robel=1/(1/dg-(ws/(1-ws))*vs1/(Msa*(1-eps1))); % masse volumique
apparente effective en kg/m3 du GNE dans composite à X=1
k0=10^(-5.24-3.83*log10(robe0)); % permeabilite du composite à X=0
en m2, corrélation de SM [Solar Energy 2006]. Problème: cette
corrélation a été établie dans la direction axiale (qui serait
inférieure à la perméabilité radiale) mais avec des densités
% de GNE faibles (<60 kg/m3) pour lesquelles le composite est
quasi isotrope. Eq 20 de thèse H. Lahmidi.
k1=10^(-5.24-3.83*log10(robel)); %permeabilite du composite à X=1
en m2, corrélation de SM.
%k0=1e-15; %variante si TM négligé 1e-10
%k1=1e-16; %variante si TM négligé 1e-10
b0=1.507e-9*k0^-.9461; % coeff Klinkenberg du composite
à X=0 en Pa. Eq 19 de thèse H. Lahmidi.
b1=1.507e-9*k1^-.9461; % coeff Klinkenberg du composite
à X=1 en Pa.
b0=0; %variante si coeff Klinkenberg négligé
b1=0; %variante si coeff Klinkenberg négligé

%%%%%%%%%%%%%%%%%%%%%%%%%%%%%%%%%%%%%%%%%%%%%%%%%%%%%%%%%%%%%%%%%%%%%%%%
%Itération sur X (noté x) par pas de dx variable jusqu'à convergence
sur temps de réaction t à X=0.99
dtr99=1;
dx=.02;
k=1; % initialisation du nombre de boucles nécessaires jusqu'à
convergence
temps99(1)=0;
while (dtr99>.01)
    % Initialisation
    t=0; % temps
    x1=0; % taux de réaction initial du front "de masse"
    x2=0; % taux de réaction initial du front "de chaleur"
    x=0; % taux de réaction global initial
    deltat=0; % incrément de temps
    Tf2=Tc; % Température initiale au front de chaleur
    Tsw=Tc; % Température initiale à la paroi de l'échangeur
en contact avec le sel
    Pf1=Pc; % Pression initiale au front de masse
    rf1=rdif; % Position initiale du front de masse
    rf2=rsw; % Position initiale du front de chaleur
    Tf1=dh/(ds-R*log(Pf1/1e5)); % Température au front de
masse
    Pf2=1e5*(exp(-dh/(R*Tf2)+ds/R)); % Pression de vapeur au front
de chaleur
    n1=2*lambda0*(Tf1-Tf2)/(Dec*(rsw*rsw-rdif*rdif)*log(rf2/rf1));
%dx1/dt c-à-d vitesse de réaction au front de masse

```

```

n2=dh*k0*((Pf1^2-Pf2^2)+2*b0*(Pf1-Pf2))/(mu*R*Tc*Dec*(rsw*rsw-
rdif*rdif)*log(rf2/rf1)); %dX/dt c-à-d vitesse de réaction au front
de chaleur
n3=n1+n2; %dX/dt vitesse de réaction totale au taux de
réaction X
Tempfront2=Tc; % température retenue ici pour le front de chaleur
temps(1)=t;
avancement(1)=x;
avancement1(1)=x1;
avancement2(1)=x2;
dx=dx/2; % delta X à la lère boucle k égal à 0.01
k=k+1;
jdiscret=1;
jj=99*2^(k-2)+1; %Astuce pour n'enregistrer finalement que 100
valeurs de t(X) quelque soit le dX final après k boucles

for j=2:jj
x1=x1+n1*dx/n3;
x2=x2+n2*dx/n3;
x=x+dx;
rf1=(rdif^2+x1*(rsw^2-rdif^2))^0.5;
rf2=(rsw^2-x2*(rsw^2-rdif^2))^0.5;

Tsw=(lambda1*Tf2/log(rsw/rf2)+hsw*rsw*Tc)/(lambda1/log(rsw/rf2)+hsw*rs
w);
DTf2=10; %initialisation du critère de convergence sur la
température calculée au front de chaleur par itération
i=1;

%%%%%%%%%%%%%%%%%%%%%%%%%%%%%%%%%%%%%%%%%%%%%%%%%%%%%%%%%%%%%%%%%%%%%%%%
%Itération pour convergence par méthode de Newton-Raphson
while (DTf2>1e-9)
i=i+1;
T2=Tf2(i-1); %changement de nom nécessaire pour le
calcul symbolique
% syms T2 dh ds R Tc Tsw Pc mu lambda0 lambda1 k0 k1
b0 b1 rf1 rf2 rdif rsw; %Calcul symbolique effectué une fois

Pf2=1e5*(exp(-dh/(R*T2)+ds/R)); %Pression d'équilibre
pour la température du front de chaleur au pas précédent avec
Tf2(1)=Tc, valeur par défaut quand k=1
c=2*mu*lambda1*R*Tc*(T2-
Tsw)*log(rf1/rdif)/(dh*k1*log(rsw/rf2))-Pc*(Pc+2*b1);
Pf1=-b1+(b1^2-c)^(0.5); % racine positive de
l'équation du 2nd degré en Pf1
Tf1=dh/(ds-R*log(Pf1*1e-5));
Tf2i=Tf1-dh*log(rf2/rf1)*(k1*((Pc^2-Pf1^2)+2*b1*(Pc-
Pf1))/log(rf1/rdif)-k0*((Pf1^2-Pf2^2)+2*b0*(Pf1-
Pf2))/log(rf2/rf1))/(2*mu*R*Tc*lambda0); % autre façon de calculer Tf2

fct=T2-Tf2i; %fonction à dériver
% derivef=diff(fct,T2); % Calcul symbolique effectué
une fois et dont le résultat est reproduit et affecté à la variable
derivef2

%
derivef2=(dh*log(rf2/rf1)*((k0*(2*b0*((100000*dh*exp(ds/R -
dh/(R*T2)))/(R*T2^2) +

```



```

(R*Tc*lambda1*mu*log(rf1/rdif))/(dh*k1*log(rsw/rf2)*(Pc*(Pc + 2*b1) +
b1^2 - (2*R*Tc*lambda1*mu*log(rf1/rdif)*(T2 -
Tsw))/(dh*k1*log(rsw/rf2)))^(1/2))) + (20000000000*dh*exp((2*ds)/R -
(2*dh)/(R*T2)))/(R*T2^2) - (2*R*Tc*lambda1*mu*log(rf1/rdif)*(b1 -
(Pc*(Pc + 2*b1) + b1^2 - (2*R*Tc*lambda1*mu*log(rf1/rdif)*(T2 -
Tsw))/(dh*k1*log(rsw/rf2)))^(1/2)))/(dh*k1*log(rsw/rf2)*(Pc*(Pc +
2*b1) + b1^2 - (2*R*Tc*lambda1*mu*log(rf1/rdif)*(T2 -
Tsw))/(dh*k1*log(rsw/rf2)))^(1/2)))/log(rf2/rf1) +
(k1*((2*R*Tc*b1*lambda1*mu*log(rf1/rdif))/(dh*k1*log(rsw/rf2)*(Pc*(Pc
+ 2*b1) + b1^2 - (2*R*Tc*lambda1*mu*log(rf1/rdif)*(T2 -
Tsw))/(dh*k1*log(rsw/rf2)))^(1/2)) -
(2*R*Tc*lambda1*mu*log(rf1/rdif)*(b1 - (Pc*(Pc + 2*b1) + b1^2 -
(2*R*Tc*lambda1*mu*log(rf1/rdif)*(T2 -
Tsw))/(dh*k1*log(rsw/rf2)))^(1/2)))/(dh*k1*log(rsw/rf2)*(Pc*(Pc +
2*b1) + b1^2 - (2*R*Tc*lambda1*mu*log(rf1/rdif)*(T2 -
Tsw))/(dh*k1*log(rsw/rf2)))^(1/2)))/log(rf1/rdif)))/(2*R*Tc*lambda0*m
u) - (R^2*Tc*lambda1*mu*log(rf1/rdif))/(100000*k1*log(rsw/rf2)*(ds -
R*log((Pc*(Pc + 2*b1) + b1^2 - (2*R*Tc*lambda1*mu*log(rf1/rdif)*(T2 -
Tsw))/(dh*k1*log(rsw/rf2)))^(1/2)/100000 - b1/100000))^2*(b1/100000 -
(Pc*(Pc + 2*b1) + b1^2 - (2*R*Tc*lambda1*mu*log(rf1/rdif)*(T2 -
Tsw))/(dh*k1*log(rsw/rf2)))^(1/2)/100000)*(Pc*(Pc + 2*b1) + b1^2 -
(2*R*Tc*lambda1*mu*log(rf1/rdif)*(T2 -
Tsw))/(dh*k1*log(rsw/rf2)))^(1/2)) + 1

```

```

reduc=(Pc*(Pc + 2*b1) + b1^2 -
(2*R*Tc*lambda1*mu*log(rf1/rdif)*(T2 -
Tsw))/(dh*k1*log(rsw/rf2)))^(1/2); % ce terme n'apparaissait pas dans
le développement de derivef donné par Matlab; c'est moi qui est trouvé
ce facteur commun sur le modèle de ce que j'avais dans le précédent
programme où la dérivation avait été faite par MuPad

```

```

derivef2=(dh*log(rf2/rf1)*((k0*(2*b0*((1e5*dh*exp(ds/R
- dh/(R*T2)))/(R*T2^2) +
(R*Tc*lambda1*mu*log(rf1/rdif))/(dh*k1*log(rsw/rf2)*reduc)) +
(2e10*dh*exp((2*ds)/R - (2*dh)/(R*T2)))/(R*T2^2) -
(2*R*Tc*lambda1*mu*log(rf1/rdif)*(b1 -
reduc))/(dh*k1*log(rsw/rf2)*reduc))/log(rf2/rf1) +
(k1*((2*R*Tc*b1*lambda1*mu*log(rf1/rdif))/(dh*k1*log(rsw/rf2)*reduc) -
(2*R*Tc*lambda1*mu*log(rf1/rdif)*(b1 -
reduc))/(dh*k1*log(rsw/rf2)*reduc))/log(rf1/rdif)))/(2*R*Tc*lambda0*m
u) - (R^2*Tc*lambda1*mu*log(rf1/rdif))/(1e5*k1*log(rsw/rf2)*(ds -
R*log(reduc/1e5 - b1/1e5))^2*(b1/1e5 - reduc/1e5)*reduc) + 1;

```

```

Tf2(i)=T2-fct/derivef2;
DTf2=abs(Tf2(i)-T2); % test de convergence : écart
absolu sur Tf2 en °C
end

```

```

%%%%%%%%%%%%%%%%%%%%%%%%%%%%%%%%%%%%%%%%%%%%%%%%%%%%%%%%%%%%%%%%%%%%%%%%
Tempfront2=Tf2(i);
Pf2=1e5*(exp(-dh/(R*Tempfront2)+ds/R));
c=2*mu*lambda1*R*Tc*(Tempfront2-
Tsw)*log(rf1/rdif)/(dh*k1*log(rsw/rf2))-Pc*(Pc+2*b1);
Pf1=-b1+(b1^2-c)^(0.5);
Tf1=dh/(ds-R*log(Pf1*1e-5));
n1=2*lambda0*(Tf1-Tempfront2)/(Dec*(rsw*rsw-
rdif*rdif)*log(rf2/rf1));
n2=dh*k0*((Pf1^2-Pf2^2)+2*b0*(Pf1-Pf2))/(mu*R*Tc*Dec*(rsw*rsw-
rdif*rdif)*log(rf2/rf1));

```

```

n3=n1+n2; %dx/dt vitesse de réaction totale au taux
de réaction X
deltat=dx/(n3*60); % incrément de temps en minute pour le pas
dx choisi
t=t+deltat;
if (j==2^(k-2)*jdiscret+1)
jdiscret=jdiscret+1 ;
temps(jdiscret)=t ;
avancement(jdiscret)=x;
disp(avancement(jdiscret))
avancement1(jdiscret)=x1 ;
avancement2(jdiscret)=x2;
limhsw(jdiscret)=abs((Tsw-Tc)/(Tempfront2-Tc));
end
Tf2=Tempfront2;
end
temps99(k)=temps(jdiscret);
dtr99=abs(temps99(k)-temps99(k-1))/temps99(k); % test de
convergence : écart relatif sur t à X=.99
end

vec_tout(:,1)=temps';
vec_tout(:,2)=avancement';

disp('temps en min pour X=0 à 0,99 par pas de 0,01')
temps'
disp('avancement massique pour X=0 à 0,99 par pas de 0,01')
avancement1'
disp(' nombre de boucles pour convergence sur dx : k')
k
disp(' écart relatif en % sur t à X=.99 : dtr99')
dtr99*100
if (k>5)
disp(' convergence sur dx difficile : k>5')
end
end

```

Appendix C: Technical specifications of the main components of the experimental setup

C.1 THERMOCHEMICAL REACTOR

N° INFORME REPORT N° OCT020321799-1		INFORME DE PRUEBA DE PRESIÓN Pressure test HÓJA 1 DE 2 (Sheet OF)		TUV NORD CERTIFICATION	
CLIENTE: Nombre: EPCO SISTEMAS Referencia cliente: FEDECO 08 Centro de trabajo:		LUGAR: Planta/Unidad: Nombre: Fecha prueba: No. de serie:		TARRAGONA TALLER 30/03/2017	
REFERENCIAS GENERALES / GENERAL DATA					
Serie/Código Línea: Identificación: Plano n°: Drawing n°: Distribución cliente: Descripción:		COMPONENTE: Component: No. de serie: Serie n°:		Parte/Part: Part/Part: No. de fabricación: Manufacturing No.	
ALCANCE DE LA PRUEBA / PRESSURE TEST APLICATION					
SE HA REALIZADO LA PRUEBA DE PRESIÓN HIDRÁULICA AL DEPÓSITO.					
MÉTODO DE ENSAYO / TEST METHOD					
Procedimiento de prueba: Standard/Protocol: Técnica de admisión: Admission technique:		Norma/Código de ensayo: Standard/Code test: Condición de la superficie: Surface condition:		Criterio de aceptación: Acceptance criteria: Tipo de prueba: Type of test:	
ENVUÑO: 100% ENSAYO VISUAL DIRECTO		ASME B31.3 INTERNA Y EXTERNA		ASME B31.3 LIMBLANCA ARTIFICIAL 1000 L/1st	
DATOS TÉCNICOS DEL ENSAYO / TEST TECHNICAL DATA					
Marca/Marka - N° serie - Rango: Manufacturer - Serial n° - Range: Marca/Marka - N° serie - Rango: Manufacturer - Serial n° - Range: Presión de prueba: Test pressure:		Fluido de prueba: Test fluid:		Fecha última calibración: Last calibration date: Fecha última calibración: Last calibration date: T° de prueba: Test temperature:	
80 BAR		AGUA DEMINERALIZADA		30°C	
DATOS TÉCNICOS PARA COMENTARIOS / TECHNICAL DATA FOR COMMENTS					
ELEMENTO ELEMENT	FLUIDO DE PRUEBA TEST FLUID	T° DE PRUEBA PRESSURE TEST T°	PRESIÓN DE PRUEBA TEST PRESSURE	TIEMPO DE MTO. PRESSURE TEST TIME	RESULTADO RESULT
DEPÓSITO	AGUA DEMINERALIZADA	30°C	80 BAR	90 MINUTOS	SATISFACTORIO
CROQUIS / SKETCH					
RESULTADO FINAL / FINAL RESULT					
SATISFACTORIO		LA PRESIÓN SE HA MANTENIDO CONSTANTE DURANTE LA PRUEBA.		RESULTADO	
SATISFACTORIO		SATISFACTORIO.		RESULTADO	
FROM: INFORME REPORT N°		MOJEL A. RIAL TUV Inspector / Inspeccionador		N° DE CONTROL DE CALIDAD FABRICANTE Manufacturer Quality Control N° DE CONTROL DE CALIDAD TUV Certified Part Quality Control	
TUV NORD CERTIFICATION 57 Calle Europa, 67 - 43005 TARRAGONA - SPAIN - TARRAGONA - SPAIN Tel: 34 977 01 31 Fax: 34 977 01 30 E-mail: tspan@tuvnord.com www.tuvnord.com					



PROPELLANT (POURING DIVISION)

INSPECTION CERTIFICATE & MILL TEST REPORT - EN 10204 3.1

100 8041208-TEV N020 REG.No-410881119-83 INVOICE NUMBER (MTR NO.) 801286-2
 EXPIRY DATE: 21.01.2023 DATE 20/06/2023
 AD 2008 MEXCELATI W04-07201423 WT 103704 Q MATERIAL SPECIFICATION ASTM A182-000-1.1B / ARME SAUERSTEINEM - 13
 AS PER W0402019 EXPIRY DATE: FEBRUARY 2017
 PED 57020-K-008 REG.No-07201423 WZ 022114 Q PURCHASE ORDER NO. 8011449
 EXPIRY DATE: FEBRUARY 2017 DESCRIPTION STAINLESS STEEL FORGED FLANGES

CHEMICAL ANALYSIS

Item Description	Item No.	Qty	%C	%Mn	%Si	%S	%P	%Ni	%Cr	%Mo	%Nb	%N
316L316L 6" W008F 1208 8185	80651	20.000	0.0289	1.078	0.150	0.0218	0.0034	16.890	10.071	2.049	0.0006	0.0000
316L316L 4" W008F 1208 8184	30875	483.890	0.0199	1.049	0.100	0.0206	0.0056	16.292	10.071	2.049	0.0006	0.0000
316L316L 4" W008F 1208 8185	80675	161.890	0.0194	1.008	0.098	0.0206	0.0056	16.292	10.071	2.049	0.0006	0.0000
316L316L 4" W008F 1208 8186	37164	20.000	0.0148	1.008	0.100	0.0206	0.0056	16.292	10.071	2.049	0.0006	0.0000
316L316L 6" W008F 1208 8485	37164	10.000	0.0209	1.008	0.100	0.0206	0.0070	16.292	10.071	2.049	0.0006	0.0000
316L316L 1.1/2" W008F 1208 8485	31643	31.000	0.0221	1.050	0.100	0.0220	0.0090	16.089	10.071	2.049	0.0020	0.0020

MECHANICAL PROPERTIES

S/n	Item No.	Tensile Strength	Proof Stress Rp-0.2 %	Proof Stress Rp-1.0%	Elongation %	Reduction of Area	Hardness			IMPACT TEST-CHARPY V-NOTCH AT 20 DEGS. C. 100 Joules		
							LO-D	REN	REN	1	2	3
1	80675	517.658	281.270	203.370	59.78	60.28	153.0	153.0	153.0	188.0	188.0	188.0
2	80675	517.658	281.270	203.370	59.78	60.28	153.0	153.0	153.0	179.0	179.0	179.0
3	37164	517.658	281.270	203.370	59.78	60.28	153.0	153.0	153.0	179.0	179.0	179.0
4	37164	517.658	281.270	203.370	59.78	60.28	153.0	153.0	153.0	196.0	196.0	196.0
5	37164	517.658	281.270	203.370	59.78	60.28	153.0	153.0	153.0	202.0	202.0	202.0
6	37164	517.658	281.270	203.370	59.78	60.28	153.0	153.0	153.0	188.0	188.0	188.0

1 MATERIAL CONFORMS TO NACE MR 0175 / ISO 15156 - 3089 & NACE MR 0185 - 2013
 2 INDUCTION / AQUEOUS / CONCAST
 3 SOLUTION ANNEALED AT 1080°C AND WATER QUENCHED
 4 CONFORM WITH THE SPECIFICATION (100% DEFECTIVE)
 5 SATISFACTORY
 6 NO CORROSION TESTED WITH MOBILE SPECTRO
 7 PASSED HAC TEST IN ACCORDANCE WITH ASTM A262 PRACTICE B
 8 NO CHANGE IN MECHANICAL PROPERTIES OBSERVED ON ORAN SOAKING
 9 MATERIAL HAS BEEN CHECKED AND FOUND TO BE FREE FROM RADIOACTIVE CONTAMINATION & FREE FROM MERCURY CONTAMINATION
 10 MATERIAL WAS MEASURED IN SAMPLE TESTED & INSPECTED IN ACCORDANCE WITH PRELICATED SPECIFICATION & FOUND TO MEET THE REQUIREMENTS
 11 NO WELD REPAIR WAS PERFORMED & ALL THE ITEMS ARE FREE OF WELD REPAIR

12 CERTIFY THAT THE MATERIAL DESCRIBED ABOVE HAS BEEN TESTED AND CONFORMS WITH THE ORDER/CONTRACT AND IS OF INDIA ORIGIN
 13 MANUFACTURER'S STAMP

14 FACTORY : Survey No. 1401, Sarveili & G-75, MIDC Tanager Industrial Area Bazar, Dist. Thane, Maharashtra-401 206, INDIA. Tel: (91) 902088356 to 1841. Fax: (91) 2215857. E-MAIL: info@vera.com
 15



CERTIFIED MATERIAL TEST REPORT

ASTM A193-A193M-14

Size & Description 3/4"-10 X 6"
Stud
Sampling Plan per BS EN ISO 3289:2007, AQL 1.5

Material: B8 CL2 - 304
PO #: TGD1385
Heat #: 171010HRP
Batch Lot #: -

Date: 02-08-17

CHEMICAL COMPOSITION (%)

Element	C	Mn	Si	P	S	Cr	Mo	Ni	Al	V
Spec	0.08 MAX	2.00 MAX	1.00 MAX	0.045 MAX	0.030 MAX	16.0-20.0	-	8.00-11.0	-	-
Results	0.02	1.81	0.39	0.031	0.025	18.88	-	8.07	-	-

MECHANICAL PROPERTIES Test Method per ASTM A193/A193M-14

Item	Tensile Strength		Elongation		Reduction of Area		Hardness (Max)		Macro Etch per ASTM E381-01 (For Carbon & Alloy Steels only)			Minimum Tempering Temperature
	min, ksi	min, MPa	min (%)	min (%)	min (%)	min (%)	Rockwell B	Brinell	Surface Condition	Random Condition	Center Segregation	
Spec	120	100	22.0	22.0	35.0	35.0	35 HRC	221	A1	A2	C1	-
Results	134	205	20.80	24.80	34.00	34.00	-	-	S2	R2	C2	-

Heat Treatment: -

Charpy Impact Test (for L7/L7M): -
Quenching Temperature (if applicable): 860

Surface Coating: BRIGHT

DIMENSIONS:

Item	RD	MO GD
PI Spec	High Limit	2A
	Low Limit	2A
A1	Passed	
A2	Passed	
A3	Passed	

3 Digit Code	Heat Mark
-	B8CL2

Comments: Passed

Parts are manufactured, sampled, tested and inspected in accordance with ASTM A193/A193M-14 or ASTM A320/A320M-14 or ASME SA193/SA193M (for L7/L7M). All tests are in accordance with the methods prescribed in the applicable ASTM specification. We certify this data is a true representation of information provided by the material supplier and our testing laboratory.



Inspection Certificate per BS EN10204 3.1.

Fernando Pacheco
Quality Manager
Lamons



CERTIFIED MATERIAL TEST REPORT
ASTM A194/A194M-14

Size & Description : 3/4"-10

Material : GR 8
PO Number : T081388
Heat # : J72-0038
Batch Lot # : -

3 Digit Code	Heat Mark
-	GR8

Date : 8/3/2017

CHEMICAL COMPOSITION (%)

Elements	C	Mn	Si	P	S	Cr	Mo	Ni	Al	V
Spec	0.08 MAX	2.00 MAX	1.00 MAX	0.045 MAX	0.030 MAX	18.0-20.0	-	8.0-12.0	-	-
Results	0.04	1.26	0.58	0.035	0.022	18.20	-	8.00	-	-

MECHANICAL PROPERTIES Test Method per ASTM A194/A194M-14

Item	Hardness (Min or Range)		Proof Load (lb) only up to 1-1/2"	Micro Etch per ASTM E281-02 (Carbon & Alloy Steels only)		
	Retained	Delivered		Surface Condition	Random Condition	Center Segregation
Spec	32 HRC MAX	1.01 - 3.00	26,720	S2	R2	C3
Results	27-58	-	Passed	S2	R2	C2

Minimum Temperature
Calculus
-

Hardness after 24 hour Treatment	Standard	Results
-	-	-

Charpy Impact Test (per ASTM & EN): N/A

Surface Condition : BRIGHT

Parts are manufactured, sampled, tested and inspected in accordance with ASTM A194/A194M-14 or ASME SA194/SA194M. All tests are in accordance with the methods prescribed in the applicable ASTM specification. We verify this data is a true representation of information provided by the material supplier.

Inspection Certificate per DG EN10204 3.1.



Fernando Pacheco
Quality Manager
Lamons

SIDERINOX

SIDERINOX S.p.A. - Sezione Cassella 20091 Montebello (MI) Italia
 Ufficio Commerciale: Tel. 02 84881811 - Fax 02 848818250/251
 Ufficio Amministrativo: Tel. 02 84881811 - Fax 02 848818250
 Ufficio Tecnico: Tel. 02 848818222 - Fax 02 848815850
 Ufficio Assistenza: Tel. 02 848818345 - Fax 02 848818250
 Cassella e-mail: cx@siderinox.it - Site web: www.siderinox.it

Capitale Sociale Euro 3.300.000 i.a.
 Dot. Pisanesi e Rag. Imp. M.N. 01825519157
 R.E.A. Milano N. 878136
 Centro Meccanografico n. 46034382
 Partita IVA 01825519157

Autista CON SU PERM
 di SESTRO ALCA
 certificato da SIVOL
 n° 90 606*

CERTIFICADO DE ENSAYO EN 10204		3.1	N° 457840 del 25.03.2016	Hoja 1 / 1
Cliente INOXCENTER, S.L.U.				
DOT N 975 del 25.03.2016		Pedido SIDERINOX N 995 del 14.03.2016		Pedido del Cliente N° N 116011920 del 14.03.2016
Descripción del producto Tubo inox redondo Ø 60,8 x 1,6 mm AISI 316L apacado EN 10357 soldado longitudinalmente				
Dimensión 60,8 x 1,6 mm	Acero EN 1.4404 / AISI 316L	Cantidad (m) 2196	Peso (kg) 3794	
Norma de producción EN 10357	Laminado Pdo	Tolerancias EN 10357 / EN 10357	Factor de soldadura √=1	
Marca SIGLA PRODUCTOR - DIMENSION - ACERO - COLADA - NORMA DE PRODUCCIÓN - EJECUCIÓN - INSPECTOR E.C. - INSPECTOR DE PRODUCCIÓN				
Proceso de soldadura		Superficie WRB		

COMPOSICIÓN QUÍMICA DE LA COLADA

Colada	% C	% Mn	% P	% S	% Si	% Cr	% Ni	% Mo	% Ti
53032	0,080 - 0,030	1,800 - 2,000	0,080 - 0,040	0,080 - 0,010	0,500 - 1,000	16,500 - 18,500	10,000 - 15,000	2,000 - 2,500	0,050 - 0,030
	0,018	0,900	0,034	0,001	0,450	16,700	10,000	2,010	

Los valores químicos corresponden al certificado emitido por la Acente según las normas EN 10204 / 10204-2 / ASNT A200 y están archivado en nuestro sede.

RESULTADO DE LA PRUEBA

Lote	Clase de prueba	ID1	ID2	PRUEBA DE TRACCIÓN N				DUREZA
				Esfuerzo		Carga de rotura	Estiramiento	
				R _p 0,2%	R _p 1%			
T18022987	PK1	L	M	235	318	649	48	
T18023010	PK1	L	M	231	318	636	48	
T18023016	PK1	L	M	236	321	650	48	
T18023017	PK1	L	M	233	317	632	48	
T18023059	PK1	L	M	245	322	642	49	
T18023087	PK1	L	M	241	320	630	48	
T18023099	PK1	L	M	232	315	636	49	
T18023093	PK1	L	M	236	324	650	49	
T18023094	PK1	L	M	237	321	638	48	

Examen visual	Prueba de ensanchamiento	Prueba de cavidad
OK	EN 10204 OK	SEP 1025 OK
Control dimensional	Prueba de espesamiento	Control no destructivo Estado Cumari
OK	EN 10333 OK	SEP 1014 OK
Prueba entintada	Prueba de pliegue de la soldadura	Prueba de corrosión intersticial
OK	N.P.	EN ISO 3651-3 N. P.

Se declara que el material entregado está conforme en cuanto a lo concordado al pedido

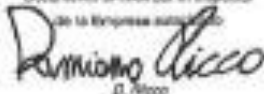
Nota:

Certificaciones:
 UNI EN ISO 9001
 DE PED 97/23/EC Ale 1, Punto 4.3, Apartado 3
 AQAP de n. 7293-95-TU a-e-7296-06-TU


Certificaciones:
 ISO 9001:2015 UNI EN ISO 15001-4/108 EN ISO 15014-1
 Personal N.º 3. UNI EN ISO 16733
 Personal N.º 1. UNI EN ISO 16733

Carb. Col. - Rev. 3 - 0014

Documento emitido por el inspector

de la Empresa SIDERINOX

 D. Nicos

Documento emitido por el representante

de la Empresa Autorizado

 W. Anselmo



52450 中國廣東省佛山市順德區均安鎮
No.270, Sec.4, Jiangshan Rd., Shiqiao Shiqiang
Chang-Hua, Taiwan, R.O.C.
TEL: +886-4-8839999 FAX: +886-4-8899770

允強實業股份有限公司
YC INOX CO., LTD.
INSPECTION CERTIFICATE



客戶名稱 Customer	客戶編號 Customer No.	客戶地址 Customer Ad.	客戶電話 Customer Tel.
產品名稱 Product	商標號碼 Commercial Mark No.	訂貨日期 Date of Order	訂貨數量 Order No.
規格名稱 Specification	商標號碼 Commercial Mark No.	訂貨日期 Date of Order	訂貨數量 Order No.
鋼號 Steel Grade	鋼號 Steel Grade	鋼號 Steel Grade	鋼號 Steel Grade
項目 Item No.	產品名稱 Product Description	數量 Quantity	單位 Unit
1	304 WELDED PAPER	114060379	張
2	A312W312MA 130	4500390659	張
3	TP31671BL	C140900011	張
4			
TOTAL:		1390	張
<p>STANDARDS: ASTM A479/EN 10254</p> <p>Visual Inspection (Surface) and Dimension Check: OK</p> <p>100% Alloy Verification (MAI): OK</p> <p>Hardness according to MAICE MS0075 / ISO 15156-2:2009: Satisfactory.</p> <p>Hardness according to MAICE MS0075-2012: Satisfactory.</p> <p>This certificate complies to EN ISO 10094:2004.</p>			
Surveyor By	Visual Inspection (Surface) and Dimension Check: OK		
MAI	<p>100% Alloy Verification (MAI): OK</p> <p>100% Hardness Test (MAI): OK</p> <p>100% Hydrostatic Test (MAI): OK</p> <p>100% Flaming Test (MAI): OK</p> <p>Gauge Length: 50mm</p>		
Signature By		Manager of Quality Assurance Department	
MAI		<p>100% Alloy Verification (MAI): OK</p> <p>100% Hardness Test (MAI): OK</p> <p>100% Hydrostatic Test (MAI): OK</p> <p>100% Flaming Test (MAI): OK</p> <p>Gauge Length: 50mm</p>	

C.2 HEAT EXCHANGERS

Standard data

Min. working temperature	see graph
Max. working temperature	see graph
Min. working pressure	Vacuum
Max. working pressure	see graph
Volume per channel H, L, litres (ga)	0.095 (0.025)
Max particle size mm (inch)	1.2 (0.05)
Max. flowrate * m ³ /h (gpm)	14.5 (64)
Min no of plates	6
Max no of plates	150

*) Water at 5 m/s (16.4 ft/s) (connection velocity)

Standard dimensions*

AlfaNova 52

A measure mm	=	$11 + (n \times 2.48) \pm 4.5$
A measure inch	=	$0.43 + (n \times 0.098) \pm 0.18$
Weight kg	=	$1.9 + (n \times 0.22)$
Weight lb	=	$4.19 + (n \times 0.48)$

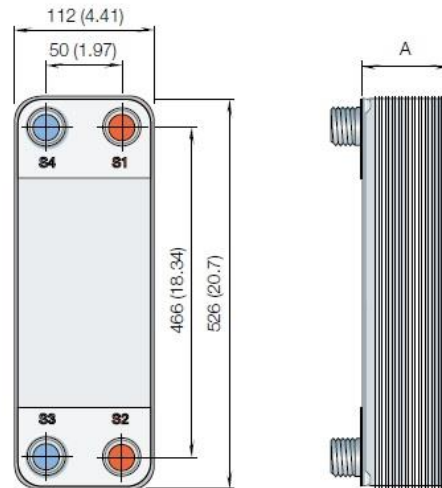
AlfaNova 52 HP

A measure mm	=	$13 + (n \times 2.48) \pm 4.5$
A measure inch	=	$0.51 + (n \times 0.098) \pm 0.18$
Weight kg	=	$2.3 + (n \times 0.22)$
Weight lb	=	$5.07 + (n \times 0.49)$

(n = number of plates)

Standard materials

Cover plates	Stainless steel
Connections	Stainless steel
Plates	Stainless steel
AlfaFusion filler	Stainless steel



C.3 AMMONIA STORAGE TANK

CALDERAS MUNGUA, S.L.

CALDERAS MUNGUA, S.L. Camelo Echegaray, 20-B. Apdo., 40-46100 MUNGUA (Vizcaya)- Tfno: 94-674.01.71 FAX: 94-674.49.13

Informe n°/Report Nr: I-439

Fecha/Date: 19/05/15

DECLARACIÓN DE CONFORMIDAD CE (Directiva Equipos a Presión 97/23/CE)

CERTIFICATE OF CONFORMITY EC (Pressure Equipment Directive 97/23/CE)

El Fabricante: CALDERAS MUNGUA, S.L. declara bajo su responsabilidad que el equipo a presión:

The Manufacturer declares under his responsibility that the equipment pressure:

Descripción del equipo a presión: <i>Pressure equipment description:</i>		DEPOSITO HORIZONTAL			
Tipo: <i>Type:</i>	D.H.	Modelo: <i>Model:</i>	4	Marca Fab.: <i>Mark Mfg.:</i>	C.M.
Nº de fabricación: <i>manufacturing Nr.:</i>	439	Nº serie o lote: <i>Serial number:</i>	1	Año de fabricación: <i>Manufacturing year:</i>	2015

Recinto/Chamber	1	Cuerpo (Shell)	2	N/A
Presión máxima admisible <i>Permissible maximum pressure:</i>	PS(bar):	20		
Temperatura mínima/máxima admisible <i>Permissible minimum and maximum temperature:</i>	TS(°C):	-10°C / +250°C		
Volumen interno <i>Internal volume:</i>	V (Liter):	4		
Fluido contenido/grupo: <i>Fluid/group:</i>		Agua		
Categoría: <i>Category:</i>		I		
Presión de prueba <i>Test pressure:</i>	PT (bar):	30		
Fluido utilizado para la prueba <i>Pressuring fluid:</i>		Agua		
Fecha de Prueba <i>Date of test</i>		19/05/15		

Cumple la Directiva del Parlamento Europeo y del Consejo, 97/23/CE, relativa a los equipos a presión.
Comply with the Pressure Equipment Directive 97/23/CE

Procedimiento de evaluación de la conformidad utilizado: A
Conformity evaluation procedure

Ref. Certificado de Examen CE de:
Conformity evaluation procedure

Organismo de Control Notificado que ha realizado el control:
Approved Certification Body who has realized the control

TDV Rheinland Ibérica Inspección,
Certification & Testing, S.A.,
Número: 1027
Bº Peruri, 33 Ed. 8 - 1º C
48940 Leizaola (Bizkaia)

Código o norma de diseño aplicado: ASME Sección VIII
Design Code or standard apply
Otras directivas o normas aplicadas:
Others Directives or standards applied

Nombre/Name: /Firma/Signature:
Cargo/post:
Lugar y fecha/Location and date:

Hilario I. Jodó Sainz de Rozas
Ingeniero Industrial
Mungia, 19 de mayo de 2015



C.4 CAPACITIVE LEVEL PROBE

Multicap DC 12 TE, DC 11 TEN/TE5

Capacitance values of the probe	<ul style="list-style-type: none"> Basic capacitance: approx. 30 pF Temperature spacer: approx. 5 pF Active build-up compensation: < 10 pF
Additional capacitances	<ul style="list-style-type: none"> Probe 250 mm from a conductive vessel wall: <ul style="list-style-type: none"> Probe rod: approx. 1.3 pF/100 mm in air Probe rope: approx. 1.0 pF/100 mm in air Insulated probe rod in water: <ul style="list-style-type: none"> approx. 38 pF/100 mm DC 12 TE approx. 50 pF/100 mm DC 11 TEN/TE5 Insulated probe rope in water: approx. 20 pF/100 mm Rod probe with ground tube: <ul style="list-style-type: none"> insulated probe rod: in air approx. 6.4 pF/100 mm; in water approx. 50 pF/100 mm uninsulated probe rod: in air approx. 5.6 pF/100 mm
Probe lengths for continuous measurement in conducting liquids	<ul style="list-style-type: none"> EC with $AC_{max} = 2000$ pF (EC 47 Z, EC 72 Z, FEC 12): <ul style="list-style-type: none"> Rope probe up to 8000 mm (up to 20000 mm in non-conducting liquids) Rod probe up to 3000 mm EC with $AC_{max} = 4000$ pF (EC 37 Z, EC 11 Z): <ul style="list-style-type: none"> Rope probe up to 20000 mm Rod probe up to 3000 mm
Accuracy	<ul style="list-style-type: none"> Length tolerances: <ul style="list-style-type: none"> up to 1 m: +0 in, - 5 mm rod probe/ -10 mm rope probe up to 3 m: +0 in, -10 mm rod probe/ -20 mm rope probe up to 6 m: +0 in, -30 mm up to 20 m: +0 in, -40 mm <p>The following specifications apply to fully insulated probes operating in conducting liquids:</p> <ul style="list-style-type: none"> Linearity error: < 1 % for 1 m ** Temperature dependence of the probe rod: <ul style="list-style-type: none"> < 0.1 % per K DC 12 TE ** < 0.12 % per K DC 11 TEN/TE5 ** Pressure dependence of the probe rod: 0.12...0.34 % per bar ** Temperature dependence of the probe rope: < 0.1 % per K ** Pressure dependence of the probe rope: < 0.1 % per bar ** <p>** Error in non-conducting materials insignificant</p>
Process connections	<ul style="list-style-type: none"> Parallel thread G 1/2 A or G 1 A: DIN ISO 228/1, with sealing ring 27x32 or 33x39 to DIN 7603 Tapered thread 1/2 - 14 NPT or 1 - 11 1/2 NPT: ANSI B 1.20.1 DIN flanges without raised face: DIN 2527, Form B DIN flanges with tongue: DIN 2512, Form F DIN flanges with groove: DIN 2512, Form N ANSI flanges: ANSI B 16.5 Sanitary thread: DIN 11851 Triclamp coupling: ISO 2852
Materials	<ul style="list-style-type: none"> Aluminium housing (F6, T3): GD-Al Si 10 Mg, DIN 1725, plastic coated (blue/gray) Plastic housing (F10): fibre-glass reinforced polyester (blue/gray) Stainless steel housing (F8): stainless steel 1.4301 (AISI 304), unwarnished Seal for housing cover: <ul style="list-style-type: none"> F6, T3 housings: O-ring in EPDM (elastomer) F10 housing: O-ring in silicone rubber Sealing ring for process connection G 1/2 A or G 1 A: Elastomer-fibre, asbestos-free, resistant to oils, solvents, steam, weak acids and alkalis, up to 300 °C and 100 bar Temperature spacer: Stainless steel SS 304 (1.4301) or similar Probe rod, ground tube, process connection, screening, build-up compensation, latching weight for rope probe: AISI 316L (1.4435) Probe rope: AISI 316 (1.4401) <p>Further material specifications see product structure on Page 11...17</p>

C.5 LIQUID TRAP VESSEL

CALDERAS MUNGUA, S.L.

CALDERAS MUNGUA, S.L. Carmelo Echegaray, 26-B. Apdo., 40-40100 MUNGUA (Vizcaya)- Tfno: 94-674.01.71 FAX: 94-674.49.13

Informe nº/Report Nr: I-440

Fecha/Date: 19/05/15

DECLARACIÓN DE CONFORMIDAD CE (Directiva Equipos a Presión 97/23/CE)

CERTIFICATE OF CONFORMITY EC (Pressure Equipment Directive 97/23/CE)

El Fabricante: CALDERAS MUNGUA, S.L. declara bajo su responsabilidad que el equipo a presión:

The Manufacturer

declares under his responsibility that the equipment pressure:

Descripción del equipo a presión: <i>Pressure equipment description:</i>		DEPOSITO HORIZONTAL			
Tipo: <i>Type:</i>	D.H.	Modelo: <i>Model:</i>	4	Marca Fab: <i>Mark Mfg.:</i>	C.M.
Nº de fabricación: <i>manufacturing Nr.:</i>	440	Nº serie o lote: <i>Serial number:</i>	1	Año de fabricación: <i>Manufacturing year:</i>	2015

Recinto/Chamber	1	Cuerpo (Shell)	2	N/A
Presión máxima admisible <i>Permissible maximum pressure:</i>	PS(bar):	20		
Temperatura mínima/máxima admisible <i>Permissible minimum and maximum temperature:</i>	TS(°C):	-10°C / +250°C		
Volumen interno <i>Internal volume:</i>	V (Liter):	6		
Fluido contenido/grupo: <i>Fluid/group:</i>		Agua		
Categoría: <i>Category:</i>		I		
Presión de prueba <i>Test pressure:</i>	PT (bar):	30		
Fluido utilizado para la prueba <i>Pressuring fluid:</i>		Agua		
Fecha de Prueba <i>Date of test</i>		19/05/15		

Cumple la Directiva del Parlamento Europeo y del Consejo, 97/23/CE, relativa a los equipos a presión.
Comply with the Pressure Equipment Directive 97/23/CE

Procedimiento de evaluación de la conformidad utilizado: A
Conformity evaluation procedure

Ref. Certificado de Examen CE de:
Conformity evaluation procedure

Organismo de Control Notificado que ha realizado el control:
Approved Certification Body who has realized the control

TUV Rheinland Ibérica Inspection,
Certification & Testing, S.A.,
Número: 1027
Bº Peruri, 33 Ed.8 - 1º C
48940 Leizaola (Bizkaia)

Código o norma de diseño aplicado: ASME Sección VIII
Design Code or standard apply
Otras directivas o normas aplicadas:
Others Directives or standards applied

Nombre/nombre: /Firma/Signature:
Cargo/post:
Lugar y fecha/Location and date:

Hilario I. Idoá Sainz de Rozas
Ingeniero Industrial
Mungia, 19 de mayo de 2015



Appendix D: Detailed procedures for manipulation of the setup inspired on the hybrid compression / thermochemical refrigeration system

D.1 NON-ASSISTED DECOMPOSITION PHASE (MAIN PROCEDURE)

This procedure begins with several assumptions. First, it is assumed that all valves are closed at the beginning of the procedure. It is also assumed that the whole setup is already charged with ammonia and no traces of air (or whatever other gas) are present in it. The reactive salt inside the reactor is assumed completely charged (i.e. $X = 1$). The ammonia storage tank is supposed to contain enough liquid ammonia to occupy the “non-measured” volume, i.e. the volume of tank not measured by the level probe. At the same time, the liquid ammonia inside the tank is assumed to be low enough to not surpass the maximum measurable level (20 mA for the level probe) after complete decomposition reaction is achieved. Finally, it is assumed that all the ammonia inside the setup, including the liquid ammonia inside the storage tank, is at ambient temperature. The procedure follows this order:

1. Initiate data acquisition with the following variables to be registered: thermocouples TC-01 to TC-08; temperature probes CT-01 to CT-05; pressure transmitters CP-01 to CP-03; and level probe CN. A rate of data acquisition of $\Delta t = 10$ s is recommended.
2. Open valve V-08 slowly to equilibrate the pressures of the condenser and the storage tank. Keep an eye on the level of liquid ammonia inside the tank while doing this step.
3. Turn on the thermal bath “Winus Chiller C2-W3” with a set temperature of 15 °C. At this temperature, the liquid/vapor equilibrium pressure is 7.3 bar, and the equilibrium temperature of the solid/gas reaction is 45.2 °C. The cooling down of ammonia in the condenser will set a natural circulation between the condenser and the storage tank. Liquid ammonia will flow from condenser to the storage tank, while ammonia at ambient temperature from the storage tank will slowly vaporize and flow to the condenser.
4. Wait until the condenser-storage tank segment reaches steady state, which can be verified when the level of liquid ammonia inside the storage tank remains constant or just with very slight oscillations.

5. Turn on the thermal bath "Ministat 125" with the fluid circulation pump at 4500 rpm and a set temperature of 65 °C. With this temperature, a difference of about 20 °C is expected with respect to the reaction's equilibrium temperature.
6. Wait until both the reactive composite and the "Ministat 125" reach the set temperature. Verify this with the readings of thermocouples TC-01 to TC-04.
7. Successively open valves V-07, V-06, V-03 and V-02. It is suggested to verify, after each valve opening, that the pressure inside the tube reaches the same equilibrium value of the condenser-storage tank segment.
8. Increase the rate of data acquisition to $\Delta t = 1$ s.
9. Open valve V-01. A slight pressure increase should be noticed in the setup (this can be checked by means of the transmitter CP-01). The endothermic reaction will start and the phase named "adiabatic phase" should be noticeable in the temperature readings from inside the reactor. Verify a temperature drop measured by the thermocouple TC-03 (placed at the reactor's innermost radius). The reaction's advancement should soon become visible at the temperatures measured by TC-01 to TC-04, and a bit later at the temperature difference between TC-05 and TC-06. Monitor the temperatures inside the reactor and the level of liquid ammonia inside the reservoir tank.
10. After the adiabatic phase has finished (which should not take more than 2 min), decrease back the rate of data acquisition to $\Delta t = 10$ s.
11. Simultaneously to the reaction, trace the experimental $X = f(t)$ curve and compare it to the theoretical curve obtained by the simulations at the corresponding operating conditions. Keep track of the heat transfer fluid's temperature difference between inlet and outlet of the reactor's thermal coating.
12. Monitor the operating pressure. In non-assisted decomposition phase, the condenser imposes the operating pressure. Since the "Winus Chiller C2-W3" has its own control system for the set temperature, the temperature probe at the condenser's outlet registers slight oscillations in the temperature of the ammonia. At the same time, oscillations in pressure are registered by CP-01. Both oscillations are perfectly synchronized.
13. At the end of the decomposition reaction, the reactor will remain steady at a temperature very close to that of the thermal coating. After this is verified, close valve V-01 and stop the "Ministat 125". Then, close the rest of the valves and stop the "Winus Chiller C2-W3".
14. The experimental $X = f(t)$ is derived from the readings of the level probe. The evolutions of pressures and temperatures can be compared to that of the reaction curve to detect any anomalies, if that is the case.

D.2 SYNTHESIS PHASE (MAIN PROCEDURE)

It is assumed that at the beginning of this procedure, all valves are closed and the whole setup contains only ammonia as working fluid. The procedure is as follows:

1. Initiate data acquisition with $\Delta t = 10$ s.
2. Initiate operation of the "Ministat 125" with a set temperature of 5 °C, and operation of the "Julabo MC-12" at a set temperature of 10 °C.
3. Wait until both the thermal bath and the reactive composite reach steady state at the target temperature.
4. By means of valve V-15 and the plastic tube leading to the upper ventilator of the protective chamber, slowly evacuate ammonia gas from the evaporator-reactor segment until pressure in that line reaches 1.5 bar approximately. Then, close valve V-15 again.
5. Open valve V-09, then very slowly open valve V-DE until pressure in the evaporator-reactor segment reaches the desired operating pressure for the synthesis phase.
6. Set data acquisition to $\Delta t = 1$ s.
7. Open valve V-01 and verify temperature readings of TC-01 to TC-04. All these thermocouples should register a steep increase in temperature inside the reactive composite, which verifies that the so-called adiabatic phase of the reaction has begun.
8. Once the adiabatic phase is over (after 2-3 min), re-set data acquisition to $\Delta t = 10$ s.
9. During the reaction, keep an eye on the inlet-outlet temperature difference of the heat transfer fluid circulating through the thermal jacket.
10. The reaction can be considered finished when the temperature readings of TC-01 to TC-04 remain almost constant and at a value close to the temperature of the heat transfer fluid of the thermal jacket.
11. When the reaction is finished, close valve V-01. Then close all valves in the segment that connects the reactor and the liquid reservoir. Once all temperature readings inside the reactor remain steady, shut down the "Ministat 125" and the "Julabo MC-12".

D.3 COMPRESSION-ASSISTED DECOMPOSITION PHASE (MAIN PROCEDURE)

This section contains the description of the steps for carrying out the decomposition reaction (endothermic reaction) assisted with mechanical vapor compression, with condensation of the compressed ammonia and its storage in the liquid reservoir.

The primary objective of this procedure is to demonstrate the feasibility of a decomposition phase assisted with compression by means of a membrane compressor. The main point of such a procedure is to reduce activation temperature of the thermochemical reaction.

The secondary objectives of this procedure are:

- 1) To verify the feasibility of the coupling between the compressor and the reactor.
- 2) To obtain the X-t curve (advancement degree vs time) of the compression-assisted decomposition.
- 3) To analyze the compressor's influence on the X-t curve.

It is assumed that at the beginning of this procedure all valves are closed, the whole setup contains ammonia only at ambient temperature, the reactive salt is almost completely charged ($X \approx 1$) and the storage tank contains sufficient liquid ammonia to fill the volume not measured by the probe. The procedure is as follows:

1. Initiate data acquisition with $\Delta t = 10$ s and the following variables to be registered: thermocouples TC-01 to TC-08, temperature probes CT-01 to CT-05, pressure transmitters CP-01 and CP-02, and level probe CN.
2. Open valve V_08 to connect the condenser to the liquid storage tank, then open valve V-07 to record the pressure reading at the condenser-storage tank segment by means of transmitter CP-02.
3. Boot up the "Winus Chiller C2-W3" thermal bath and introduce the desired set temperature. Check the equilibrium pressure of ammonia's vapor-liquid equilibrium at this temperature, then check the equilibrium temperature of the solid/gas ammonia/barium chloride reaction at that pressure. After turning on the thermal bath, check the level of liquid inside the storage tank: it should decrease steeply, since part of this ammonia evaporates, flows to the condenser and remains inside it as liquid. It takes some minutes for the ammonia inside the tank to reach the target temperature of the thermal bath. After reaching the

target temperature, some of the liquid ammonia in the condenser will come back to the storage tank.

4. Once the level of liquid and its temperature is stable, the condenser/storage tank segment can be considered at steady state. In this state, the pressure will still undergo some slight oscillations, caused by the temperature control of the “Winus Chiller C2-W3” (at VLE, temperature imposes pressure).

5. Boot up the “Ministat 125” thermal bath and turn it on at a set temperature higher than the reaction’s equilibrium temperature. The total time of reaction will be shorter with higher temperatures (the difference between thermal bath temperature and reaction’s equilibrium temperature dictates the rate of reaction). For acceptable reaction times (not too long, not too short), it is recommended to set the thermal bath’s target temperature to be at least 15 °C above the reaction equilibrium temperature. It is highly recommended to set the bath’s circulation pump at 4500 rpm.

6. Wait until both the reactive composite and the “Ministat 125” reach steady state. Verify that both have reached the set temperature.

7. Close valve V-07, then open valves V-02, V-03, V-06 and V-10. After, open slightly valve V-14 to slowly evacuate ammonia gas from the [V-01 to V-07] segment until pressure in this segment is just slightly above atmospheric pressure. Then, close valve V-14.

8. Open valves V-04 (compressor’s aspiration) and V-05 (compressor’s discharge) to send ammonia gas to the compressor. Close valve V-06.

9. Re-verify that the reactor is at steady state at the set temperature, valve V-01 is closed, the condenser/storage tank segment is at steady state at the set temperature, valves V-06 and V-07 are closed and valves V-04 and V-05 are open. Check also that the pressure at both the compressor’s suction and discharge are lower than 2 bar (the specified compressor cannot start operating above this value).

10. Set the data acquisition interval to $\Delta t = 1$ s.

11. **As quickly as possible** turn on the compressor, then open valve V-07, then open valve V-01 slowly while checking the pressure readings of transmitter CP-01. While opening valve V-01, make sure to not surpass 2 bar at the compressor’s suction. If this value is surpassed, momentarily close valve V-01 and wait for the compressor to draw out ammonia until pressure falls back to under 2 bar. The compressor should need just a few seconds to increase its discharge pressure up to the condenser’s pressure.

12. Upon opening of the valve V-01, the so-called “adiabatic phase” begins. It is characterized by a steep decrease in all temperature readings inside the reactor. This phase usually lasts for about 1 minute, and it is important to register temperatures in this phase, which justifies the $\Delta t = 1$ s for the data acquisition. After the adiabatic phase is over, the interval of data acquisition should be set back to at least $\Delta t = 10$ s.
13. During the reaction, keep an eye on the compressor’s suction pressure. The experimental $X = f(t)$ curve can be derived and plotted in the meantime.
14. As in other reactions of this setup, the end of reaction is characterized by all temperature readings inside the reactor being at steady state and very close to the “Ministat 125” set temperature. Another general indicator is the stagnation of the level of liquid ammonia inside the storage tank. For this particular reaction, yet another sign of reaction ending is the decrease in pressure at the reactor-to-compressor segment, which means that the rate of ammonia suction by the compressor outweighs the rate of ammonia gas release by the reaction.
15. When the ending of the decomposition reaction is verified by the signs listed in the previous step of this procedure, stop the compressor and close valves V-04 and V-05. Immediately after, close valve V-02 and verify that the pressure readings by the CP-01 transmitter do not increase notably. A big increase in this temperature reading might indicate the decomposition reaction is not yet over and the reactive composite keeps releasing ammonia gas.
16. After re-verifying the reaction’s end with the CP-01, change the set temperatures of the “Ministat 125” and “Winus Chiller C2-W3” baths to ambient temperature. Keep valve V-07 closed and valve V-08 open. Wait until the setup reaches the new steady state. Keep track of the level of liquid ammonia inside the storage tank and verify that it remains close to constant (the gradual increase in temperature implies a gradual increase in level). Keep an eye on the temperatures inside the reactor, too. They should gradually come back to ambient temperature.
17. After the setup reaches its new steady state, stop the “Ministat 125” and “Winus Chiller C2-W3” thermal baths. Then, close all valves of the setup.
18. Collect all the data registered and plot the experimental $X = f(t)$ curve. Compare it to the numerical $X = f(t)$ curve obtained by simulation of the reaction at the same operating conditions. It is also interesting to cross-check the relevant readings of temperature and pressure. When taken in the same segment, both readings are usually synchronized. The combined information of pressure and temperature can eventually help detect anomalies in the setup’s operation.

D.4 SYNTHESIS PHASE FROM AMMONIA BOTTLE (ALTERNATE PROCEDURE)

This is an alternate procedure for carrying out the synthesis reaction from an ammonia bottle instead of from the reservoir of the setup itself. This alternate procedure is useful for preliminary tests on the setup.

This procedure assumes that at the beginning, all valves are closed and the whole setup (except for the reactor) is filled with ammonia gas. The procedure is as follows:

1. Boot up the computer and the data acquisition software. Check that all transmitters, probes and measurement devices are correctly branched into the Agilent equipment and that data acquisition functions properly.

2. Start data acquisition with only the measurement devices involved in this process (i.e. CT-01, CP-01, and from TC-01 to TC-06). For the preliminary steps prior to the actual reaction, a rather large time step is recommended (e.g. $\Delta t = 10\text{-}20$ s).

3. Boot up the "Ministat 125" thermal bath. Choose a rotational speed of 4500 rpm for the centrifugal pump, and a set temperature of 5 °C for the thermal bath. This is the lowest operational set temperature if the bath is operating with pure water. It is recommended to use this temperature to facilitate heat transfer across the reactor's coating (which sometimes may be limiting).

4. Wait until the "Ministat 125" reaches the set temperature, as well as the reactive salt inside the reactor (the latter can be checked by means of the temperature probes from TC-01 to TC-04).

5. If the setup's pressure is higher than atmospheric (e.g. it contains ammonia gas because of operation, or pressurized nitrogen due to leak tests), reject gas through the purge valve until the overall pressure decreases to near 1 bar. If the setup contains ammonia gas, it is strongly recommended to protect the vacuum pump with a cold trap before continuing with this procedure.

6. Turn on the vacuum pump and the pressure indicator connected to it, then open valve V-PV. Wait until that section reaches the lowest possible pressure (which depends on the vacuum pump's power). Write that value down.

7. Sequentially, open valves V-15, V-10, V-02 and V-01. After this, the section delimited by the reactor, valve V-03, valve V-09 and valve V-14 should be at vacuum.

8. Sequentially, open valves V-14, V-BA and V-MB to apply vacuum to the tube connecting the bottle of ammonia to the setup.

9. Wait again until the whole section remains steady at vacuum. Check the pressure readings at the vacuum indicator and write the value down. This value may be slightly higher than that recorded in step 6, as a greater section of the setup has to be kept at vacuum.

10. Close valves V-15 and V-PV and shut down the vacuum pump.

11. Close valves V-MB, V-BA, V-14, V-10, V-02 and V-01.

12. Verify that the "Ministat 125" has indeed reached the set temperature. Turn on the weighting scales under the bottle of ammonia et write down the mass showed in the readings.

13. Open the general valve of the ammonia bottle (V-GB).

14. Twist the pressure regulator (V-MB) until the manometer close to the ammonia bottle reads a pressure of about 3.5 bar. At this pressure, the equilibrium temperature for the $\text{BaCl}_2/\text{NH}_3$ solid/gas reaction is about 30 °C. Thus, the recommended set temperature of 5 °C for the thermal bath (see Step 3) should be enough to dissipate the heat rejected by the exothermal reaction.

15. Sequentially, open valves V-BA, V-14, V-10 and V-02. Ammonia gas will progressively fill the section delimited by valves V-01, V-03, V-09 and V-15. As a side verification, it would be interesting to write down the mass readings by the scales after opening each valve, to later compare (through an equation of state) each Δm with the corresponding ΔV gained at the section by the opening of the valve.

16. Reduce the time step of data acquisition to $\Delta t = 1$ s.

17. Open valve V-01. Ammonia will enter the reactor and the exothermic reaction will begin. Verify the proper development of the adiabatic phase: thermocouples TC-01 to TC-04 should read a steep increase in temperature inside the reactive composite. These readings should reach a value close to the reaction's equilibrium temperature. In addition, all readings should increase to the same temperature: if there is a gradient from the innermost thermocouple to the outermost, it means that mass transfer within the composite is limiting. The advancement of the reaction should be soon visible by a temperature decrease in the outermost thermocouple.

18. The adiabatic phase is expected to last less than 5 minutes. However, the reaction will advance very quickly within this time lapse, and it may be difficult

to write down the weight readings by the scale. Therefore, it is recommended to record these readings on video during the first 5 minutes of reaction.

19. After the adiabatic phase comes to an end, the time step for data acquisition may be increased to $\Delta t = 10$ s. As for the weight readings, it suffices to write them down only at each $\Delta X = 0.01$. The mass of reacted ammonia that corresponds to each $\Delta X = 0.01$ can be easily inferred from the total mass of reactive salt by means of the reaction's stoichiometry. It is important to remember that in this procedure, the scales are the only measurement device that allows to calculate the advancement degree of reaction (X). The level probe of the ammonia reservoir does not proceed, as the charging is done directly from the bottle.

20. If enough ammonia gas is available, the operating pressure should remain constant along the reaction. Therefore, it is recommended to keep an eye on the pressure indicator CP-01 and the surface of the ammonia bottle (especially at the bottom). If the former detects a pressure decrease, or if the latter is covered in frost, increase the heating power connected to the ammonia bottle.

21. Heat transfer across the reactor's surface might be limiting at some point. Therefore, it is recommended to keep an eye on the ΔT of the external heat transfer fluid between the coating's inlet and outlet. If this temperature difference is large, it is recommended to reduce the set temperature of the "Ministat 125". If set temperatures lower than $0\text{ }^{\circ}\text{C}$ are required, a water/glycol mixture should be used for the thermal bath.

22. Two major indicators will point out that the synthesis reaction has come to an end. First, the weight readings by the scales will remain steady, as no more ammonia is being accepted by the reactive composite. Second, the temperature readings by thermocouples TC-01 to TC-04 will remain steady at a value not far from the set temperature of the thermal bath, as no more heat is being released by the reaction.

23. After the end of the synthesis reaction is confirmed, turn off the "Ministat 125" thermal bath. Successively, close valve V-GB, close the pressure regulator V-MB, and close valves V-BA, V-14 and V-01. After this, check that the pressure and temperature readings for the ammonia gas inside the setup remain steady.

24. Collect and analyze the data. Compare the real mass of ammonia introduced to the reactor with the theoretical value that was predicted from the reaction's stoichiometry. Obtain the reaction's $X-t$ curve.

D.5 CHARGE OF AMMONIA (AUXILIARY PROCEDURE)

The main goal of this procedure is to fill the setup's reservoir with liquid ammonia for further usage internally in the setup. The need for filling the ammonia reservoir may come after periods of idleness or maintenance of the setup. The key component in this procedure is the level probe inside the reservoir (CN), as it is the only source of information about the state of charge of the reservoir. The scales under the ammonia bottle allow for an additional verification of the amount of ammonia introduced in the setup. It is also strongly recommended to attach a heating system to the ammonia bottle. The valves should follow the configuration shown in table A.1.

Table A.1. Initial configuration of the valves for charging ammonia into the experimental setup.

Always closed	V-01	V-02	V-04	V-05	V-09	V-11	V-12	V-13	V-DE
Closed at the beginning	V-15	V-BA	V-GB	V-MB	V-PV	-	-	-	-
Open at the beginning	V-08	V-14	-	-	-	-	-	-	-
Always open	V-03	V-06	V-07	V-10	-	-	-	-	-

This procedure assumes that any section not containing ammonia has been submitted to vacuum. The following steps are suggested:

1. Boot up the control computer and the data acquisition software. Check that data acquisition functions properly and all transmitters, probes and measurement devices are correctly branched into the Agilent equipment.

2. Start data acquisition with only the measurement devices involved in this process, i.e. the level probe and all pressure and temperature transmitters englobed in the ammonia's way from bottle to reservoir. For the preliminary steps prior to the actual procedure, a rather large time step is recommended (e.g. $\Delta t = 10\text{-}20$ s).

3. Turn on the "Minichiller" thermal bath with a set temperature of -5 °C. Wait until it reaches that temperature.

4. Turn on the electronic scales and write down the current value.

5. Turn on the vacuum measurer and the vacuum pump. Open valve V-PV and wait until the section reaches the lowest possible pressure. Write down that pressure.

6. Open valves V-BA and V-15 to apply vacuum inside the tube connecting the ammonia bottle to the setup.

7. Once the segment has reached the lowest possible pressure, close valve V-PV and turn off the vacuum pump.

8. Close valve V-14 and re-verify that the “Minichiller” thermal bath has reached the set temperature.

9. Open the general valve of the ammonia bottle (V-GB).

10. Open the pressure regulator (V-MB) until reaching a pressure of 5 bar in the segment. At this pressure, the vapor/liquid phase change temperature of pure ammonia is around 5 °C. Thus, the set temperature of the “Minichiller” thermal bath (around -5 °C) should be enough to ensure condensation of the vapor ammonia.

11. Turn on the heating system attached to the ammonia bottle. From this point on, check regularly the lower part of the bottle to see if frost is appearing, in which case more heating power is needed.

12. Successively, open valves V-14, V-10, V-03, V-06, V-11, V-12, V-09 and V-13. Ammonia vapor will progressively fill the segment delimited by valves V-02, V-04, V-05 and V-15.

13. Open **simultaneously** valves V-07 and V-08. Ammonia vapor should begin condensing and accumulating inside the reservoir. To make sure, check the pressure reading of transmitter CP-02, and compare the corresponding theoretical condensing temperature with the temperature reading of transmitter CT-05. These two temperatures should be quite similar.

14. Having verified that ammonia is condensing, keep track of the temperature readings of thermocouples TC-07 and TC-08. These temperatures should drop not too long after ammonia has started condensing.

15. After thermocouples TC-07 and TC-08 have dropped in temperature, start keeping track of the readings of the level probe (CN). Wait until the reservoir is close to full.

16. Close valve V-14 well before the maximum level of liquid ammonia is reached. Due to inertia, liquid ammonia will continue to accumulate inside the reservoir for a little time after closing the valve.

17. Wait until the level of liquid ammonia has stabilized. If maximum level has not been reached, carefully allow some more ammonia into the condenser by alternatively re-opening and re-closing valve V-14.

18. Once the target level of liquid ammonia has been reached, close completely valves V-GB, V-BA and V-14. Turn down the heating system attached to the bottle of ammonia. Write down the weight reading shown by the electronic scale.

19. Turn off the "Minichiller" thermal bath. Close valves V-08, V-11, V-12 and V-13. Collect all data from the data acquisition software.

Appendix E: Extended results of the experimental study of the decomposition and compression-assisted decomposition phases of the hybrid compression/thermochemical refrigeration system

Table A.2. List and operating conditions of all reactions carried out with the experimental hybrid compression/thermochemical refrigeration system.

#	Phase	P_c	$T_{eq,NH_3} (P_c)$	$T_{eq,R} (P_c)$	T_c	ΔT_{eq}	P_{cond}
		bar	°C	°C	°C	°C	bar
S1	Synthesis	3.5	-5.4	29.8	5.0	-24.8	-
D1	Decomposition	7.2	14.6	45.0	68.0	+23.0	7.2
S2	Synthesis	3.5	-5.4	29.8	5.0	-24.8	-
D2	Decomposition	7.2	14.6	45.0	68.0	+23.0	7.2
S3	Synthesis	3.5	-5.4	29.8	5.0	-24.8	-
D3	Decomposition	7.2	14.6	45.0	68.0	+23.0	7.2
S4	Synthesis	3.5	-5.4	29.8	9.0	-20.8	-
D4	Decomposition	3.5	-5.4	29.8	40.0	+10.2	3.5
S5	Synthesis	5.0	4.1	37.1	5.0	-32.1	-
D5	Compression-assisted decomposition	1.0	-33.6	6.7	50.0*	+43.3	5.0
S6	Synthesis	5.0	4.1	37.1	9.0	-28.1	-
D6	Decomposition	5.0	4.1	37.1	80.0	+42.9	5.0
S7	Synthesis	5.0	4.1	37.1	9.0	-28.1	-
D7	Compression-assisted decomposition	1.0	-33.6	6.7	50.0	+43.3	3.7
S8	Synthesis	4.0	-1.9	32.5	9.0	-23.5	-
D8	Compression-assisted decomposition	1.0	-33.6	6.7	50.0	+43.3	4.4

E.1 Extended results from the synthesis phases

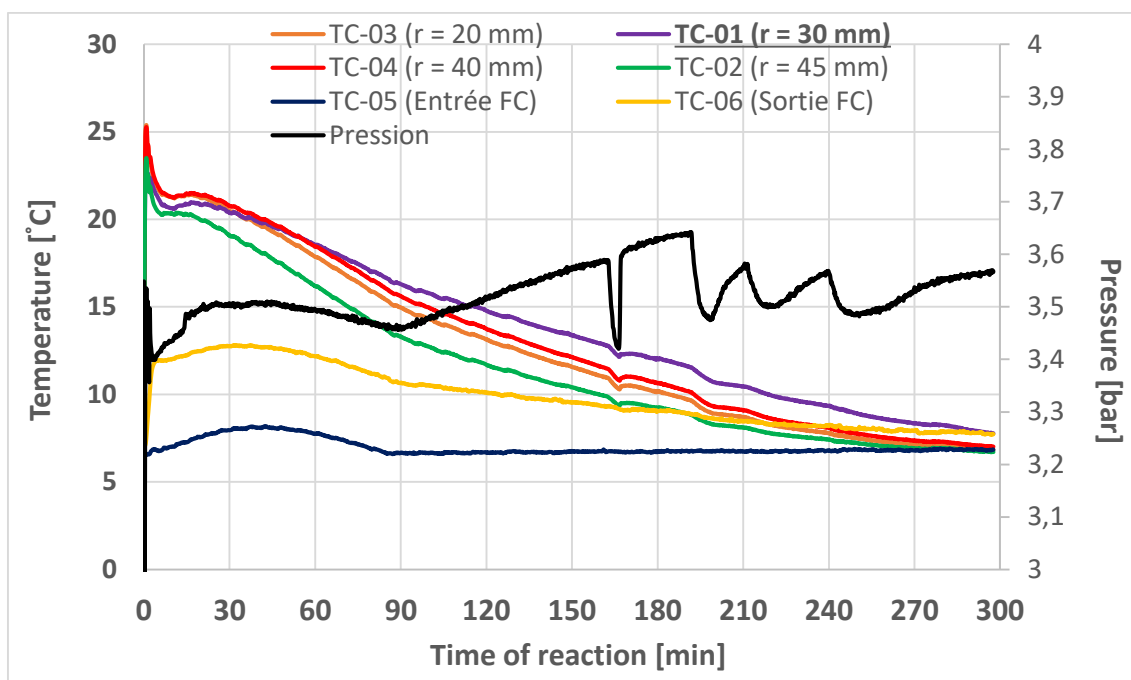


Figure A.19. Evolution of reactor pressure and temperatures in experiment S1.

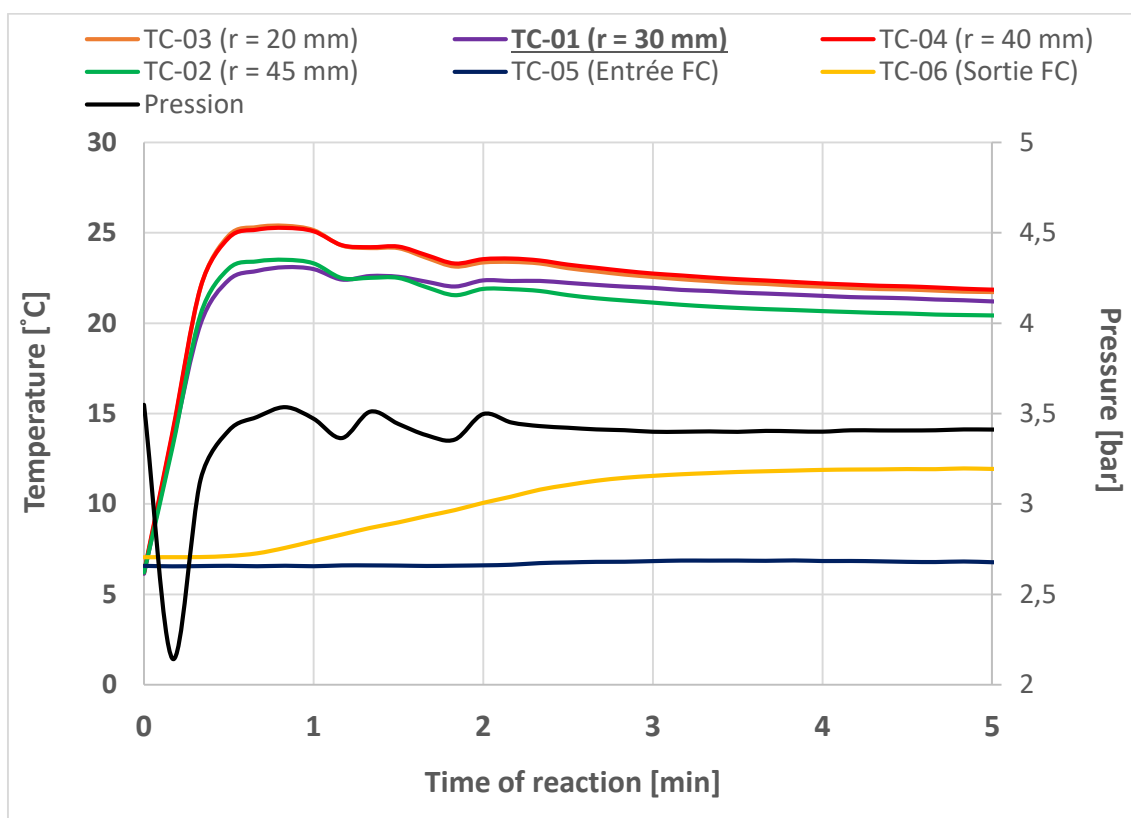


Figure A.20. Evolution of T and P during the first 5 minutes of experiment S1.

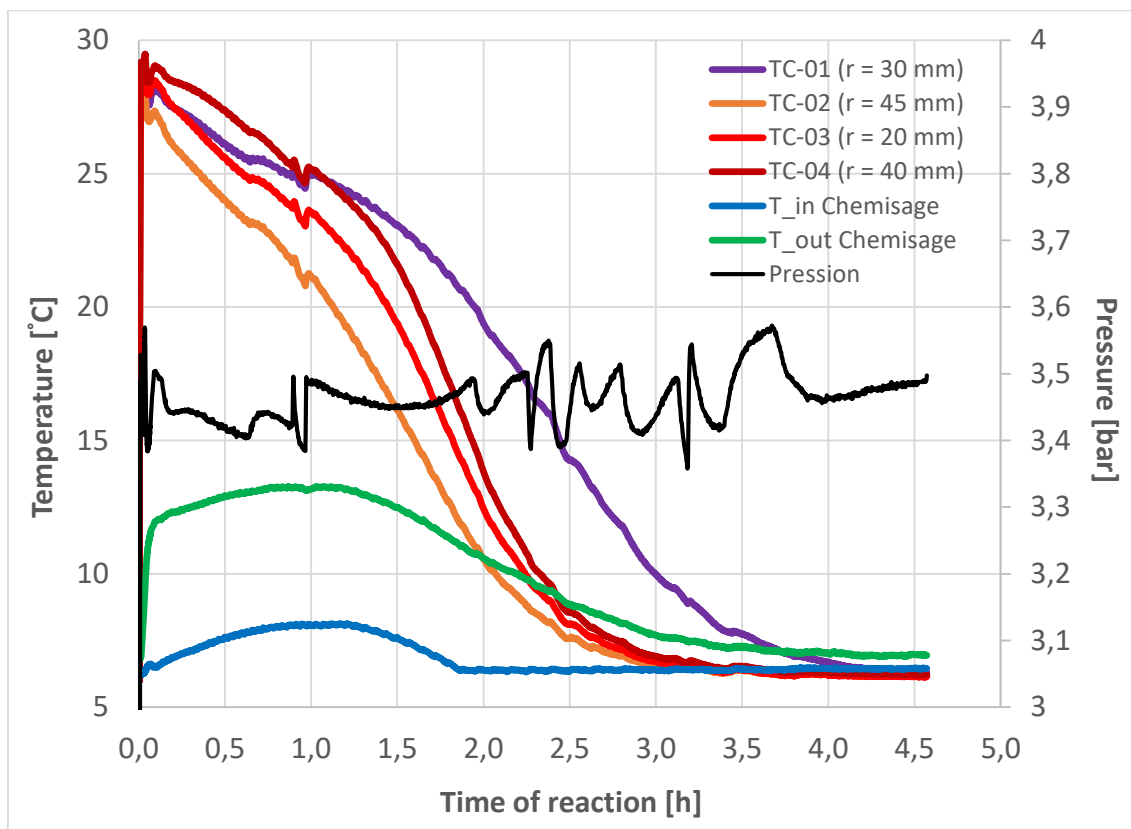


Figure A.21. Evolution of reactor pressure and temperatures in experiment S2.

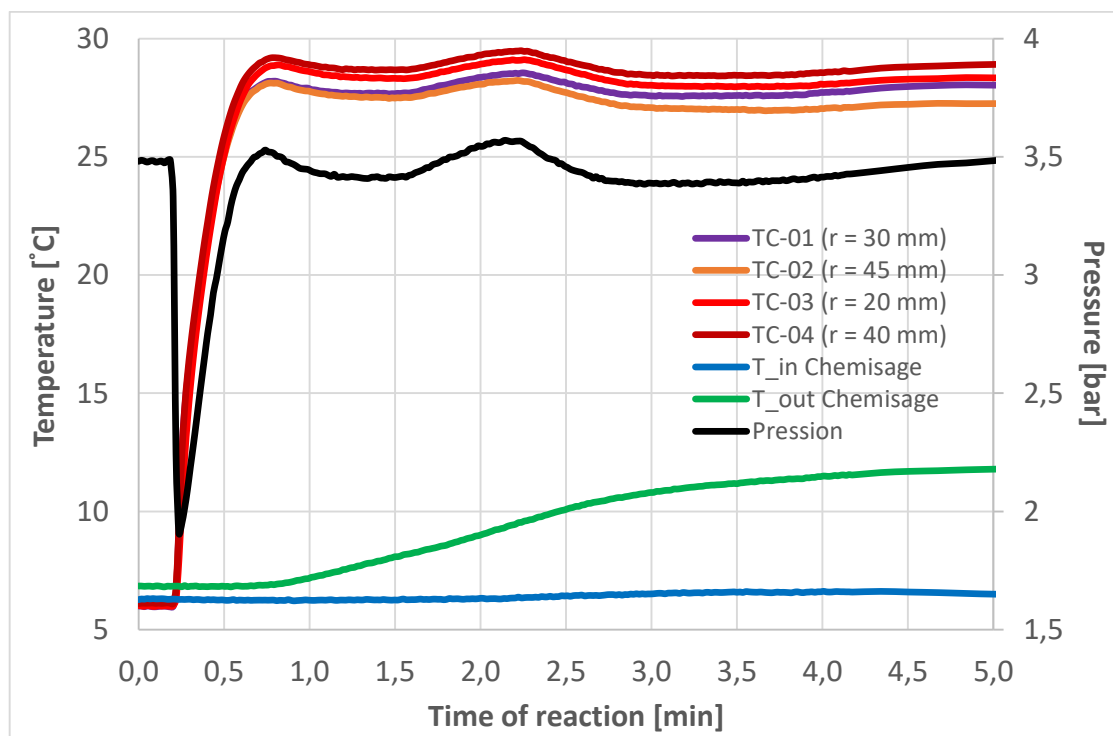


Figure A.22. Evolution of T and P during the first 5 minutes of experiment S2.

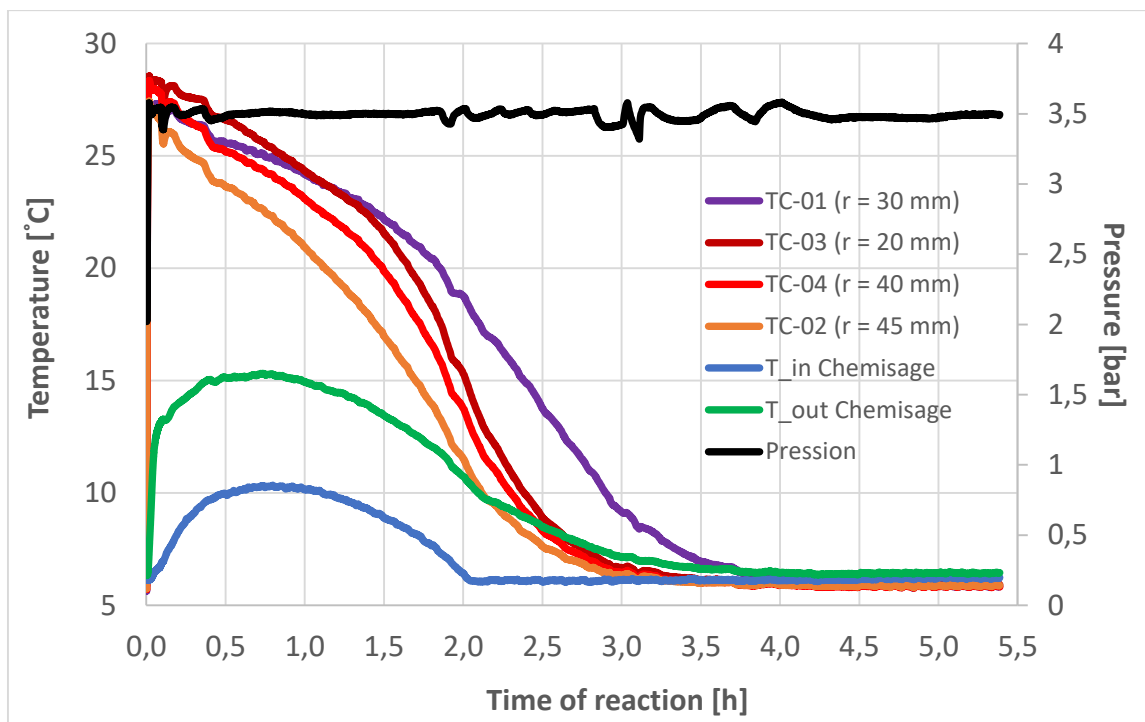


Figure A.23. Evolution of reactor pressure and temperatures in experiment S3.

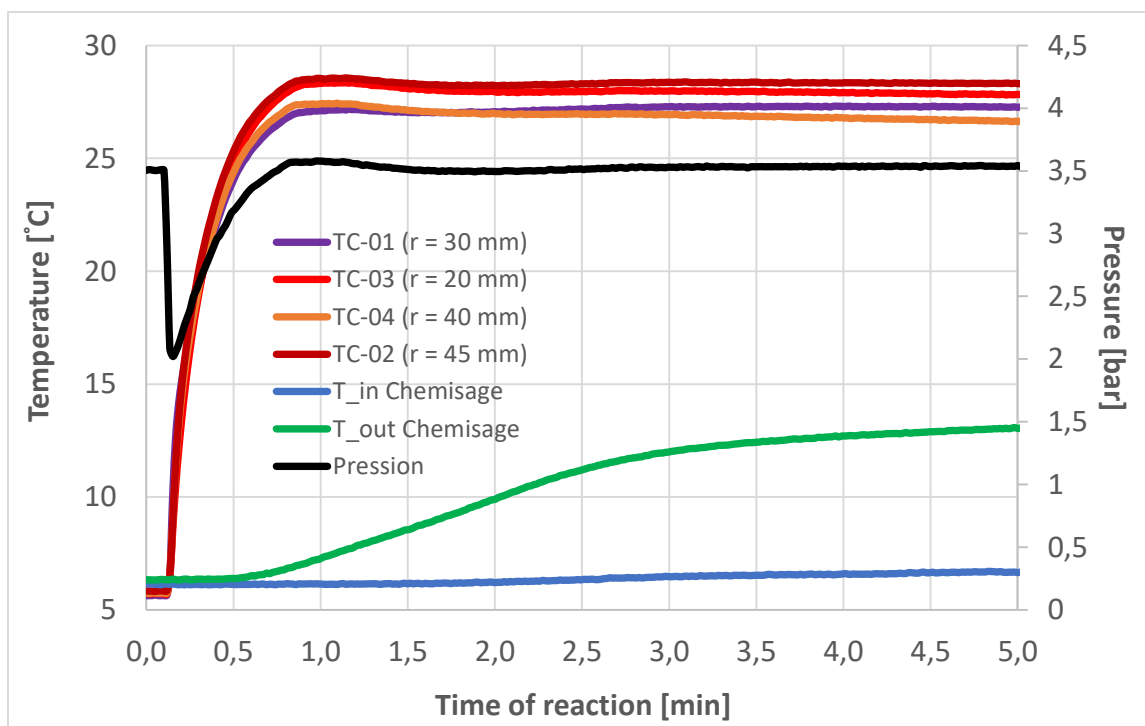


Figure A.24. Evolution of T and P during the first 5 minutes of experiment S3.

E.2 Extended results from (non-assisted) decomposition phases

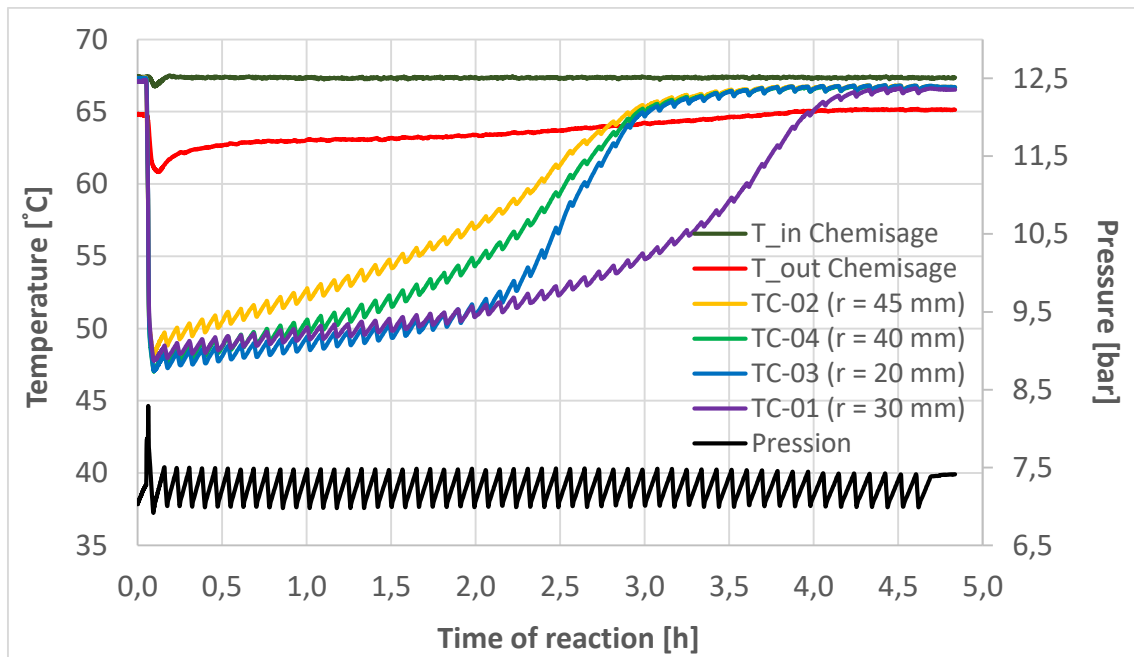


Figure A.25. Evolution of reactor pressure and temperatures in experiment D1.

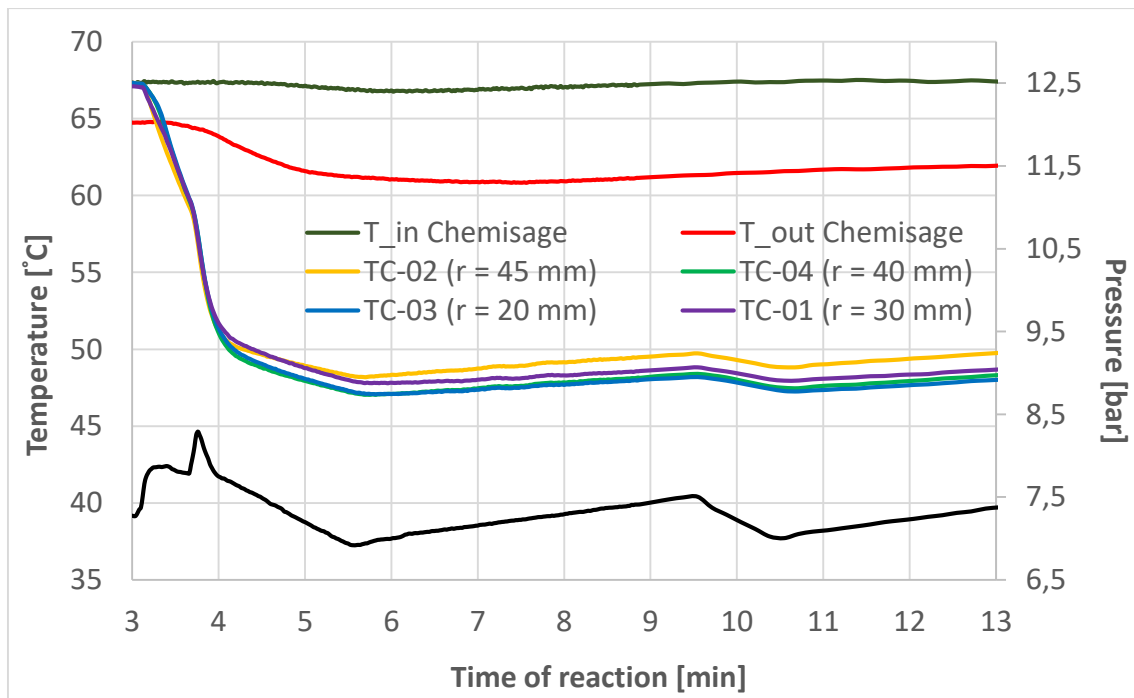


Figure A.26. Evolution of T and P from minute 3 to minute 13 of experiment D1.

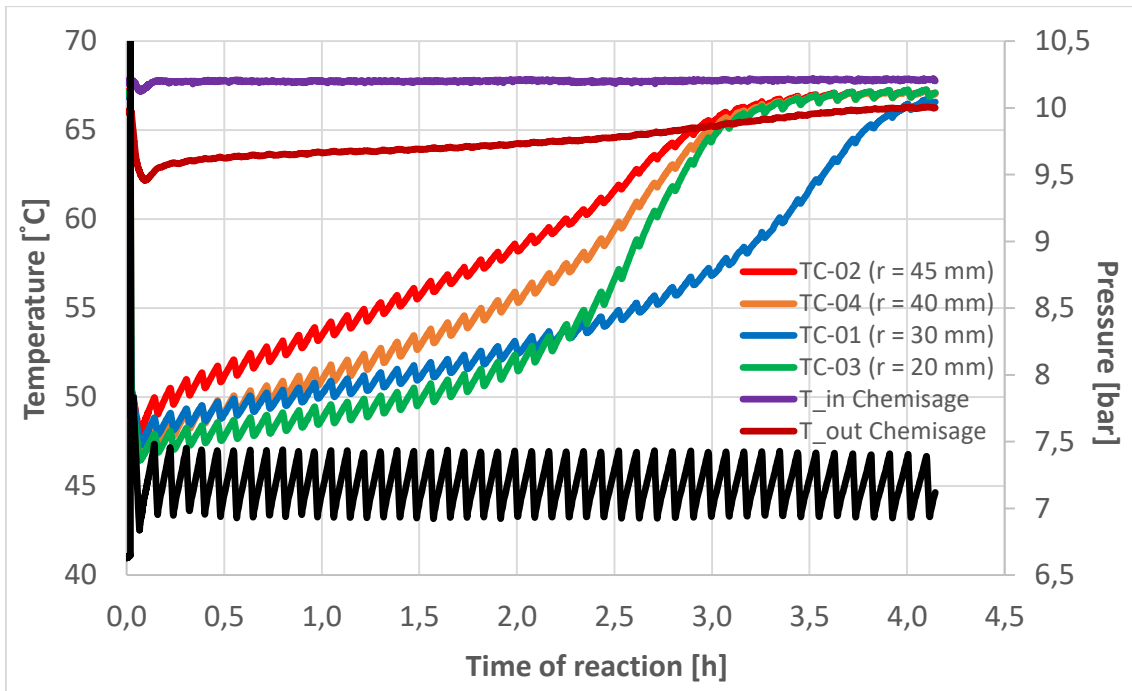


Figure A.27. Evolution of reactor pressure and temperatures in experiment D2.

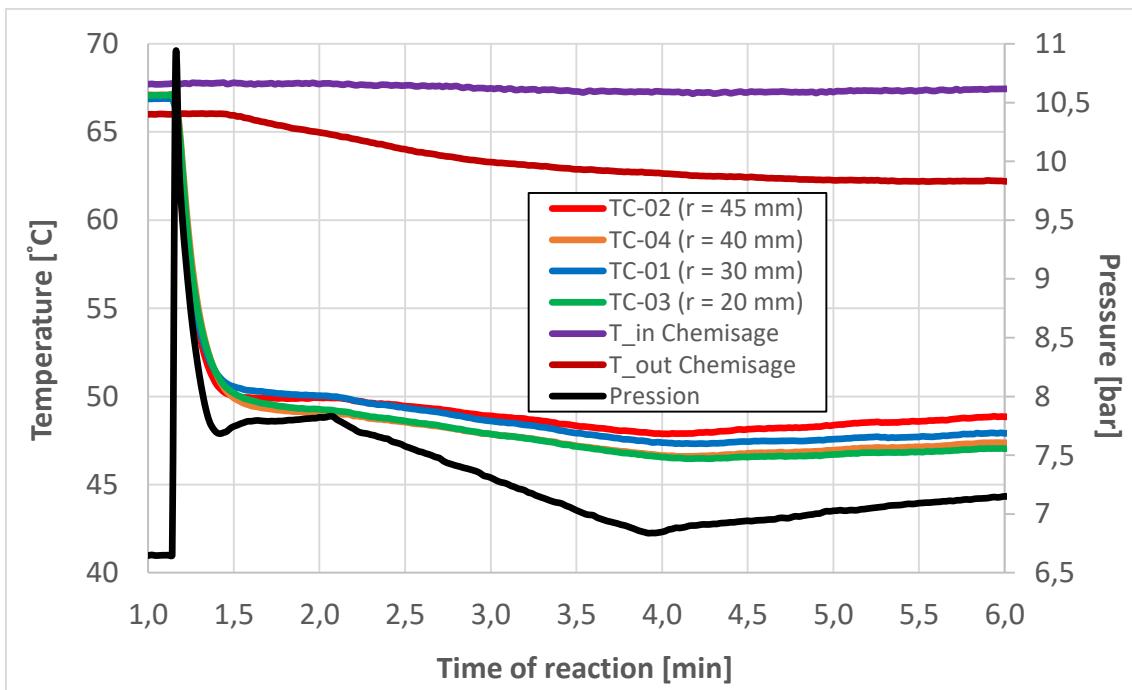


Figure A.28. Evolution of T and P during the first 5 minutes of experiment D2.

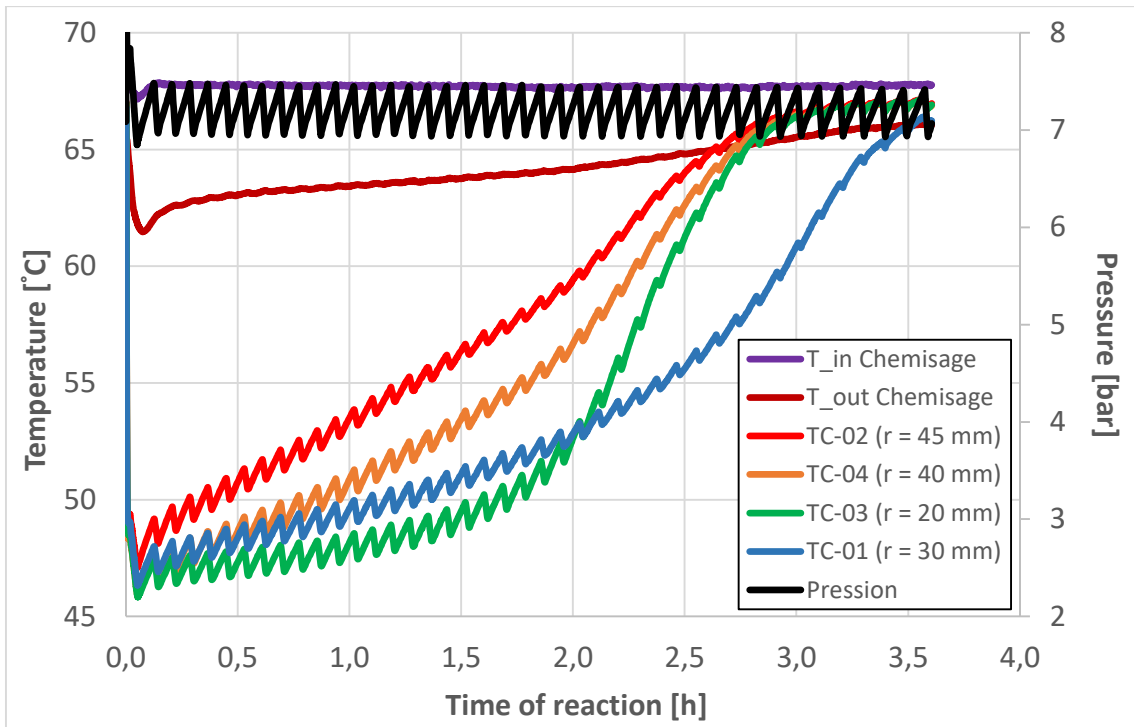


Figure A.29. Evolution of reactor pressure and temperatures in experiment D3.

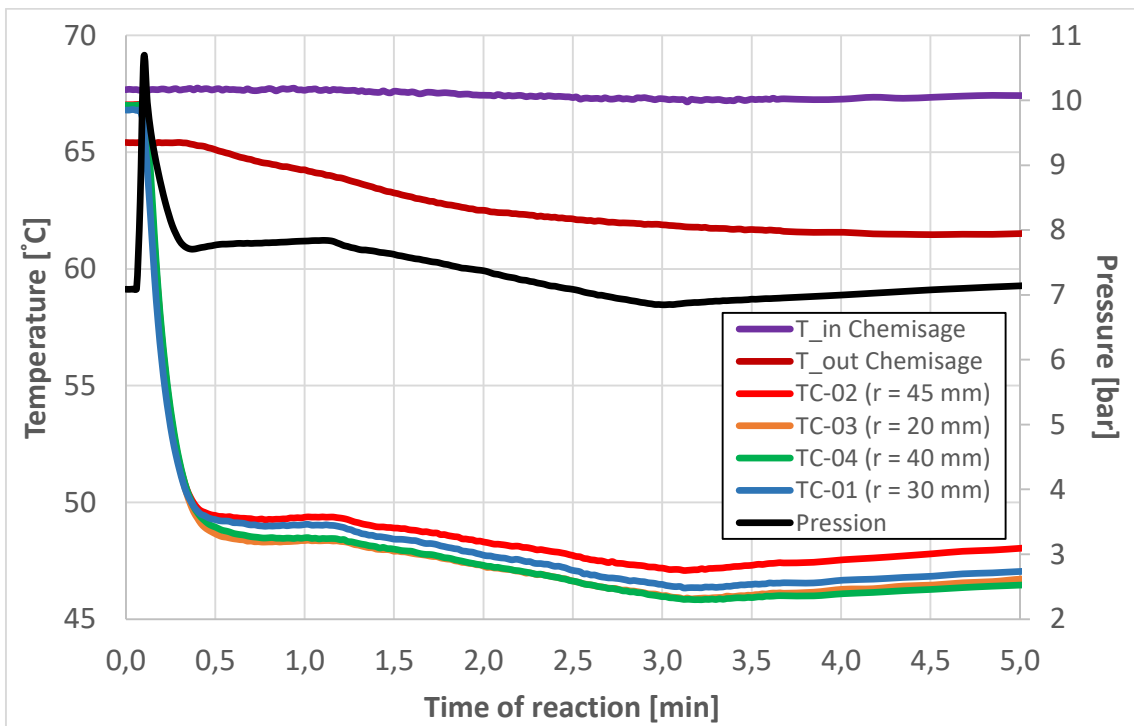


Figure A.30. Evolution of T and P during the first 5 minutes of experiment D3.

E.3 Extended results from compression-assisted decomposition phases

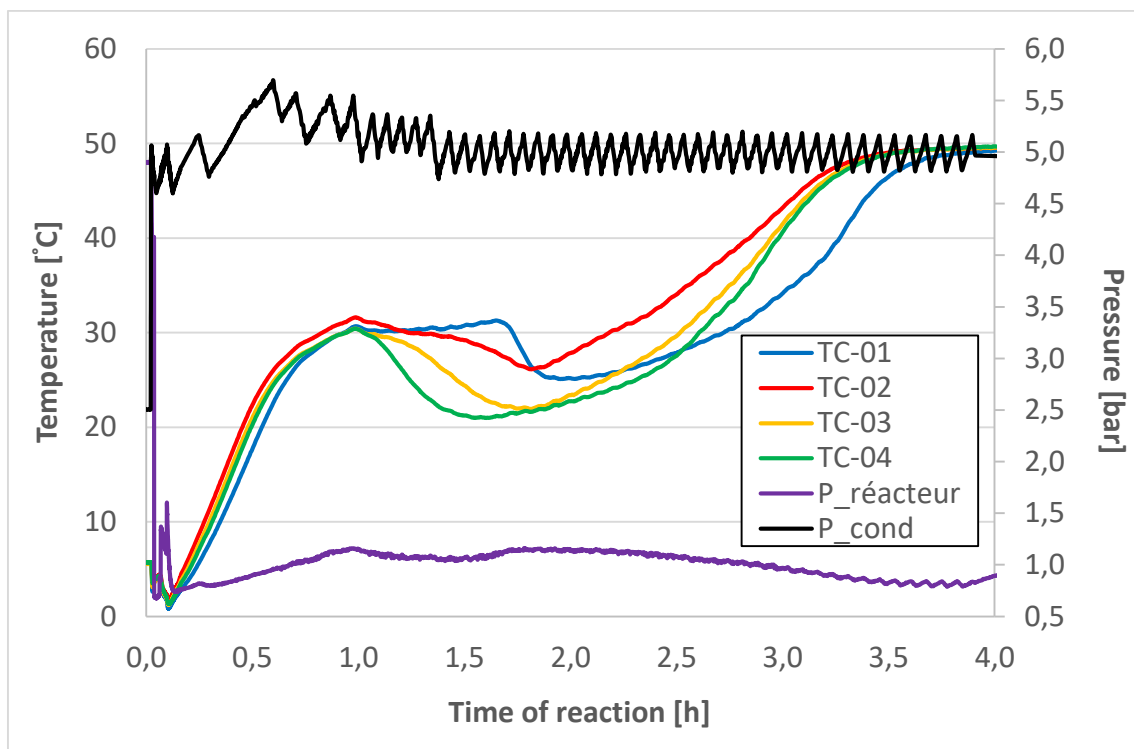


Figure A.31. Evolution of reactor pressure and temperatures in experiment D5.

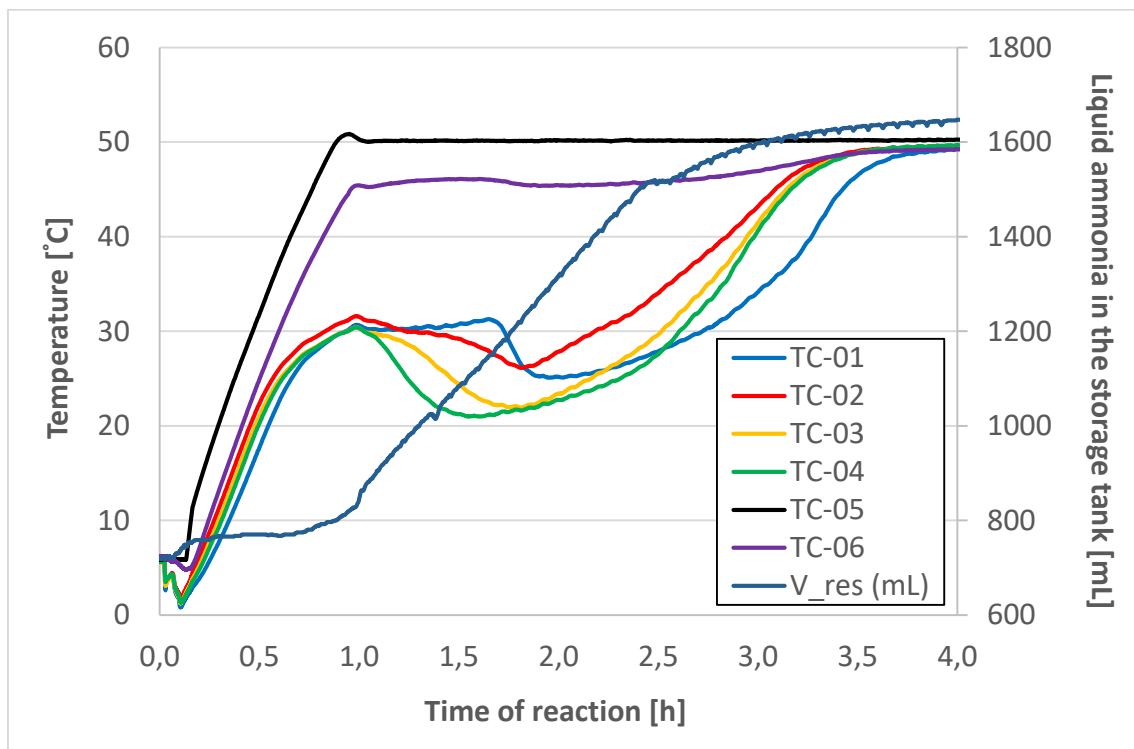


Figure A.32. Evolution of coating T and stored ammonia during experiment D5.

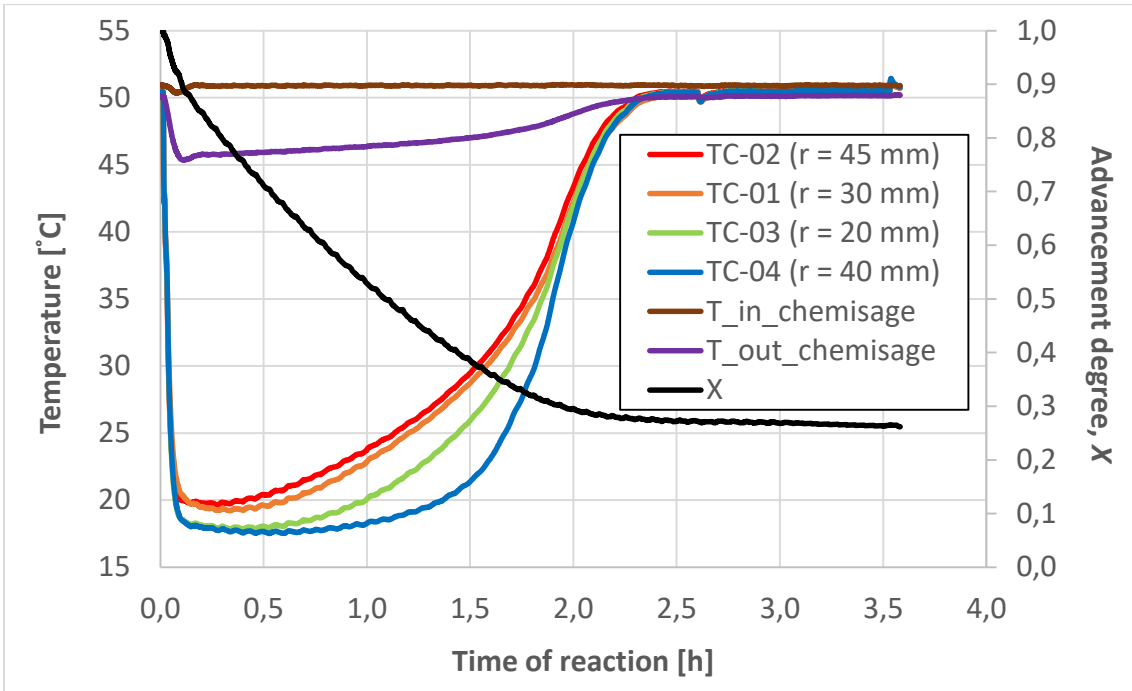


Figure A.33. Evolution of the temperatures and X in experiment D7.

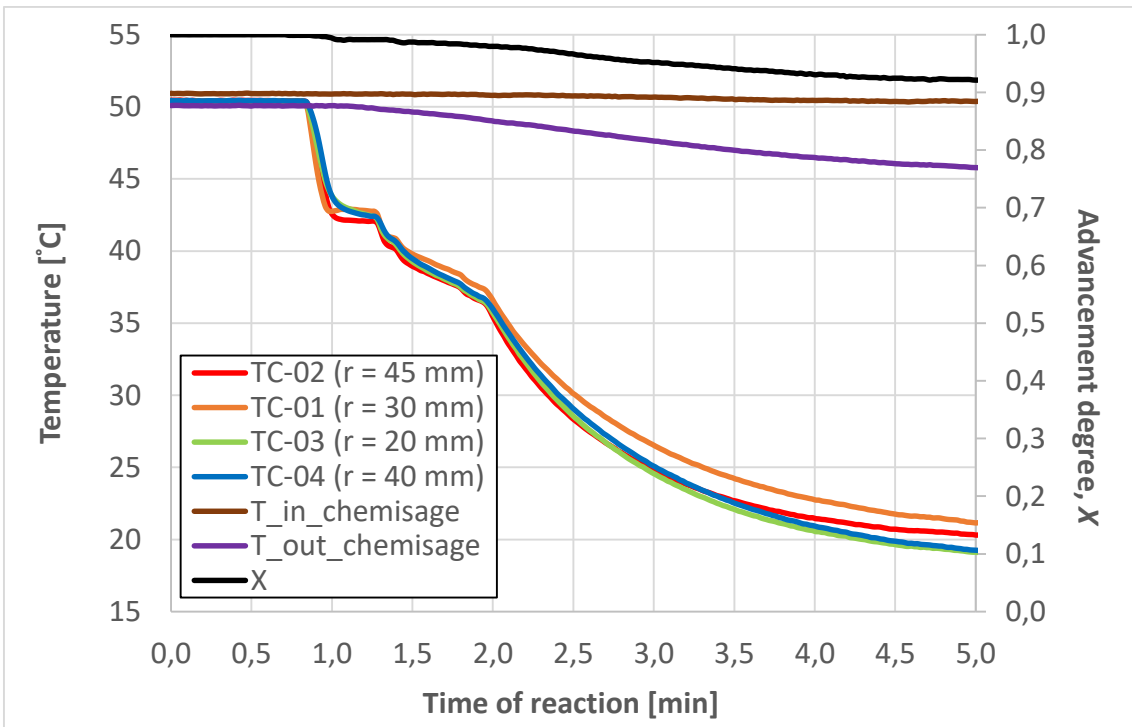


Figure A.34. Evolution of the T and X in the first 5 minutes of experiment D7.

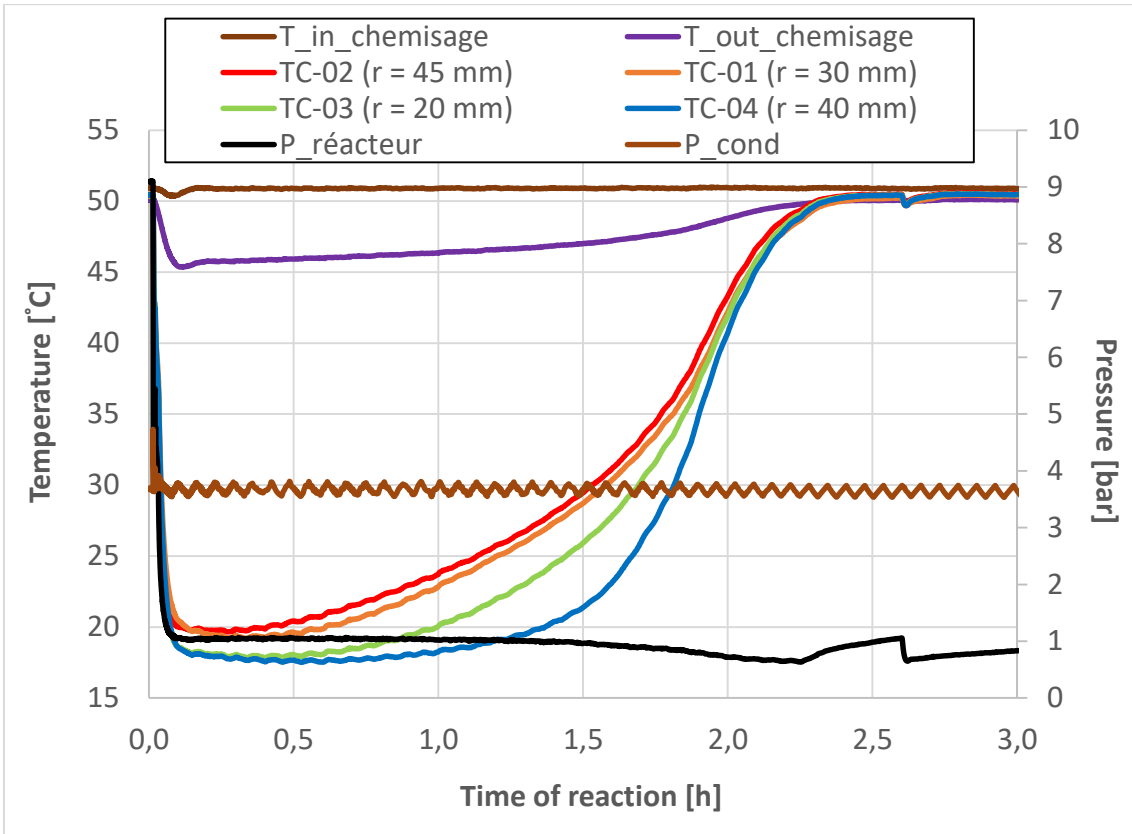


Figure A.35. Evolution of pressures and temperatures in experiment D8.

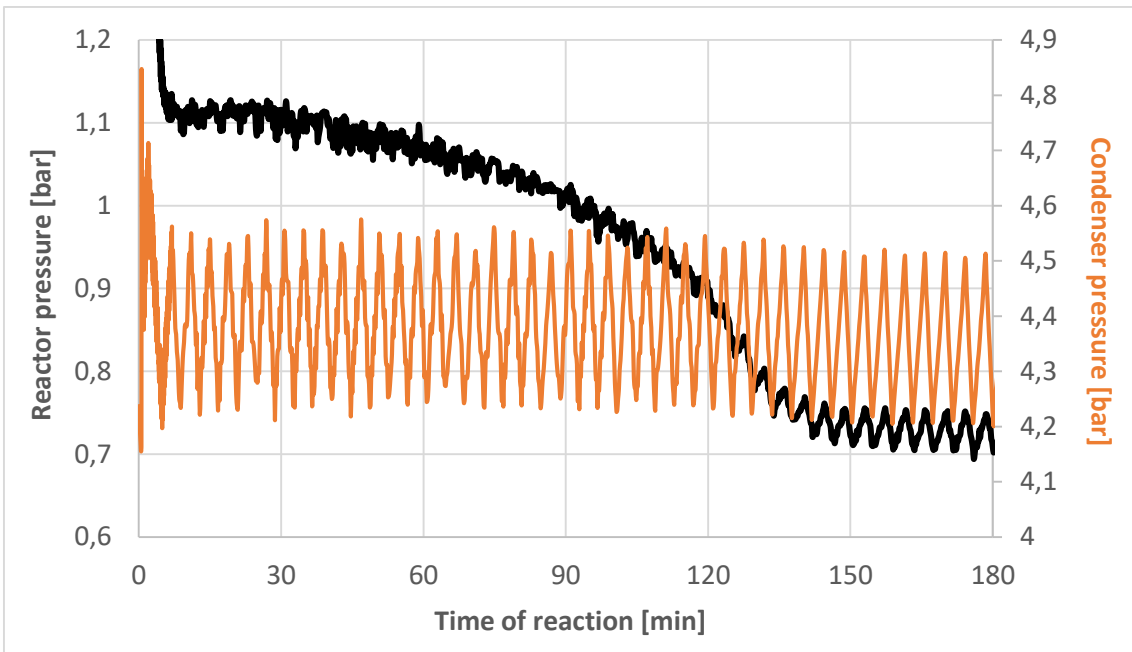


Figure A.36. Evolution of reactor and condenser pressures in experiment D8.



UNIVERSITAT
ROVIRA i VIRGILI